Synthesis of 2D Quantum Materials for Nanoelectronic and Nanophotonic Applications

Thesis by

Wei-Hsiang Lin

In Partial Fulfillment of the Requirements for
the Degree of
Doctor of Philosophy

CALIFORNIA INSTITUTE OF TECHNOLOGY
Pasadena, California

2021
Defended March 24, 2021

Wei-Hsiang Lin
ORCID: 0000-0003-0037-1277

ACKNOWLEDGEMENTS

To start, I would like to acknowledge both of my thesis advisors, Professor Harry Atwater and Professor Nai-Chang Yeh.

Professor Harry is a truly unique advisor who treats his students with respect and he always has their back. It has been a great honor to work with him.

Professor Yeh is a great advisor and I thank her for the time she spent proofreading my thesis even though time is the hardest thing for her to squeeze out.

I would like to thank Professor George Rossman for being so generous and sharing his facilities with me so I could start my research easily at Caltech.

Second, I would like to acknowledge Professor Stevan Nadj-Perge and Professor Joseph Falson for their willingness to be on my thesis committees. I am extremely grateful to Professor Stevan Nadj-Perge for agreeing to serve as the chair.

Over the years, I have been very lucky for having the opportunity to work with some of the best postdocs. I am glad that I had Dr. Howard Lee, Dr. Victor Brar, Dr. Deep Jariwala, and Dr. Pin Chieh Wu who would always share their ideas and give me advice.

There are so many other scientists, postdocs, and grad students that I have been fortunate to work with and I would like to thank here: Seokmin Jeon, Seyoon Kim, Michelle Sherrott, William Whitney, Laura Kim, Souvik Biswas, Cora Went, Joeson Wong, Dagny Fleischman, Phillip Jahelka, Wen Hui (Sophia) Cheng, and Yonghwi Kim.

I also want to thank all the staff members of the KNI for support and training: Guy de Rose, Melissa Melendes, Matt Sullivan-Hunt, Nils Asplund, Steven Martinez, Bert Mendoza, Nathan Lee, Alex Wertheim, and Barry Baker. They have helped me immensely, and have made the many hours I spent in the subbasement so much more enjoyable. So much appreciation additionally needs to be given to the incredible administrators who hold everything together: Jennifer, Tiffany, Liz, Lyann, Jonathan, and Kam.

ABSTRACT

2D materials have attracted tremendous attention for a variety of properties such as ultra-low body thickness, ultra-high mobility, and tunable bandgap. These unique merits of the 2D materials bring in the significant improvements and new perspectives in the digital CMOS scaling, analog performance, as well as the 3D integration of wafer stacking.

In this thesis, we explore van der Waals materials for future CMOS technologies. Chapter 2 introduces a compatible and a single-step method for synthesizing high-mobility monolayer graphene (MLG) in merely a few minutes by means of plasma-enhanced chemical vapor deposition (PECVD) techniques without the need of active heating. This environment enables graphene growth on different surfaces at relatively low temperatures, which paves ways to a CMOS-compatible approach to graphene synthesis. Chapter 3 describes the development of a synthesis method that controls the growth of large-area h-BN films from monolayer to 30 atomic layers, and summarizes the characterizations of the properties of these h-BN films that demonstrate the high-quality of these materials.

New degrees of freedom possess the immense potential and attract huge attentions as the imminent end of “Moore’s Law”. Compared with the traditional charge degree of freedom, spin and valley are the other two additional internal degree of freedom in solid-state electronics which enable the spintronic and valleytronic devices with high integration density, fast processing speed, low power dissipation, and non-volatility. Monolayer transition-metal dichalcogenides (TMDCs) in the 2H-phase are semiconductors promising for opto-valleytronic and opto-spintronic applications because of their strong spin-valley coupling. In chapter 4, we report detailed studies of opto-valleytronic properties of heterogeneous domains in CVD-grown monolayer WS_2 single crystals. By illuminating WS_2 with off-resonance circularly-polarized light and measuring the resulting spatially resolved circularly-polarized emission (P_{circ}), we find large circular polarization increases significantly to nearly 90% at 80 K. In Chapter 5, it is reported that valley polarized PL of monolayer WS_2 can be efficiently tailored at room temperature (RT) through the surface plasmon-exciton interaction with plasmonic Archimedes spiral (PAS) nanostructures. The DVP of WS_2 using 2 turns (2T)

and 4 turns (4T) of PAS can reach up to 40% and 50% at RT, respectively. Further enhancement and continuous control of excitonic valley polarization in electrostatically doped monolayer WS_2 are demonstrated. Under the circularly polarized light on WS_2-2TPAS heterostructure, 40% valley polarization of exciton without electrostatic doping is icreased to 70% by modulating the carrier doping via a backgate. This enhancement of valley polarization may be attributed to the screening of momentum-dependent long-range electron-hole exchange interactions. The demonstration of electrical tunability in the valley-polarized emission from WS_2-PAS heterostructures provides new strategies to harness valley excitons for application in ultrathin valleytronic devices.

In contrast to future optical switch applications, in Chpater 6, it is reported that Ternary tellurides based on alloying different 2D transition metal dichalcogenides can result in interesting new 2D materials with tunable optical and electrical properties. Additionally, such alloys can provide opportunities for significantly improving the electrical contact properties at the metal-semiconductor interface. In particular, realization of practical devices based on the 2D materials will require overcoming the typical Fermi-level pinning limitations of the electrical contacts at the metal-semiconductor interface and ultimately approaching the ideal Schottky-Mott limit. In this work, we develop a simple method of stacking 3D/2D electrical metal contacts onto dangling-bond-free 2D semiconductors in order to surmount the typical issue of Fermi-level pinning. Specifically, contacts of Au, graphene/Au, and WTe_2/Au are transferred onto $WS_{1.94}Te_{0.06}$ alloy-based devices via a new transfer method. The $WS_{1.94}Te_{0.06}$ field-effect transistors (FETs) with WTe_2/Au contacts reveal a field-effect mobility of 25 $cm^2V^{-1}s^{-1}$, an on/off current ratio of 10^6, and extremely low contact resistance of 8 kΩ μm. These electrical properties are far more superior to similar devices with either Au or graphene/Au contacts, which may be attributed to the fact that the work function of WTe_2 is close to the band edge of the $WS_{1.94}Te_{0.06}$ alloy so that the resulting metal-semiconductor interface of the FETs are free from Fermi-level pinning. The Schottky barrier heights of the $WS_{1.94}Te_{0.06}$-FETs with WTe_2/Au contacts also follow the general trend of the Schottky-Mott limit, implying high-quality electrical contacts. Finally, in Chapter 7, several promising opportunities were proposed for future CMOS integrated circuits based on monolayer semiconductors.

PUBLISHED CONTENT AND CONTRIBUTIONS

(1) Lin, W.-H.; Li, C.-S.; Wu, C.-I.; Rossman, George. R.; Atwater, H.A.; Yeh, N.-C. 2H-1T′ Phase-Engineered Synthesis of Monolayer $WS_{2x}Te_{2(1-x)}$ Alloys for Two-Dimensional Metal-Semiconductor Contact at the Schottky-Mott Limit. (To be submitted)
W.-H. Lin conceived the research ideas, and participated in all the measurements and data analysis. W.-H. Lin and N.-C. Yeh wrote the manuscript.

(2) Lin, W.-H.; Wu, P.C.; Akbari, H.; Rossman, George. R.; Atwater, H.A.; Yeh, N.-C. Electric Tuning and Boosting Valley-Polarized Emission of Monolayer WS_2 Sandwiched in Plasmonic Archimedes Spiral (PAS) Nanostructures. (To be submitted)
W.-H. Lin conceived the research ideas, and participated in all the measurements and data analysis. W.-H. Lin, N.-C. Yeh and H.A. Atwater wrote the manuscript.

(3) Akbari, H.; Lin, W.-H.; Vest, B.; Jha, P. K.; Atwater, H. A. Temperature-Dependent Spectral Emission of Hexagonal Boron Nitride Quantum Emitters on Conductive and Dielectric Substrates. *Phys. Rev. Applied* **2021**, *15* (*1*), 014036. https://doi.org/10.1103/PhysRevApplied.15.014036.
W.-H. Lin conceived the CVD h-BN synthesis and transferring process.

(4) Lin, W.-H.; Tseng, W.-S.; Went, C. M.; Teague, M. L.; Rossman, George. R.; Atwater, H. A.; Yeh, N.-C. Nearly 90% Circularly Polarized Emission in Monolayer WS2 Single Crystals by Chemical Vapor Deposition. *ACS Nano* **2020**, *14* (*2*), 1350–1359. https://doi.org/10.1021/acsnano.9b05550.
W.-H. Lin conceived the research ideas, and participated in all the measurements and data analysis. W.-H. Lin, N.-C. Yeh and H.A. Atwater wrote the manuscript.

(5) Chen, Y.-C.; Lin, W.-H.; Tseng, W.-S.; Chen, C.-C.; Rossman, George. R.; Chen, C.-D.; Wu, Y.-S.; Yeh, N.-C. Direct Growth of Mm-Size Twisted Bilayer Graphene by Plasma-Enhanced Chemical Vapor Deposition. *Carbon* **2020**, *156*, 212–224. https://doi.org/10.1016/j.carbon.2019.09.052.
W.-H. Lin conceived the KPFM measurements.

(6) Tsai, S.-H.; Lei, S.; Zhu, X.; Tsai, S.-P.; Yin, G.; Che, X.; Deng, P.; Ng, J.; Zhang, X.; Lin, W.-H.; Jin, Z.; Qasem, H.; Zhou, Z.; Vajtai, R.; Yeh, N.-C.; Ajayan, P.; Xie, Y.-H.; Wang, K. L. Interfacial States and Fano–Feshbach Resonance in Graphene－Silicon Vertical Junction. *Nano Lett.* **2019**, *19* (*10*), 6765–6771. https://doi.org/10.1021/acs.nanolett.9b01658.
W.-H. Lin conceived the PECVD graphene synthesis and polymer-free transferring process.

(7) Lin, W.-H.; Brar, V. W.; Jariwala, D.; Sherrott, M. C.; Tseng, W.-S.; Wu, C.-I.; Yeh, N.-C.; Atwater, H. A. Atomic-Scale Structural and Chemical Characterization of Hexagonal Boron Nitride Layers Synthesized at the Wafer-Scale with Monolayer Thickness Control. *Chem. Mater.* **2017**, *29* (*11*), 4700–4707. https://doi.org/10.1021/acs.chemmater.7b00183.
W.-H. Lin conceived the research ideas, and participated in all the measurements and data analysis. W.-H. Lin, and H.A. Atwater wrote the manuscript.

(8) Whitney, W. S.; Sherrott, M. C.; Jariwala, D.; Lin, W.-H.; Bechtel, H. A.; Rossman, G. R.; Atwater, H. A. Field Effect Optoelectronic Modulation of Quantum-Confined Carriers in Black Phosphorus. *Nano Lett.* **2017**, *17* (*1*), 78–84. https://doi.org/10.1021/acs.nanolett.6b03362.
W.-H. Lin conceived the Raman measurements.

(9) Boyd, D. A.; Lin, W.-H.; Hsu, C.-C.; Teague, M. L.; Chen, C.-C.; Lo, Y.-Y.; Chan, W.-Y.; Su, W.-B.; Cheng, T.-C.; Chang, C.-S.; Wu, C.-I.; Yeh, N.-C. Single-Step Deposition of High-Mobility Graphene at Reduced Temperatures. *Nature Communications* **2015**, *6* (*1*), 6620. https://doi.org/10.1038/ncomms7620.
W.-H. Lin participated in all the measurements and data analysis.

TABLE OF CONTENTS

LIST OF FIGURES

Chapter 1

INTRODUCTION

The allotropes of carbon atoms can exhibit significantly different properties when arranged in quasi-zero-dimensional (0D, *e.g.*, fullerene)[1], one-dimensional (1D, *e.g.*, carbon nanotubes)[2], two-dimensional (2D, *e.g.*, graphene), and three-dimensional (3D, *e.g.*, diamond) structures. Among these allotropes, graphene, a single layer of sp^2-bonded carbon atoms arranged in a honeycomb lattice[3,4], is the first monolayer material ever isolated. Thought to be an impossible goal for many decades, the successful isolation of monolayer graphene in 2004[5] not only led to intensive research by scientists but also inspired renewed interest in carbon-based electronics worldwide[6,7]. To date, graphene has demonstrated to be one of the most promising 2D materials for nanoelectronic and optoelectronic technologies ranging from RF electronics[8–10], semitransparent electrodes[11], low-power switches[12], to tunable plasmonic devices for THz and mid-infrared applications[13,14].

In fact, the active research in graphene-based materials only represents the beginning of emerging intense investigations of the 2D materials family. There has been a surge in the research of 2D materials beyond graphene, triggered by the desire to find insulating and semiconducting complements of the 2D materials. For instance, hexagonal boron nitride (h-BN)[15] is a 2D insulator suitable as a substrate material because it is free of dangling bonds, low in the surface corrugation level, and both thermally and chemically stable. Therefore, h-BN can serve as an excellent interface dielectric material to prevent the formation of charge scattering and trap site in the transistor structures made of 2D semiconductors[16]. Another class of 2D materials are the transition metal dichalcogenides (TMDCs). The TMDCs have electronic properties spanning from semiconductors (*e.g.*, MoS_2, $MoSe_2$, WS_2, WSe_2), insulators (*e.g.*, HfS_2), semimetals (*e.g.*, WTe_2), to metals (*e.g.*, NbS_2, VSe_2) and even superconductors (*e.g.*, $NbSe_2$)[17]. Furthermore, van der Waals heterostructures based on stacking different 2D materials can result in interesting new properties due to the wide range of possibilities to combine and tailor different arrangements of the constituent materials[18].

The 2D materials represent the ultimate scaling of materials dimension in the vertical direction. Thus, nanoelectronic devices based on 2D materials are promising for further miniaturization following Moore's Law and as a high-mobility option in the rising field of large-area and low-cost electronics, which is currently dominated by low-mobility amorphous silicon and organic semiconductors. The rich and unique properties of 2D materials and their heterostructures offer a new dreamland for technological creation and innovation, and have attracted intense research activities aiming to advance nanoelectronic, optoelectronic, and even valleytronic and spintronic applications[19].

1.1 Electronic structures of monolayer graphene

Monolayer graphene is a single atomic layer with a 2D honeycomb lattice consisting of two inequivalent carbon atoms labeled as A and B inside the unit cell, as shown in Figure 1.1.

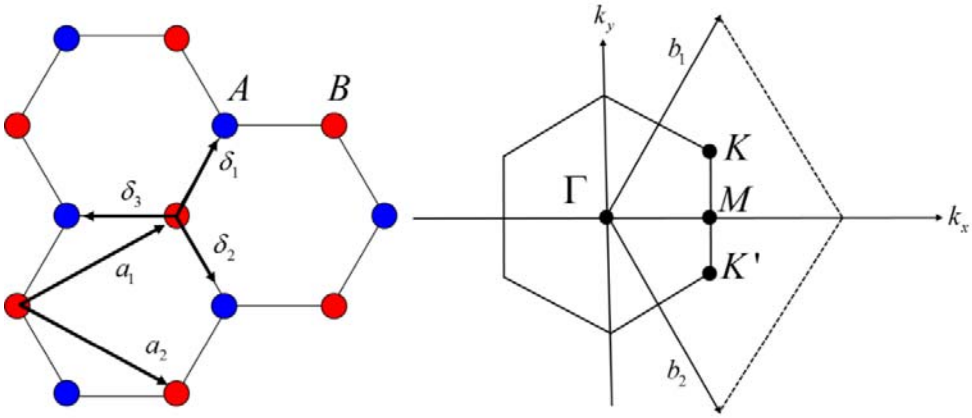

Figure 1.1 (a) The honeycomb lattice in monolayer graphene (MLG) with a two-atom basis in a unit cell. (b) The first Brillouin zone (BZ) of graphene. Two Dirac cones are located at K- and K′-points of the BZ[6].

The primitive lattice vectors $\mathbf{a_1}$ and $\mathbf{a_2}$ can be expressed in Cartesian coordinates as

$$\overline{a_1} = \frac{a}{2}(3, \sqrt{3}) \ , \ \overline{a_2} = \frac{a}{2}(3, -\sqrt{3}) \tag{1.1}$$

where a = 1.42 Å is the nearest-neighbor C-C distance in MLG. The nearest-neighbor vectors δ_i, i= 1, 2, 3, are given by

$$\overline{\delta_1} = \frac{a}{2}(1,\sqrt{3}) \ , \ \overline{\delta_2} = \frac{a}{2}(1,-\sqrt{3}) \ , \ \overline{\delta_3} = -a(1,0)\,. \tag{1.2}$$

The corresponding reciprocal lattice vectors are given by

$$\overline{b_1} = \frac{2\pi}{3a}(1,\sqrt{3}) \ , \ \overline{b_1} = \frac{2\pi}{3a}(1,-\sqrt{3})\,. \tag{1.3}$$

$\mathbf{b}_1$ and $\mathbf{b}_2$ are rotated by 30° with respect to the vector $\mathbf{a}_1$ and $\mathbf{a}_2$ in real space, respectively. In the reciprocal lattice, there are two degenerate and inequivalent points K and K′ located at the corners of the first Brillouin zone (BZ). They are called Dirac points since the electron energy dispersion in the vicinity emulates that of massless Dirac particles. Their positions in momentum space are given by

$$\overline{K} = (0,\frac{4\pi}{3\sqrt{3}a}) \ , \ \overline{K}' = (0,-\frac{4\pi}{3\sqrt{3}a})\,. \tag{1.4}$$

Below we describe the tight-binding model for the electronic π-bands in MLG. Two Bloch functions (Ψ_A and Ψ_B) are constructed from p$_z$-orbits for the two atomic sites A and B as follows:

$$\Psi_A = \frac{1}{\sqrt{N}}\sum_{R_A} e^{iK\cdot R_A} u_a(r-R_A) \ , \ \Psi_B = \frac{1}{\sqrt{N}}\sum_{R_B} e^{iK\cdot R_B} u_a(r-R_B)\,. \tag{1.5}$$

Here N represents the number of lattice sites in the crystal and the factor $1/\sqrt{N}$ ensures that the Bloch state is normalized, K denotes the wave-vector, and $u_a(r-R_{A(B)})$ is the atomic orbital for site A (B) at position $R_{A(B)}$. The tight-binding Hamiltonian for electrons in MLG in the approximation of nearest-neighbor hopping has the form

$$\hat{H}_{MLG} = -t\sum_{i=1}^{3}[\hat{a}^{+}_{R-\delta_i}\hat{b}_R + H.C.] \tag{1.6}$$

where $\hat{a}^{+}_{R}(a_R)$ indicates the creation (annihilation) operator of the atomic state for site A on position R (with a similar definition used for site B), and t = 2.8 eV is the nearest-neighbor hopping energy.

Assuming that there is no electron orbital overlap between A and B, we can deduce the Dirac equation, which describes electrons (holes) with energy near the bottom of the lowest conduction band (the top of the highest valence band), as given below

$$H_{MLG} = \begin{pmatrix} 0 & -t\gamma(\vec{k}) \\ -t\gamma^*(\vec{k}) & 0 \end{pmatrix}. \tag{1.7}$$

The energy bands of MLG derived from this Hamiltonian take the form

$$E(k_x, k_y) = \pm t\sqrt{1 + 4\cos\frac{\sqrt{3}k_x a}{2}\cos\frac{k_y a}{2} + 4\cos^2\frac{k_y a}{2}} \tag{1.8}$$

where k_x and k_y are measured relative to the Dirac point at K and K′.

Figure 1.2 shows the energy dispersion in the reciprocal space. The upper (lower) part of the dispersion curves describes π* (π)-band (*i.e.*, anti-bonding (bonding) band). The electronic energies have values at ±3*t*, ±*t*, and 0, respectively, at the high symmetry points Γ, M, and K(K′) of the Brillouin zone. Since there are two π-electrons per unit cell, the lower π-band is filled by π-electrons with spin up and spin down, while the π* -band is empty. This places the Fermi wave vector of MLG at K (or K′) point. In the absence of excess doping, the Fermi energy is located at the Dirac point, which may be set to 0 for simplicity. The existence of a zero-energy gap at K (or K′) points originates from the AB symmetry that two carbon sites A and B in the honeycomb lattice are identical to each other. If the A and B sites are occupied by different atoms (*e.g.*, boron and nitrogen), then the on-site energy would be different, therefore opening up an energy gap.

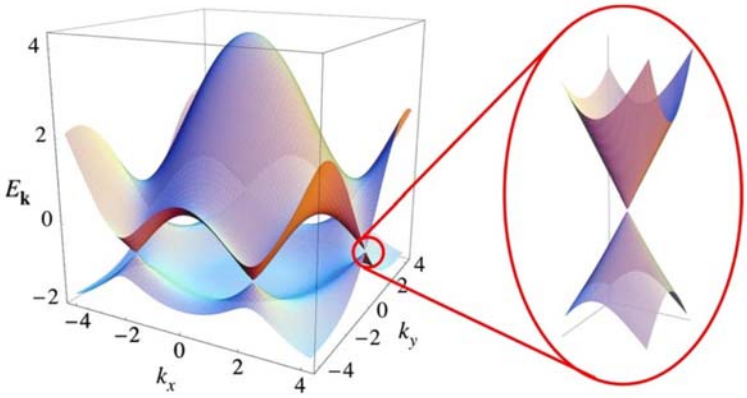

Figure 1.2. The band structure of MLG. (Left) The energy dispersion of MLG. (Right) The band structure in the vicinity of Dirac point.

In condensed matter physics, Schrodinger-type equation is often employed to describe the electronic properties of materials. However, in MLG, the unique honeycomb lattice potential gives rise to quasiparticles which are massless Dirac fermions that can be described by the Dirac-type equation at low energies. Since the band edge at Γ-point is around 10 eV above the Fermi-level, only the low energy range around the Dirac points is relevant for electronic transport. For electrons with sufficiently low energy, one can apply Taylor's expansion to Eq. (1.8) around the K- and K′- points, which yields the following relation:

$$E(k) = \pm\hbar v_F k = \pm\hbar v_F \sqrt{k_x^2 + k_y^2}\ . \tag{1.9}$$

The Fermi velocity v_F, defined as $v_F = (1/\hbar)(dE/dk)$, is readily obtained from Equation (1.9):

$$v_F = \frac{3ta}{2\hbar} = \frac{3(1.421\times10^{-10}m)(3.033eV)}{2(6.582\times10^{-16}eVs)} \approx 9.8\times10^5\,\frac{m}{s}. \tag{1.10}$$

The Dirac Hamiltonian can also be obtained by expanding the wave vector *k* in Eq. (1.7) near the Dirac points. We first expand it near K (let $k = K+q$ with $|q| << |K|$) and find

$$-t\gamma(\vec{k}) = \sum_{i=1}^{3} e^{-iK\cdot(\delta_1-\delta_i)} \approx v_F(ip_x + p_y)\,. \tag{1.11}$$

Note that the momentum operators p_x and p_y are defined with respect to the Dirac point K. Substituting Eq. (1.11) into the Hamiltonian in Eq. (1.7), we obtain the Dirac Hamiltonian near the K valley. Similar process can be carried out for the K′ valley. Overall, the Dirac equation is given by

$$H_{MLG,\tau_v}\psi_{D,\tau_v} = \begin{pmatrix} 0 & v_f(ip_x + \tau_v p_y) \\ v_f(-ip_x + \tau_v p_y) & 0 \end{pmatrix} \begin{pmatrix} \psi_{A,\tau_v} \\ \psi_{B,\tau_v} \end{pmatrix} = E \begin{pmatrix} \psi_{A,\tau_v} \\ \psi_{B,\tau_v} \end{pmatrix} \tag{1.12}$$

where τ_v = 1 (−1) for the K (K′) valley. In the above equation, ψ is the envelope function (or called spinor wave function), which can be transformed back to the real-space wave function. For instance, the real-space wave function of site A is written as

$$\Psi_A = \sum_R [a_1 e^{i\vec{K}\cdot\vec{R}}\psi_A(\vec{R}) + a_2 e^{i\vec{K}\cdot\vec{R}}\psi'_A(\vec{R})]\varphi_A(\vec{r}-\vec{R}) \tag{1.13}$$

where a_1 and a_2 are coefficients to be further determined.

The density of states (DOS) of MLG can be derived as

$$g_n \sim \int \frac{1}{|\vec{\nabla}_k \varepsilon_n(k)|} dS \sim \frac{k}{\hbar v_F} \tag{1.14}$$

where dS represents the constant energy surface. In particular, the DOS is found to be zero at the Dirac point. For the effective mass, we write

$$\vec{P}_n = mv = m\frac{1}{\hbar}\vec{\nabla}_k \varepsilon_n(k) \rightarrow \frac{1}{m} = \frac{1}{\hbar^2 k}\vec{\nabla}_k \varepsilon_n(k) \sim \frac{v_F}{\hbar k} \tag{1.15}$$

and the mass is also found to be zero at the Dirac point. The DOS of MLG are linear in momentum and can be manipulated by applying a gate voltage. In MOSFET, the Fermi energy of material is tuned by the gate electrode to accumulate or repel carriers in the channel, thus controlling the current to achieve the switching function. This concept can be directly applied to 2D-material systems so that the conductance changes with Fermi energy *via* the field effect. This approach allows us to obtain information about the band structure and the electronic quality of the material. The DOS of ideal MLG is identical for both electrons and holes at low-energies and vanishes at the Dirac point. The Dirac voltage (V_D) is defined by the gate voltage that modulates the Fermi level to the Dirac point. However, the minimum conductivity (σ_{min}) is usually found to be non-zero in practical measurements at V_D because the presence of structural disorder, unintentional doping from fabrication processes, and residual atmospheric adsorbates will all induce extrinsic carriers in the system. At low carrier densities, the system breaks up into electron and hole puddles, therefore raising the difficulty in modulating the Fermi energy of these puddles simultaneously to the Dirac point at a specific gate voltage. In an accurate picture, the σ_{min} occurs at the charge neutrality point (CNP) where the overall induced electrons in the conduction band are equal to the overall induced holes in the valence band. The carrier density in the MLG can be modulated by changing the gate voltage. The simple capacitance relation of $Q = ne = CV$ gives rise to the relation between carrier density and applied gate voltage.

$$n(cm^{-2}) = \frac{C_{BG}(V_{BG} - V_{CNP})}{e} \approx 7.25\times 10^{10}(V_{BG} - V_{CNP}) \tag{1.16}$$

where $C_{BG} \sim 11.6$ nF/cm^2 is defined as the capacitance per unit area for 285 nm thick SiO_2, C_{BG} denotes the back-gate voltage, and V_{CNP} indicates the shift of charge neutral point (CNP) where the σ_{min} occurs. The relation between Fermi energy E_F and the carrier density can also be expressed as[20]

$$E_F(n) = -\text{sgn}(n)\hbar v_F\sqrt{\pi|n|} \tag{1.17}$$

with n as the two-dimensional carrier density. In the absence of both long- and short-range scattering, the field-effect carrier mobility can be roughly estimated by employing the semi-classical Drude model that gives electronic mobility $\mu = 1/ne\rho$.

Figure 1.3 shows the electric field effect in exfoliated MLG on SiO_2 at low-temperature environment as adapted from Ref.[21]. The insets show its low-energy dispersion, indicating the changes in the position of the Fermi energy E_F with varying the gate voltage. The ambipolar behaviors are found for MLG carriers. Positive and negative voltages correspond, respectively, to electron and hole transport. The rapid decrease in resistivity (ρ) by adding charge carriers in the vicinity of the CNP indicates high mobility, which is extracted to be around 15,000 cm^2/Vs at low carrier concentrations even under ambient environment. At high carrier densities, the carrier mobility is found to be around 5,000 cm^2/Vs and does not change significantly with increasing temperature up to 300 K.

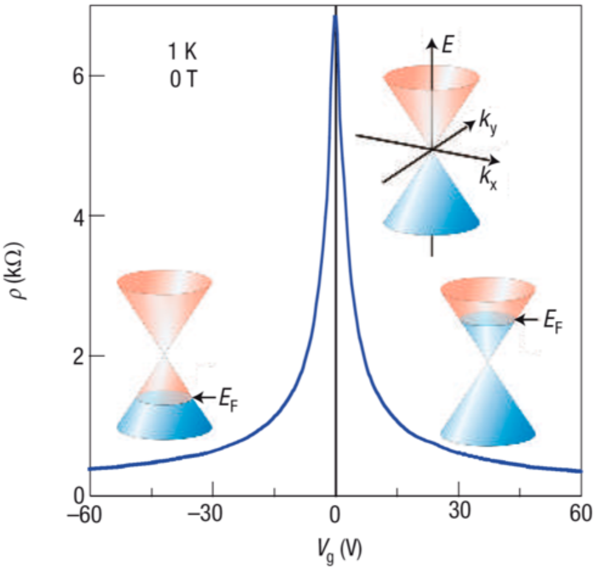

Figure 1.3. Ambipolar electric field effect in MLG. The insets show its low-energy dispersion, indicating the change in the position of Fermi energy E_F with varying the gate voltage.

The complete picture of carrier transport in MLG should include both long- and short-range scattering in a self-consistent diffusive transport model, which gives[22,23]

$$\rho = \rho_L + \rho_S = (ne\mu_c + \sigma_{\min})^{-1} + \rho_S \tag{1.18}$$

where ρ_L is the resistivity induced by long-range scattering from charged-impurity Coulomb scattering, mobility constant μ_C is determined by the long-range scattering, and ρ_S is a carrier density-independent resistivity dominated by short-range scattering. For an ideal MLG, the theoretical minimum conductivity is expected to be $\sigma_{\min} = 4e^2 / \pi h$ at the CNP[24,25]. The minimum conductivity shown in MLG may be affected by the following factors. At low carrier densities, disorder induced potential fluctuation[26,27] breaks up the electron liquid into electron-hole puddles in MLG. Ripples in MLG give rise to overlapping of π-electron orbitals and vary the local states available for carriers transport, resulting in inhomogeneous distributions of the carriers. Besides the structural corrugations, the origin of the electron-hole puddles in MLG can be charged impurities on MLG or in the supporting substrate, both of which result in local chemical potential fluctuations. In conclusion, with the peculiar dispersion in MLG carriers behave as massless relativistic particles (Dirac fermions) with electron-hole symmetry, leading to several unusual and unique properties such as unconventional quantum Hall effect, high room-temperature carrier mobility, high thermal conductivity[28], quantum valley Hall effects[29–31], and so on that have been only discovered in the past decade. These findings make MLG highly promising for the development of post silicon electronics by means of electric field effects[32], energy band gap engineering[33], integrated graphene circuits[34], and high-frequency devices[35].

1.2 2D-Field effect transistors

The conventional field-effect transistor (FET) is a three-terminal device which consists of a semiconductor channel that connects the source and drain electrodes. These two electrodes serve as two reservoirs of mobile charged carriers (electrons or holes) and are connected by the channel material. Therefore, a low-resistance contact at the metal/semiconductor interface is important to access the channel properties and operate the entire device properly. The third electrode (gate) is separated from the channel by a gate dielectric (*e.g.*, SiO_2, HfO_2, and SiN_x). Figure 1.4 shows the basic structures of FETs, including conventional Si metal–oxide–semiconductor field-effect transistors (MOSFETs), III–V high-electron-mobility transistors (HEMTs), and 2D TMDC FETs. Note that typical 2D TMDC FETs do not possess PN junctions as those present in conventional Si MOSFETs due to the lack of precisely controlled doping methods for atomically thin TMDCs. The transistor is operated by grounding the source contact and applying a drain voltage, V_{DS}. The applied gate-to-source voltage (V_{GS}) modulates the conductivity of the semiconductor channel through shifting the Fermi level of the semiconductor channel, while the applied drain-to-source voltage (V_{DS}) drives the free mobile carriers in the channel flowing from the source side to the drain side, resulting in a drain-to-source current (I_{DS}) passing through the device.

Figure 1.5 (a) shows the typical transfer characteristics of an n-channel FET. Figure 1.5 (b) illustrates the ideal output characteristics of an n-channel FET, which exhibit both linear and saturation regions at low and high-field regimes, respectively. With no gate bias ($V_{GS} = 0$), the device is in the OFF state since large thermal barriers, governed by the Fermi-Dirac distribution, exist for the injection of both electrons into the conduction band (CB) and holes into the valence band (VB). As such, the 2D channel remains highly resistive, preventing any current flow. When a positive voltage is applied to the gate ($V_{GS} > 0$), the energy bands in the 2D channel are displaced downwards by an amount equal to the surface potential $q\Psi_s$, where q is the electronic charge. This allows the injection of electrons from the source into the conduction band of the 2D channel, and as such current starts to flow as shown in Figures 1.5 (c). This thermionic electronic current initially increases exponentially with increasing magnitude of V_{GS} until the ON state ($V_{GS} = V_{TH;}$ threshold condition) is reached where the so-called band movement nearly stops. Similarly, when a negative voltage is applied to the gate ($V_{GS} < 0$), the energy bands in the 2D channel are displaced upwards allowing the injection of holes from the drain into the valence band of the 2D channel as shown schematically in Figures 1.5 (d). The hole current also increases exponentially with increasing magnitude of V_{GS} until the on-state is reached. For high performance CMOS circuitry, both n-type and p-type transports are essential alongside Ohmic contacts. In the case of 2D materials, achieving n-type FETs and p-type FETs using a single material has been rather challenging. Furthermore, the contacts are most often Schottky barriers in nature, which limits carrier injection and ultimately the device performance.

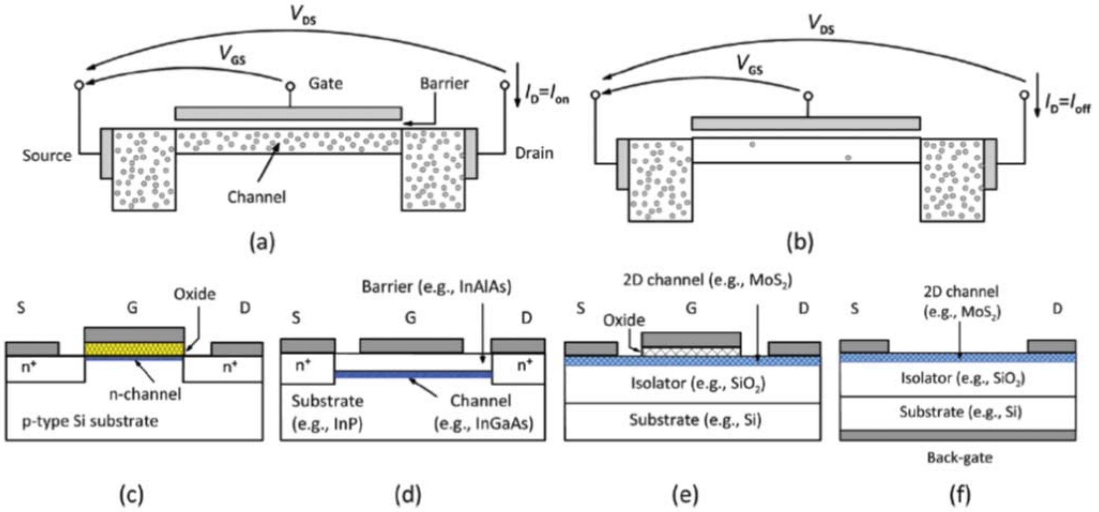

Figure 1.4. Basic structure of a FET (a) in the ON-state and (b) in the OFF-state. (c) Conventional Si n-channel MOSFET. (d) HEMT. (e) Top-gated 2D TMD FET. (f) Back-gated 2D MOSFET[36].

To assess the potential of novel 2D materials for FET channels, it is not sufficient to consider only one material property alone such as the carrier mobility. Instead, a set of properties should be examined to get a realistic impression on the suitability of the new material for transistors. Therefore, we list several figures of merit that are generally considered to evaluate emerging transistor technologies[36,37].

1. Correlation between the on/off current ratio and the energy bandgap of 2D materials.

For FETs to be used in digital logic applications, a high on–off ratio (I_{on}/I_{off}) in the range of $10^4 - 10^7$ is desired. Hence, a good FET should be able to deliver high I_{on} for high-speed switching, while its off-state current I_{off} ($V_{GS} = 0$, $V_{DS} = V_{DD}$) should remain as low as possible to allow a low static power consumption. A standard value for I_{off} in high-performance logic devices is 100 nA μm^{-1}. While the on-current of a FET is not directly related to the bandgap (E_g) of a material, the off-current strongly depends on E_g according to the following equation,

$$\frac{I_{on}}{I_{off}} \propto \exp\left(\frac{E_g}{mk_BT}\right), \qquad (1.19)$$

where m is a factor depending on the FET design. The estimation suggests that the material bandgap should be larger than 460 meV for m equal to 2 at room temperature to obtain $I_{on}/I_{off} > 10^4$.

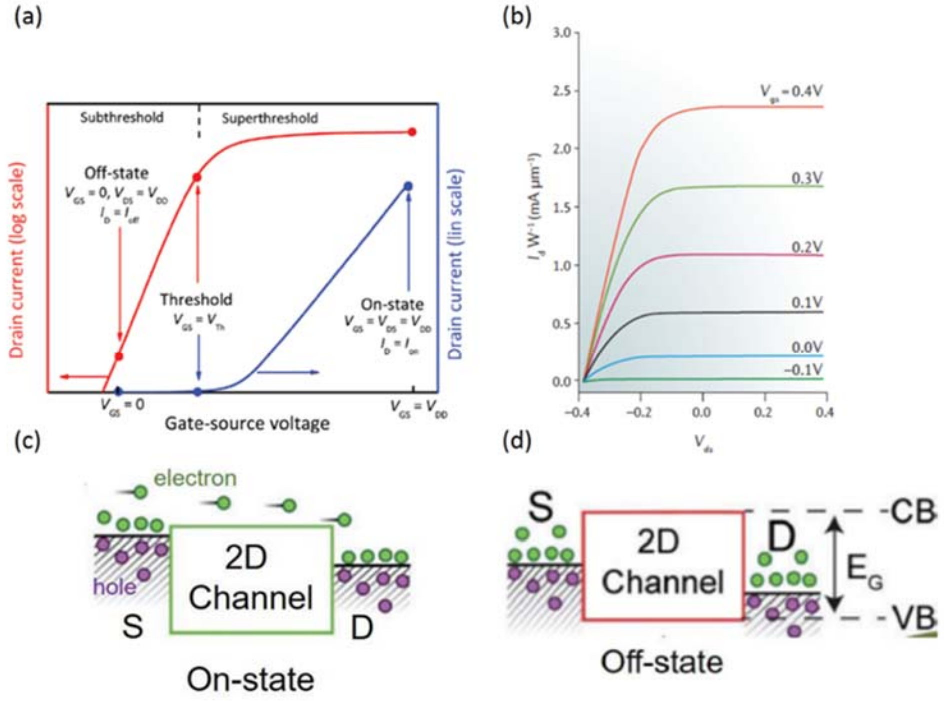

Figure 1.5. (a)Transfer characteristics of an n-channel (I_{DS}−V_{GS}) of an n-type 2D FET, showing the modulation of drain current as function of the applied gate voltage (V_{GS}). (b) Ideal output characteristics ($I_{DS} - V_{DS}$) of an n-channel 2D FET under different V_{GS}. Energy band diagrams of transistor (c) On-state and (d) Off-state[36,38,39].

The estimation suggests the material bandgap should larger than 460 meV under m is equal to 2 at room temperature to obtain $I_{on}/I_{off} > 10^4$.

2. Correlation between on-state current, carrier mobility and effective mass of the 2D channel materials.

In general, the performance of a transistor like the switching speed is largely dictated by its current carrying capability. In an ideal long-channel FET without considering the effects of RC, the I_{on} for a channel length L_{CH} in the linear region (small V_{DS}) can be expressed as

$$I_{on} = \frac{W}{L_{CH}} C_{ox} \mu \left[(V_{GS} - V_T) V_{DS} - \frac{V_{DS}^2}{2} \right], \tag{1.20}$$

where W is the channel width, V_T is the threshold voltage, and C_{ox} is the capacitance per unit area of the gate dielectric. When the drain-to-source voltage (V_{DS}) exceeds the overdrive voltage, the carrier density in the channel becomes pinched-off near the drain, and I_{on} saturates to

$$I_{on} = \frac{W}{2L_{CH}} C_{ox} \mu [(V_{GS} - V_T)^2]. \tag{1.21}$$

In this regime, the current has a quadratic relationship with the overdrive voltage. As the lateral field becomes greater than the critical field strength of the semiconductor channel, the carrier in the channel reaches its saturation velocity (v_{sat}) as a result of optical phonon emission, a scattering process in which hot carriers lose energy and forward velocity along the transport direction due to increased scattering with the lattice. In this velocity saturation regime, the I_{on} in a transistor saturates to a maximum of

$$I_{on} = WC_{ox} (V_{GS} - V_T) v_{sat} . \tag{1.22}$$

These expressions for I_{on} highlight the importance of mobility, saturation velocity, and channel length scaling in FETs. Before reaching the velocity saturation regime, I_{on} generally scales as the channel length shortens due to the reduction of channel resistance. As the transistor operates in the velocity saturation regime, I_{on} scales linearly with the overdrive voltage. Logic FETs should be fast, react quickly on variations of their input signals, and show a large on-state current. For this purpose, fast carriers are needed. Measures for the speed of carrier transport are given by the mobility μ, and the saturation velocity v_{sat}. The mobility is inversely proportional to the carrier effective mass m_{eff} and a light m_{eff} is a precondition for a high μ. Under high-field conditions, the carrier velocity no longer follows the field linearly. The high-field velocity for holes shows a soft saturation and approaches v_{sat} at high fields. For electrons, the situation is more diverse.

When the channel length becomes sufficiently short, the contribution of contact resistance to the total device resistance in a FET can overpass that of the channel resistance. At this point, contact resistance starts to dominate the transistor performance, and I_{on} stops to scale with the channel length, hindering further device miniaturization. Therefore, forming ultralow contact resistance is key to continuously boosting the device performance through downscaling.

3. Contact Resistance (R_c)

For a FET with ideal contacts, the output characteristics should exhibit linear, ohmic-like I-V responses in the low-field regimes and only consume a negligible voltage drop to drive a high current. Such a low-resistance contact can transparently pass the required current, and the I_{on} of the device is mainly determined by the channel resistance which can be efficiently modulated by the electrostatic gate control or through the reduction of channel length. A good contact is critical to minimize the device on-resistance (R_{on}) and, hence, the power losses of the electrical system. The contact resistance (R_c) is used to described the performance of the Ohmic contact, which is referred to as the contact length. In general, the specific contact resistance (ρ_c) can be express as:

$$\rho_c = \left(\frac{\partial J}{\partial V} \right)^{-1}_{V=0}, \qquad (1.23)$$

where J is the current density determined by the transport mechanism (*e.g.*, thermionic emission or tunneling) and V is the applied bias across the metal-semiconductor junction. In general, the specific contact resistivity depends on the metal-semiconductor Schottky barrier height and on the doping concentration (N_D) of the semiconductor under the contacts. The metal-2D semiconductor contacts are characterized by the Schottky barriers (SBs) and can be defined as

$$\begin{aligned} \phi_{SB-n} &= \phi_M - \chi_S \, (n\text{-type}) \\ \phi_{SB-p} &= E_g + \chi_S - \phi_M \, (p\text{-type}) \end{aligned}, \qquad (1.24)$$

where ϕ_M is the work function of the metal and χ_S is the electron affinity of the semiconductor.

For a given material, the actual SB height can be approximated by Equation (1.25), where S is the Schottky pinning factor. For $S = 0$, which indicates strong pinning, SB height is independent of the work function of the metal; whereas for S approaching unity, the Bardeen limit converges to the Schottky limit.

$$\begin{aligned} &\phi_{SB-n} = (S \times \phi_M - \chi_S) + (1 - S)\phi_{IS}, \\ &S \equiv \partial\phi_{SB-n} / \partial\phi_M. \end{aligned} \tag{1.25}$$

Here, we consider the different semiconductor doping level N_D that induced different mechanisms of carrier transport at the interface owing to the different thicknesses of the space charge region W formed at the metal/semiconductor interface. Typically, for lightly doped semiconductors ($N_D < 1 \times 10^{17}$ cm^{-3}), the thermionic emission current dominates the current transport at the interface (Figure 1.6) and the specific contact resistivity can be described by the relation:

$$\rho_c = \frac{k_B}{qA^*T} \exp\left(\frac{q\phi_{SB}}{k_B T}\right), \tag{1.26}$$

where k_B is the Boltzmann constant, A^* is the Richardson constant, and q is the elementary charge. Under this thermionic emission dominant regime, the specific contact resistivity (or contact resistance) is nearly independent of the doping concentration (N_D) due to the fact that the Schottky barrier width is large, and the carriers must be thermally excited over the contact barrier. Consequently, the contact resistance of a FET in this regime strongly depends on the Schottky barrier height at the contact interface. This scenario applies to the state-of-the-art 2D TMD FETs fabricated to date owing to the lack of efficient doping techniques.

For heavily doped semiconductors ($N_D > 1 \times 10^{19}$ cm^{-3}; Figure 1.6 (e)), the space charge region, that is, the Schottky barrier width at the metal-semiconductor interface, becomes sufficiently narrow to allow direct tunneling of electrons through the interface. This is the case for modern Si transistor technology in which nearly ohmic characteristics are realized by introducing a high doping concentration under the contact areas. Under this condition, the specific contact resistivity R_c strongly depends on the doping concentration and the influence of the Schottky barrier height becomes almost transparent so that ρ_c can be written as:

$$\rho_c \propto \exp\left(\frac{\phi_{SB}}{\sqrt{N_D}}\right). \qquad (1.27)$$

Accordingly, a low-resistance contact is a metal-semiconductor contact in which the energy barrier at the interface is negligible, transparent for carrier tunneling, or even absent (*i.e.* ohmic contact, Figure 1.6(c)). As a result, one can expect a linear (non-rectifying) current-voltage (I-V) characteristics (Figure 1.6(f), red curve) for an ohmic-contact FET operated in low-field regimes before reaching the pinch-off or velocity saturation regime. In contrast, a non-negligible high contact barrier leads to non-ideal output characteristics deviating from the ohmic conduction (Figure 1.6(f), black curve).

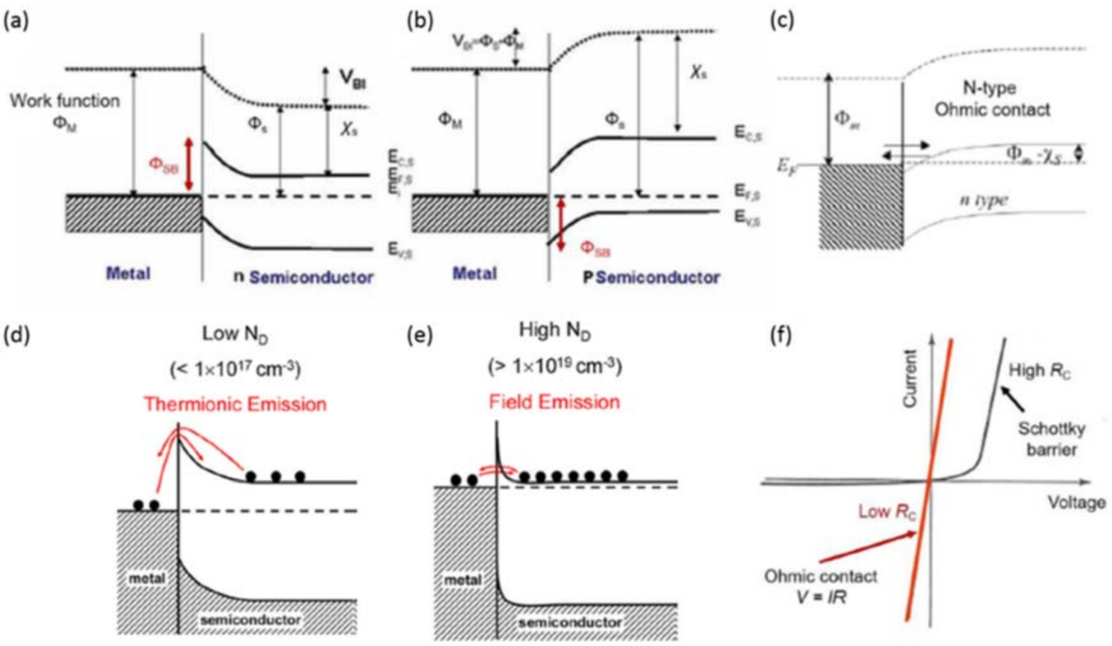

Figure 1.6. The band diagram of metal-semiconductor for (a) n-type semiconductor, (b) p-type semiconductor. (c) Ideal Schhottky barrier-free ohmic contact for n-type semiconductor. (d,e) Schematic illustration of the different carrier transportation mechanisms through the contact barrier for different doping levels. (f) Comparison of the I-V characteristics of ohmic and Schottky contacts.

1.3 Nanophotonics: light-,atter interaction in TMDCs materials

The field of nanophotonics is concerned with the nature of interactions between light and materials at a scale near or smaller than the wavelength of light. The light-matter interactions are controlled by nanostructuring metals, dielectrics, or semiconductors in order to realize novel functions, such as the focusing of light to very small volumes, spectrally selective transmission or reflection, or the deterministic accumulation of phases. Modern nanophotonics seeks to control fully the complex electromagnetic field, such as the amplitude, phase, and polarization in the near- and far-field limits. Using this approach, light can be manipulated in ways not allowed by conventional optical components so that we can replace conventional bulky optics with wavelength-scale structures. This great technology may be applied in various fields, including chemical sensing, holographic displays, hyper-spectral imaging, and many others, which take advantage of the feasibility of controlling light-matter interactions at nanoscales.

Transition metal dichalcogenide (TMDCs) have emerged as a new class of 2D semiconductors that display distinctive properties at the monolayer thickness. Their optical properties are of particular interest and importance. The most basic description of the light-matter interactions in monolayer TMDCs is given by the complex dielectric function of the materials. Techniques exist to determine the dielectric function of TMDC monolayers, such as the Lorentz model, the hybrid Lorentz-Drude-Gaussian, and the variation dielectric Kramers-Kronig function[40] based on the Lorentz model. Here, we used the simple Lorentz model as provides decent fittings to the results presented in experimental reports[41].

The complex dielectric function $\varepsilon(E)=\varepsilon_1(E)+i\varepsilon_2(E)$ of a monolayer WS_2 sample as a function of the photon energy $E=\hbar\omega$ can be expressed in terms of the superposition of Lorentzian oscillators:

$$\varepsilon_{WS_2}(\omega)=\varepsilon_\infty+\sum_{j=1}^{N}\frac{f_j}{E_j^2-E^2-iE\gamma_j}\quad . \tag{1.27}$$

Here ε_∞ is the DC permittivity, f_j and γ_j are the oscillator strength and the damping factor of the j-th oscillator, respectively, and E_j runs from 500 nm to 800 nm (A- exciton range). We may also express the material response in terms of the optical conductivity $\sigma(E)=\sigma_1(E)+i\sigma_2(E)=-i\left(\frac{\varepsilon_0 E}{\hbar}\right)[\varepsilon(E)-1]$. For 2D materials, we further present this result in the form of the sheet conductivity $\sigma^s(E)=\sigma(E)d$, where d is the sample thickness.

To find the optical characteristics of the designed structures, the transmission (*T*), reflection (*R*) and absorption (*A*) spectra are calculated based on the transfer matrix method (TMM)[42,43]: Using Maxwell's equation and applying boundary conditions for the electric field between the adjacent layers, the light propagation through the *i*-th boundary and (*i*-1)-th layer can be expressed via the transfer matrices:

$$\begin{bmatrix} M_{11} & M_{12} \\ M_{21} & M_{22} \end{bmatrix}=\begin{bmatrix} \frac{\sqrt{\varepsilon}+1}{2} & \frac{\sqrt{\varepsilon}-1}{2} \\ \frac{\sqrt{\varepsilon}-1}{2} & \frac{\sqrt{\varepsilon}+1}{2} \end{bmatrix}\begin{bmatrix} e^{\frac{-i2\pi d_{SiO_2}\sqrt{\varepsilon}}{\lambda}} & 0 \\ 0 & e^{\frac{i2\pi d_{SiO_2}\sqrt{\varepsilon}}{\lambda}} \end{bmatrix}\begin{bmatrix} \frac{n_{SiO_2}+\sqrt{\varepsilon}}{2\sqrt{\varepsilon}} & \frac{n_{SiO_2}-\sqrt{\varepsilon}}{2\sqrt{\varepsilon}} \\ \frac{n_{SiO_2}-\sqrt{\varepsilon}}{2\sqrt{\varepsilon}} & \frac{n_{SiO_2}+\sqrt{\varepsilon}}{2\sqrt{\varepsilon}} \end{bmatrix}\begin{bmatrix} e^{\frac{-i2\pi d_{SiO_2} n_{SiO_2}}{\lambda}} & 0 \\ 0 & e^{\frac{i2\pi d_{SiO_2} n_{SiO_2}}{\lambda}} \end{bmatrix}\cdots \tag{1.28}$$

$$A=1-\left|\frac{M_{21}}{M_{11}}\right|^2-\left|\frac{1}{M_{11}}\right|^2 \quad . \tag{1.29}$$

The calculated results are shown in Figure 1.7 and Figure 1.8.

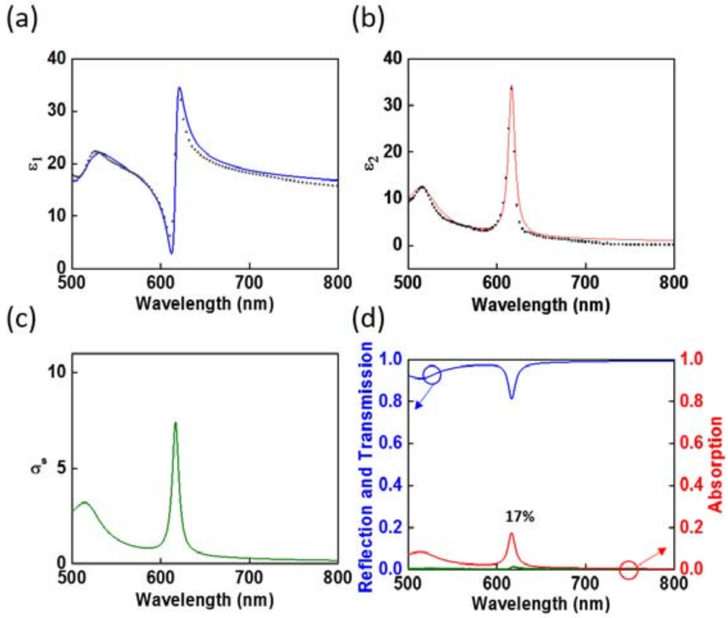

Figure 1.7. (a) Real and (b) imaginary component of the complex dielectric function of WS2 monolayer. (c) Real part of the sheet conductivity (in units of $G_0 = 2e^2/h$) and (d) Reflection, transmission and absorption of the free-standing monolayer of WS2. The fitting parameters used are: $\varepsilon_\infty = 7.45,\ E_1 = 2.01\,\mathrm{eV},\ f_1 = 1.87,\ \gamma_1 = 0.03;\ E_2 = 2.4\,\mathrm{eV}, f_2 = 3.55, \gamma_2 = 0.185;$ $E_3 = 2.83\,\mathrm{eV}, f_3 = 8.42, \gamma_3 = 0.23;\ E_4 = 3.13, f_4 = 42.75, \gamma_4 = 0.64.$

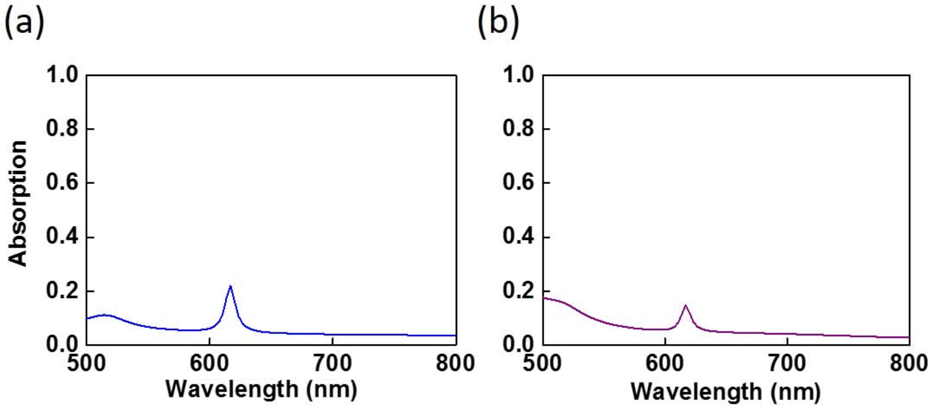

Figure 1.8. Absorption spectra in visible range of the WS2 monolayer on (a) 20 nm SiO2 substrate and (b) 100 nm Au substrate.

Monolayer TMDCs not only exhibit strong light-matter interactions, but also possess a set of unique properties that make them promising for a variety of applications, ranging from next-generation logic to integrated photonics and quantum computing. The valley degrees of freedom are particularly interesting for potential commercialization of TMDC-based technology. While Moore's Law may continue beyond 2030, the typical improvement in MOSFET fabrication every 2 years is no longer sustainable. Meanwhile, photonic technology continues to improve, but connecting between photonics and electronics remains a challenge. In this context, the strong spin-valley coupling in TMDCs provides an efficient pathway of coupling the electronic degrees of freedom (*i.e.*, spin, valley, and bandgaps) with the photonic degrees of freedom (*i.e.*, circularly polarized light and wavelengths).

1.4 The scope of this thesis

In the research field of 2D materials, two major challenges remain before these materials can meet the industrial standards for electronic and photonic applications. The first challenge comes from the material side. Although various methods have been demonstrated to synthesize 2D materials in large scale, numerous material and growth issues are still unsolved, including low-temperature growth, reduced defect/impurity density, reliable and scalable doping, and damage-free transfer processes. For example, the monolithic-3D integration requires processes with a low thermal budget (< 400 °C) to prevent degradation of the underlying devices, dielectric layers, and interconnects. Therefore, it is urgent to develop low temperature deposition methods of 2D materials on various substrates while simultaneously maintaining reasonable material quality. The second challenge originates from the device level, which is how to make ohmic contacts to the 2D semiconductors. Ultra-low resistance contacts are the key to fully access the intrinsic transport properties of the 2D materials, achieve high I_{on} in the 2D monolayer transistors, and connect them to high-performance transistor applications. Although tremendous efforts have been made in reducing the contact resistances of TMDC devices, the electrical contacts to TMDCs, especially to monolayers, are constrained by either Schottky or vdW contacts that normally result in a high contact resistance R_C of 1−10 kΩ μm. Such high R_C to TMDCs is orders of magnitude higher than those to Si and III-V semiconductors, and is still far away from fulfilling the stringent ITRS 2024 requirement ($R_C < 130$ Ω μm).

This thesis explores the intersection of three topics identified among 2D quantum materials, which are: synthesis methods, nanophotonics, and nanoelectronics. In Chapter 2, we develop a growth method for synthesizing large-scale graphene monolayers with high material qualities such as low impurity, low strain, and good electron mobility for high performance transistor devices. Given that 2D materials are easily affected by the surrounding dielectric environments, it is critically important to ensure that the synthesized 2D materials are free of dangling bonds and are thermally and chemically stable. In Chapter 3, the development of a hybrid low-pressure (LP) and atmosphere-pressure chemical vapor deposition (APCVD) system for synthesizing h-BN thin films is described. The system utilizes controlled precursors to grow uniform, layer by layer thickness controlled, wafer-scale h-BN films with thicknesses ranging from monolayer to 10 nm.

The characterization of these h-BN films are detailed. These results demonstrate a new standard and a state-of-the-art approach for large-area synthesis of h-BN, potentially enabling applications in nanoelectronic and nanophotonic devices. Compared with the traditional charge degrees of freedom, spin and valley are two additional internal degrees of freedom in solid-state electronics that can enable spintronic and valleytronic devices with high integration density, fast processing speed, low power dissipation, and non-volatility. In Chapter 4, we report detailed studies of opto-valleytronic properties of heterogeneous domains in CVD-grown monolayer WS_2 single crystals. These results offer the initial groundwork for future devices that explore the spin-valley coupling as robust information carriers with reduced power consumption compared to conventional MOSFET-based electronics. In particular, the much enhanced valley polarization of our monolayer WS_2 single crystals at room temperature is promising for future development of valley-dependent optoelectronic devices in energy-efficient information processing. In Capter 5, we describe the combination of metal-dielectric-metal (MDM) chiral plasmonic nanostructures with monolayer WS_2 for investigating the monolayer WS_2 exciton-plasmon interaction and manipulating the valley-polarized photoluminescence (PL) at room temperature. Although TMDC monolayers show several desirable properties for enhancing the performance of nanoscale transistors, the strong Fermi-level pinning at the metal-TMDC interfaces, lack of efficient doping methods, and high contact resistances have severely impeded the development of monolayer semiconductor transistors with high performance. Therefore, in Chapter 6, we attempt to provide better understanding of the electrical contacts to TMDC monolayers, and demonstrate promising solutions to reduce the contact resistance for monolayer 2D semiconductors. Lastly, in Chapter 7, we provide a summary of this thesis and propose several promising research directions for the next generation 2D nanoelectronics and electrically tunable light-matter interactions in quantum materials.

Chapter 2

SYNTHESIS AND PROPERTIES OF THE 2D SEMI-METAL GRAPHENE

The semiconductor industry has advanced at an exponential rate over the last few decades. In recent years, the interconnect has become a major limiting factor on the performance of very large-scale integrated (VLSI) systems. The interconnect delays have begun to exceed transistor delays, and this trend worsens with the shrinking device channel length and further increases the electrical resistance. The large demand of higher levels of integration and interconnect performance, such as the supply current and voltage, number of 1/0 resources and global wires, often dominates the total power consumption in VLSI systems. Despite the incorporation of innovative device structures and new materials into VLSI systems to reduce power dissipation and improve heat removal, energy dissipation and high device temperature remain major challenges in this field.

Graphene, a monolayer of carbon atoms forming a two dimensional honeycomb lattice structure, is one of the promising 2D materials not only for transistors but also for interconnects because of its ballistic transport, high intrinsic mobility, high thermal conductivity, and high current carrying capacity. Therefore, combining current copper interconnects with graphene could both lower the energy dissipation of the copper wires and increase the heat transfer from the poor thermal conducting low-K dielectrics to reduce the temperature increase of the devices. In this context, improving the fundamental material properties and inventing a graphene growth process compatible with CMOS technologies are critically important for scalable applications of graphene in VLSI systems.

Scalable graphene growth may be achieved by copper-assisted thermal chemical vapor deposition (T-CVD). The high-temperature (~ 1000 °C) chemical vapor deposition (CVD) system is considered as a preferable way to synthesize uniform and large-size high-quality graphene on Cu. However, T-CVD growth of graphene generally requires multiple processing steps and relatively long time in both the substrate preparation and graphene growth. Moreover, high-temperature processes at ~1000 °C in the T-CVD synthesis are incompatible with applications relevant to the semiconducting industry, and the high thermal budget adds further constraints on mass production.

In Section **2.1** of this Chapter, we describe our successful development of a single-step method for synthesizing high-mobility monolayer graphene (MLG) in merely a few minutes by means of plasma-enhanced chemical vapor deposition (PECVD) techniques without the need of active heating. In contrast to the T-CVD method, the plasma in the PECVD process can provide a rich chemical environment, including a mixture of free radicals, photons, energetic electrons, excited molecules, and active ions. This environment enables graphene growth on different surfaces at relatively lower temperatures, which paves ways to a CMOS-compatible approach to graphene synthesis.

Another important technical challenge for graphene-related applications is the transfer of graphene from growth substrates to other targeted surfaces. In the case of T-CVD or PECVD-grown graphene, common methods for transferring graphene sheets from Cu to other substrates all involve polymer-assisted transfer processes, in which a polymer layer, such as polymethyl methacrylate (PMMA), polydimethylsiloxane (PDMS), thermal released tap, poly (bisphenol A carbonate) (PC), or special self-release polymers, is used as a temporary rigid support to prevent folding or tearing of the graphene sample during the chemical etching of the Cu substrate. However, removing the residual contamination on the surface of graphene remains a challenge. In particular, the cleanliness of graphene is extremely important to the investigation of its intrinsic properties. Therefore, removing the polymer residue after transfer of graphene is critically important. A clean transferring technique that successfully addresses this critical issue for PECVD (T-CVD)-grown graphene is presented in Section **2.2**.

For device applications, the delicate nature of monolayer graphene requires special handling. Section **2.3** describes the nanoscale patterning techniques for processing graphene-based devices. Finally, several examples of graphene-based device applications are presented in Section **2.4**.

2.1 Synthesis of graphene by plasma-enhanced chemical vapor deposition (PECVD)

2.1.1 Experimental setup of the PECVD system

The experimental setup of PECVD for graphene synthesis is shown in Figure. 2.1 The PECVD system consists of a microwave plasma source, a growth chamber, and a gas delivery system. The plasma source (Opthos Instruments Inc.) includes an Evenson cavity and a power supply (MPG-4) that provides an excitation frequency of 2450 MHz. The Evenson cavity matches the size of the growth chamber, which primarily consists of a 1/2-inch quartz tube (with the inner and outer diameters being 10.0 mm and 12.5 mm, respectively) and components for vacuum control. The reactant gas delivery system consists of four mass flow controllers (MFCs) for CH_4, Ar, H_2, and O_2. An extra variable leak valve is placed before the CH_4-MFC for precise control of the partial pressure of CH_4. During the growth process, the pressure of the system is maintained at ~ 25 mTorr. For the PECVD growth substrates, we use 25 μm-thick Cu-foils (Alfa Aesar with purity = 99.9996%). Prior to the graphene synthesis, the Cu-foils are always sonicated in Aceton and isopropylalcohol (IPA) for 5 minutes, then dried by nitrogen gas before being inserted into the growth chamber. Several pieces of (1.5×0.8) cm^2 Cu-foils may be first placed on a quartz boat and then introduced into the growth chamber, as shown in the top inset of Figure. 2.1.

The graphene synthesis on Cu substrates is first preceded by the removal of native copper oxide when the Cu-foils are exposed to H_2 plasma at 40 W power for 2 minutes. Planarization of the Cu surface ensues simultaneously within 2 minutes after the oxide removal. The growth chamber is subsequently evacuated until the pressure reaches ~ 25 mTorr, and then a mixture of CH_4 and H_2 gases with steady partial pressures are introduced, where H_2 is used to enhance the dissociation of hydrocarbon. During the initial growth process, graphene nucleates on both the top and bottom sides of the Cu-foils. Continuous exposure of the Cu-foils to plasma at 40 W for 5 ~ 15 minutes in a mixture of CH_4 and H_2 gases (middle inset of Figure. 2.1) leads to continuing graphene growth. After the growth, the plasma-heated sample is cooled back to room temperature within at least 30 minutes without breaking the vacuum. The presence of Cu deposits on the quartz tube and holder during PECVD-growth process typically indicates a successful run (see the bottom inset of Figure. 2.1) because it implies a proper etching rate of Cu surfaces that enables graphene nucleation and growth.

Our empirical studies find that 40 W is the optimal plasma power for the growth of both monolayer graphene (MLG) and bilayer graphene (BLG), and the resulting gas and substrate temperatures under continuous plasma exposure are found to be ~ 425 °C and ~ 400 °C, respectively. The atomic structure of monolayer graphene grown by this PECVD method is show in the Figure. 2.2.

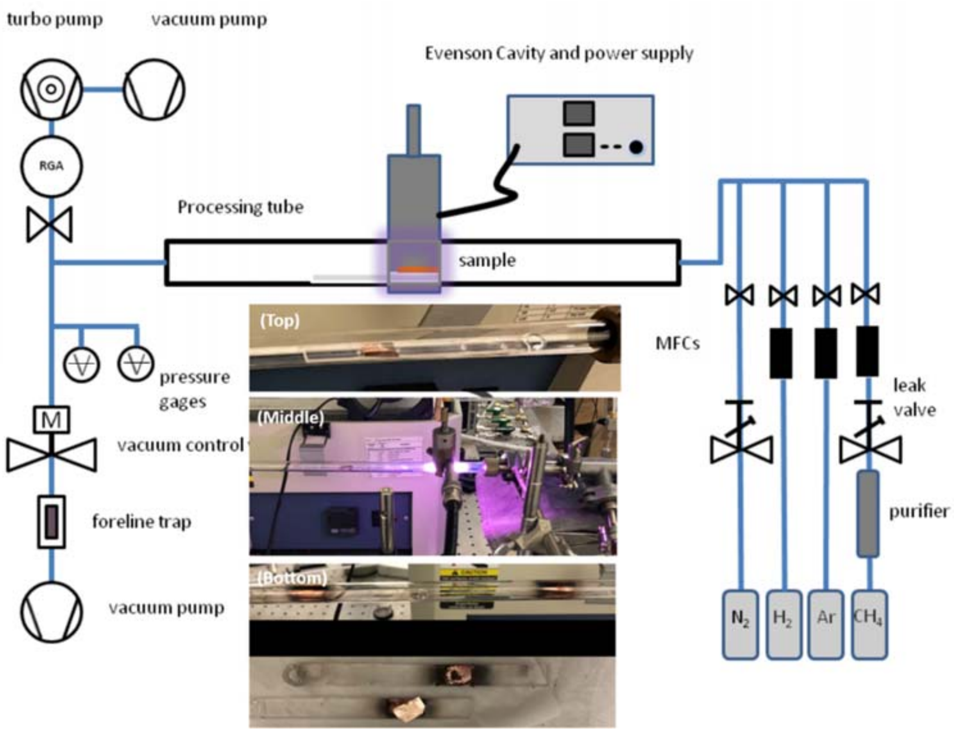

Figure. 2.1. Schematic of the PECVD setup. Top inset: Photograph showing a 25 μm thick polycrystalline Cu-foil (purchased from Alfa Aesar with purity 99.9996%) being placed on a quart boat and inserted into the PECVD growth chamber that consists of a ½-inch quartz tube and vacuum components. Middle inset: Photograph showing continuous exposure of a Cu-foil to microwave plasma in a mixture of CH_4 and H_2 gas for ensuing graphene growth on Cu. Bottom inset: Photograph showing Cu deposit on both quartz tube and quartz boat after graphene growth due to the etching of Cu-foil during the growth process. The deposition of Cu is taken to be a signature for a successful run[44,45].

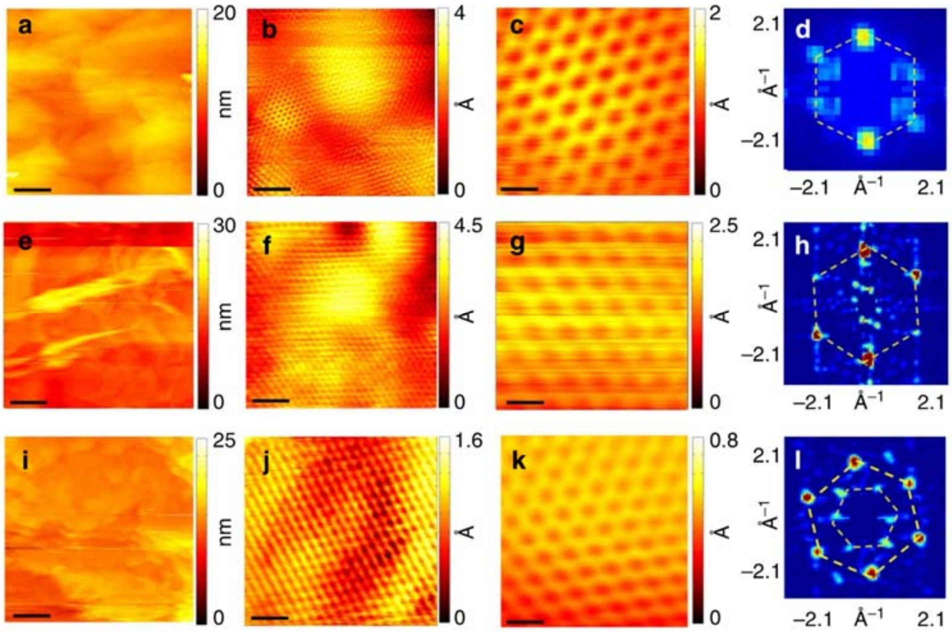

Figure. 2.2. Topographies of PECVD-graphene on copper. STM topographies of PECVD graphene at 77 K over successively decreasing areas (first three columns) and the corresponding Fourier transformation (FT) of large-area topography (fourth column) for samples grown on (a–d) Cu foil; (e–h) Cu (100) single crystal; and (i–l) Cu (111) single crystal. The scale bars for a, e, and i are 40 nm; for b, f, and j are 2nm; and for c,g, and k are 0.4nm.

2.1.2 The growth of single crystalline bilayer graphene

The PECVD-growth processes of BLG are similar to the single-step PECVD-growth of MLG except that the twist angle between the layers of the BLG may be controlled by the ratio of partial pressures of CH_4 and H_2. By optimizing the control of P_{CH4}/P_{H2}, we show that BLG samples display an overall small spread of angular distributions (from AB-stacking to around 7.5°), where the interlayer orientation is identified by combined measurements of the hexagonal single crystalline edges between two layers and Raman spectroscopy.

Comparing the conditions for growing MLG on Cu, a critical parameter to achieve the growth of BLG on Cu is to adjust the ratio of P_{CH4}/P_{H2}[46]. The rationale for this approach is as follows: the second layer of graphene is known to grow underneath the first layer if excess carbon atoms migrate between the Cu surface and the first layer of graphene, which suggests that a pathway to achieve large-area BLG is to balance the growth rate between the first and second layers of graphene by slowing the growth rate of the first layer sufficiently to enable excess carbon atoms the necessary time to migrate beneath the first layer and to form the second layer[47–49]. Moreover, during the PECVD process, the growth rate of graphene depends on the rate of etching Cu-foils[50], and the presence of H_2 gas as well as the resulting radicals are not only the catalysts necessary to decompose CH_4 into C- and H-atoms for ensuing graphene growth, but also the agent that controls the etching rate of both graphene[51] and the Cu-foil. Therefore, by adjusting the partial pressure of CH_4, P_{CH4}, and keeping H_2 as the major gas flow in the growth chamber, we can control the ratio of P_{CH4}/P_{H2} to optimize the growth of BLG. Figure 2.3 shows representative SEM images for single crystalline MLG and BLG samples grown on the backside of Cu-foils after 3 minutes of PECVD process, where the P_{CH4}/P_{H2} ratios for MLG and BLG growth under the same H_2-flow rate (2.5 sccm) are 0.1 and 0.04, respectively. In the case of graphene samples grown on Cu-foils without extra processing except rinsing in IPA, the average lateral dimension of the single crystalline MLG flakes is found to range from 2 μm ~ 5 μm, whereas the average diameters of the first- (light gray region) and second-layer (dark gray region) graphene in the BLG samples are around 3 μm and 1 μm, respectively, as shown in Figure 2.3 (a) and (b). In contrast, for Cu-foils pretreated by extra planarization processes, the average domain sizes of the single crystalline MLG and BLG samples are found to be around 15 μm and 5 μm, respectively, as shown in Figure 2.3 (c) and (d). Graphene growth under this condition was used for the construction of Raman database because the crystalline sizes thus obtained are sufficiently large to satisfy the resolution limit of our Raman spectroscopy.

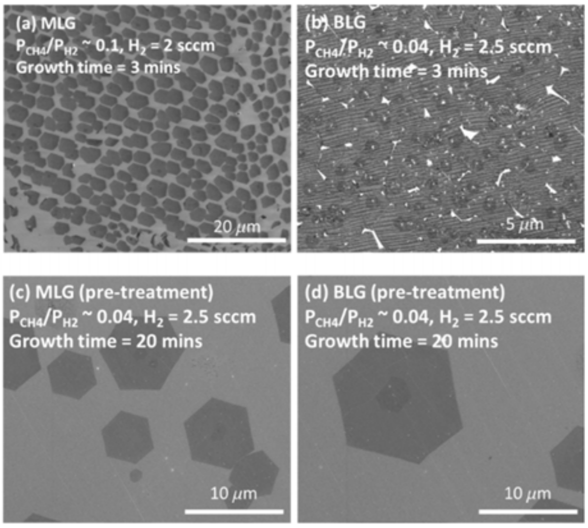

Figure. 2.3. SEM images for single crystalline MLG and BLG samples grown by PECVD on Cu foils. The lighter and darker gray colors represent the imaging contrasts between regions of MLG and BLG, respectively. (a) - (b) Graphene grown on Cu foils that have been prepared by simple sonication in ACE and IPA for 5 minutes before insertion into the growth chamber. Single crystalline MLG or BLG were first grown on the Cu foil, then gradually coalesced into a large MLG or BLG film with increasing growth time. (c) - (d) Graphene grown on pretreated Cu foils that have been first cleaned by acetic acid to remove CuO_x, sonicated in ACE and IPA for 5 minutes, and then inserted into furnace for annealing at 1050 °C in Ar and H_2 environment for 35 minutes to achieve planarization of the Cu surface, and finally placed into the PECVD system for graphene growth. The growth time was 20 minutes with $P_{CH4}/P_{H2} \sim 0.04$.

2.1.3 Raman spectroscopic characterizations of monolayer, bilayer, and twisted bilayer graphene

Raman spectroscopy with 514 nm laser wavelength and an incident power intensity of ~ 2.5 mW is used to characterize the properties of PECVD-grown graphene, and the typical acquisition time per spectrum is limited to ~ 10 s to prevent overheating the sample by laser. In general, the primary Raman modes associated with graphene characteristics include the doubly degenerate zone center E_{2g}-mode associated with the sp^2 in-plane phonon vibrations (the G-band at ~ 1584 cm^{-1}), the second-order scattering of zone-boundary phonons (the 2D-band at ~ 2700 cm^{-1}), and the D (~ 1350 cm^{-1}) and D′ (~ 1620 cm^{-1}) bands that are characteristics of defect-induced inter- and intra-valley scattering. Additionally, the intensity ratio of the 2D- to G-bands, the peak position, and the linewidth of the 2D-band are all dependent on whether the sample is MLG, BLG, or twisted bilayer graphene (tBLG).

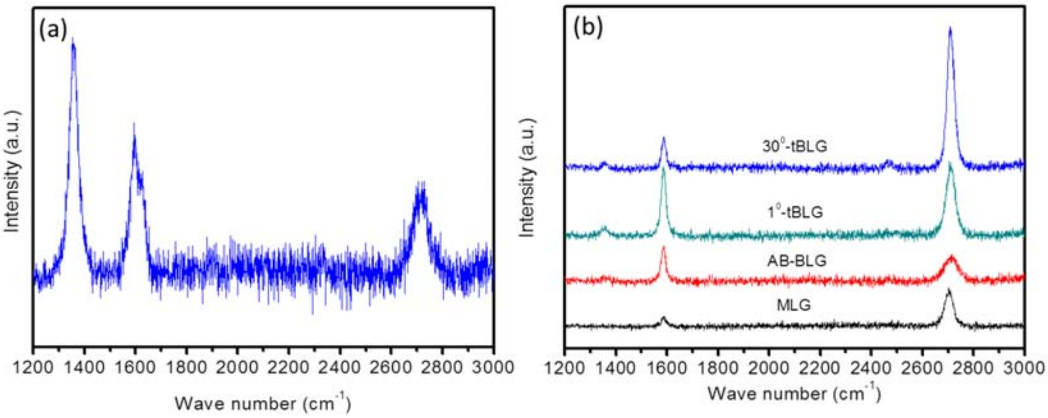

Figure. 2.4. (a) Representative Raman spectrum of graphene grown on the top-side of Cu-foil. The strong intensities of D- (~ 1350 cm^{-1}) and D′-bands (~ 1620 cm^{-1}) are indicative disordered graphene, and the lower intensity of the 2D-band (~ 2700 cm^{-1}) to the G-band (~ 1584 cm^{-1}) is consistent of a multilayer graphene sample. (b) Raman spectra of MLG, BLG, and tBLG grown on the bottom side of Cu-foil. The Raman spectrum of each curve has been vertically shifted for clarity. The black, red, green, and blue curves represent the Raman spectra of MLG, AB-stacking BLG, 1°-tBLG, and 30°-tBLG, respectively, and we note the complete absence of the D-band in MLG grown on the bottom

side of Cu-foil. On the other hand, the appearance of the D-band in the blue curve (30°-tBLG) is attributed to the interlayer interaction of tBLG.

For graphene grown on the top side of Cu foils, the Raman spectra always reveal D and D′ bands in addition to the G and 2D bands associated with pristine graphene, as exemplified in Figure. 2.4 (a). The apparent disorder may be attributed to direct bombardment of energetic particles on graphene grown on the top side of Cu-foils during the PECVD process, and the smaller peak intensity of the 2D-band than the G-band suggests the growth of multilayer graphene. In contrast, high-quality MLG and BLG, in both forms of hexagonal single crystals and large films, are found on the bottom side of Cu-foils through proper control of the ratio of CH_4 to H_2 partial pressures (*i.e.*, P_{CH4}/P_{H2}), as manifested by the absence of D and D′ bands in the Raman spectra shown in Figure. 2.4 (b).

For the growth of BLG, the twist angles between layers are generally randomly oriented without proper control of the PECVD growth parameters. To achieve control of the twist angles in the PECVD-grown tBLG, we explore an alternative and more cumbersome way in an effort to enlarge the grain size of single crystalline BLG samples. Specifically, we subject the Cu-foils to two steps of pretreatment by first soaking them in acetic acid (CH_3COOH) to remove the surface CuO_x, and then annealing them in Ar and H_2 environment for 30 mins at 1050 °C to smooth the surface of the Cu-foils. These pretreated Cu-foils are subsequently inserted into the PECVD system for graphene growth. Using the pretreated Cu-foils as the growth substrate, the average grain sizes of PECVD-grown MLG and BLG samples become 15 μm and 5 μm, respectively. The edges of these larger samples become clearly visible under an optical microscope, which makes the identification of the twist angle much easier. Additionally, we note that BLG samples grown on these pretreated Cu-foils do not exhibit preference for small twist angles. Using these larger BLG single crystals, we proceed to construct a database for the Raman spectra for tBLG.

2.1.4 Raman spectroscopic analysis of twisted bilayer graphene (tBLG)

Twisted bilayer graphene samples are separated from the Cu-substrates and transferred onto SiO_2/Si-substrates (Si wafers with a layer of 285 nm-thick thermal dry oxide on top) by means of the bubbling transfer method in buffered NaOH solution with the aid of PMMA[52], which ensures that our graphene samples are free of metal residues after the transfer. The Raman spectra of MLG and various BLG samples are exemplified in Figure 2.5 (a) and (b), where apparent variations in the Raman spectra are found in tBLG samples with different twist angles. The Raman modes for the G- and 2D-bands of MLG are located around 1584 cm^{-1} and 2685 cm^{-1}, respectively, whereas those for the BLG samples are located around 1585 cm^{-1} and 2700 cm^{-1}, respectively. The slight deviation of the G-band with respect to the typical value of 1582 cm^{-1} is attributed to excess carrier doping from the environment (such as atmospheric adsorption of H_2O and O_2)[20,53] or the substrate[54]. Here we remark that the peak position and FWHM of each Raman mode have been obtained by fitting the peak to a single Lorentzian function. For MLG, the 2D-to-G intensity ratio (I_{2D}/I_G) and the FWHM of the G-, and 2D-bands are found to be ~ 4, 25 cm^{-1} and 40 cm^{-1}, respectively. For BLG with AB stacking ($\theta = 0°$), the (I_{2D}/I_G) ratio and the FWHM of the G- and 2D-bands are ~ 0.6, 21 cm^{-1} and 60 cm^{-1}, respectively. For tBLG with $\theta = 30°$, the (I_{2D}/I_G) ratio and the FWHM of the G- and 2D-bands are ~ 4, 17 cm^{-1}, and 30 cm^{-1}, respectively.

Within the tBLG samples, different interlayer twist angles are found and are manifested in the Raman spectroscopy by different (I_{2D}/I_G) ratios, different degrees of enhancement in the G-band intensity that are associated with the resonant electron-hole pairs between the π- and π^* van Hove singularities (VHS) in the density of states, and the appearance of twist-angle dependent R- and R′-bands, where R- and R′-bands are the results of static interlayer potential-mediated inter- and intra-valley double-resonance Raman scattering processes[55,56]. Here we note that the VHS arise from the overlap of two Dirac cones, and that optical excitation processes that take place at the VHS will contribute to the G-band intensity[57,58]. Generally, the intensity of the G-band in BLG is slightly stronger than that in MLG due to the interferences of laser light in the stacked layers and multi-reflections of light when the number of graphene layers is smaller than 10[59,60]. Similarly, the different interlayer orientation changes the linewidth and position of the 2D-band; the 2D-band in the BLG is blue-shifted relative to that in MLG, and the blue-shift is non-monotonic with increasing twist angle.

Figure 2.5 (a) shows the Raman spectra of MLG, AB-BLG ($\theta = 0°$), and tBLG with twist angle $\theta = 1.2°$, 4°, and 30°. The FWHM of the 2D-band of AB-BLG and 30°-tBLG is found to be ~ 60 cm^{-1} and ~ 25 cm^{-1}, respectively. The tiny D-band in the Raman spectrum of 30°-tBLG (left inset in Figure 2.5 (a)) is activated by the interlayer coupling[61], and the 2D-band linewidth is slightly smaller than that of MLG (~35 cm^{-1}). Overall, the FWHM of the 2D-band is broader for a smaller twist angle. Additionally, the absence of defective peaks such as the D- and D′-bands at around 1350 cm^{-1} and 1620 cm^{-1} affirms the appearance of the R′-band at 1625 cm^{-1} (right inset in Figure 2.5 (a)), where the R′-band can only appear at a small twist angle ($3° < \theta < 9°$) and becomes inaccessible at a large twist angle, because the latter would require a large reciprocal rotational vector q, where $q \equiv |\mathbf{b}_{1(2)} - \mathbf{b}'_{1(2)}|$ is the absolute value of the difference between the reciprocal vectors $\mathbf{b}_{1(2)}$ and $\mathbf{b}'_{1(2)}$ for the top and bottom layers, respectively[61–64]. Although the D′-band associated with the disordered sp^2 carbon and the rotated angle dependent R′-band occur in the same Raman spectral range, we may exclude the possibility of D′ because it is associated with high defect densities[65,66]. Finally, Raman spectra for tBLG with the interlayer orientation around the resonant critical angles (12° and 14°) are plotted separately in Figure 2.5 (b), where the resonance due to VHS significantly enhances the intensity of the G-band so that the Raman spectra of other tBLG in Figure 2.5 (a) would have been difficult to resolve if they were plotted together on the same scale. The θ-dependent, non-dispersive R-band located in the range of 1400 cm^{-1} ~1500 cm^{-1} is also visible for the Raman spectra near the resonant conditions, as marked in Figure 2.5 (b). All these Raman spectral characteristics are found to compare favorably with previous reports[67,68].

In general, for a given excitation laser energy (~ 2.41 eV), the Raman spectroscopy for BLG with an interlayer twist angle larger than the critical angle will exhibit characteristics resembling those of the Raman spectrum of MLG because all optical excitation processes effectively occur in an isolated Dirac cone. On the other hand, for tBLG with twist angles smaller than the critical angle, the resulting Raman spectra will be significantly different from those of MLG because the two closely spaced Dirac cones associated with the bilayers in the momentum space will result in significantly different scattering paths.

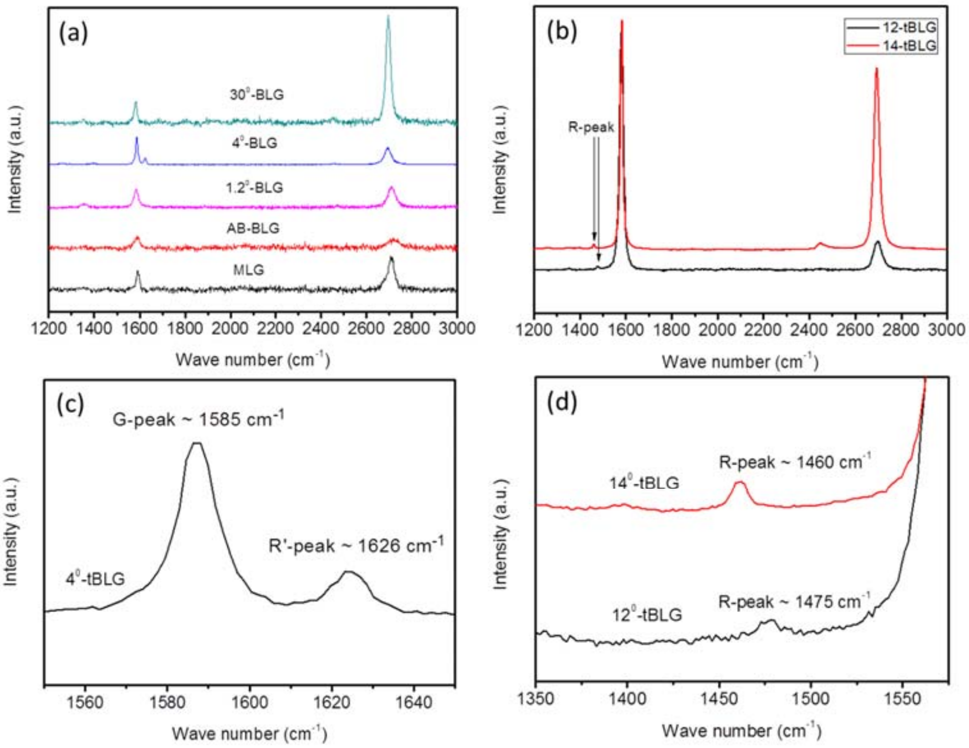

Figure 2.5. (a) The Raman spectra for MLG, AB-BLG, and tBLG samples with $\theta = 1.2°$, 4° and 30°. A non-dispersive D-peak is found in the Raman spectrum of 30°-tBLG. (b) The Raman spectra for tBLG samples with $\theta = 12°$ and 14°. (c) - (d) Twist-angle dependent Raman spectral features of R- and R′-bands, where R- and R′-bands occur due to static interlayer potential mediated inter- and intra-valley double-resonance Raman scattering processes. The R-band appears between 1400 cm^{-1} and 1500 cm^{-1} and R′-band positions around 1625 cm^{-1}.

To ensure that the majority of the PECVD-grown tBLG samples are controlled within the small-angle configurations, the ratio of P_{CH4}/P_{H2} during the PECVD growth must be kept to be sufficiently small, because small P_{CH4}/P_{H2} ratios can help reduce the growth rate of BLG and increase the interlayer coupling, which tends to favor the formation of smaller-angle tBLG (including the AB-BLG)[69–73]. After the PECVD synthesis, we verify the quality of the MLG and BLG samples by Raman spectroscopy by noting the absence of the D-band and the presence of well-defined G-band and 2D-band characteristics. To determine the twist angle of the BLG single crystals, we directly measure the crystalline edges between the first and second layers in the SEM images, and also analyze the peak positions of rotational R- and R′-bands in the Raman spectra.

Figure 2.6 shows a collection of the optical images and spatially resolved Raman spectroscopic maps for samples of MLG, very small-angle tBLG (with $\theta <\sim 1°$), 4°-tBLG, 7°-tBLG, 14°-tBLG, and 30°-tBLG.

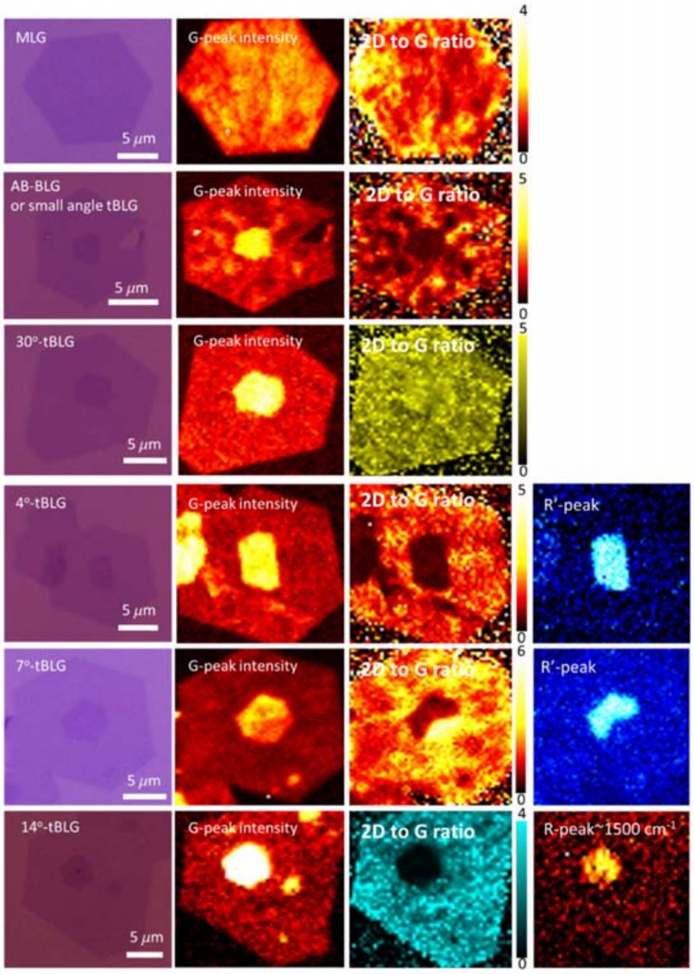

Figure 2.6. Optical images and spatially resolved Raman maps taken on MLG and BLG samples with varying twist angles. The Raman maps include maps of the G-band intensity, 2D-to-G intensity ratio, and the R- and R′-bands whenever they appear for specific twist angles. The peculiar R′-band mapping shown in the case of 7°-tBLG indicates that only one half of the BLG has $\theta = 7°$ whereas

the other half of the BLG has $\theta = 30°$, as confirmed by point Raman spectrum. In the case of 14°-tBLG Raman mapping, the R-band indicates inter-valley scattering, which only appears in the BLG region.

2.1.5 Work function analysis on tBLG

Kelvin probe force microscopy (KPFM) is a technique that enables nanoscale spatially resolved measurements of the surface potential difference between an atomic force microscopy (AFM) tip and the sample[74–76]. The contact potential differences (CPD) measured by the strength of the electrostatic forces between a conductive probe and the sample in the KPFM can reflect on the surface potential difference between two materials, which can be directly transformed into work function[77].

We perform surface potential measurements of the PECVD-grown BLG samples by KPFM of the Bruker Dimension Icon AFM system (Model: PFQNE-AL). To prevent possible charge transfer between the substrate and graphene due to such extrinsic effects as electron-hole puddles, doping domains in graphene[78], and quantum capacitances[79], we first transfer the PECVD-grown single crystalline BLG flakes onto the Au (111)/mica substrates. Measurements of the BLG surface potential are then carried out on the BLG/Au(111)/mica sample by KPFM in ambient environment. We further note that the distance between the AFM tip and sample has been fixed at 5 nm and the Au (111)/mica has been grounded throughout the KPFM measurement. The surface potential difference thus determined can be converted to work function (φ) by considering the work function of Au (111)/mica, which has been calibrated to be 4.7 eV by ultraviolet photoelectron spectroscopy (UPS). Thus, the work function of BLG is given by $|\varphi| = |(4.7\text{ eV}) - (\text{surface potential difference})|$.

The main panel of Figure 2.7 (a) shows a spatially resolved surface potential map of a sample obtained by the KPFM under ambient environment and with the pixel steps at 0.5 μm, and the inset is a Raman map of the G-band intensity on the same sample. In Figure 2.7 (b), representative Raman spectra are shown for the MLG region (green cross) and the nearly AB-stacking BLG region (solid-blue circle). The absence of any discernible D-band intensity suggests a high quality of our PECVD-grown graphene single crystals. The work function measured along the red line in Figure 2.7 (a) is illustrated in Figure 2.7 (c), where the work functions of MLG and BLG are found to be 4.48 eV and 4.58 eV, respectively. Both values are consistent with results reported previously. We note that the surface potential difference between MLG and BLG is around 100 mV, which is comparable to previous reports of the graphene surface potential increasing with the number of layers. Importantly, we do not find any discernible surface potential differences for tBLG with different interlayer twist angles.

We have also performed UPS measurements on large MLG and BLG films, and found that their work functions are 4.65 eV and 4.72 eV, respectively, as shown in Figure 2.7 (d). The work function measurements for MLG and BLG large films are performed via normal emission UPS by using monochromatic He I radiation with 21.2 eV photon energy as the UV source. The UPS characterization has been carried out in ultra-high vacuum (UHV), and the work function difference between MLG and BLG is found to be ~ 80 meV, which is on the same order of magnitude as the results obtained from KPFM. The slight difference between the results from KPFM and UPS may be attributed to environmental issues, such as atmospheric humidity for KPFM studies in ambient environment.

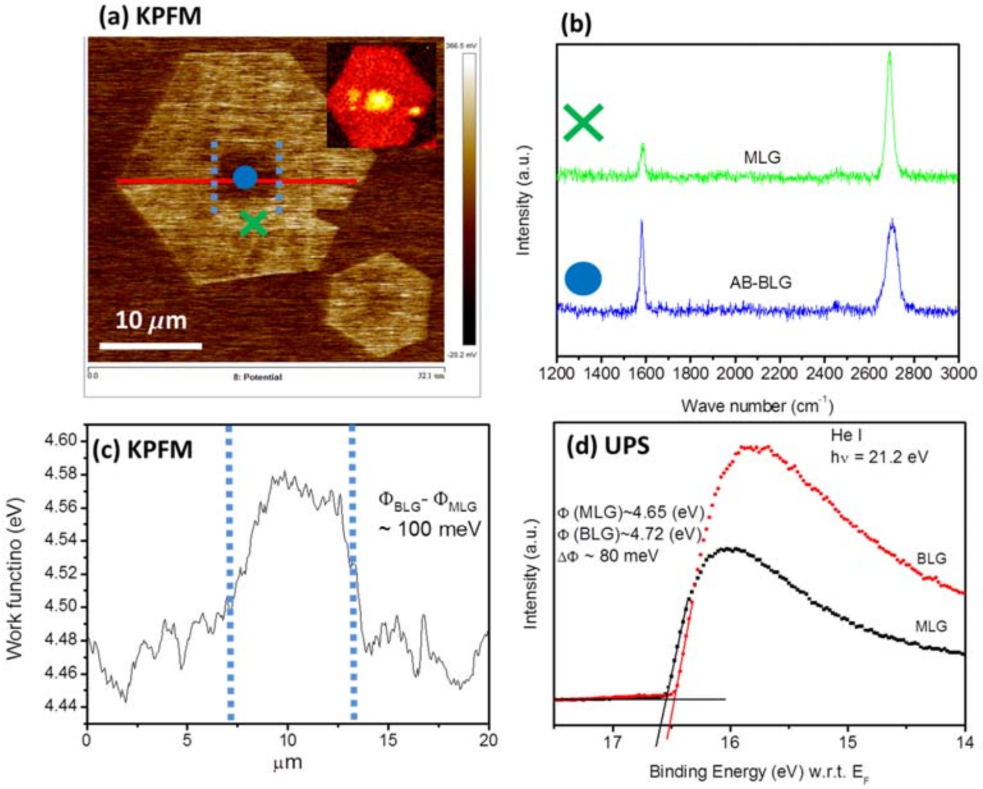

Figure 2.7. (a) Mapping of the surface potential of a large graphene film by KPFM. The inset shows the corresponding Raman map of the G-band intensity of the same sample. (b) Raman point spectra taken on an MLG area (green cross) and a nearly AB-stacking BLG area (blue solid-circle). (c) Spatial evolution of the work function measured along the red line depicted in (a), showing an apparent increase of the work function in the BLG area. (d) UPS measurements of the work functions of both MLG and BLG films, yielding values of 4.65 eV and 4.72 eV, respectively.

2.2 Transferred techniques for PECVD (T-CVD)-grown graphene

2.2.1 Experimental setup and procedures of the polymer-free graphene transferred method

The graphene films were grown on 25μm thick poly crystalline Cu foils in a similar process[80] described earlier in Section **2.1**. In a standard polymer-based graphene transfer method, such as using PMMA as the temporary supporting layers via spin-coating, a rigid support is needed for transferring graphene from Cu substrates to another substrate in order to prevent destroying the atomically thin graphene. Another interesting approach for graphene transfer involves using an amorphous carbon (a-C) transmission electron microscopy (TEM) grid as supporting layers[81]. To bond the graphene and the a-C TEM grid, a drop of isopropanol (IPA) is placed on top of the grid to wet both the a-C TEM grids and the underlying graphene film. As the IPA evaporates, surface tension draws the graphene and a-C film together into close contact. Therefore, in our new transfer method, surface tension is an important factor. The polymer-free transfer method developed in this study is shown in Figure 2.8. To control the surface tension of our etching solution, we mixed an IPA solution to reduce the surface tension as low as possible. For the same purpose of reducing surface tension around the graphene sample, we also designed a graphite holder to reduce the external force from ambient or solution that would apply on the graphene and to prevent it from degrading (folding or tearing) during the transfer process. All comparisons discussed below are made between the layers from the same CVD-grown graphene sample, but transferred with different methods.

Figure 2.8 illustrates the experimental set-up for the preparation of large-area monolayer graphene which can be applied on any substrates. A clean Petri dish was filled with 1: 10 mixed etchant, which is made by 1 part isopropyl alcohol (IPA) and 9 parts 0.1M ammonium persulphate solution ($(NH_4)_2S_2O_8$). A thin graphite holder with a diameter of 1 cm was then carefully placed at the etchant-air boundary, serving as a confinement area for the monolayer graphene and preventing it from attaching to the edge of the holder. The copper was etched with mixed etchant, and the monolayer graphene film floated on the surface of the solution. Two syringes, one empty and the other containing a mixture of DI water and isopropyl alcohol solution, were loaded into the syringe pump before the pumps were turned on. To control the surface tension for graphene in the solution, the etchant was pumped through the influent transfer lines at a rate of 0.3 ml/min, and the mixed water solution was simultaneously injected at the same rate. After the etchant became an overall mixture of water and isopropyl alcohol, the substrate was soaked in the solution. The solution was then pulled out with the syringe to lower the graphene onto the substrate, and the sample was heated at 60 °C in air for over 10 minutes to enable graphene flattening.

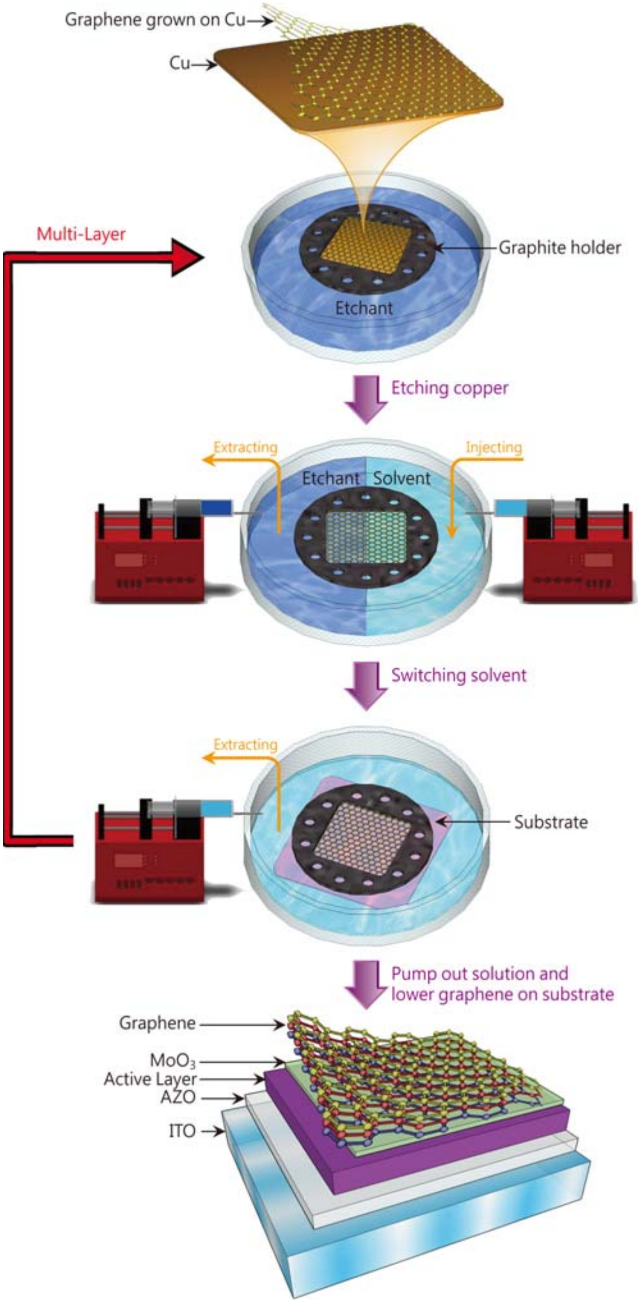

Figure 2.8. Schematic illustration of the polymer-free transfer process.

2.2.2 Optical properties comparison between the polymer-free transferred and PMMA-transferred monolayer graphene

Since graphene can be used as a transparent conductive electrode, high conductivity and optical transmittance should not be compromised after transfer. The residues left from the conventional polymer-assisted transfer method may degrade the conductivity and transmittance of the graphene sheet. Accordingly, Figure 2.9 shows the electrical and optical properties of graphene after transfer to glass and SiO_2 (300nm)/Si substrates. The transmittance of the graphene transferred by this polymer-free method was measured on glass by layers, from a single layer to multiple stacked layers. Figure 2.9 (a) shows the photos of stacked graphene layers on glasses sequentially created using the polymer-free transfer process. The quality of the graphene transferred on glass and SiO_2 is checked with Raman spectroscopy, as shown in Figure 2.9 (b). The sharp 2D peaks at around 2700 cm^{-1} indicate that the single-layer graphene sheets are still intact with the polymer-free transfer method. As the layer number increases, the intensity of the 2D peak decreases as expected. The transmittance of the stacked graphene layers was measured using a spectrophotometer (Jasco, V-670) with bare glass as a reference. The transmittance data, as a function of wavelength for the stacked graphene layers, is shown in Figure 2.9 (c). In addition, the inset shows the transmittance at λ= 550 nm as a function of the number of stacked graphene layers in each stacked layer. By fitting the data to Beer's law, we find that the attenuation coefficient α is 2.65% per layer, which is near the theoretical value of 2.3%[82,83]. The slightly higher attenuation for our stacked graphene layers may result from the wrinkles induced during the transfer process. Figure 2.9 (d) shows a comparison of sheet resistance between the stacked graphene layers transferred by the conventional PMMA method and the polymer-free transfer method on SiO_2 substrates. The sheet resistance of monolayer graphene and four-layer graphene transferred by the PMMA method on the SiO_2 substrate are 2.2 kΩ/□ and 450Ω/□, respectively. On the other hand, the sheet resistance of monolayer graphene is 810Ω/□, and that of four stacked graphene layers is 230Ω/□ on SiO_2 substrates. Although the sheet resistance will also be affected by the quality of the original graphene layers grown on Cu, we demonstrated that, from the same sample of CVD-grown graphene on Cu, the resistance of graphene sheets produced from the polymer-free transfer method is always lower than that from the PMMA transfer method.

The difference in the sheet resistance of graphene transferred with these two methods may be attributed to PMMA residues on the graphene and the better surface quality of graphene transferred with the polymer-free method. To investigate these points, the chemical composition and surface quality of the graphene are studied with scanning tunneling microscopy (STM), alongside X-ray and ultraviolet photoelectron spectroscopy (XPS and UPS).

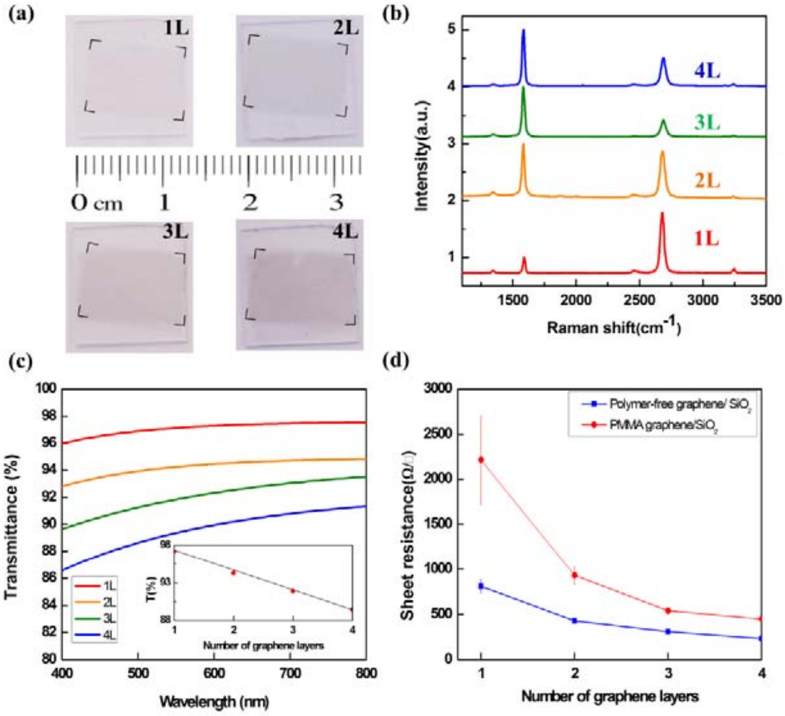

Figure 2.9. Optical and electrical properties of graphene sheets. (a) Photographs of 1.2× 1.0 cm^2 films with 1 to 4 layers of stacked graphene film on glass. (b) Raman spectra of graphene with 1, 2, 3, and 4 layer(s). (c) Transmittance of n-layer graphene films shown in (a). The inset is the transmittance, T(%), at $\lambda = 550$ nm as a function of the number of stacked graphene layers, n. (d) The sheet resistance of graphene with different numbers of layers on SiO_2.

2.2.3 Atomic structure of the polymer-free transferred monolayer graphene

Studies have reported atom-resolved STM images of CVD-grown graphene sheets after their transfer to other substrates. However, in order to obtain STM graphene images with atomic resolution, extra cleaning efforts need to be performed after the transfer. For example, in-situ high temperature anneal[84] is used for several hours to dispose of organic residuals remaining after the transfer processes. In our study, atom-resolved STM images of CVD-grown graphene, after transfer from Cu to silicon substrate, can be obtained using the polymer-free transfer method without additional in-situ cleaning processes. Figure 2.10 shows representative STM images of the as-loaded graphene sheet transferred onto silicon (111) substrates. The atom-resolved honeycomb structure is clearly visible in Figure 2.10 (a) with an 8nm × 8nm scale and also in Figure 2.10 (b) with a 2nm × 2nm scale. Topographic STM measurements are made over numerous regions across the sample; therefore, honeycomb structures of graphene can be obtained. As shown by the histogram in Figure 2.10 (c) and 2.10 (d), we found the height of surface corrugations of up to ± 0.6 nm over a lateral distance of 8 nm and ± 0.3 nm over a lateral distance of 2 nm, which is in good agreement with the results reported previously[84–87]. The observed atomic spacing is consistent with the lattice constant of graphene, and the appearance of the distorted hexagonal lattice in the STM image indicates strong surface tension originating from the interaction between graphene atoms and the Si substrate. STM images with atomic resolution can be achieved at most of the location on the film which indicates the excellent surface quality of the graphene sheet transferred with the polymer-free transfer method. On the other hand, for CVD-graphene transferred by the PMMA-assisted method, the atom-resolved STM images could not be obtained without using in-situ high temperature annealing to remove PMMA residues.

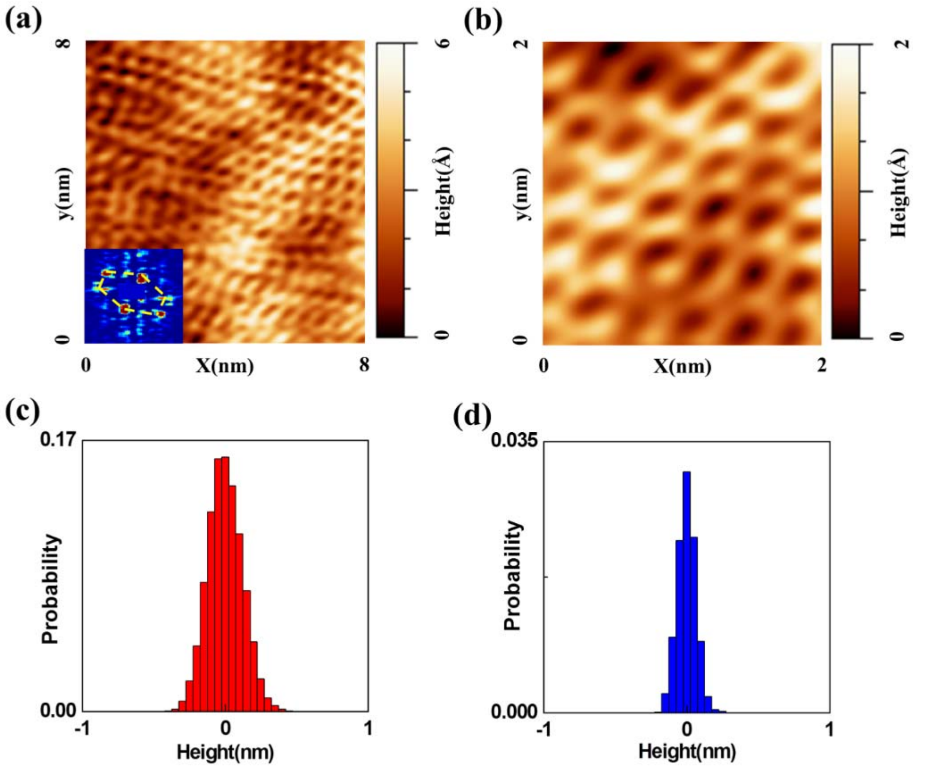

Figure 2.10. Representative STM images of the graphene sample after its transfer to a Si (111) substrate, with $V_{sample} = 0.2$ V and $I_{tunnel} = 0.1$ nA. The image size is 8 nm × 8nm in Figure 2.10 (a) and 2 nm × 2nm in Figure 2.10 (b). The inset in Figure 2.10 (a) is the Fourier transformation (FT) of large-area topography. The histogram of surface morphology of graphene is shown in Figure 2.10 (c) and Figure 2.10 (d).

2.2.4 Chemical residues measurements on the transferred monolayer graphene

In addition to atomic structures examined with STM, the chemical and electronic structures of the transferred CVD-graphene sheets are also investigated via UPS and XPS. Figure 2.11 (a) and 2.11 (b) show a secondary-electron onset, which represents the vacuum levels of the samples and can be used to determine its work function, and valance band spectra of polymer-free transferred graphene samples and PMMA-assist transferred graphene samples obtained from UPS using He II radiation. The binding energies of the spectra are all referenced to the Fermi level. The work function Φ is determined from the secondary electron energy threshold as $\Phi = h\nu - E_F - E_{cutoff}$, where $h\nu$, E_F, and E_{cutoff} are respectively the photon energy of He II radiation (40.8 eV), the Fermi level energy (0 eV), and the measured secondary-electron high-binding energy cutoff. E_{cutoff} was determined using a linear extrapolation of the high binding-energy cutoff region. E_{cutoff} of the polymer-free transfer graphene film was determined to be 36.25 eV, corresponding to a work function of 4.55 eV, which is consistent with the reported value of pristine graphene film[88]. The work function of the PMMA-assist transferred graphene sheet is 4.3 eV. The lower work function of 4.3 eV indicates that the Fermi level is affected by the impurity left on the graphene surfaces from the transfer process. Figure 2.11 (b) displays the valence band spectra of the polymer-free transferred graphene; the spectra retain the main features of the pristine graphene reported previously[89], which are C 2p π bands between 0 and 4 eV, C 2p σ+π bands at roughly 6 eV, C 2p σ states at 7.9 eV, C 2*s*-2*p* hybridized states at 10.5 eV, and C 2s σ states at 13.3 eV. However, these features in the valence spectra of the PMMA-assist transferred graphene are relatively smeared, especially for energy levels closer to the Fermi level (*i.e.*, 2p σ+π and 2p π). Parts of the delocalized 2p π states tend to bond with PMMA residues left on the graphene surface, which result in the depression of the 2p π electron states in the valence band and reduce the conductivity of the graphene sheets after being transferred.

Using XPS, chemical residues left on the graphene by conventional PMMA transfer and polymer-free transfer processes are compared and examined. Figure 2.11 (c) shows the XPS carbon 1s core levels of graphene. In the polymer-free transferred graphene sample, the C 1s spectrum can be deconvoluted with a sp^2-hybridized C-C peak at 284.4V (± 0.1eV) and sp^3-hybridized C-C at 285.1V (± 0.1eV), which is a result of amorphous graphitic carbon and defects. Meanwhile, the PMMA-transfer graphene sample spectrum contains various chemical bonds associated not only with the

sp^2- and sp^3- hybridized carbon of the graphene, but also with various binding peaks from the PMMA residues on the graphene surface and extra function groups of the carbon atoms that originate from the PMMA (inset Figure). The peaks at 286.5 eV (± 0.1eV), 287.4 eV (± 0.2eV), and 289.1 eV (± 0.2V) are associated with the bonding of carbon atoms in polymer backbone (C3), the carboxyl function group (C4), and the methoxy function group (C5) in the PMMA residues[90,91]. Both UPS and XPS data show that fully removing the PMMA residues on graphene is difficult, and the residue would affect the quality of the graphene after being transferred.

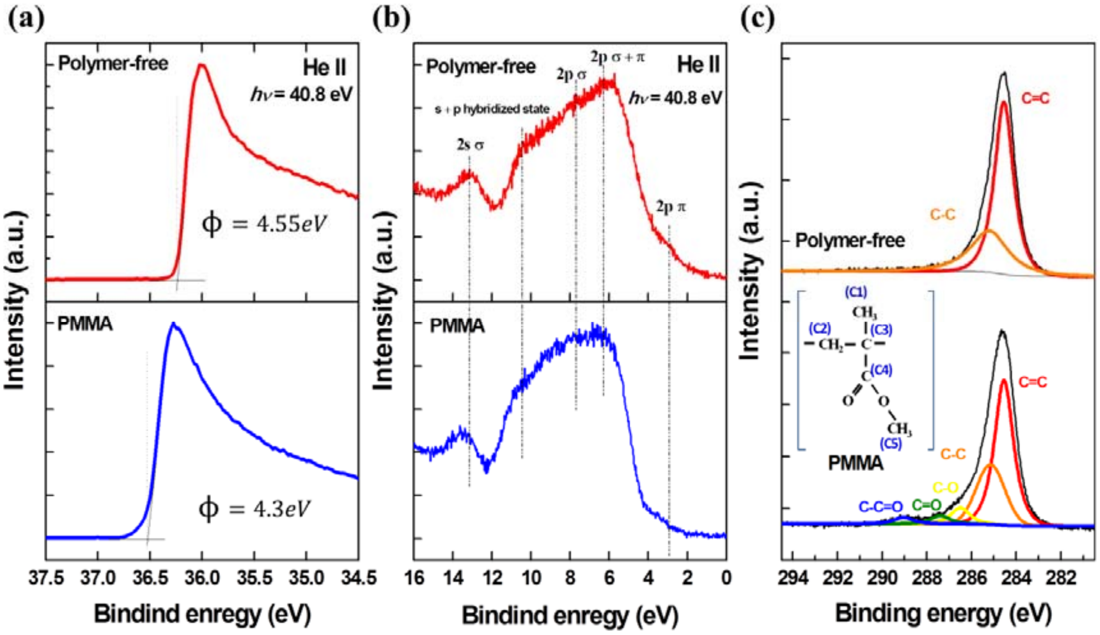

Figure 2.11. The ultraviolet photoelectron spectra and X-ray photoelectron spectra of graphene transferred by the polymer-free method and the PMMA method. (a) The work function of He II UPS valence-band spectra of the polymer-free transferred graphene sample and the PMMA transferred graphene sample. (b) Relative variation of He II UPS valence-band spectra of polymer-free transferred graphene sample and PMMA transferred graphene sample. (c) C 1s core-level XPS of polymer-free transferred graphene sample and PMMA transferred graphene sample.

2.3 Device fabrication techniques for graphene nanoribbons

Graphene is a great material for electronic devices because of its extraordinary properties, including high mobility, high thermal conductivity, and high transparency. However, the intrinsic zero bandgap makes it very difficult to achieve a high on/off current ratio of the field-effect transistors (FETs). In order to overcome this drawback, many attempts have been made to open the bandgap of graphene by various techniques, including hydrogenation, doping, and lithographic patterning. Patterning graphene into nanoscales with sub-10nm widths was suggested as a strategy to open a band gap. Graphene nanoribbons (GNRs) can confine carriers in graphene in the lateral dimension, which can induce a bandgap whose magnitude depends on the width of the GNRs according to the following formula (Equation 2.1)[92]

$$\Delta E(w) = \frac{hv_0}{2w} = \frac{2.07eV \cdot nm}{w}, \qquad (2.1)$$

where $v_0 = 10^{15}$ nm/s is the Fermi velocity of graphene and w is the width of graphene expressed in nanometers.

In this section, we present a comparative study between a top-down e-beam lithographic etching method and a helium/neon ion-beam lithographic patterning method for developing graphene into GNRs.

2.3.1 E-Beam Lithography

E-beam lithography is a resist patterning technique. An electron is scanned across a surface in a pattern defined by a CAD file. The scanned beam exposes a resist that has been coated onto the surface. Immersion of the resist in a developing solution causes the pattern to be revealed in a manner depending on the type of resist used. The process procedure was described as follows (Figure 2.12). First, graphene was transferred on the target substrate (Au(111)/mica). A drop of PMMA 950 A2 was spin coated on top of the graphene with 3500 rpm for 1min. After the spin coating process, the sample was baked on a hotplate at 180 °C for 2 minutes. Then, exposure of

PMMA by electron beam was performed at 100 keV accelerating voltage. Development process was performed in a cold solution (-10 ~ -20°C) of 3-parts isopropanol (IPA) and 1-part methyl isobutyl ketone (MIBK) for 1 minute. Lastly, O2 plasma was used to etch away the unmasked part of the graphene, and then PMMA was removed by Acetone. The graphene nanoribbons patterned by E-beam lithography techniques are shown in Figure 2.13 and the atomic structures of the patterned GNRs are shown in Figure 2.14.

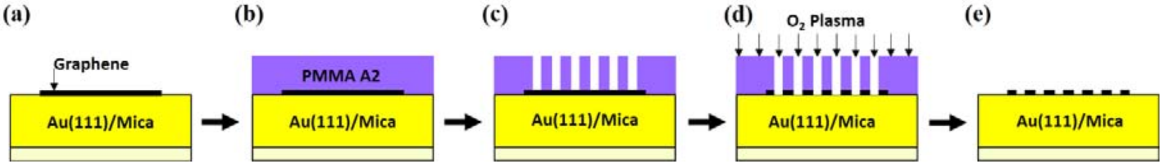

Figure 2.12. (a) Transfer graphene to Au(111)/Mica. (b) Spin coating PMMA A2 on G/Au/Mica (3500rpm, 1 min, Ace = 5) and baking it at 180 °C for 2 min. (c) E-beam exposure for different electron dose and cold develop (-10~-20°C) in MIBK:IPA=1:3, for 1min. (d) O_2 Plasma etching (10 sccm O_2, 20 mtorr, 80 W, 15sec), (e) PMMA removal process in 65 °C Acetone for 45 min.

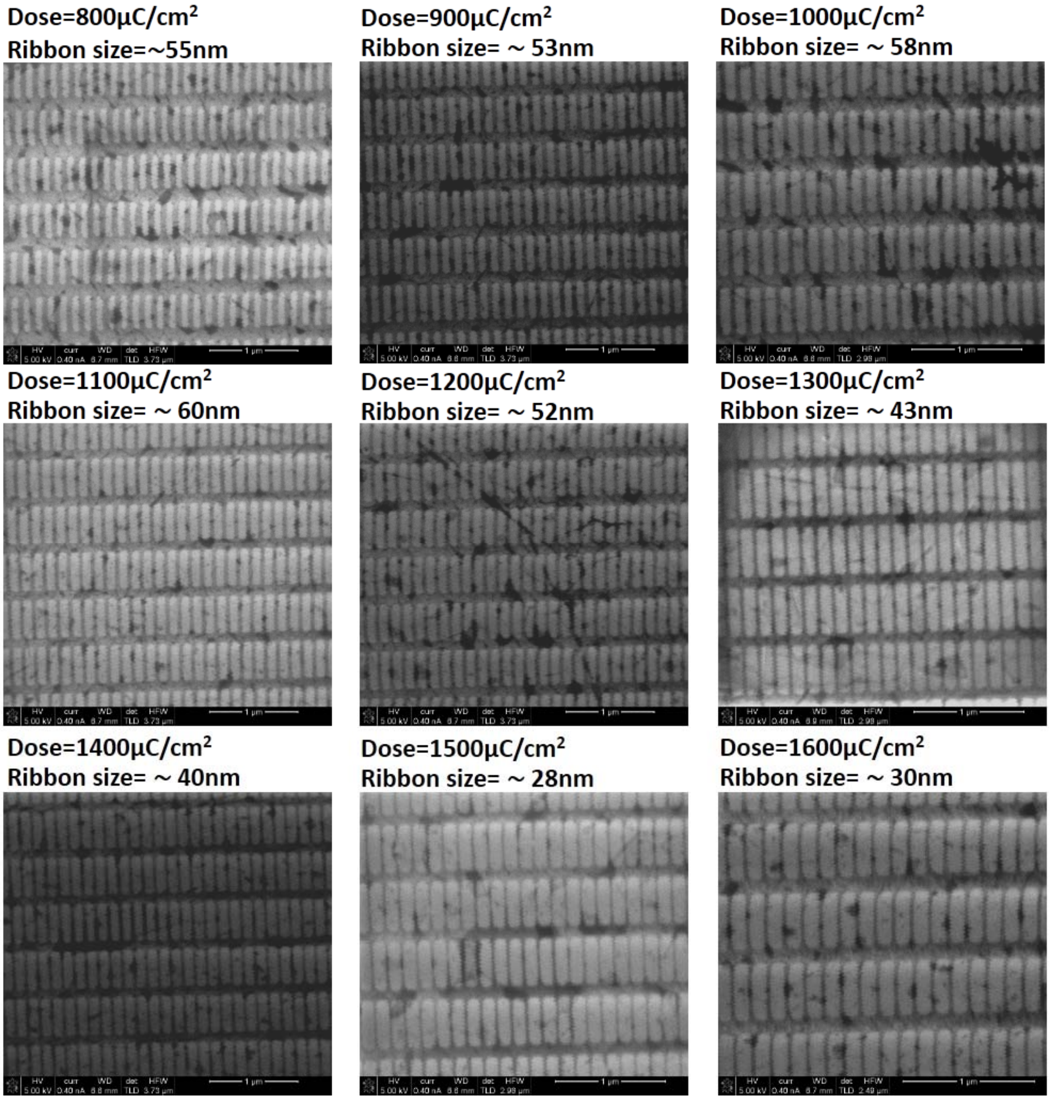

Dose=800μC/cm^2
Ribbon size=~55nm

Dose=900μC/cm^2
Ribbon size= ~ 53nm

Dose=1000μC/cm^2
Ribbon size= ~ 58nm

Dose=1100μC/cm^2
Ribbon size= ~ 60nm

Dose=1200μC/cm^2
Ribbon size= ~ 52nm

Dose=1300μC/cm^2
Ribbon size= ~ 43nm

Dose=1400μC/cm^2
Ribbon size= ~ 40nm

Dose=1500μC/cm^2
Ribbon size= ~ 28nm

Dose=1600μC/cm^2
Ribbon size= ~ 30nm

Figure 2.13. SEM images of graphene nanoribbons with different patterned widths ranging from 28 nm to 60 nm.

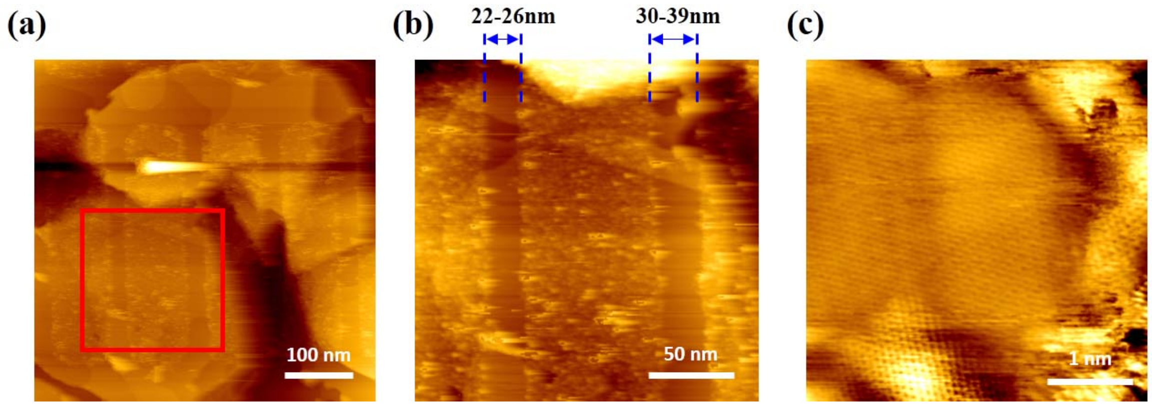

Figure 2.14. STM measurements on the edge structures of the graphene nanoribbons. (a) A representative STM image of the GNRs on a Au (111) substrate, with $V_{sample} = 0.02$ V and $I_{tunnel} = 2$ nA. The image size is 500 nm × 500 nm. (b) Topography of the GNRs with $V_{sample} = 0.02$ V and $I_{tunnel} = 2$ nA, and the image size is 200 nm × 200 nm (c) Topography of GNRs with $V_{sample} = 0.02$ V and $I_{tunnel} = 2$ nA, and the image size is 5 nm × 5 nm.

2.3.2 Helium/Neon focused ion beam lithography

The focused ion beam (FIB) of a helium ion/neon ion microscope (HIM/NIM) is an attractive tool for precise etching of encapsulated graphene devices because of its short de-Broglie wavelength, its sub-nanometer probe size, and the small beam spreading in materials. Ion irradiation has been performed using a Carl Zeiss Orion NanoFab helium/neon ion microscope and the NPVE pattern generator from FIBICS Inc. We used a 30 keV He^+ beam at normal incidence and an ion current of 0.5 pA. The beam dwell time was 0.2 µs and the beam step size 0.2 nm. The smallest aperture of 5 µm was selected, giving the narrowest ion beam. The number of repeats was varied to achieve the desired dose.

The Orion NanoFab presented the capability and performance of this novel microscope. Controlling the feature size and material removal via conventional gallium FIB systems is now surpassed by using neon and helium ion beams. The Orion NanoFab has been applied to a wide range of applications, including nanomachining 5 nm pores for patterning devices in graphene as shown in Figure 2.15. Comparison of the edge roughness of GNRs patterned by E-beam lithography and those patterned by Helium/Neon focused ion beam lithography is shown in Figure 2.16.

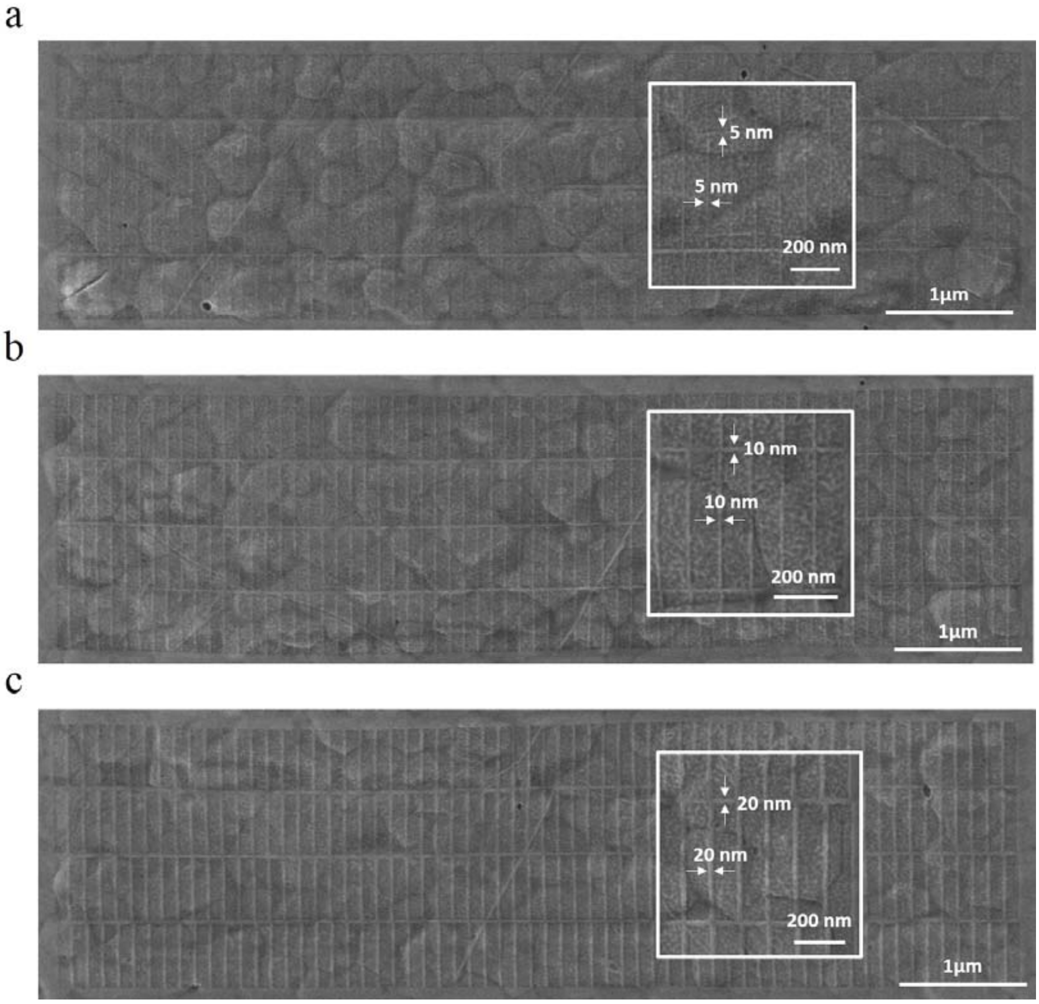

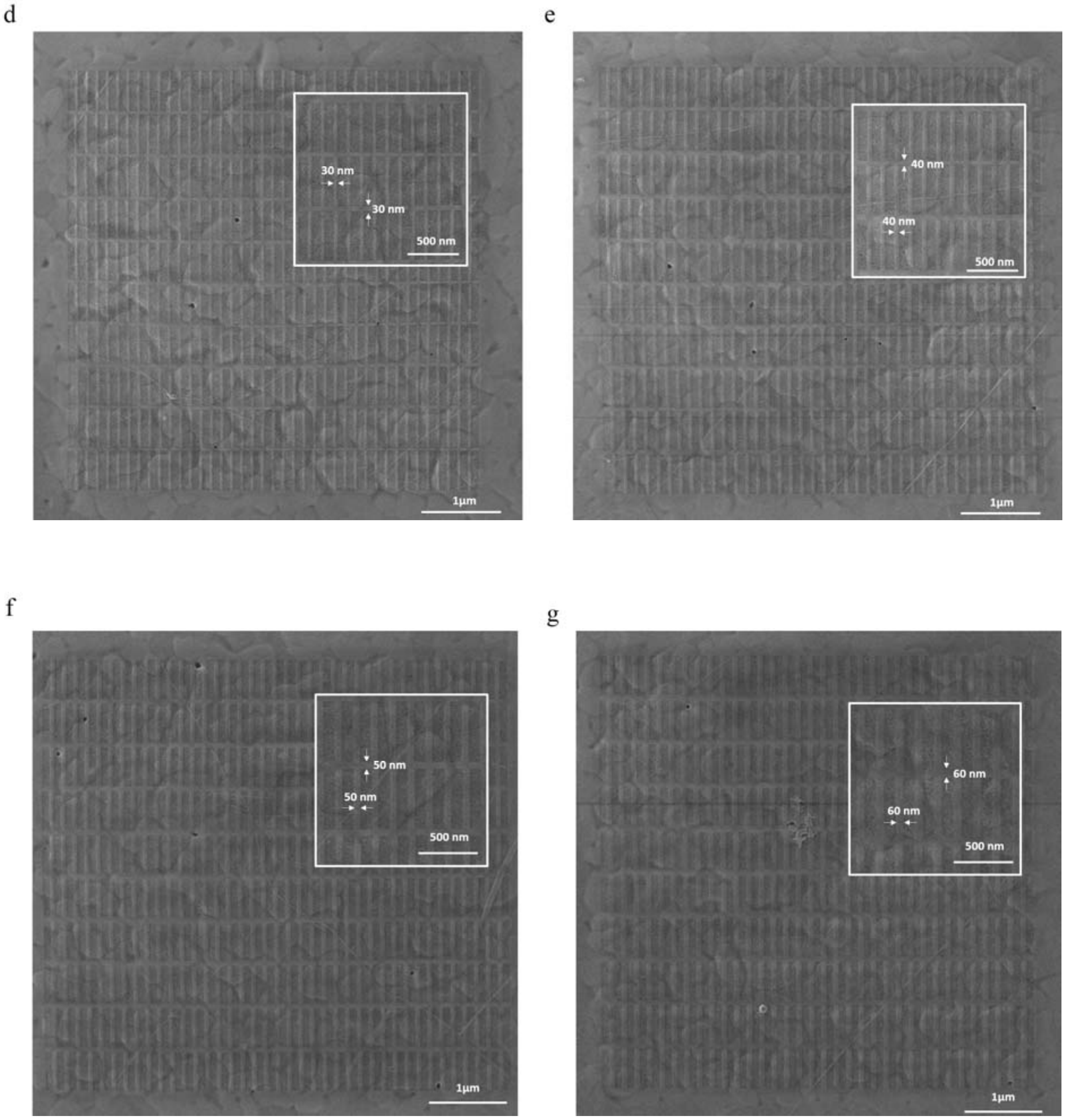

Figure 2.15. HIM images for helium ion etching on graphene nanoribbons with the width from 5 nm to 70 nm respectively.

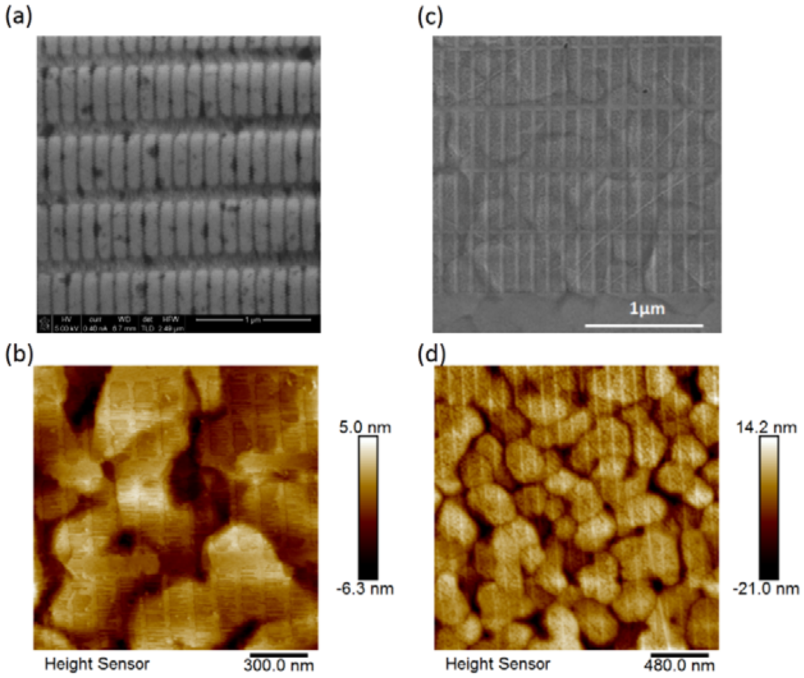

Figure 2.16. Comparison of the edge roughness of GNRs patterned by e-beam lithography (left panels) and by Helium/Neon focused ion beam lithography (right panels).

2.4 Graphene device technologies

2.4.1 Electrical mobility measurements on monolayer graphene-based field effect transistors

Field-effect-transistors (FETs) were fabricated with monolayer graphene sheets transferred onto boron nitride (BN)/SiO_2 (300 nm) substrates using both polymer-free and the conventional polymer-assisted methods. The source and drain area of the back-gated FETs were defined by a shadow mask with gate lengths of 50 μm. Figure 2.17 (a) shows the room-temperature electrical resistance vs. gate voltage characteristics of FETs. The charge neutrality points of FETs with polymer-free graphene and conventional graphene monolayers are located around a gate bias of 7 volts and 10 volts, respectively. The width of the peak around the charge neutrality point for polymer-free graphene FET is much narrower than that of the conventional graphene FET, which indicates the higher carrier mobility of polymer-free graphene. The field-effect mobility of the graphene-based transistor can be obtained by measuring the slop of the characteristics curve near the charge neutrality point. The field effect electron mobility of the graphene sheet on BN substrate transferred by the polymer-assisted method[93] is about 41000 $cm^2\ V^{-1}\ sec^{-1}$, which is similar to the reported value of CVD-grown graphene transferred on BN substrate[38]. In contrast, the mobility of polymer-free graphene monolayer on BN surface is as large as 63000 $cm^2\ V^{-1}\ sec^{-1}$, which is 50% larger than that of the graphene sheet transferred from the same CVD sample but using the conventional transfer method. Figure 2.17 (b) shows the conductivity vs. carrier concentration of the graphene-based transistor. The higher minimum conductivity of polymer-free graphene implies less structural defects in the polymer-free graphene, as compared to that of the graphene sheet transferred with the conventional method[22].

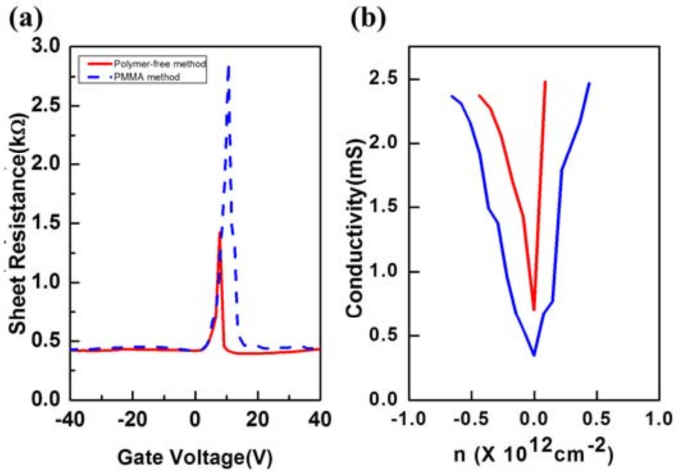

Figure 2.17. (a) Resistance versus gate voltage curves of the polymer-free-graphene/BN and PMMA-graphene/BN back-gated transistors. (b) Conductivity as a function of carrier density (n) of the polymer-free-graphene/BN and PMMA-graphene/BN transistors.

2.4.2 Electrical FET devices analysis on tBLG

In this subsection, we describe our investigation of the back-gated two-terminal field-effect transistor (FET) devices based on the PECVD-grown BLG samples in order to elucidate their electrical transport properties.

PECVD-grown single crystalline BLG flakes and large BLG films are transferred onto (100) p^{++}-Si chips (with resistivity ranging from 0.001 to 0.005 Ω-cm), which serve as the gate electrode with a capping layer of 285 nm-thick SiO_2. The carrier density (n) in the BLG can be tuned by a back-gated voltage (V_g) via the relation $n = C_{ox}/e(V_g - V_{CNP})$, where $C_{ox} = 11.6$ nF/cm^2 is defined as the capacitance per unit area of the 285 nm-thick SiO_2, and V_{CNP} indicates the shift of charge neutrality point (V_{CNP}) originated from unintentional doping in BLG. Nearly AB-stacking BLG single crystalline flakes are chosen as the material for the two-terminal back-gated device fabrication. For large BLG films, we also intentionally selected a BLG region with small twist angles for device fabrication.

To fabricate the two-terminal devices, source and drain contacts are defined by electron-beam lithography. A combination of Pd (10 nm thick) and Au (40 nm thick) are thermally evaporated onto the source and drain as contact electrodes. The BLG channel with a 1 μm-width (*W*) and a 3 μm-length (*L*) is subsequently defined by electron-beam lithography, and then etched by reactive ion etchant (RIE). The optical micrograph of a representative two-terminal device is shown in Figure. 2.18 (a), where the two black lines indicate the BLG channel with aforementioned dimensions, and the inset shows schematics of the device cross-section. Prior to the electrical measurement, lithographically patterned devices are baked in the forming gas environment (Ar and H_2) at 350 °C to remove chemical residues (such as PMMA residues remained on the BLG channel during the sample transfer and electron-beam lithography process) and atmospheric adsorbents like H_2O and O_2. Electrical measurements on the two-terminal devices are taken at room temperature and in vacuum environment (@ ~ 20 mTorr).

Figure 2.18 (b) and 2.18 (c) show representative measurements of the source-drain conductivity (σ) and resistivity (ρ) of BLG samples as a function of the gate voltage (V_g) in the vicinity of the charge neutrality point (CNP), where the black (red) curve represents the data taken on a back-gated FET device based on a single crystalline AB-BLG flake (a large BLG film). The source-drain voltage (V_{sd}) has been kept at 10 mV for the electrical measurements, which ensures that the corresponding back-gate electric field (E_{bg}) is restricted within the range of ±2.3 MV/cm to prevent from possible breakdown of the SiO_2 dielectric layer. The back-gate voltage (V_g) is swept from −70 V to 70 V, with the drain current (I_{sd}) passing through the BLG channel measured simultaneously. Thus, the conductivity (σ) can be obtained via the relation $\sigma = \frac{L}{W}\frac{I_{sd}}{V_{sd}}$. We have examined over 20 BLG devices, and all of them exhibit the V-shaped conductance (σ) as a function of V_g.

The ambipolar behavior revealed in the electrical transport measurements in Figure. 2.18 (b), where the conductivity in the negative back-gate voltage regions exhibits higher values relative the positive back-gate voltage regions, may be attributed to the asymmetric effects of the Fermi-energy sweep across p-p and p-n junctions in the BLG. Representative current on-off ratios, *i.e.*, (I_{on}/I_{off}), for devices based on the single crystalline BLG flake and the large BLG film are found to reach around 8 and 5, respectively. Additionally, the shift of charge neutrality point (CNP) is found to be around 25 V for the device based on the single crystalline BLG flake and around 28 V for the device based on the large BLG film. The shift in CNP could involve influence from substrate-induced electron-hole puddles, ripples, and residual atmospheric adsorbates[94].

The slight difference in conductivity (and also resistivity) between the single crystalline BLG flake and the large BLG film may be attributed to the presence of structural disorder, higher concentrations of nucleation centers, or even wrinkles caused short-range scattering encountered in the large BLG film based devices. The sub-linear behavior at high values of V_g, which corresponded to saturation of conductivity in the limit of higher carrier density as shown in Figure 2.18 (b) for both groups of BLG samples, may be attributed to the presence of short-range scattering sites (such as atomic defects). In contrast, long-range scattering mechanisms associated with charged impurity scattering and electron-hole puddles are known to dominate at low carrier density (*i.e.*, at low V_g) and determine the minimum conductivity at CNP.

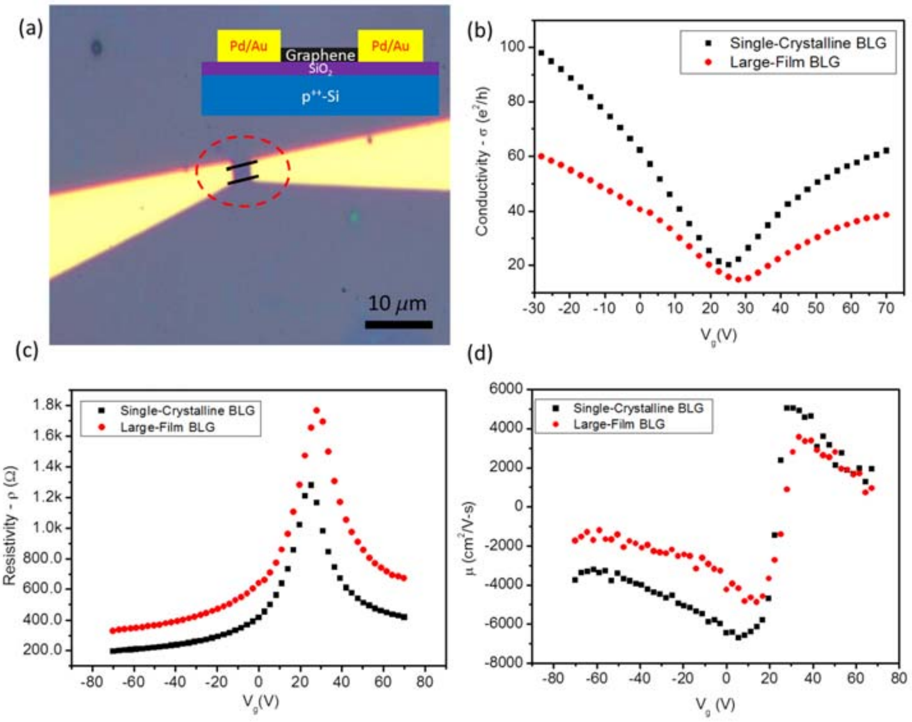

Figure 2.18. Electrical transport measurements of BLG samples: (a) Main panel: optical micrograph of a two-terminal back-gated FET device based on a BLG sample. The area enclosed by two black lines represents the BLG channel with a 3-µm length and a 1-µm width. Inset: Schematic side-view

of the FET device. (b) Representative conductivity versus gate-voltage (σ-vs.-V_g) curves for a single crystalline BLG (black squares) and a large BLG film (red circles), measured in units of (e^2/h). (c) Representative resistivity versus gate-voltage (ρ-vs.-V_g) curves for a single crystalline BLG (black squares) and a large BLG film (red circles). Both σ-vs.-V_g and ρ-vs.-V_g data have been taken with the source-drain voltage (V_{sd}) kept constant at 10 mV. (d) Carrier mobility of both the single-crystalline BLG (black squares) and large BLG film (red circles) derived from σ-vs.-V_g measurements and the direct-transconductance method. For single crystalline AB-BLG, the highest electron and hole mobility values are 5000 cm^2/Vs and 7000 cm^2/V-s, respectively. For large-film BLG, the highest electron and hole mobility values are 4000 cm^2/V-s and 5000 cm^2/V-s, respectively.

The carrier mobility (μ) of the BLG is also extracted by employing the direct-transconductance method via the relation $\mu \approx \frac{1}{C_{ox}} \frac{d\sigma\left(V_g\right)}{dV_g}$, where the mobility is measured in units of cm^2/V-s, as shown in Figure 2.18 (d). The carrier mobility in the vicinity of CNP for both groups of BLG devices is found to be in the range of 4000 to 7000 cm^2/V-s, which is consistent with previous reports for BLG on SiO_2/Si[95], although these values are generally smaller than those found in MLG[93,96,97].

Figure 2.19 shows the temperature dependent electrical measurements of a two-terminal FET device based on a nearly AB-stacking BLG single crystal from 300 K to 100 K. It is known that the temperature dependence of the conductivity behavior of graphene systems (both MLG and BLG) consists of contributions from several competing factors, including thermal activation of carriers from valence band to conduction band, electron-phonon scattering, temperature dependent screening effects, and activated carriers that are locally and thermally excited above the random-distributed charged disorder. For a perfect AB-stacking BLG known as a zero-gap semiconductor, direct thermal excitations of carriers from valence band to conduction band can comprise of an important contribution to the temperature dependent transport, which leads to reduced conductivity with decreasing temperature in the vicinity of CNP, which is analogous to the findings in MLG. On the other hand, the insulating temperature dependence of the conductivity at high carrier densities in our BLG samples suggests that the dominant transport mechanism is thermally mediated, which differs from the metallic conductivity of MLG at high carrier densities. Finally, we note that for very small twist angles near the magic angle, flat Moiré bands with a small energy gap emerge so that an insulator-to-superconductor transition can be induced by tuning the gate voltage at very low temperatures. Further systematic studies of the electrical transport properties of our PECVD-grown small-angle tBLG samples at low temperatures as a function of the twist angle will not only help verify the quality of these samples for superconductivity, but also elucidate the evolution of transport mechanisms with changing Moiré bands.

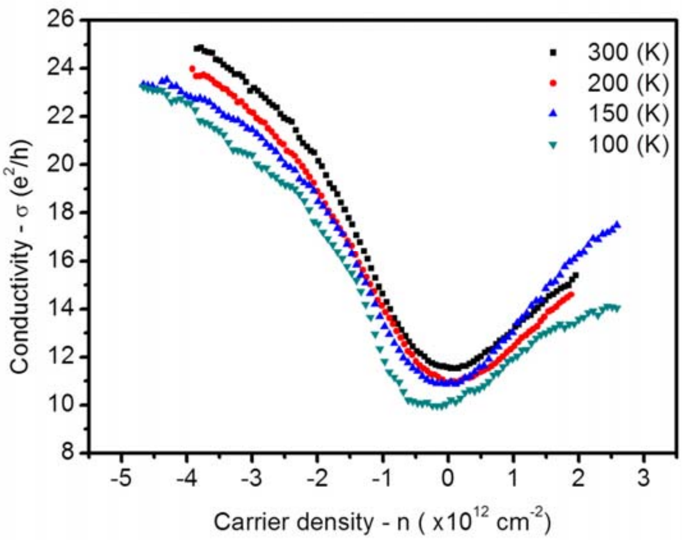

Figure 2.19. Conductivity σ of a back-gated FET device based on a nearly AB-stacking BLG single crystal is measured as a function of the carrier density n = C_{ox}/e ($V_g - V_{CNP}$) at various constant temperatures from 100 K to 300 K, where C_{ox} = 11.6 nF/cm^2. Insulating temperature dependence is found at both low and high carrier densities for this BLG device. Here we have horizontally shifted each isotherm of the σ (n) curve to the charge neutrality point (CNP) where n = 0 for easier comparison of the conductivity at different temperatures.

2.4.3 Graphene-based vertical tunneling devices

Monolayer graphene is grown on copper foils using the plasma-enhanced chemical vapor deposition (PECVD) described in Section **2.1**. A <100> n^{++}-Si substrate with a dopant concentration of 10^{19} cm^{-3} is used as the substrate, and a 300 nm field oxide is deposited using the LOCOS process around each contact region to define the tunneling area and isolate individual devices. The Si substrate is subsequently treated with buffered oxide etcher (BOE), immediately followed by the wet transfer of the graphene. The monolayer graphene is etched into a disk with a diameter larger than the contact region using oxygen plasma, followed by photo-lithography and e-beam evaporation of the side contacts (Cr/Au 10/100 nm).

Figure 2.20 (a) shows the cross-section illustration of our device structure. A degenerately doped n-type silicon (n^{++}-Si) was used as a substrate and electrode, and was thermally oxidized to form a thick SiO_2 insulating layer. The defined tunneling area with diameter of 190 µm was masked with Si_xN_y to prevent the oxidation. After removing the Si_xN_y and hydrogen fluoride acid treatment, a n^{++}-Si tunneling area was exposed. Few-layer h-BN and monolayer graphene were then transferred to form a heterostructure on top of the n^{++}-Si tunneling area, respectively. Note that at each transferring step, annealing treatment at 300 °C in H_2:Ar atmosphere was applied to thoroughly remove the organic contamination and clean the surface. Afterwards, a very thin aluminum layer was evaporated, which would be rapidly oxidized into the Al_2O_3 layer to protect our Gr/h-BN samples. Conventional optical lithography was then used for electrode and graphene disk shape patterning. Figure. 2.20 (b) shows the top-view optical image of our tunneling structure with Gr/h-BN etched into circular shape. The chromium-gold (Cr/Au) electrodes were grounded during the electrical measurement, and an alternative voltage bias was applied to the highly doped silicon.

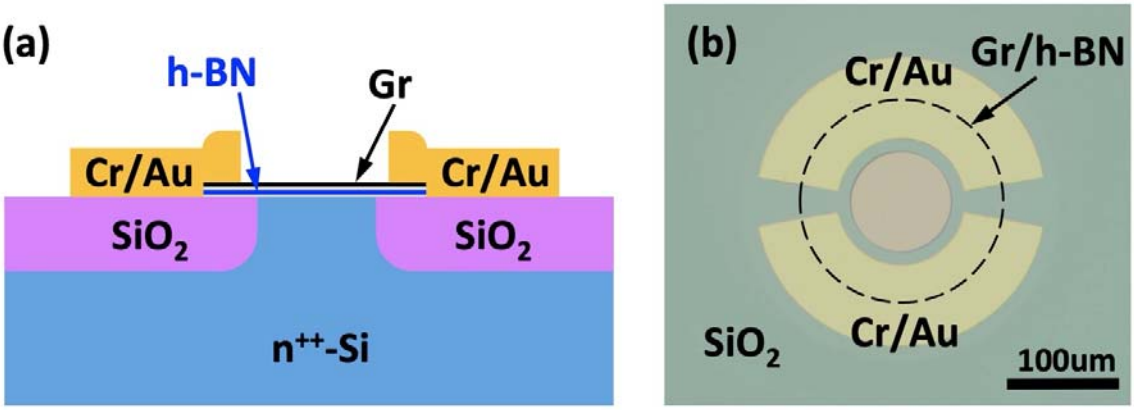

Figure 2.20. Graphene (Gr)-boron nitride (h-BN) heterostructure in our silicon-based tunneling device. (a) The side-view schematic of the tunneling device structure. (b) The top-view of the optical image of the tunneling device. The black dash circle labels the area with graphene coverage.

The tunneling spectroscopy at low temperature (1.9K) was then measured on the as-fabricated tunneling device, and the result was shown in Figure 2.21 (a). Here, two obvious dips are observed in the reverse bias region at -0.58 V and -1.06 V (denoted as $V_{M,1}$ and $V_{M,2}$). It is known that the derivative current (dI/dV) can represent the density of states (DOS) of a material (see supporting information). These two dI/dV valleys indicate two DOS minimums and may result from the secondary Dirac points (SDPs) induced by Gr/h-BN Moiré pattern formation. SDP detections have been reported by several works; however, up to date, the SDP observations were all done by scanning tunneling spectroscopies, which are atomic-scale results. Here, our tunneling device is micrometer-size, and n^{++}-Si is used as one of the electrodes. Thus, our result could be more macroscopic and representing an overall electron transport performance in large-scale CVD-grown Gr when supported by CVD-grown h-BN. Additionally, as described above and shown in Figure 2.22 (a) insert, when a reverse voltage is applied, electrons tunnel from n^{++}-Si to Gr, propagated laterally in Gr, and then collected by Cr/Au contacts. On the other hand, with forward bias applied, electrons are moving from Gr to n^{++}-Si, travel inside the heavily doped silicon substrate, and then collected by Cr/Au. It has been reported that electron mean free path in degenerately doped silicon crystal is around 10 nm at low temperature. Consequently, during the travel in silicon, electrons would undergo plenty of inelastic scattering processes and lose their transport information. Therefore, in this subsection, we focus our discussion on dI/dV signals in reverse bias region.

Multiple tunneling devices were fabricated and measured, and the two dI/dV dips around $V_{M,1}$ and $V_{M,2}$ occur repeatedly. We can then correlate these $V_{M,1}$ and $V_{M,2}$ values to energies of SDPs, $E_{SDP,1}$ and $E_{SDP,2}$, respectively, by multiplying an electron charge and realizing the difference from the primary Dirac point. All $E_{SDP,1}$ and $E_{SDP,2}$ values are extracted from measured tunneling spectra, and their average values (red and blue hollow squares), standard deviation (red and blue boxes), and extreme values (red and blue error bars) are plotted in Figure. 2.22 (b). It is reported that, with the superposition of Gr and h-BN layers, the SDP energy and the Moiré wavelength (λ_M) of the created Moire pattern depend on the rotation angle (θ) between the stacked Gr and h-BN as

$$E_{SDP} = \frac{2\pi\hbar v_F}{\sqrt{3}\lambda_M} \tag{2.2}$$

and

$$\lambda_M = \frac{1.018 a_{CC}}{\sqrt{2.036[1-\cos(\theta)]+1.018^2}} \tag{2.3}$$

where a_{CC} is graphene lattice constant (~ 0.246 nm) and v_F is electron Fermi velocity[98,99]. It is obvious that E_{SDP}, λ_M and θ are entangled to each other, and one of these parameters can delineate the created Moiré supperlattice. Equation (2.2) shows that Moiré patterns with specific Moiré wavelengths are generated in our Gr/h-BN heterostructure, and Equation (2.2) is capable of determining the relative rotation angles between our Gr and h-BN layers. As shown in Figure 2.22. (b), the values of $V_{M,1}$ and $V_{M,2}$ are 0.62 ±0.11 V and 1.12 ±0.08 V from our results of tunneling transport experiment, and the two Moiré wavelengths and rotation angles between Gr and h-BN lattices corresponding to these two E_{SDP}'s can be calculated through Equations (2.2) and (2.3), which are around 3.8 nm and 2.1 nm for Moiré wavelengths and ~ 3.4° and ~ 6.5° for rotation angles, respectively, as labelled in Figure 2.22 (b).

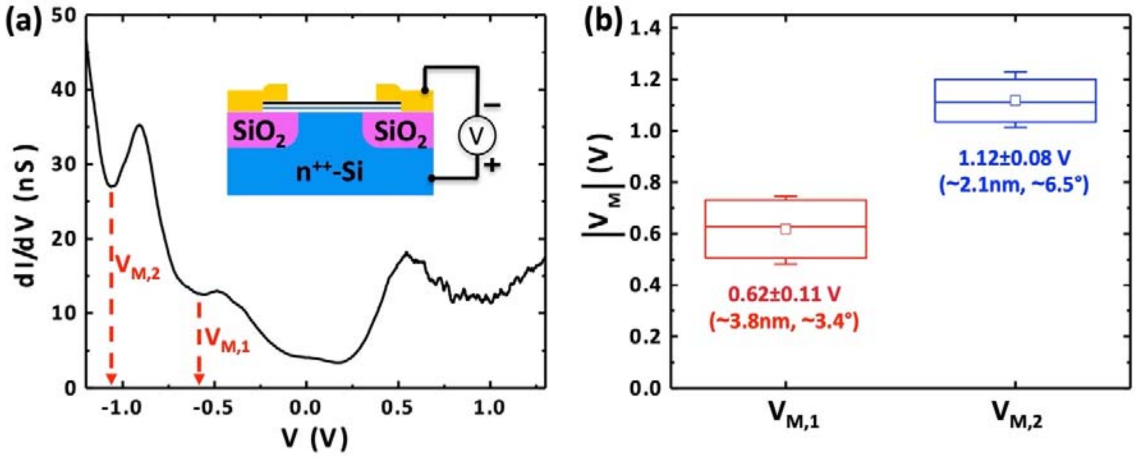

Figure 2.21. Tunneling spectroscopy characterization on the graphene/boron nitride in the vertical tunneling device. (a) First order tunneling spectroscopy of the graphene/ boron nitride in a tunneling device at 1.9 K. The two obvious local minimums are labeled as $V_{M,1}$ and $V_{M,2}$, respectively. The inset shows the cross-section device configuration and the measurement setup. (b) Summarized $V_{M,1}$ and $V_{M,2}$ positions from multiple devices. Their average values (red and blue hollow squares), standard deviation (red and blue boxes), and extreme values (red and blue error bars) are all indicated.

The corresponding Moiré wavelengths and rotation angles are calculated by Equations (2.2) and (2.3) and labelled beneath the average and standard deviation values.

We used a micrometer-scale tunneling device to investigate the macroscopic electronic property in a CVD-grown and transferred Gr/h-BN heterostructure. Our tunnelling spectroscopy result shows two additional DOS local minimums other than the primary Dirac point. Several Gr-h-BN stacks are fabricated and measured, and these two local minimums occur repetitively around $0.62 \pm 0.11\ V$ and $1.12 \pm 0.08\ V$, which can be associated to $0.62 \pm 0.11\ eV$ and $1.12 \pm 0.08\ eV$ away from the primary Dirac point, and can be attributed to the generated Gr/h-BN Moiré patterns. With the relationship between Moiré periodicity and SDP energy given in Equations (2.2) and (2.3), these two values of SDP energies correspond to Moire periodicities of 3.8 nm and 2.1 nm. This discovery can provide us a deeper understanding about a CVD-grown and transferred scalable Gr/h-BN heterostructure and be informative when Gr/h-BN devices become commercial and applicable to our everyday life.

2.4.4 Applications in graphene-based organic solar cell

The polymer-free transfer method not only preserves the superior properties of high-quality graphene sheets, but also enhances the capabilities of its applications to soft electronics. Most of the graphene transfer methods require pressing PMMA or other polymer templates on the targets in order to transfer graphene to other substrates, which would be difficult to place graphene sheets directly on top of devices made of organic and polymeric materials, because the mechanical force would destroy or degrade the underlying devices. As a result, for most soft electronics, graphene is used as the bottom layer in the devices, which limits the range of applications for graphene. Here we apply the polymer-free transfer method to make two different bulk-heterojunction polymer solar cells with graphene as the top contact layers. The device structure is illustrated in Figure 2.23 (a) and the J-V (current density versus voltage) characteristics of the devices under AM1.5G illumination are shown in Figure 2.23 (b). The devices are so-called inverted structures with aluminum doped zinc oxide (AZO) at the bottom as cathodes and molybdenum-oxide (MoO_x)/graphene on the top as anodes. The active layers used in the solar cells are poly-3-hexylthiophene with [6.6]-phenyl-C61-

butyric acid methyl-ester (P3HT:PCBM) and poly{[4,8-bis-(2-ethyl-hexyl-thiophene-5-yl)-benzo[1,2-b:4,5-b']dithiophene-2,6-diyl]-alt-[2-(2'-ethyl-hexanoyl)-thieno[3,4-b]thiophen-4,6-diyl]} with [6,6]-phenyl C_{71} butyric acid methyl-ester (PBDTTT-C-T:PC$_{71}$BM), respectively. The power conversion efficiencies are about 2.2% and 4.3% for P3HT:PCBM and PBDTTT:PC$_{70}$BM based devices, even without the top reflective metals to increase the light absorption in the active layers. With the devices presented above, we show that the polymer-free transfer method not only is a superior process to transfer high quality CVD-grown graphene, but also can integrate graphene into most places of the soft electronic devices, thereby enhancing the capabilities of graphene-based applications.

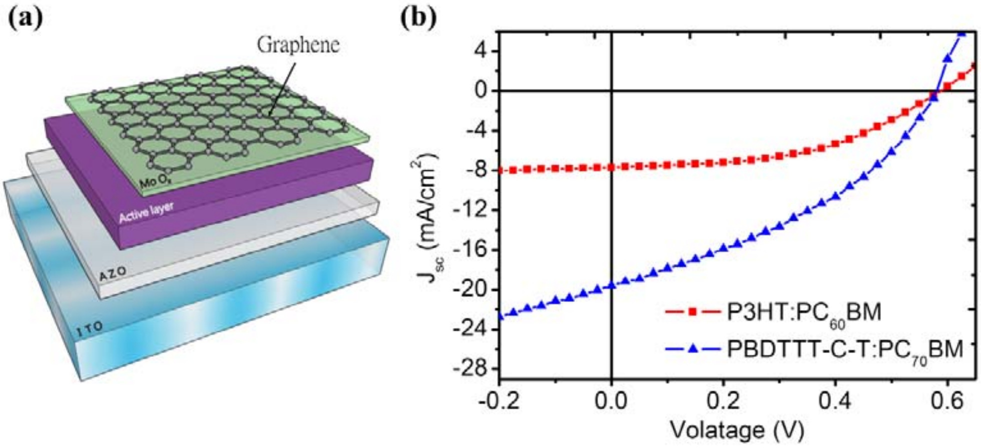

	V_{OC} (V)	J_{SC} (mA/cm^2)	FF (%)	PCE (%)
P3HT:PC$_{60}$BM	0.587	7.7	48.0	2.2
PBDTTT-C-T:PC$_{70}$BM	0.576	19.6	37.7	4.3

Figure 2.22 (a) The device structures of a polymer solar cell with graphene sheets as the top layer. (b) The J-V characteristics of the solar cells. The device parameters are listed in the bottom.

Chapter 3

SYNTHESIS AND PROPERTIES OF 2D INSULATOR: HEXAGONAL BORON NITRIDE

There has been an urgent need for an appropriate insulator within the 2D materials' family to fabricate well behaved 2D-based transistors. Hexagonal boron nitride (h-BN) is a promising 2D insulator candidate by providing a substrate that is free of dangling bonds, low in corrugation level, and thermally and chemically stable. Besides, ultra-thin 2D layered semiconductors offer great potential for extending Moore's law of the transistor density in an integrated circuit. h-BN provides an excellent interface dielectric material to avoid the formation of charge scattering and trap site in the transistor structures made of 2D semiconductors. Also, h-BN itself is an intriguing material with a wide bandgap, allowing for deep ultra-violet (DUV) emission in the UVC (200 nm ~ 280 nm) range which is critical for water sanitation and biological and chemical manufacturing processes. Additionally, h-BN has been shown to host photoactive defects that can emit single photons, paving the way for creation of solid-state single photon emitters at room temperature. Therefore, a reliable and controllable synthesis method to improve fundamental h-BN materials properties is needed. This chapter describes the development of a synthesis method that controls the growth of large-area h-BN films from monolayer to 30 atomic layers, and summarizes the characterizations of the properties of these h-BN films that demonstrate the high-quality of these materials.

3.1 Atomic-scale structural and chemical characterization of hexagonal boron nitride layers synthesized at the wafer-scale with monolayer thickness control

Since the isolation of graphene on an insulating substrate[3,21,97,100–103], a variety of other layered materials have been isolated and characterized, and have opened up an exciting field of research. However, the electronic quality of two-dimensional (2D) active layers in devices is highly sensitive to their immediate environment owing to the large surface-to-volume ratio. Therefore, a crystalline 2D material that can serve the role of an insulating substrate, encapsulating layer, or gate dielectric is highly desirable in device applications. Hexagonal boron nitride (h-BN) has emerged as a promising material for these applications. It has been observed experimentally that encapsulating other 2D materials in h-BN not only enhances the performance of devices, but also extends their durability to long time-scales[104,105]. However most previous studies have used mechanically exfoliated h-BN derived from bulk crystals which does not allow for control over layer thickness and sample lateral size. While numerous reports about chemical vapor deposition (CVD) synthesis of h-BN already exist[106–123] ranging from low pressure CVD (LPCVD) for monolayer growth to ambient pressure CVD (APCVD) for multilayer growth, most of these approaches do not yield precise thickness control from the monolayer scale to thick multilayers over large areas. Many previous experiments have reported on use of solid ammonia-borane as the boron and nitrogen source. The sublimation of a solid source gives poor control of precursor flow rate and partial pressure in the growth chamber over large length scales. Further, monolayer to sub-2nm growth of h-BN is a process catalyzed by the Cu surface and requires low growth pressures. However, the catalytic activity of Cu surface is diminished after growth of 1-2 nm h-BN on its surface and thus growth of thicker h-BN films occurs solely via van der Waals epitaxy, requiring higher growth pressures. No system has yet been developed that can achieve both of these growth condition regimes; therefore, most prior work on CVD grown h-BN has not been able to control both BN thickness and lateral thickness uniformity over technologically relevant areas. Our CVD methods developed in this work feature precursor flow and pressure control systems which combine the merits of both LPCVD and APCVD by allowing precise control over the precursor flow rate and partial pressure of the precursor in the growth zone over a wide range of growth chamber pressure and temperatures. This permits growth of high quality mono to sub 5-layer h-BN films on a Cu foil which require low growth pressures as well as thicker h-BN films on Cu foils, by switching to APCVD mode.

We image the atomic structure of monolayer h-BN/Au sheets and monolayer h-BN/graphene/Au heterostructures using scanning tunneling microscopy (STM). Atomic STM images of CVD-grown monolayer h-BN/Au film monolayers and h-BN/graphene heterostructures indicate high crystalline quality. The crystalline structures and chemical compositions of the resulting h-BN films are also characterized by atomic force microscopy (AFM), Raman spectroscopy, infrared transmission measurements, and x-ray photoelectron spectroscopy (XPS). The electrical properties of the thin and thick h-BN films were systematically measured on metal-insulator-metal (MIM) tunneling devices to understand the dielectric properties of these films. Our results demonstrate a new standard and state-of-the-art for large area synthesis of h-BN films, potentially enabling applications in nanoelectronic and nanophotonic devices.

3.2 CVD synthesis of mono- and multilayer h-BN with atomically thickness control

The h-BN films were grown using a home-built hybrid CVD setup. Figure 3.1 (a) shows the schematic of the growth setup. The setup comprises of a 52 mm inner diameter (I.D.) horizontal split tube furnace (MTI Corporation). The solid precursor ammonia-borane (NH_3-BH_3) powder, (97% purity, Sigma-Aldrich) is contained in a home-made quartz container, attached to the main growth chamber (22 mm I.D. quartz tube) via a leak valve and heated separately from the quartz tube via use of a resistive heating belt. Cu foils (25 μm, 99.999% pure, Alfa Aesar, item no. 10950) are used as the catalytic growth substrates. Copper foil was soaked and sonicated in acetone and isopropyl alcohol (IPA) for 30 min consecutively to remove organic impurities. Then, it was washed with deionized water and dried with nitrogen gas. The pressure in the growth chamber can be independently controlled via an angle valve at the vacuum pump while the pressure in the precursor bubbler can be controlled via the leak valve and carrier gas flow rates. The monolayer and multilayer h-BN was synthesized using a pressure controllable CVD system. The copper foil was inserted into the center of a 22 mm I.D. quartz tube, heated by a horizontal split-tube furnace. The Ammonia borane (NH_3-BH_3) (97% purity, from Sigma-Aldrich), stable in an atmospheric environment, was used as the precursor. It was loaded in a homemade quartz container which is isolated from the main

CVD system with a leak valve to control the flow rate. The quartz tube inlet and outlet were blocked by filters to prevent the BN nanoparticles from diffusing into the gas line. First, the quartz tube was pumped down to 5×10^{-3} torr, and then ultrahigh purity grade hydrogen gas was introduced during the temperature ramp-up of the furnace (pressure ~ 100 mtorr, flow rate ~ 50 sccm). The copper foil was annealed at 950°C in hydrogen for 60 min to obtain a smooth surface. After annealing, the ultrahigh purity argon gas (300 sccm) was introduced into the system and waited for 30 min to stable the tube environment. The precursor was heated to 130°C and decomposed to hydrogen gas, monomeric aminoborane, and borazine gas. After the precursor temperature reached 130°C, the manual valve between the quartz tube outlet and the pump was slowly closed and stopped until the pressure reached 20 torr. When the desired pressure was achieved, the leak valve to the precursor was opened. The typical growth time is 3 min for monolayer h-BN layer and 20 min for the 20 nm thickness h-BN layer. To atomically control the thickness of the h-BN layer, it is very important to have a leak valve to control the flow rate of the precursor. Also, we can change the growth rate of the h-BN by changing the pressure of the growth environment. After growth, the tube furnace was cooled down with the cooling rate ~16°C/min.

To grow ultrathin (< 1.5 nm) h-BN films, we use a growth pressure of ~ 2 Torr. Figure 3.1(b) and (c) show an optical photograph and atomic force microscopy (AFM) analysis of a wafer-scale h-BN monolayer which has transferred onto a 285 nm SiO_2/Si substrate. Raman spectra acquired over six different spots on the sample (denoted by x), as seen in the adjacent plot suggests that the sample thickness and quality is uniform over the entire cm^2 scale. Likewise, the growth mode can be switched from a slow growth rate of ~ 0.3 nm/min in catalytically controlled CVD at low pressures to a high growth rate of 1 nm/min at near atmospheric pressures (~500 Torr). Figure 1c illustrates the large area uniformity of ~ 15 monolayer h-BN as inferred from the optical micrograph and corresponding Raman spectra. To validate the precise control of layer thickness and growth uniformity, a series of growth experiments were performed for varying times at both low and ambient pressures to produce h-BN films of varying layer number/thicknesses. These h-BN films were then characterized with several spectroscopic techniques to characterize their structure and chemical composition. Atomic scale structure and areal homogeneity of h-BN films were revealed by scanning tunneling microscopy (STM) for CVD-grown monolayer h-BN. Despite numerous reports on CVD synthesis of h-BN, little is known about the atomic scale electronic structure for layers grown on polycrystalline Cu foils, due to the roughness of the Cu foil substrate which renders STM difficult. Also, the film thickness inhomogeneity seen in most prior reports[124–128] would prevent image formation by direct electron tunneling through h-BN.

To estimate the domain size in our CVD grown h-BN films, we perform scanning electron microscopy of sub-monolayer growth directly on the copper substrate. A sub-monolayer growth would provide strong contrast in the SEM between the insulating h-BN and conductive copper foil. Figure 3.2 below shows some SEM micrographs of sub monolayer growths and analysis of domain sizes. Figure 3.2 (a) shows a large scale SEM image with different h-BN domain sizes. The sharp geometric and triangular edge features suggest the highly crystalline nature of the growth as verified by STM, TEM, and Raman in the manuscript. Figures 3.2 (b) and (c) show the higher magnification images of triangular h-BN domains with edge length of ~ 500 nm and ~ 1 μm, respectively. The statistical distribution of domain size is plotted in Figure 3.2 (d) which shows that the average domain size of h-BN is ~ 750 nm.

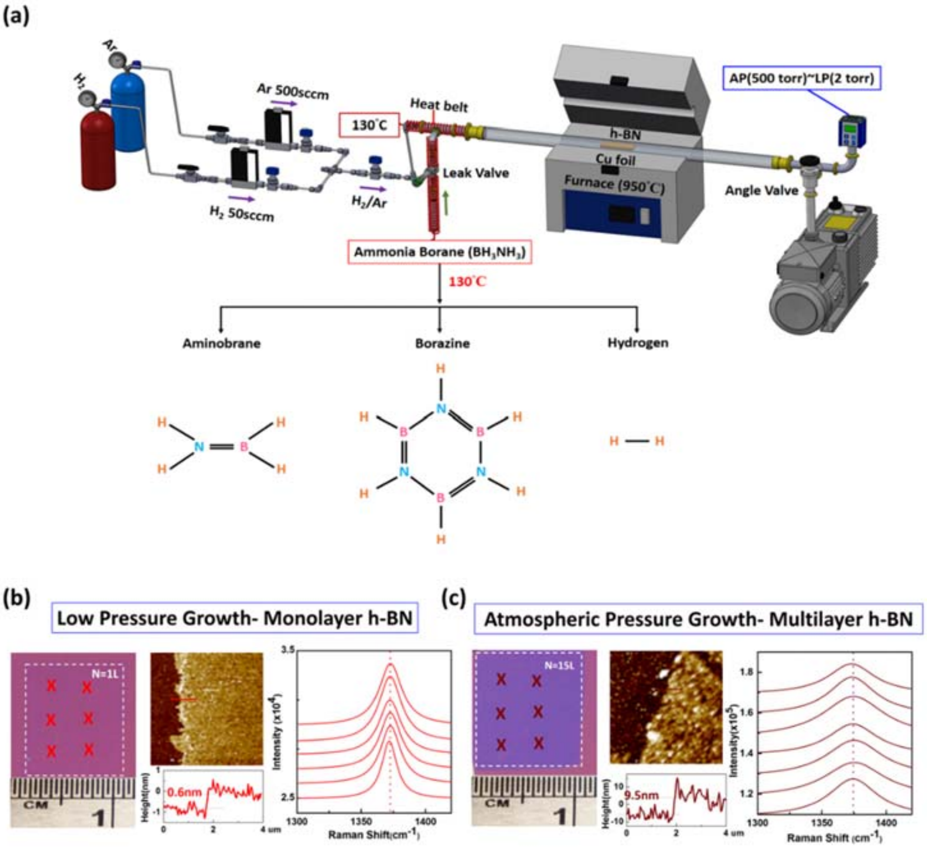

Figure 3.1. (a) Schematic diagram of hybrid atmospheric pressure and low pressure CVD system used for h-BN grow. (b) Photograph of a large and uniform monolayer h-BN film on a 285 nm thick SiO_2/Si substrate, and the corresponding AFM image and Raman spectra. (c) Photograph of a large and uniform multilayer h-BN film on a 285 nm thick SiO_2/Si substrate, and the corresponding AFM image and Raman spectra.

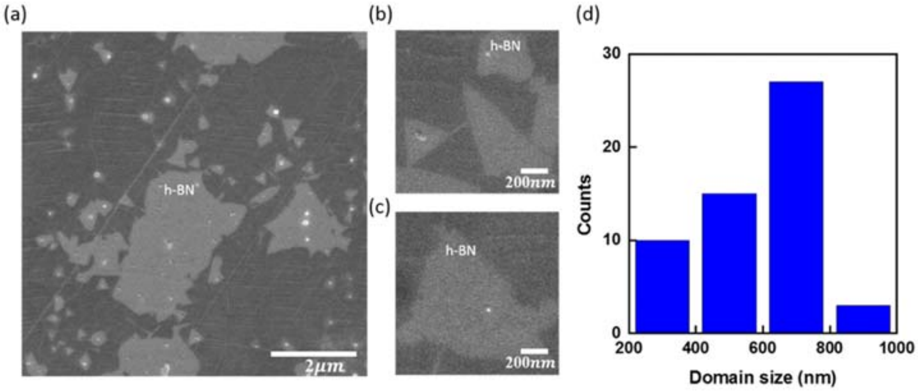

Figure 3.2. (a)-(c) SEM images showing triangular ad-layer with different domain size. (d) Histograms for the h-BN domain size.

As shown in Figure 3.3 below, we can systematically vary the thickness of grown h-BN films from monolayer to 30 layers. We show the optical photograph and atomic force microscopy (AFM) analysis of these h-BN samples that have been transferred onto 285 nm SiO_2/Si substrates.

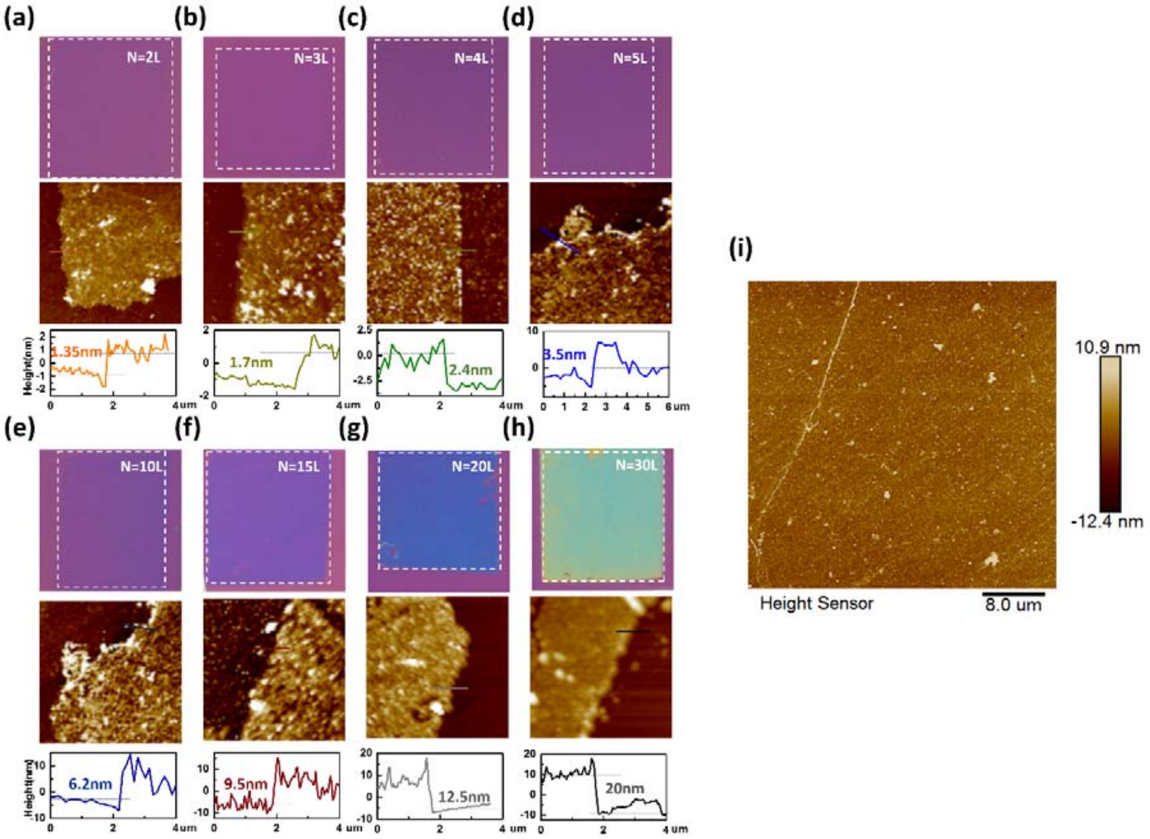

Figure 3.3. (a) - (d) Photograph of 2-layer h-BN to 5-layer thinner h-BN on SiO_2/Si substrate within the white dashed line and corresponding AFM images of bi-layer h-BN to 5-layer h-BN on SiO_2/Si substrate and the height profile. (e) - (h) Photograph of thicker multilayer h-BN (10 layers ~ 30 layers) on SiO_2/Si and the corresponding substrate AFM images of multilayer h-BN (10 layers ~ 30 layers) on SiO_2/Si substrate and the height profile. (i) A representative atomic force microscopy (AFM) image below shows a large scale $40\ \mu m \times 40\ \mu m$ topography image of a 5-layer h-BN sample to show the thickness uniformity of the film. This h-BN film was grown on Cu and transferred onto 285 nm SiO_2/Si substrate. The root mean square roughness extracted from this AFM micrograph is 0.69 nm.

3.3 Growth mechanism of h-BN

In a previous report, Bhaviripudi[129] *et al.* elucidated the kinetic model for CVD synthesis of graphene. Similar to this report, Figure 3.4 below depicts a steady state gas flow of a mixture of borazine, hydrogen, and argon gases on the surface of a Cu catalyst at a synthesis temperature (typically 950 °C). The main thermos-kinetics of the CVD process and reaction of borazine molecules include several steps:

The borazine species first (1) get transported to the reaction region, followed by (2) adsorption on Cu surfaces, then (3) dehydrogenation of $B_3H_6N_3$ to form active boron and nitrogen species. Therefore, (4) surface diffusion of B and N species occurs on the Cu surface leading to (5) growth of h-BN domains, and ultimately, (6) inactive species (such as hydrogen) diffuse away from the surface through the boundary layer. The above process can be classified into two regimes: the mass transport region ($h_g \ll K_s$), primarily involving diffusion through the boundary layer, and the surface reaction region (catalysis; $h_g \gg K_s$). Here h_g denotes the mass transfer coefficient, and K_s represents the surface growth rate. In these growth regimes, the total pressure P_{TOT} determines whether boron nitride growth proceeded by catalysis or otherwise. For h-BN growths on Cu in LPCVD mode, we note that h_g increases as a result of lowering the total pressure, which promotes surface catalysis ($h_g \gg K_s$), tending to grow from monolayer to thin multi-layer h-BN. In APCVD growth conditions, we note an increase in the surface growth rate K_s and decrease in the mass transfer coefficient h_g, which makes the mass transport flux dominant over surface reactions ($h_g \ll K_s$). This means the h-BN growth will continue to happen until elimination of all the high temperature pyrolyzed species of ammonia-borane, which ultimately leads to growth of thick multilayer h-BN without the need of surface catalysis of Cu. Therefore, we can systematically vary the thickness of grown h-BN films by using a leak valve to control the flow rate of the borazine (or partial pressure of the borazine). In Figure 3.4 below, we show the quantitative dependence of h-BN film thickness on the partial pressure of the precursor (borazine). The growth temperature was fixed at 950 ºC, while the precursor temperature was fixed at 130 ºC.

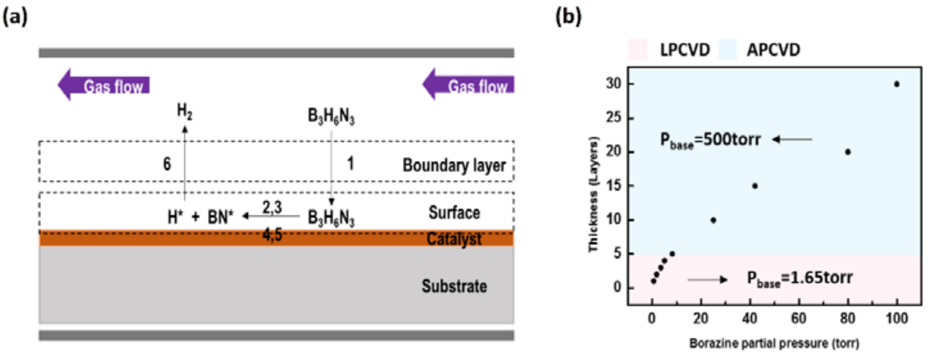

Figure 3.4. (a) Processes involved during h-BN synthesis on Cu in a CVD process. (b) A plot of film thickness with respect to the Borazine partial pressure.

3.4 Atomic structures of monolayer h-BN and multilayer h-BN

Notably, h-BN is difficult to characterize using STM due to its insulating character. To enable adequate sample conductance, many research groups have used a graphene/ h-BN heterostructure which exploits the conductance of graphene to visualize the atomic structure of the h-BN layer underneath the graphene. In contrast, we are able to use STM to directly image our CVD-grown monolayer h-BN films on Au (111)/mica substrates transferred using the polymer free transfer method. Figure 3.5 (a) is a schematic of the STM measurement configuration for monolayer h-BN sheets on Au (111) substrates. Figure 3.5 (b) shows a representative STM image of the monolayer h-BN sheet on Au (111) without any post transfer annealing. The atomically-resolved h-BN honeycomb structure is clearly visible, superimposed on the Au (111) herringbone reconstruction pattern. The appearance of the distorted hexagonal lattice in the STM image indicates strong surface tension originating from the interaction between boron nitride atoms and the Au (111) substrate herringbone reconstruction. Figure 3.5 (c) shows schematic of STM measurements of the monolayer h-BN sheet on monolayer graphene/Au (111) substrate and Figure 3.5 (d) and (e) show topographic STM images acquired from two different areas of the single-layer h-BN on graphene. Both the atomic lattices of h-BN and longer range moiré patterns can be clearly revealed. The moiré pattern is formed by interference between the h-BN layer and underlying graphene/Au (111) substrate, and can be attributed to their lattice mismatch (a = 0.252 nm, b = 0.246 nm) and rotational misalignment. The h-BN and graphene sheets interact through van der Waals forces, and display the same topographic conformal mapping to the underlying Au (111). However, the relative rotation angle between the graphene and h-BN sheets can be modified by tiny wrinkles and bubbles inevitably introduced during the transfer process of h-BN onto graphene, as seen in Figure 3.5 (d) (left) and original grain boundary of h-BN and graphene. Changing the rotation angles between the h-BN and graphene lattices, leads to Moiré patterns with different periodicities and orientations as observed in Figure 3.5 (d) and (e) (center). The periodicity of Moiré pattern presented in Figure 3.5 (d) is 3.4 nm and 2.0 nm in Figure 3.5 (e). The twist angle between the h-BN and graphene lattices can be ascertained from the structure of the Moiré pattern and is given by

$$\theta = \cos^{-1}[1 - \frac{a^2b^2 - \lambda^2(b-a)^2}{2ab\lambda^2}]$$

where a is the h-BN lattice constant, b is the graphene lattice constant, and λ is the periodicity of the Moiré pattern. Thus, the twist angle θ of Figure 3.5 (d) and (e) is found to be (4 ± 0.1) ° and (7 ± 0.1) °, respectly. Alternatively, the twist angle θ can also be extracted by performing a fast Fourier transform (FFT) analysis of the STM images, as shown in the inset of Figure 3.5 (d) and (e). The outside set of spots corresponds to the reciprocal lattice of h-BN, while the inner set of spots is assigned to the Moiré pattern stemming from the rotation between the monolayer h-BN and graphene substrate. The atomic resolution STM images presented here can be achieved in image locations over a wide area of the wafer-scale sample, indicating excellent h-BN sheet surface quality for layers transferred with the polymer-free[38] transfer method and supporting the existence of high crystalline quality in CVD-grown h-BN down to the monolayer level. The STM results provide information about the atomic scale structure and crystallinity of monolayer h-BN. However, they do not provide information about macroscopic-scale h-BN film thickness homogeneity, composition, or structure.

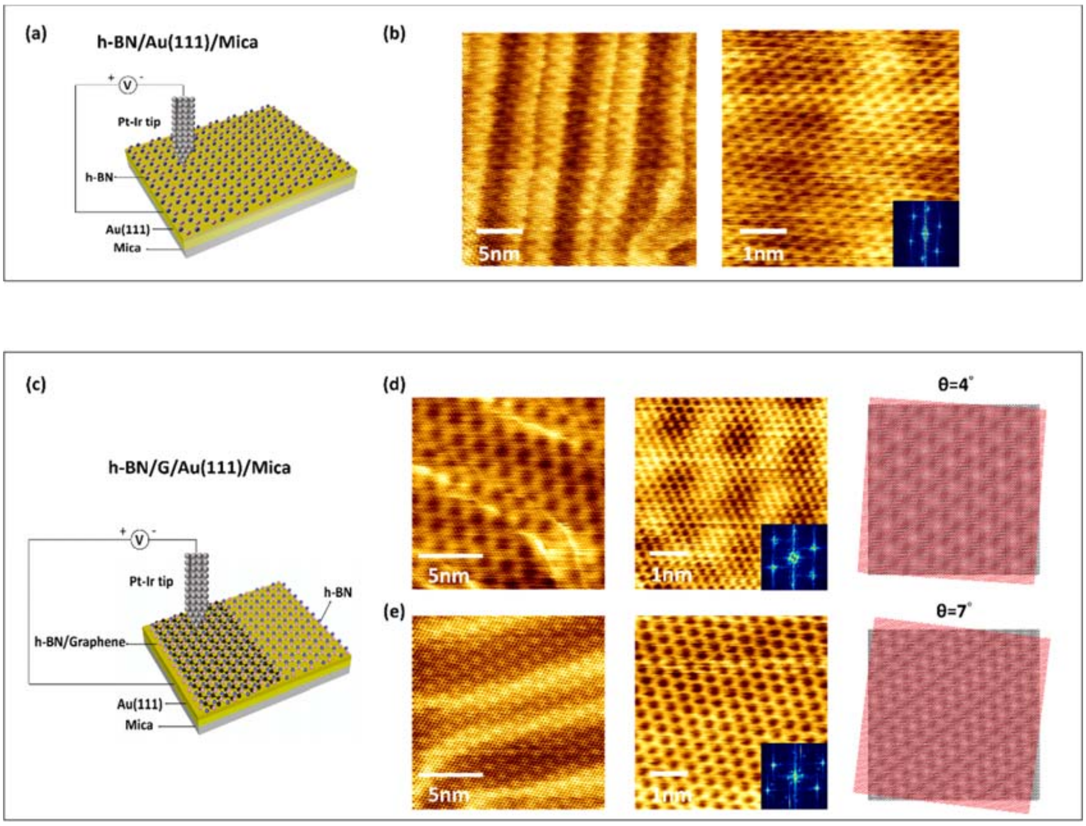

Figure 3.5. (a) STM measurement schematics on monolayer h-BN film. (b) The representative STM image of the h-BN after transfer to the Au (111) substrate, with V_{sample} = 0.5 V and I_{tunnel} = 0.5 nA. The image size is 25 nm × 25 nm (Left) and 5 nm × 5 nm (Right). (c) STM measurement schematics on monolayer h-BN/graphene heterostructure. (d) Topography of a Moiré superlattice with periodicity of 3.7 nm and a 4 ° twist between h-BN and graphene. The image was acquired under V_{sample} = 0.5 V and I_{tunnel} = 0.5 nA and image size is 15 nm × 15 nm (Left) and 5 nm × 5 nm (Right). (e) Topography of a Moiré superlattice with periodicity of 2.0 nm and a 7 ° twist between h-BN and graphene. The image was acquired under V_{sample} = 0.5 V and I_{tunnel} = 0.5 nA and image size is 15 nm × 15 nm (Left) and 5 nm × 5 nm (Right). The insets of (d) and (e) are Fourier transform patterns of corresponding STM images.

Furthermore, to provide further evidence of the thickness of our growth h-BN film, we perform high resolution transmission electron microscopy (Figure 3.6) of the same film samples that were characterized using AFM. We took one 5 layers h-BN sample which is defined by our AFM measurement (Figure 3.3) and transferred on TEM grids. Here, we show a cross-section TEM with 5 fringes which is consistent with our thickness of ~ 3.5 nm determined by AFM measurements.

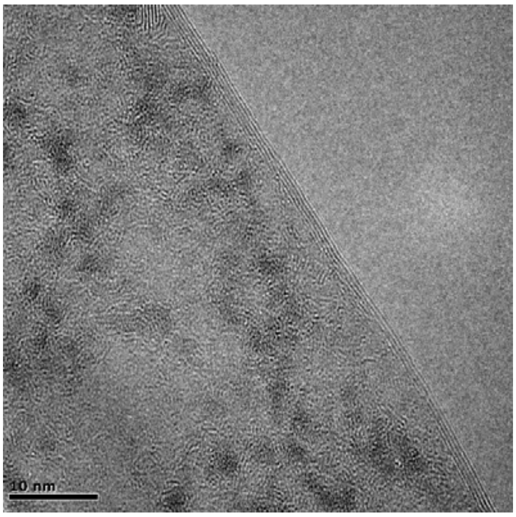

Figure 3.6. Cross–section TEM image of 5-layer h-BN.

3.5 Raman spectroscopic analysis of h-BN

Raman spectra of an h-BN layer typically have two active E_{2g} modes, one at 1366 cm^{-1}, which is strong and corresponds to vibrations of B and N moving against each other in the plane, and the other at 51.8 cm^{-1}, which is attributed to sliding between whole planes. However, the lower frequency mode is more difficult to observe because of its proximity to the Rayleigh diffusion, as well as the presence of a fluorescence background. The width, intensity, and position of these Raman features are sensitive to h-BN thickness, and these dependencies were determined by combining the Raman measurement with STM results and AFM results. We use monolayer h-BN as a thickness calibration for every run and verify the integrated intensity of this calibration point with the value marked with an arrow in Figure 3.7 (b) (Top). The integrated intensity of the h-BN layers determined using this protocol gives a reasonable estimate of the layer thickness and matches very well with the estimates given by the AFM line profiles (Figure 3.3). Figure 3.7 (a) shows Raman spectra of monolayer h-BN to 15 layers of h-BN films, showing the Raman intensity increases with the number of layers. The integrated intensity is plotted as a function of the number of layers in Figure 3.7 (b) (Top). Figure

3.7 (b) (Bottom) suggests that the peak position has a redshift as layers decrease and the FWHM become sharper as the layer number decreases.

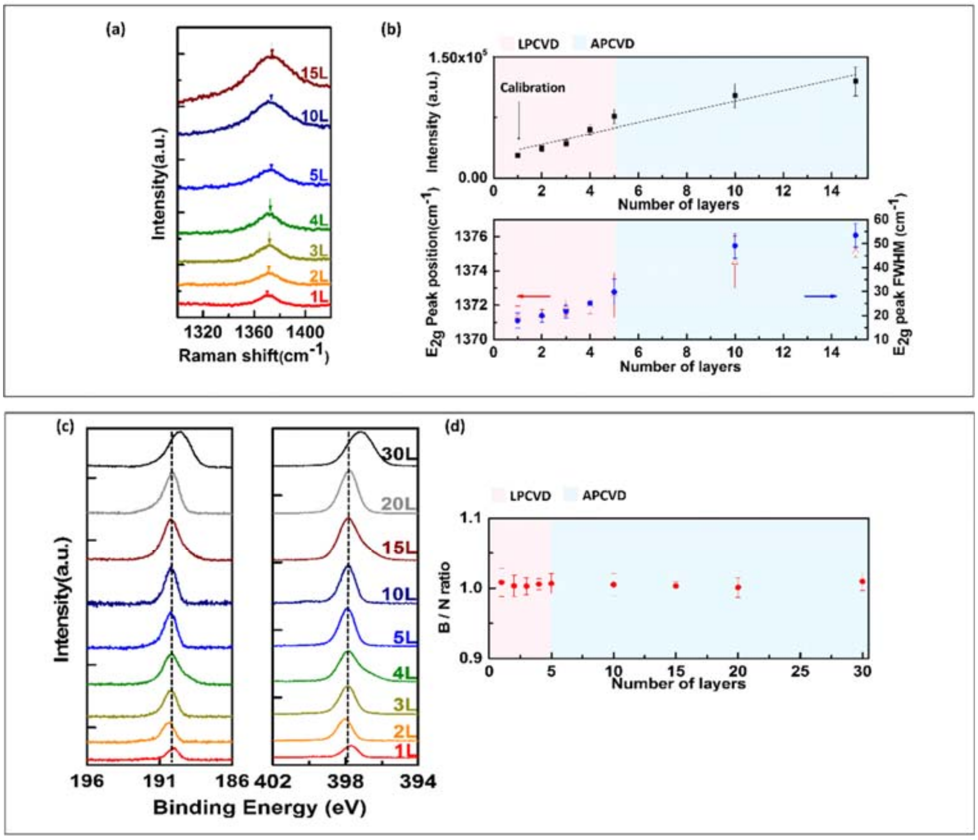

Figure 3.7. (a) Raman spectra for h-BN layers with 1-15 atomic layers. (b) (Top) Integrated intensity shows a steady increase with increase in the layer number of h-BN. (b) (Bottom left) The position of E_{2g} peak vs. number of monolayers of h-BN, showing the blue shift with increased number of h-BN layers. (Bottom right) The full width at half maximum vs. number of h-BN layers, showing a steady increase of the FWHM with h-BN thickness. (c) X-ray photoelectron spectra (XPS) from different thicknesses of h-BN layers on Cu foil. (d) High resolution B1s and N1s peaks corresponding to the thickness from 1 ~ 30 layers of h-BN films on Cu foil. (Right) Quantitative

analysis of the B1s and N1s spectra indicates that the B/N atom ratio in our films was 1 ± 0.6% across the range of thicknesses.

While Raman spectroscopy suggests the presence of B-N bonds and a linear dependence of thickness on growth time, they do not provide any information on the stoichiometry of the grown films. To probe the chemical composition, we used X-ray photoelectron spectroscopy (XPS) to determine the B/N ratio. Figure 3.7 (c) shows the XPS spectra of as-grown h-BN films on Cu foils with a film thickness varying from monolayer to 30 layers. It has been previously reported that bulk boron nitride with hexagonal phase exhibits a B 1s core level at 190.1 eV. Figure 3.7 (c) (left) shows XPS B1s core level spectra with a peak center at 190.2 eV, which is very close to the h-BN bulk phase value. Figure 3.7 (c) (right) shows that the N 1s peak is located at 397.7 eV, similarly to the reported position of the N1s spectrum (398.1 eV) for h-BN. Both the B 1s and N 1s spectra indicate that the configuration for B and N atoms is the B-N bond, implying that the hexagonal phase is the phase of our BN films. Further, it can also be seen that the intensities of the B1s and N1s increases with the increasing layer thickness of our films. In addition, we also observe that the intensity of the Cu2p peak weakens with the increasing thickness of the h-BN films (Figure 3.8), further corroborating our precise thickness-controlled growth. Finally, quantitative analysis of the B1s and N1s spectra indicates that the B/N atom ratio in our films was 1 ± 0.6% across the range of thicknesses. These results evidently confirm growth of a high quality h-BN layer and continuous film on Cu foil using ammonia borane by our optimized CVD process.

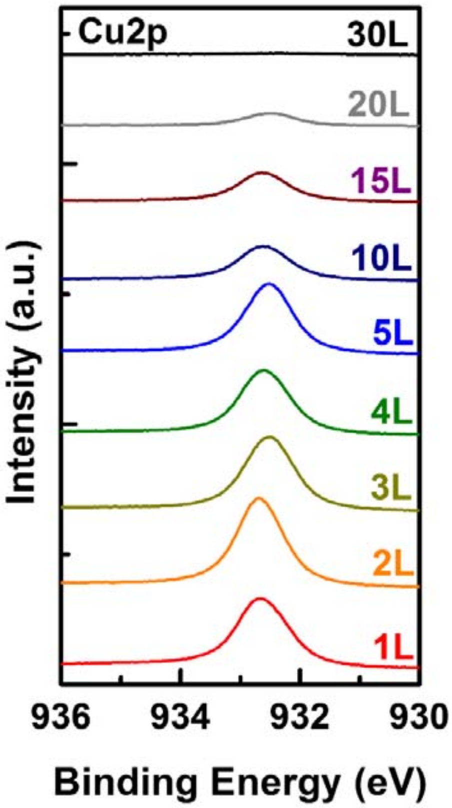

Figure 3.8. X-ray photoelectron spectra-Cu2p spectrum of 1 ~ 30 layers h-BN films on Cu foil used to identify the element present.

3.6 Electrical measurement on metal/h-BN/metal (MIM) capacitors

The large area uniformity and high crystalline quality of our CVD-grown h-BN films makes them ideal for applications as ultrathin dielectrics in optoelectronic devices. Therefore, to evaluate the dielectric strength and leakage through our h-BN films, we investigate the electronic properties of tunnel junctions in which h-BN acts as a barrier layer between two gold electrodes. The dielectric properties of the CVD h-BN films with different thicknesses were measured by fabricating metal/h-BN/metal (MIM) capacitors and measuring current–voltage (I-V) characteristics. Figure 3.9. (a) shows a schematic diagram of an Au/h-BN/Au capacitor. We use template stripped gold films as our bottom electrode with root mean square (RMS) roughness less than 0.5 nm. The h-BN films of various thicknesses were transferred onto the template stripped gold. Then, we used standard electron beam deposition techniques to deposit 100 nm gold through a shadow mask to define the top electrodes. The contact area was 10 µm × 10 µm. Figure 3.9. (b) shows I-V measurements of h-BN layers with various thicknesses from 1 to 15 layers. Mono-, bi-, and 4-layer samples show measurable low-bias conductance, which we ascribe to direct tunneling. Thicker samples are insulating at low bias and show sharp increases at a breakdown voltage that increases with thickness. The inset in the Figure 4b shows the conductance as a function of sample thickness, which decays exponentially, as expected for direct tunneling. The current densities at the two metal electrodes and through the h-BN layers of different thicknesses were investigated as a function of voltage, as plotted in Figure 3.9. (c). As shown in Figure 3.9. (c), the measured currents of the thin h-BN films agreed well with the Poole-Frenkel (PF) emission model, indicating that a trap-assisted PF emission mechanism dominated the transport mechanism for the leakage current in our h-BN films. Figure 3.9. (c) shows the PF plot using the following equation:

$$I(V)_{PF} = AqN_c\mu Vd\exp\left[\frac{-q\left(\Phi_T - \sqrt{\dfrac{qVd}{\pi\varepsilon_0\varepsilon_r}}\right)}{kT}\right]$$

where A, q, N_c, μ, Φ_T, V, d, and h are the effective area, electron charge, density of state in the conduction band, electronic mobility in the oxide, trap energy level in the h-BN, voltage, h-BN thickness, and Planck constant, respectively.

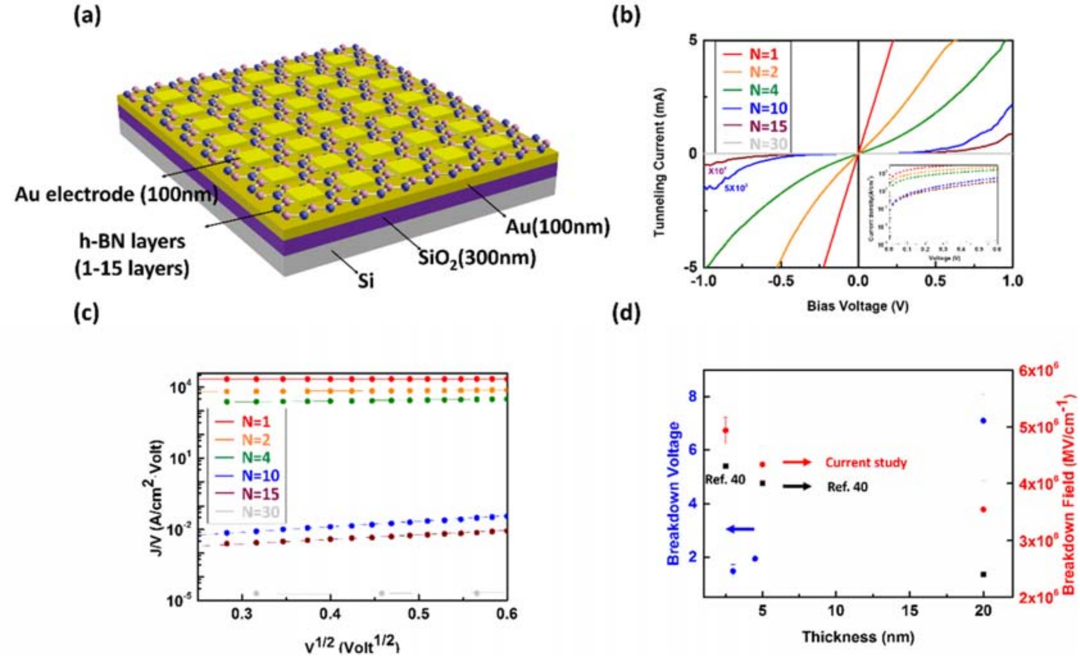

Figure 3.9. (a) A schematic diagram of the Au / h-BN / Au (MIM) capacitors fabricated on a Si substrate. (b) Characteristic I−V curves for Au / h-BN / Au devices with different thicknesses of BN insulating layer: red curve, monolayer of BN; orange, bilayer; green, four layer; navy, 10 layers; and purple, 15 layers. The inset of (a) is typical J-V characteristics of a MIM capacitor, described by the field-assisted tunneling model. The h-BN thickness range was less than 5 nm. The inset shows a PF emission plot (J/V versus $1/V^{1/2}$). (d) The breakdown characteristics as a function of the h-BN film thickness.

Finally, for thicker (> 1 nm) h-BN films, we performed irreversible dielectric breakdown measurements to determine the hard-breakdown voltage (Figure 3.10) and corresponding field strength of the ultrathin h-BN. Figure 3.9 (d) plots the breakdown field strength as a function of the h-BN thickness. In h-BN films with thicknesses less than 5 nm, the breakdown voltage increased linearly with h-BN thickness, indicating very high quality films at the few-layer limit. Breakdown field strength approaching ~ 4.3 MV/cm were observed for 4.5 nm thick BN films.

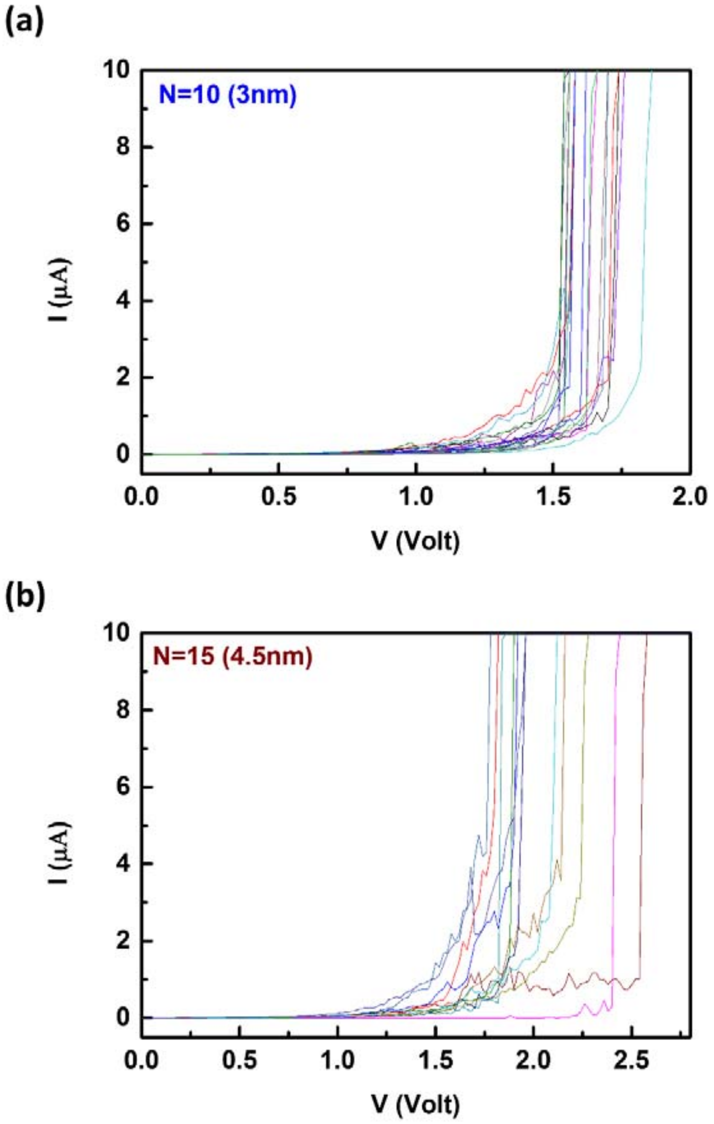

Figure 3.10. (a) The characteristic I−V curves for Au / h-BN / Au devices with 3 nm h-BN layer. (b) The characteristic I−V curves for Au / h-BN / Au devices with 4.5 nm h-BN layer.

3.7 Single photon emitters (SPE) of h-BN layers synthesized by APCVD method[130]

Solid-state single photon emitters (SPEs) are fundamental light sources for scalable quantum technologies including quantum computing, quantum precision measurement, and quantum secure communication. Over the years, SPEs have been established in a variety of solid-state systems such as zero dimensional (0D) GaAs and InGaAs quantum dots (QDs), one dimensional (1D) carbon nanotubes (CNTs) and InP nanowires, as well as three dimensional (3D) wide-bandgap diamonds and GaN. Each emitter type is characterized by the spectral diffusion, *i.e.*, temporal variations in emission energy around a nominal value, which poses a challenge to the use of solid-state quantum emitters as sources of indistinguishable single photons. However, there are many factors associated with SPEs that limit their applications. For instance, most of SPEs in QDs only work at cryogenic temperatures; the brightness and purity for SPEs from color centers in CNTs are low and the quantum efficiency of the color centers in silicon vacancy (Si-V) in diamond is low (3.5%). To date, empirical evidences have suggested that two dimensional (2D) hexagonal boron nitride (h-BN) is the most promising SPEs material with bright, linearly polarized, high quantum efficiency (50 ~ 100%), and optically stable SPEs operational at room temperature (RT) with high photon purity. Furthermore, defects in 2D h-BN also exhibit high sensitivity to the surrounding environment, which lead to tunable properties and allow predetermined positioning of SPEs by strain engineering. Efforts to engineer SPEs in h-BN have been demonstrated on a range of electron irradiation, laser processing, ion implantation, wet etching, annealing, and plasma processing methods on chemical vapor deposition (CVD) growth h-BN. Among the aforementioned methods, the CVD process is the most reliable method to grow large area h-BN films with thickness control that can host a high density of SPEs. However, the zero-phonon lines (ZPLs) of the h-BN quantum emitters have demonstrated a wide range of energies (1.6 eV ~ 2.4 eV), which implies the existence of multiple defect species by using CVD method, and it has been a significant challenge to reduce the ZPL energy distribution. A recent study demonstrates a new capability to deterministically place the ZPL between either 550–600 nm or 600–650 nm by using the gettering mode of the atmospheric pressure chemical vapor deposition (APCVD) method that manipulates the boron diffusion through the copper to determine the defect species formation. The ability to control the defect formation during h-BN growth provides a cost effective way to reduce the ZPL energy distribution and is also an important way to understand defect formation of quantum emitters in h-BN. However, searching the defect formation position remains a challenge to apply the SPEs in h-BN for practical applications.

Here, we control the dehydrogenation rate of BH_2NH_2 on different catalytic surfaces (Cu and Cu-Ni) to target and control the particular structural defects formation during the CVD growth. Previous studies indicated that the borazane on a catalytic surface underwent a two-stage weight loss process. The 2D cross-linking reaction of the B-H and N-H groups is initiated from 125 °C to 200 °C, and then dehydrogenation from unaligned chain branches continues from 600 °C to 1000 °C. The nanoparticles are most likely a complex mixture of the poly-aminoborane in the reaction, and they partially dehydrogenate derivatives. The dehydrogenation of BH_2NH_2 become easier by increasing Ni content in the Ni-Cu alloy, which implies that the introduction of the Ni can enhance the decomposition of the poly-aminobrane and help the reactions of desorption or the formation of the Ni-B and Ni-N phases. The enhanced ability of the Ni-Cu alloy in decomposing polyaminoborane residues improves the cleanliness of the alloy surface during the h-BN growth. Thus, by controlling different chemical reaction pathways, we have demonstrated further control of the ZPL energy distribution.

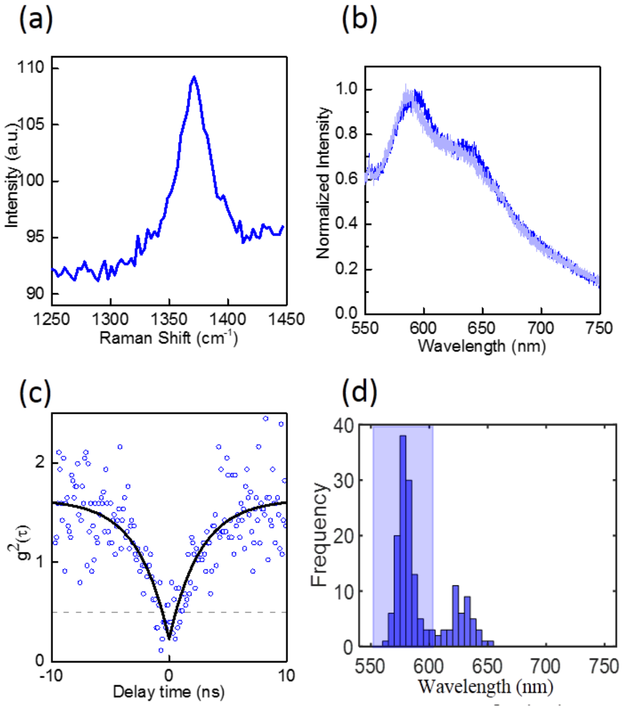

Figure 3.11. Quantum emission from APCVD h-BN from standard substrate copper. (a) Raman spectra of the h-BN. (b) Three representative PL spectra of the h-BN color center. (c) Autocorrelation measurements on the h-BN color center, confirming the quantum nature of the single photon emitters. (d) ZPL histograms showing the spectral distribution of the h-BN SPEs.

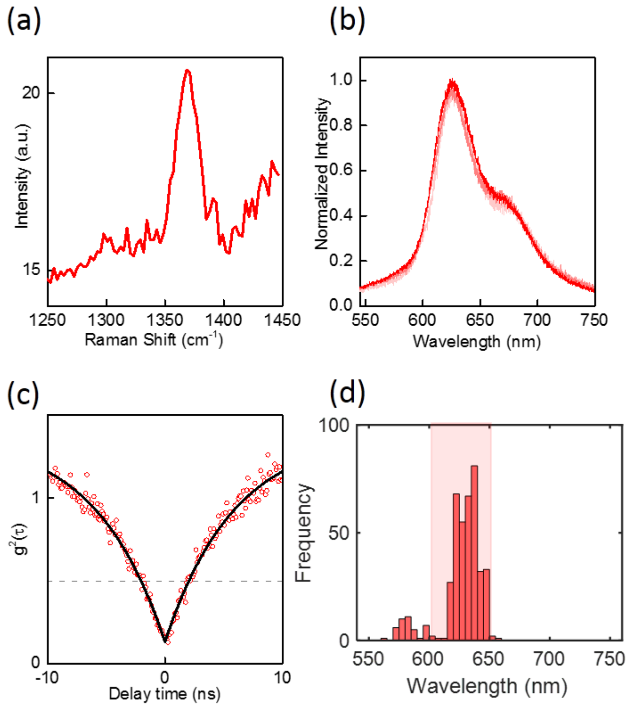

Figure 3.12. Quantum emission from APCVD h-BN from Cu-Ni alloy. (a) Raman spectra of the h-BN. (b) Three representative PL spectra of the h-BN color center. (c) Autocorrelation measurements on the h-BN color center, confirming the quantum nature of the single photon emitters. (d) ZPL histograms showing the spectral distribution of the h-BN SPEs.

From Figure 3.11 and 3.12, we found that the APCVD grown h-BN on two different substrates (Cu and Cu-Ni alloy) hosted different luminescent defect centers, with the representative room-temperature PL spectra from each displayed in Figure 3.11 (b) and 3.12 (b). To confirm the single photon nature of the emission, we recorded second-order autocorrelation measurements using a Hanbury Brown–Twiss interferometer for all three growth types, with a representative measurement from each displayed in Figure 3.11 (c) and Figure 3.12 (c). Both samples showed $g^2(\tau) < 0.5$, confirming the quantum nature of the emission. The lowest values of $g^2(\tau) \leq 0.1$were obtained consistently from the h-BN samples grown on Cu-Ni, while those obtained from samples grown on standard Cu substrates were typically around $g^2(\tau) = 0.21$. More importantly, we have demonstrated that the Cu-Ni substrate allowed for deterministic selection of SPEs with a particular emission energy, providing a template for rational incorporation of h-BN SPEs with desired properties. This result also suggests that SPE defects with ZPL energies in the region of 550 – 600 nm (Figure 3.11 (d)) are of a different structural nature from those in the region of 600 – 650 nm (Figure 3.12 (d)).

3.8 Summary of synthesis and properties of 2D insulator (h-BN)

We have imaged the atomic-scale structure of monolayer h-BN sheets on Au and Moiré patterns on monolayer h-BN/graphene heterostructures using scanning tunneling microscopy (STM). Atomic STM images of monolayer h-BN films and Moiré patterns on monolayer h-BN/graphene heterostructures revealed the high crystalline quality of the CVD grown h-BN up to the atomic level. We have also introduced a hybrid LPCVD and APCVD system that utilizes controlled precursors to grow uniform, layer-by-layer thickness-controlled, wafer-scale h-BN films with thicknesses ranging from monolayer to 10 nm. Spectroscopic characterization suggests that the films are stoichiometric and highly uniform over wafer-scale areas. Electrical measurements for metal-insulator-metal (Au/h-BN/Au) structures indicate that our CVD-grown h-BN films can act as an excellent tunnel barrier with a high hard-breakdown field strength. Successful large area CVD growth of h-BN films defines a new state-of-the-art for application of this material in future large-area, electronic and photonic devices. Furthermore, the ability to preselect the ZPL energy and emitter density makes bottom-up fabrication techniques a leading solution for quantum photonics based on h-BN.

Chapter 4

SYNTHESIS AND PROPERTIES OF 2D SEMICONDUCTOR: TRANSITION-METAL DICHHALCOGENIDES

Investigation and control of new degrees of freedom in quantum materials have attracted much research interest lately because of their potential to surmount the imminent end of "Moore's Law". Compared with the traditional charge degrees of freedom, spin and valley are two additional internal degrees of freedom in solid-state electronics, which may enable spintronic and valleytronic devices with high integration density, fast processing speed, low power dissipation, and non-volatility. Monolayer transition-metal dichalcogenides (TMDCs) in the 2H-phase are semiconductors promising for opto-valleytronic and opto-spintronic applications because of their strong spin-valley coupling. In this chapter, we report detailed studies of opto-valleytronic properties of heterogeneous domains in CVD-grown monolayer WS_2 single crystals. By illuminating WS_2 with off-resonance circularly-polarized light and measuring the resulting spatially resolved circularly-polarized emission (P_{circ}), we find significantly large circular polarization (P_{circ} up to 60% and 45% for α- and β-domains, respectively) already at 300 K, which increases to nearly 90% in the α-domains at 80 K. These results offer the initial groundwork for future devices that build on the coupled spin-valley degrees of freedom as robust information carriers that require reduced power consumption relative to conventional MOSFET-based electronics.

4.1 Nearly 90% circularly-polarized emission in monolayer WS_2 single crystals by chemical vapor deposition (CVD)

There has been a surge of intense research efforts on two-dimensional (2D) van der Waals (vdW) materials because of their interesting properties and great promise for technological applications[131–134]. These 2D materials, such as semi-metallic graphene[69,135], insulating h-BN[15,97,104,136,137], and semiconducting transition metal dichalcogenides (TMDCs)[37,138–141], can be synthesized on a wafer scale by chemical vapor deposition (CVD), which provides a feasible route towards practical applications. The electrical and optical properties of TMDCs can be significantly affected by crystal imperfections such as vacancies, impurities and grain boundaries[142–144]. In particular, vacancies in TMDCs appear to be unpreventable and are naturally formed inside the single crystalline grains during the CVD growth process. Such vacancies can be primary contributors to carrier scattering, doping effects and varying optical properties in these materials.

Among TMDCs in the 2H-phase, monolayer tungsten disulfide (WS_2) consists of a plane of tungsten atoms sandwiched between top and bottom sulfur layers. It has been found that atomic vacancies of tungsten and sulfur are common occurrences in WS_2, and that the electrical and optical properties of a given WS_2 monolayer are dominated by the type of vacancies because of differences in the defect states. For instance, monolayer hexagonal-shape WS_2 (h-WS_2) flakes with triangular heterogeneous defect domains have been synthesized by CVD under hydrogen-rich growth conditions, as reported by several research groups[145–149]. Curiously, the optical emission in the h-WS_2 flakes exhibits alternating areas of bright and dark photoluminescence (PL) emission within each h-WS_2 flake, and the resulting PL image looks similar to the radioactive hazard symbol, as exemplified by the left panel of Figure 4.1(a). According to previous studies, the α-domains with a stronger PL intensity and higher mobility are associated with W-edges and S-vacancies (SVs), and the β-domains with a significantly quenched PL intensity and lower electron mobility exhibit a blue-shifted PL peak position, and are associated with S-edges and W-vacancies (WVs). A schematic illustration of the heterogeneous defect domains for WVs and SVs in a single crystalline h-WS_2 is shown in the right panel of Figure 4.1(a).

Similar to other monolayer TMDCs in the 2H-phase, monolayer WS_2 is an ideal candidate for valleytronic applications due to its inequivalent K and K′ valleys at the edge of the Brillouin zone[150,151]. Because of strong spin-orbit coupling and time-reversal symmetry, the valence bands (VB) in the K (K′) valley have a large energy spin splitting of ~ 420 meV for WS_2 between the top spin-up (spin-down) band and the bottom spin-down (spin-up) band. This difference results in valley-dependent optical selection rules: circularly polarized light with positive helicity ($\sigma+$) couples to the K valley and the negative helicity ($\sigma-$) couples to the K′ valley[152–154]. It is therefore possible to selectively populate and manipulate the different valleys (K or K′) by means of circularly polarized light.

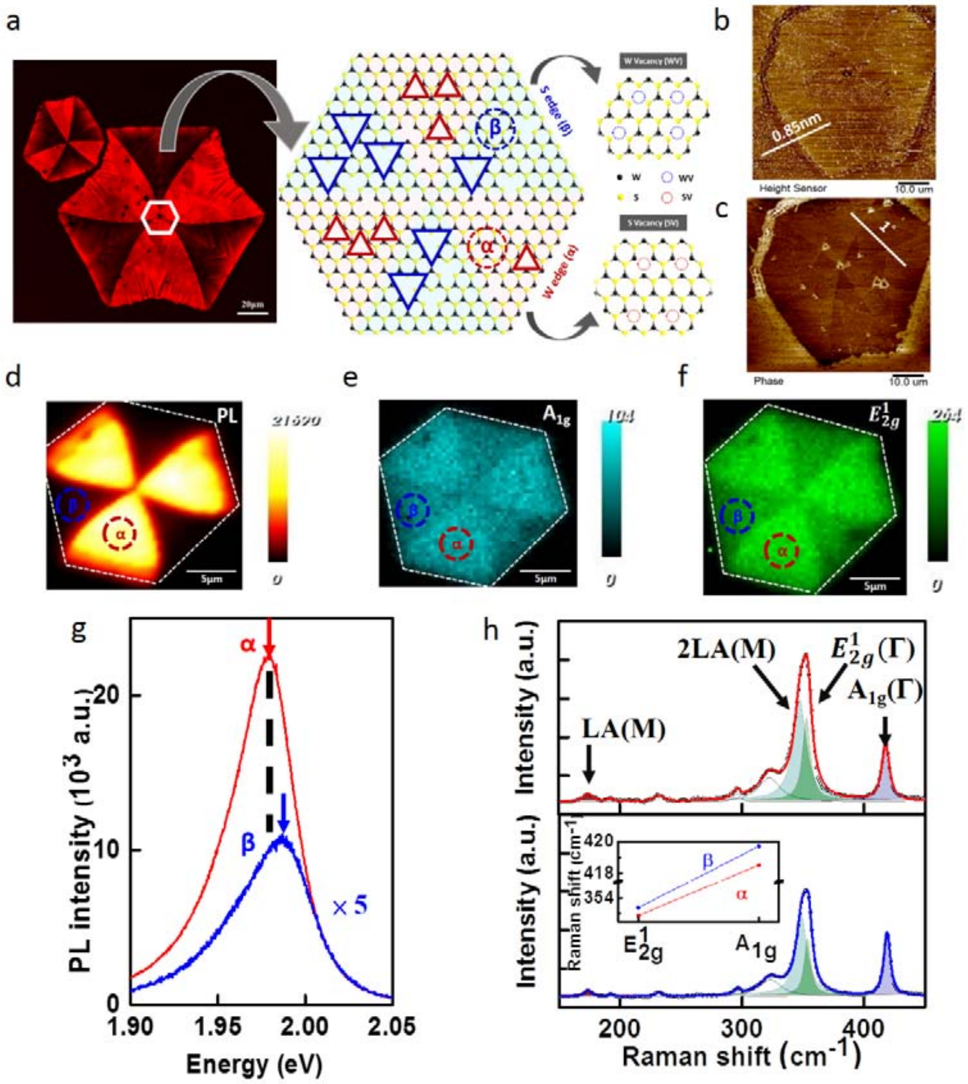

Figure 4.1. Monolayer h-WS_2 optical characterizations: (a) Left panel: Fluorescence images showing a radioactive hazard symbol-like optical emission pattern in the fluorescence intensity from a CVD-grown large monolayer WS_2 single crystal. Right panel: Schematic illustration of heterogeneous defect domains in single crystalline hexagonal WS_2. AFM measurements of (b) the surface topography and (c) the phase for a monolayer h-WS_2 single crystal. The scale bar is 10μm. (d) PL intensity mapping of a monolayer h-WS_2 single crystal at the PL peak energy of 1.96 eV. The brighter PL domain (α) and darker PL domain (β) show threefold symmetry. Similar symmetries are also found in the Raman spectral intensity mapping for (e) the A_{1g} mode and (f) the E_{2g}^{1} mode. Here the scale bars for (d-f) correspond to 5μm. (g) Representative PL point spectra for the α- and β-domains of a monolayer h-WS_2. (h) Representative Raman spectra for the corresponding α- and β-domains as in (e) and (f).

When monolayer WS_2 is illuminated with circularly polarized light of photon energies larger than the energy gap, excitons (*i.e.*, bound electron-hole pairs) are created in a single valley. The radiative decay of excitons within this valley subsequently generates circularly polarized light due to the optical selection rules. Therefore, measuring the circular polarization of photoluminescence (PL) provides a direct means to monitor the valley population. Valley populations will also be affected by intervalley scattering, a process that may be enabled by Coulomb interactions or impurity/phonon scattering[155–158]. At high temperatures or under a sufficiently high photon-excitation energy, large phonon populations will couple to the valleys, thereby reducing the valley specific populations. To date, most reports of circularly polarized PL spectra[159–163] have only been observed in systems measured at relatively low temperatures (< 30 K) or near the resonant excitation condition.

Here we report successful CVD growth (Figure 4.2) of monolayer h-WS_2 that exhibits significant circular polarization already at room temperature and nearly 90% circular polarization (CP) in the α-domains at 80 K without the resonant excitation condition. Detailed characterizations by Raman spectroscopy, PL, X-ray photoelectron spectroscopy (XPS), and conducting atomic force microscopy (CAFM) revealed that these h-WS_2 samples were of high quality, large domains, and low defect densities. Additionally, systematic studies of monolayer h-WS_2 by spatially resolved PL maps and point spectra of polarized PL emission were made on the α- and β-domains of h-WS$_2$ at both room temperature and low temperature (80K). We found that at room temperature, the PL spectra of neutral excitons exhibited a CP of ~ 50% and ~ 40% in the α- and β-domains, respectively. Moreover, the degree of circularly polarized emission in α-domains approached ~ 90% at 80K, suggesting nearly perfect valley polarization. Spatially-resolved CAFM studies revealed that the areal defect density was on the order of 10^{10} cm^{-2} in the α-domains and on the order of 10^{11} cm^{-2} in the β-domains. Following a similar analysis in Refs.164[164]and 165[165], we related the areal defect density in each domain to the corresponding PL intensity and obtained an estimate for the non-radiative recombination lifetime. Additionally, spatially resolved studies using Kelvin-probe force microscopy (KPFM) found that the work function in the β-domains was consistently larger than that in the α-domains by 0.15 eV, suggesting type-2 semiconducting band alignments along the domain boundaries that are favorable for stabilizing interfacial excitons[166]. Atomically resolved imaging and spectroscopic studies by scanning tunneling microscopy (STM) further revealed that the non-radiative defects were primarily associated with the WVs rather than SVs, consistent with the CAFM findings in regions of higher defect densities. Our results thus provide direct evidences for WVs being the primary non-radiative recombination sites in h-WS$_2$ that are responsible for the suppression of PL intensity and circular polarization.

4.2 CVD synthesis of monolayer h-WS2 with special emission pattern

We used WO$_3$ and S as precursors in an atmospheric pressure CVD system to grow monolayer h-WS$_2$ on Si/SiO$_2$ substrates. A schematic drawing of the home-built CVD system is shown in Figure 4.2. Our setup includes the following parts: a quartz tube with a diameter of 1 inch and a length of 100 cm, a one-inch inner diameter (I.D.) horizontal split tube furnace (Lindberg Blue M), and two mass flow controllers calibrated for Ar and H$_2$, with stainless steel flanges at both ends connected to a chiller water circulation system operating at 10 °C.

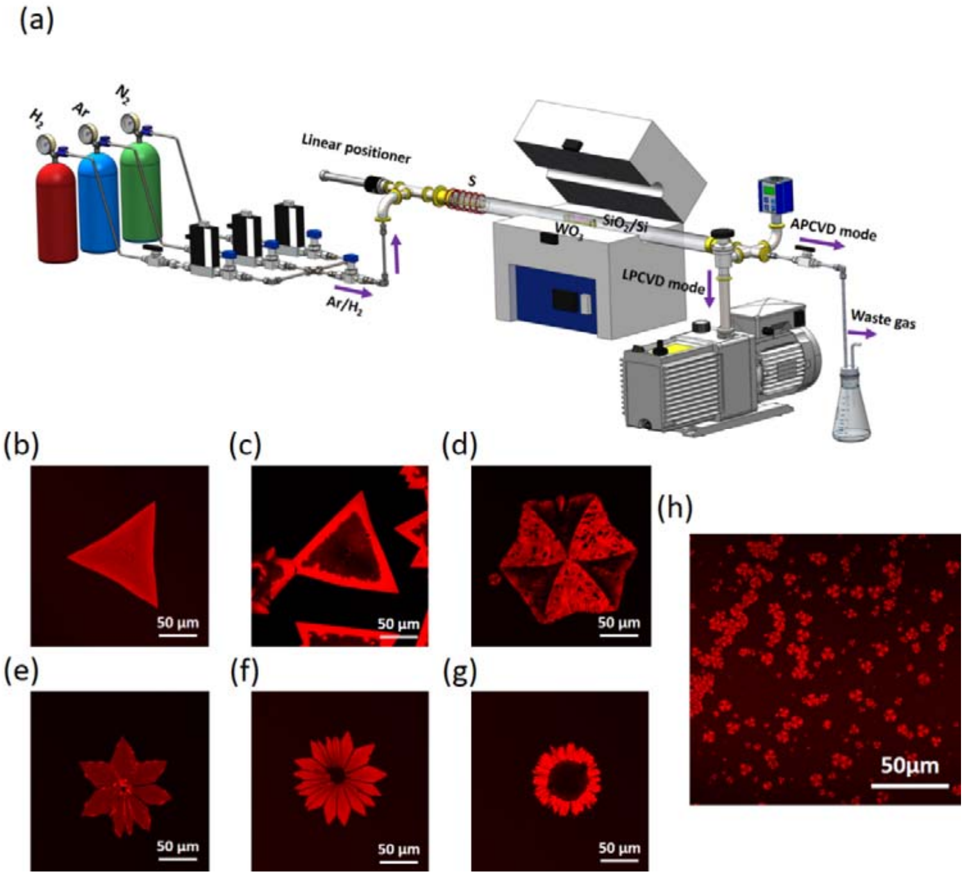

Figure 4.2. Sample preparation and growth condition: (a) Schematic diagram of hybrid atmospheric pressure and low pressure CVD system used for h-WS_2 grow. Fluorescence image of monolayer WS_2. (b) Single domain triangle shape under the Ar/H_2 (80/5 sccm) growth condition. (c) Two domains triangle shape under the Ar/H_2 (80/20 sccm) growth condition. (d) Hexagonal shape under the Ar/H_2 (80/40 sccm) growth condition. (e) Star shape under the Ar/H_2 (80/60 sccm) growth condition. (f) Flower shape under the Ar/H_2 (80/80 sccm) growth condition. (g) Sunflower shape under the Ar/H_2 (80/100 sccm) growth condition.

In the first step of the procedure, 95 mg WO_3 precursor mixed with 5mg KI was placed in a quartz boat containing the SiO_2/Si substrates set face-down directly above the W source precursor, and the quartz boat was then positioned at the center of the furnace. A second boat containing 100 mg S (Alfa Aesar, 99.999+ %) was placed upstream at 16 cm away from the W source. Next, the system was pumped down to 3×10^{-2} torr to eliminate air and moisture. After the system reached the base pressure, the Ar/H_2 (80/40 sccm) carrier gas was introduced until atmospheric pressure was achieved. The furnace was then heated up with a ramp rate of 35 °C/min to the growth temperatures (750 to 850 °C). The Sulphur component melted at 150 °C was sent into the furnace at the growth temperature to grow h-WS_2. The sample growth procedure proceeded for 10 minutes, after which the furnace was directly opened to room temperature to stop the reaction immediately.

The growth of 2D TMDCs may be divided into four routes depending on the mass flux and growth rate. The formation of nucleus is highly affected by the mass flux of the metal precursor and the size of growth domains is dominated by the growth rate. A high mass flux of the metal precursor with a low growth rate produces polycrystalline film containing small grains and lots of grain boundaries, whereas a high mass flux with a high growth rate tends to form a smoother monolayer film with large grains and fewer grain boundaries. In contrast, a low mass flux of the metal precursor prefers to form single crystals with small domains when combined with a low growth rate, and a large monolayer single-crystal when combined with a high growth rate.

In this chapter, we adapted the fourth route to form large monolayer WS_2 single crystals. Because the WS_2 growth rate is very slow, the growth can be approximately treated as a process close to thermodynamic equilibrium. Therefore, the morphology of WS_2 domain is determined by the edge energy, and the domain shape can be obtained by equilibrium Wulff construction. The different partial pressures of hydrogen gas is one of the methods to affect the Gibbs free energy of WS_2 edges in various orientations and form the equilibrium morphologies based on Wulff construction. By controlling the different partial pressures of hydrogen gas, we can control the shape of the single crystalline WS_2 from triangle, truncated triangle, hexagonal to dodecagon shapes.

The emission pattern of monolayer WS_2 single crystal can be modulated by stoichiometry, strain, doping and density of non-radiative recombination centers. We have mentioned these factors in Section 4.1 and will show later in this chapter that the W vacancies are the primary defects that behave like non-radiative centers responsible for the suppress PL. In this section, we would like to describe a novel approach that allows us to control the emission patterns of the TMDCs single crystals.

During the last step of our growth procedure, we open the furnace directly to cool the sample immediately. The sample shrinks during the cooling process in the CVD system, where the in-plane thermal expansion coefficients (CTEs) mismatch between the monolayer WS_2 and the SiO_2/Si substrate results in significant interfacial strain in the lateral direction, which in turn produces the initial crack length at the edge of the WS_2. According to the mode II cracking model, the critical crack size (c) along the edge is related to the interfacial toughness (K_{ic}) and tensile strain (σ) between the film and substrate. If the initial cracking size along the edge is larger than the critical cracking size, the crack allows to start to propagate toward the inner part of the single crystalline flake, and then leads to buckling. We find that single crystalline flakes with the side lengths exceeding 50 μm have larger initial cracks, which trigger crack propagation so that the PL properties are dominant by the resulting buckling. On the contrary, small flakes (with the side lengths < 50 μm) without sufficiently large initial cracks do not allow cracks to propagate toward the inner part of the flakes. Although the buckling process may not be the dominant reason to alter the PL properties of small flakes of h-WS_2, the formation of cracks could be the defects that induce non-radiative recombination centers or stain distributions within the flake.

Combining the aforementioned two controllable factors (namely, the mass flow rate and the growth rate) together with the rapid quenching method, we are able to fix all growth parameters except the partial pressure of hydrogen gas to systematically control the emission patterns of monolayer WS_2 flakes from triangle, truncated triangle, hexagonal, to dodecagon shapes with alternating α and β domains, as illustrated in Figure 4.3 below.

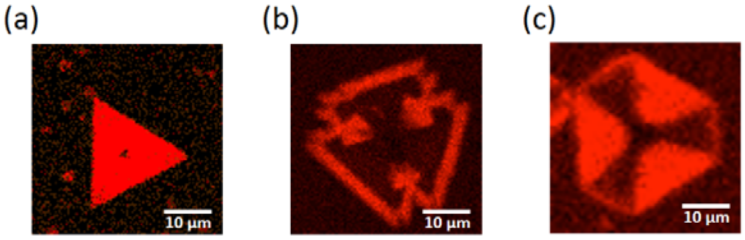

Ar/H_2 (80/5 sccm) Ar/H_2 (80/15 sccm) Ar/H_2 (80/30 sccm)

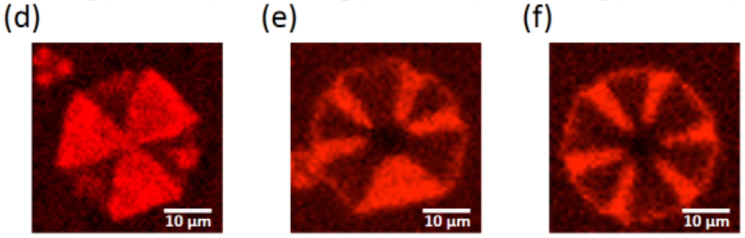

Ar/H_2 (80/40 sccm) Ar/H_2 (80/80 sccm) Ar/H_2 (80/100 sccm)

Figure 4.3. Growth conditions for controlling the emission patterns (from fluorescence images) of monolayer WS_2: (a) Single domain triangle shape under the growth condition of Ar/H_2 (80/5 sccm). (b) Metastable state transitioning from the triangle shape to the truncated triangle shape under the growth condition of Ar/H_2 (80/15 sccm). (c) Truncated triangle shape under the growth condition of Ar/H_2 (80/30 sccm). (d) Hexagonal shape under the growth condition of Ar/H_2 (80/40 sccm). (e) Metastable state transitioning from the hexagonal shape to the dodecagon shape under the growth condition of Ar/H_2 (80/80 sccm). (f) Dodecagon shape under the growth condition of Ar/H_2 (80/100 sccm).

4.3 Characterization of monolayer WS_2

Monolayer h-WS_2 samples were synthesized on SiO_2 (300 nm)/Si substrates by means of CVD, as schematically shown in Figures 4.1 and 4.2. The hexagonal flakes typically had lateral dimensions on the order of several tens to hundreds of micrometers so that optical studies at many discrete locations across a single flake could be carried out.

Our monolayer h-WS_2 samples exhibited typical fluorescence images analogous to the radioactive hazard symbol, as mentioned in the introduction and exemplified in Figure 4.1 (a) Spatially resolved topographic studies on the same samples using atomic force microscopy (AFM) revealed smooth topographic maps (Figure 4.1 (b)). Specifically, while the height difference between the WS_2 single crystal and the SiO_2/Si substrate was ~ 0.85 nm, which was consistent with the monolayer thickness of WS_2, there was no discernible height differences between the two domains of different PL intensities (Figure 4.1 (d)). Spatially resolved measurements of the AFM phase mode revealed a clear phase difference (1°) between the two domains (Figure 4.1 (c)), and the resulting phase map correlated well with the pattern shown in Figure 4.1 (d). Similarly, spatially resolved Raman spectroscopic maps for the A_{1g} and E_{2g}^1 modes of a monolayer h-WS_2 single crystal (shown respectively in Figures 4.1 (e) and 4.1 (f)) also exhibited the same pattern. Figure 4.1 (g) shows a representative PL spectrum from 1.96 eV to 2.01eV for the typical A-exciton peak of h-WS_2. The A-exciton PL peak for the α-domain is redshifted compared to that of the β-domain. This redshift may be attributed to tensile strain existed in the α-domains and/or to a higher carrier density. Moreover, the PL intensity in the α-domains is always enhanced by about one order of magnitude when compared with the β-domains. Generally speaking, the PL intensity can be modulated by a variety of factors such as stoichiometry, strain, doping and density of non-radiative recombination centers. To investigate the contributions from strain and doping effects, we performed Raman intensity and frequency mapping of the A_{1g} and E_{2g}^1 modes, which displayed contrast between the α- and β-domains (Figures 4.1 (e) ~ (f)) and were similar to the PL mapping (Figure 4.1 (d)). We found that the strain-related E_{2g}^1 mode exhibited a redshift in the α-domain relative to the β-domain (0.5 cm^{-1}), indicating a tensile-strain effect. Similarly, the redshift (1.2 cm^{-1}) of the doping-related A_{1g} mode in the α-domain relative to the β-domain implied carrier doping effects (Figure 4.1 (h)), which was consistent with the observed PL redshift (Figure 4.1 (g)). The LA (M) mode at 176 cm^{-1}, which is associated with the longitudinal acoustic phonon at the M point of the Brillouin zone, may be considered as a useful indicator of the sample quality. Specifically, a finite intensity of the LA (M) mode implies the presence of defects or disorder that satisfied the $q = 0$ Raman selection rule. Additionally, the intensity of the LA (M) mode, I(LA), may be related to the inter-defect spacing (L_D) by the expression $I(\mathrm{LA}) \propto L_D^{-2}$. As evidenced in Figure 4.4, the β-domain exhibits a larger LA (M) intensity relative to the α-domain, implying a shorter inter-defect distance and therefore a higher areal density of disorder in the *β*-domain that signifies more non-radiative recombination centers and a reduced PL intensity.

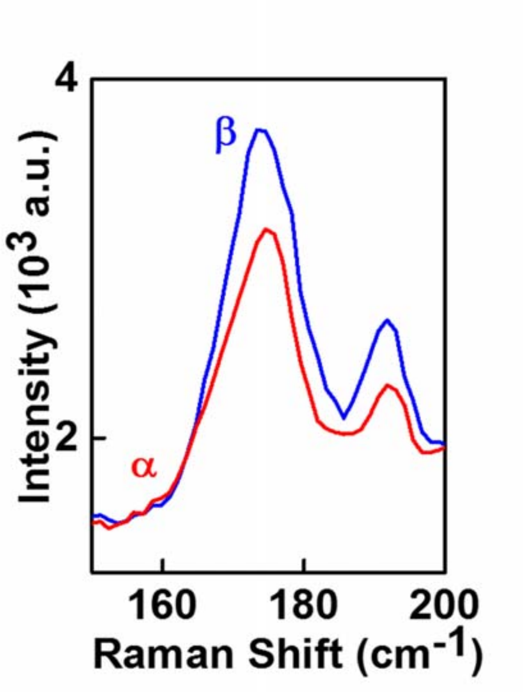

Figure 4.4. Raman spectrascopy of h-WS_2 sample at *α*-domain and *β*-domain: The LA(M) Raman mode is displayed for the *α*-domain (red) and the *β*-domain (blue).

4.4 Stoichiometry and work function of monolayer h-WS_2 single crystal

In addition to the PL/Raman spectroscopic studies, spatially-resolved X-ray photoelectron spectroscopy (XPS) was carried out on monolayer WS_2 transferred to Au (111) / mica substrates (Figure 4.5 (a)) to probe the chemical composition and stoichiometry of the h-WS_2 single crystal. High-resolution XPS mapping performed on the h-WS_2 samples revealed apparent hexagonal geometry, as exemplified in Figure 4.6 (a). Photoelectrons from core level of W and S atoms were acquired from both *α*- and *β*-domains. As shown in Figures 4.5 (b) and 4.5 (c), the corresponding binding energies in the *α*-domain (*β*-domain) were 34.31 eV (34.44 eV) for $W_{4f\,5/2}$, 32.15 eV (32.28

eV) for $W_{4f\,7/2}$, 162.87 eV (162.9 eV) for $S_{2p3/2}$, and 163.07 eV (163.1 eV) for $S_{2p1/2}$. Considering the error range of ±0.025 eV for the binding energies determined using our XPS system, the upshift in the α-domain binding energies (~ 0.13 eV) relative to those in the β-domain was prominent for the W-4f peaks, in good agreement with the valance-band maximum shift due to doping-induced Fermi level modulation. In contrast, the upshift of the S-2p peaks (~ 0.03 eV) was much smaller and essentially negligible given the error range of our XPS system. This negligible upshift of the S-2p peaks in the α-domain may be attributed to the tensile strain effect that affected the S-2p valence electrons more significantly, which contributed to a binding-energy downshift that compensated the doping-induced binding energy upshift. On the other hand, the tensile strain had much weaker effects on the W-4f core electrons so that the doping-induced energy upshifts prevailed for the W-4f peaks in the α-domain.

We have also explored the surface potential (work function) of the α- and β-domains *via* Kelvin probe force microscopy (KPFM) because the work functions of semiconductor 2D materials are sensitive to the corresponding variable Fermi level. To determine the work function of the Al-coated AFM tip, we first performed UPS measurements on the Au (111) / mica sample, which found the work function of Au (111) to be 4.8 eV, as shown in Figure 4.6 (b). Next, we performed KPFM measurements using the Al-coated AFM tip on Au (111) / mica, which yielded the value of the contact potential difference (V_{CPD}^{0}) between the Al-coated AFM tip and Au (111), where the contact potential difference (V_{CPD}^{0}) was defined as the difference between the work function of the tip (ϕ_{tip}) and that of Au (111), so that $eV_{\mathrm{CPD}}^{0} = \phi_{\mathrm{tip}} - 4.8\ \mathrm{eV}$. Finally, KPFM measurements using the Al-coated AFM tip on h-WS_2 yielded the contact potential difference (V_{CPD}) between the Al-coated AFM tip and different domains of the h-WS_2 sample so that we obtained the following relation:

$$eV_{\mathrm{CPD}} = \phi_{\mathrm{tip}} - \phi_{\mathrm{WS_2}}, \quad \Rightarrow \quad \phi_{\mathrm{WS_2}} = \phi_{\mathrm{tip}} - eV_{\mathrm{CPD}}, \tag{1}$$

where $\phi_{\mathrm{WS_2}}$ is the work function of the WS_2 sample. From spatially resolved measurements of V_{CPD}, the work function difference between the α- and β-domains can be determined, and the resulting KPFM images are shown in Figures 4.5 (d) and 4.5 (e).

A schematic representation of the band diagram with the Fermi levels for the α- and β-domains relative to the vacuum level is shown in Figure 4.5 (f). The difference in the Fermi levels between the α- and β-domains can be calculated directly from V_{CPD} using the following equation:

$$\Delta E_f = E_{f,\alpha} - E_{f,\beta} = eV_{\text{CPD},\alpha} - eV_{\text{CPD},\beta} = e\Delta V_{\text{CPD}} = \left(\phi_\beta - \phi_\alpha\right), \tag{2}$$

where $E_{f,\alpha}$ (ϕ_α) and $E_{f,\beta}$ (ϕ_β) are the Fermi levels (work functions) of the α- and β-domains, respectively. Interestingly, we note that the band diagram at the interface of the α- and β-domains is consistent with a type-2 band alignment that supports long-lived interfacial excitons.

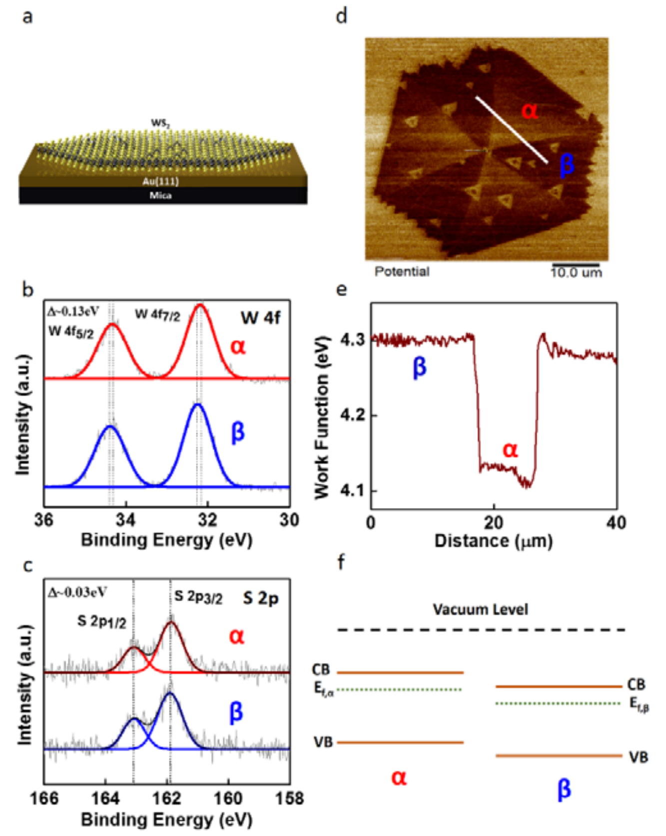

Figure 4.5. Chemical bonding and work function characterization in heterogeneous domains: (a) Schematic of the monolayer h-WS_2 on Au (111) / mica substrate. Selected XPS spectra of the α-domain (top) and β-domain (bottom) for (b) W-4f and (c) S-2p, showing an upshift by ~ 0.13 eV (~

0.03 eV) in the W-4f (S-2p) peaks of the α-domain relative to those of the β-domain. The error range for the binding energies determined by our XPS system is ±0.025 eV. (d) KPFM image of the heterogeneous domains of a monolayer h-WS_2. (e) Work function plot along the white line in (d). (f) Estimated Fermi levels ($E_{f,\alpha}$ and $E_{f,\beta}$) and the corresponding conduction band (CB) and valence band (VB) positions of the α- and β-domains with respect to the vacuum level based on KPFM.

Spatially resolved XPS mapping was conducted on a monolayer h-WS_2 single crystal to investigate the chemical composition and stoichiometry, and the resulting image is shown in Figure 4.6 (a). Additionally, to determine the spatially resolved surface potential (work function) of the α- and β-domains in monolayer h-WS_2 via the Kelvin probe force microscopy (KPFM), we first performed UPS measurements on the Au (111) / mica sample to determine the work function for Au (111) to be 4.8 eV, as shown below in Figure 4.6 (b). Next, using the known value of the Au (111) work function, we performed KPFM measurements with an Al-coated AFM tip on the Au (111) / mica sample to determine the work function of the Al-coated AFM tip. Finally, using the known value of the AFM-tip work function, we performed KPFM measurements on the h-WS_2 monolayer to obtain the spatially resolved work functions associated with the α- and β-domains, as shown in Fig. 4.5 (d).

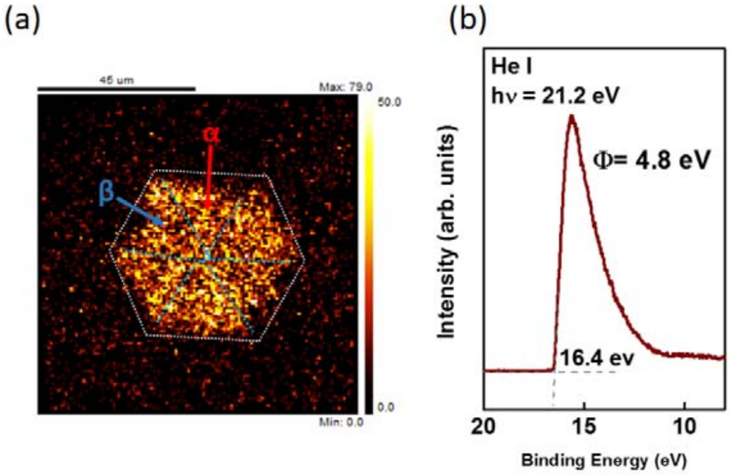

Figure 4.6. Surface characterizations of h-WS_2: (a) Spatially-resolved XPS mapping of a monolayer WS_2 flake, showing the hexagonal geometry of the sample. (b) UPS measurements of the Au (111) thin film, showing the work function of Au (111) to be 4.8eV.

4.5 Valley polarization analysis in CVD-grown monolayer WS_2

To investigate the degree of valley polarization in our monolayer h-WS_2, we performed polarization-resolved PL spectroscopy measurements at both room temperature and 80 K under the excitation of a 514 nm continuous-wave laser source, as schematically illustrated in Figure 4.7 (a). For spatially-resolved PL mapping, the sample was excited with σ_+ helicity and the laser was scanned across a (13 μm × 13 μm) area at a step size of 0.2 μm. The detection optics were set first for the σ_+ analysis and then for the σ_- analysis over the same area in two separate scans. The energy of the PL peak within the range of 1.9 eV to 2.1 eV for the σ_+ (σ_-) detection was determined, and the PL intensity map taken at the peak energy is shown in Figure 4.7 (b) for the σ_+ detection and in Figure 4.7 (c) for the σ_- detection, both obtained at room temperature (RT). These PL maps reveal the same emission pattern as the unpolarized excitation. This type of PL pattern, with lower PL intensity in the β-domain and higher PL intensity in the α-domain (about 10 times stronger than that in the β-domain), was common among all monolayer h-WS_2 single crystals that we synthesized. Given the polarization-resolved PL intensities $I(\sigma_+)$ and $I(\sigma_-)$, the degree of circular polarization (P_{circ}) is define by the following expression:

$$P_{\mathrm{circ}} = \frac{I(\sigma_+) - I(\sigma_-)}{I(\sigma_+) + I(\sigma_-)}. \tag{3}$$

Using Eq. (3), the degree of circular polarization across a monolayer h-WS_2 crystal was obtained and is illustrated in Figure 4.7 (d). The higher degree of polarization (DOP) in the α-domain (45% ~ 60%) and lower DOP in the β-domain (20% ~ 45%) was found to be well correlated to the PL intensity pattern. Similar results were also obtained for polarization-resolved mapping acquired with the σ_- excitation, as shown in Figure 4.8.

The PL spectra of the α-domain (Figure 4.7 (e)) and the β-domain (Figure 4.7 (f)) taken at RT both displayed a single peak with the maximum intensity at 1.92 eV, indicating that the RT emission characteristics were dominated by the neutral excitons. These neutral excitons exhibited very large circular polarization at both the α-domain (P_{circ} ~ 50%) and β-domain (P_{circ} ~ 40%) of our h-WS_2 samples even at RT, in stark contrast to recent reports by other groups (with P_{circ} = 0.2% ~ 32%) on monolayer WS_2, as summarized in Table 4.2. The PL peak for both domains was found to slightly blue-shift to 1.96 eV at a lower temperature (LT) 80 K. As exemplified in Figure 4.7 (g), the LT (80 K) PL intensity of the σ_+ detection at the α-domain increased threefold relative to the corresponding RT signals, whereas the PL intensity of the σ_- detection remained the same at 80 K. In particular, the DOP at the α-domain approached nearly 90% at 80 K. In contrast, the LT (80K) PL spectra at the β-domain revealed that the PL intensities for both the σ_+ and σ_- detections increased tenfold relative to the corresponding PL spectra at RT, as exemplified by Figure 4.7 (h). However, the DOP of the β-domain at 80 K remained largely the same as that at RT.

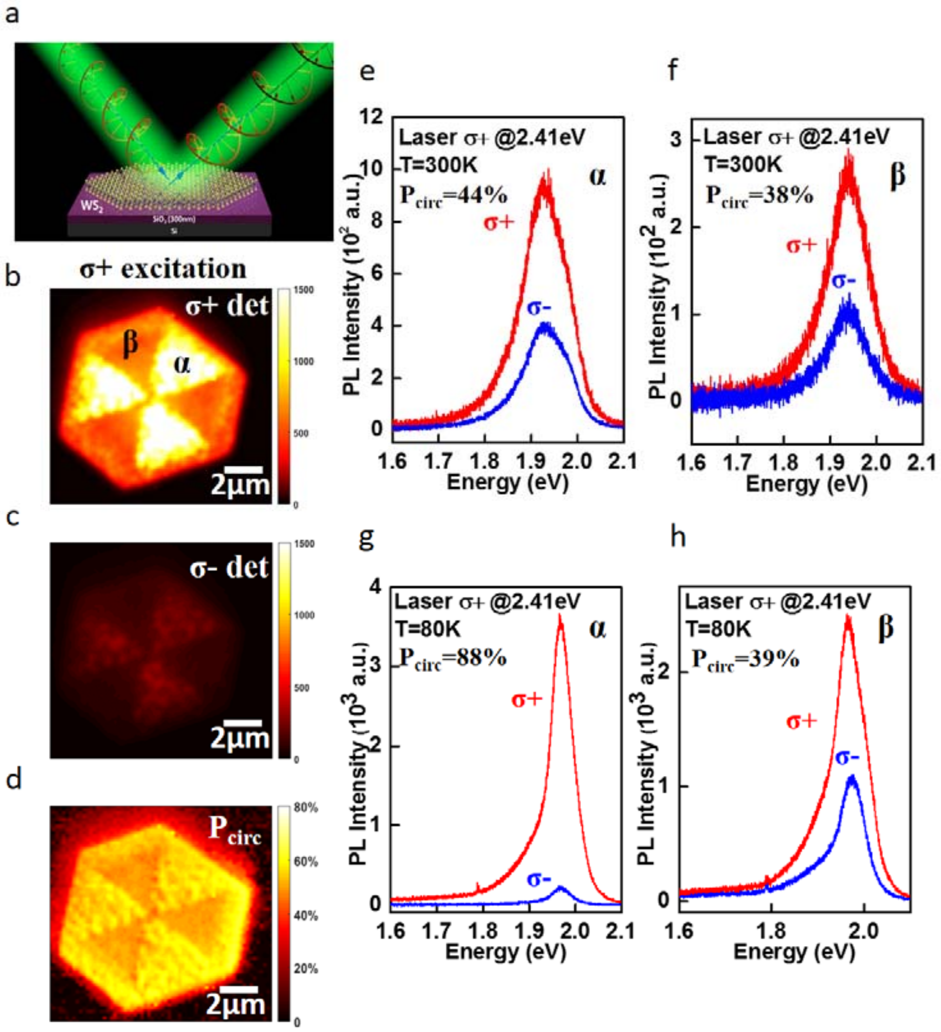

Figure 4.7. Circularly-polarized emission of monolayer h-WS_2 neutral excitons: (a) Schematic of circularly polarized emission on monolayer h-WS_2 under σ_+ 514nm (2.41 eV) excitation. (b) An

intensity map for the σ_+ polarized emission and (c) an intensity map for the σ_- polarized emission. (d) A spatial map for the degree of valley polarization P_{circ} in a monolayer h-WS$_2$ single crystal. (e-f) Representative σ_+ (red) and σ_- (blue) PL intensity spectra taken at room temperature on the α- and β-domains, respectively. (g-h) Representative σ_+ (red) and σ_- (blue) PL intensity spectra taken at 80 K on the α- and β-domains, respectively.

Here, we focused on experimental results obtained by excitations using σ_+ helicity at room temperature. Here we further demonstrate that the same behavior was confirmed when the sample was excited with the opposite σ_- helicity. Using the σ_- helicity to create excitons in the K′ valley and then detecting the σ_- and σ_+ emission, (Figure 4.8 (a)-(b)), we were able to determine the degree of circular polarization P_{circ} by the following relation:

$$P_{\mathrm{circ}} = \frac{I(\sigma_-) - I(\sigma_+)}{I(\sigma_-) + I(\sigma_+)}. \tag{4}$$

The same result was obtained for both σ_+ excitation (Figure 4.7 (d)) and σ_- excitation (Figure 4.8 (c)). Similarly, at 80K, the degree of circularly polarized emission in low-defect domains was found to approach ~ 90%, suggesting nearly perfect valley polarization.

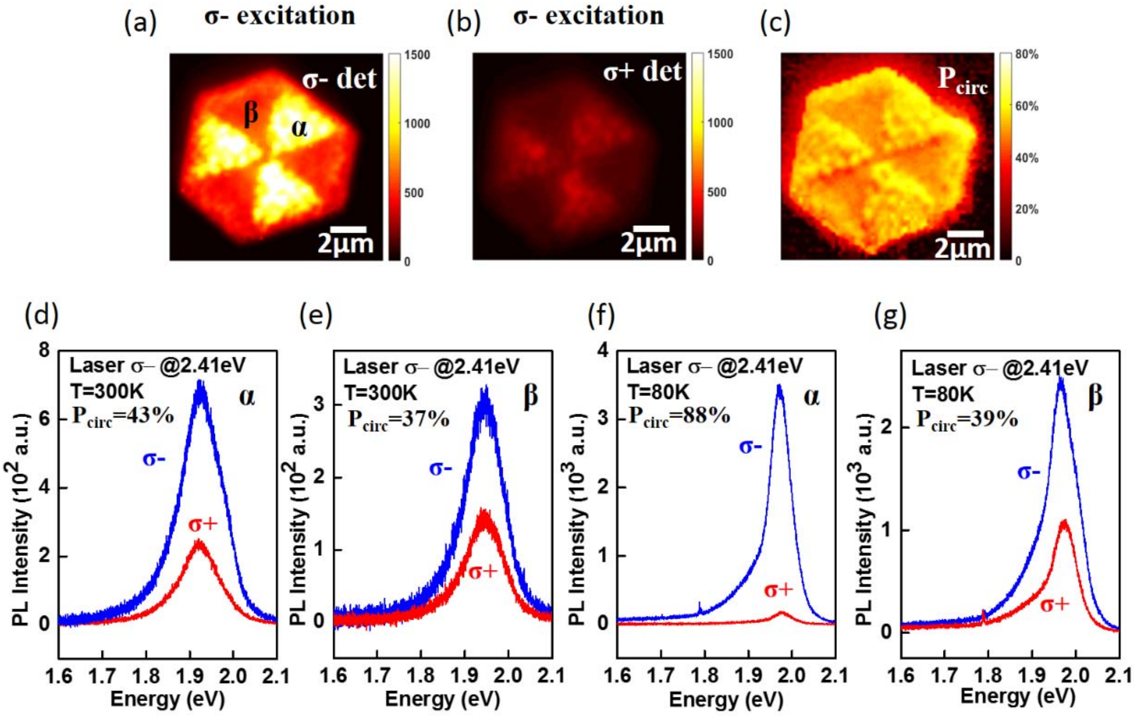

Figure 4.8. Circularly polarized emission from as-grown monolayer h-WS$_2$ under σ_- 514.3nm excitation: (a) σ_- polarized emission and (b) σ_+ polarized emission intensity mapping. (c) The degree of valley polarization P_{circ}. (d-g) σ_- (blue) and σ_+ (red) PL intensity spectra are measured at (d) the α-domain and (e) the β-domain at RT. σ_- (blue) and σ_+ (red) PL intensity spectra are measured at (f) the α-domain and (g) the β-domain at 80 K.

So far we have focused on monolayer h-WS$_2$ under σ_+ helicity excitation at room temperature (RT) and 80 K. In Figure 4.9, we show that for as-grown monolayer triangle shape WS$_2$, $P_{circ} = 55\%$ in the α-domain and $P_{circ} = 20\%$ in the β-domain at RT. At 80 K, the degree of circularly polarized emission in the low-defect α-domains increased to ~ 60%.

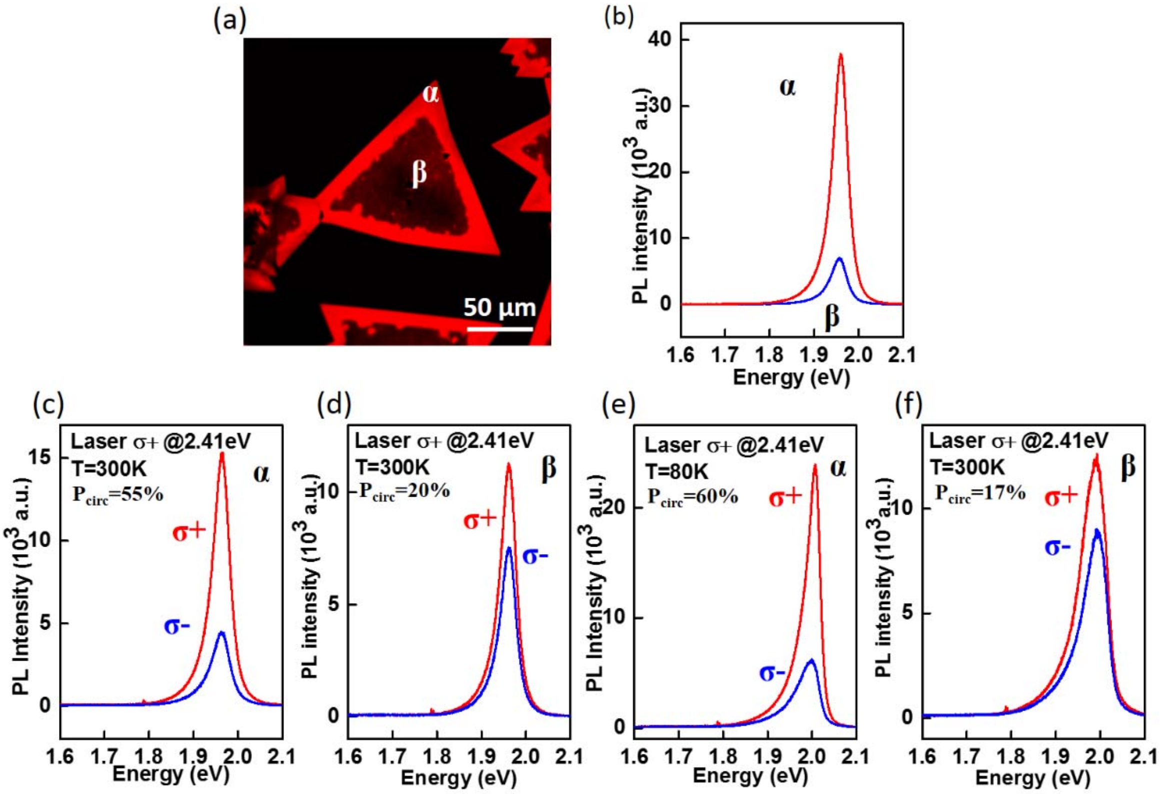

Figure 4.9. Circularly polarized emission from as-grown monolayer triangular shape WS_2 under σ_+ 514.3 nm excitation: (a) Fluorescence image showing two triangle optical emission pattern in fluorescence intensity from a CVD-grown large monolayer WS_2 single crystal. (b) PL spectra for the α- and β-domains of a triangular monolayer WS_2. Room-temperature σ_+ (red) and σ_- (blue) PL intensity spectra taken at (c) the α-domain and (d) the β-domain. Low-temperature (80 K) σ_+ (red) and σ_- (blue) PL intensity spectra taken at (e) the α-domain and (f) the β-domain.

4.6 Defect density analysis of the monolayer h-WS_2 by CAFM

Our finding of significant disparity in the DOP enhancement with decreasing temperature for two different domains is quite unusual: while the common observation of increasing PL intensity with decreasing temperature may be attributed to the reduction of thermally activated non-radiative recombination, this mechanism should have resulted in a comparable enhancement factor with decreasing temperature for the PL intensity in the same material. However, the enhancement factor for the PL intensity at LT was apparently different in different domains of the h-WS_2 single crystal, which led to significantly different DOP at LT. A feasible explanation for such disparity in the DOP enhancement with decreasing temperature may be due to negligible non-radiative recombination centers for excitons in the α-domain as opposed to more non-radiative recombination centers in the β-domain. To shed light on this issue, we performed spatially-resolved conductive atomic force microscope (CAFM) measurements to be detailed below, which facilitated precise identifications of defects that could serve as the non-radiative recombination centers and also provided direct quantifications of the areal defect density.

A schematic illustration of the experimental configuration for the conductive atomic force microscope (CAFM) measurements is shown in Figure 4.10 (a), where all data acquisition was done at RT in air. It is worth noting that careful sample preparation for the CAFM measurements was critically important to obtaining reproducible results. In particular, an atomically flat conductive substrate for the monolayer h-WS_2 sample was necessary. For this purpose, we first transferred a thick piece of CVD-grown graphite onto an atomically flat Au (111) (200 nm)/mica substrate, followed by a monolayer of h-WS_2 transferred from its CVD growth substrate onto the graphite/Au (111)/mica substrate. After the transfer, we annealed the combined sample-on-substrate in a hydrogen-argon gas mixture (with a ratio of H_2 to Ar of 1 to 3) for 3 hours to remove possible contaminants and wrinkles, which helped improve the contact uniformity between the monolayer h-WS_2 and the graphite substrate. Details of the h-WS_2 transfer and the annealing processes can be found in Methods and Supplementary Information. Lastly, a voltage was applied to the sample lead so that a current flowed between the Pt/Ir coated CAFM tip and the sample, and this current was recorded by a current amplifier. By scanning the AFM tip across the sample and recording the currents at each pixel with a pixel spacing of 0.9 nm, we obtained spatially resolved CAFM maps over different domains of the h-WS_2 sample.

In these CAFM maps, the locations of defects were easily identified as distinct high-current features: the defect locations generally exhibited more than 2 orders of magnitude higher currents than areas without defects. Additionally, the electrical characteristics of each defect could be well quantified by measurements of the current-voltage (I-V) curves, as exemplified in Figure 4.10 (b) by the comparison of a typical I-V curve obtained on a defect with a reference I-V curve obtained away from any defects. The I-V curve associated with a defect exhibited much enhanced currents at bias voltages $|V| > 0.3$ V and was nearly symmetric about zero applied bias. These defect sites were generally much more conductive than regions without defects, as demonstrated by the comparison of the differential conductance taken on and off defects in the inset of Figure 4.10 (b). In Figures 4.10 (d) ~ (i), spatially-resolved CAFM differential conductance maps taken at a bias voltage of 0.9 V are shown over different 1 μm × 1 μm areas at locations specified on the h-WS_2 single crystal in Figure 4.10 (d), which shows a spatial map of PL intensity taken on the sample after its transfer onto the substrate for the CAFM measurements. The apparent visibility of defect locations in the CAFM maps enabled direct counting of the number of the defects in both the α- and β-domains. Specifically, for the α-domain, we found 149 defects in Figure 4.10 (d), which corresponded to a defect density of 1.49×10^{10} cm^{-2}. Similarly, we obtained 175 defects (1.75×10^{10} cm^{-2}) in Figure 4.10 (e), and 359 defects (3.59×10^{10} cm^{-2}) in Figure 4.10 (f). For the β-domain, we found 822 defects (8.22×10^{10} cm^{-2}) in Figure 4.10 (g), 1370 defects (1.37×10^{11} cm^{-2}) in Figure 4.10 (h), and 1750 defects (1.75×10^{11} cm^{-2}) in Figure 4.10 (i). These CAFM measurements clearly indicated that the areal density of these highly conductive defect sites was about one order of magnitude higher in the β-domain than in the α-domain.

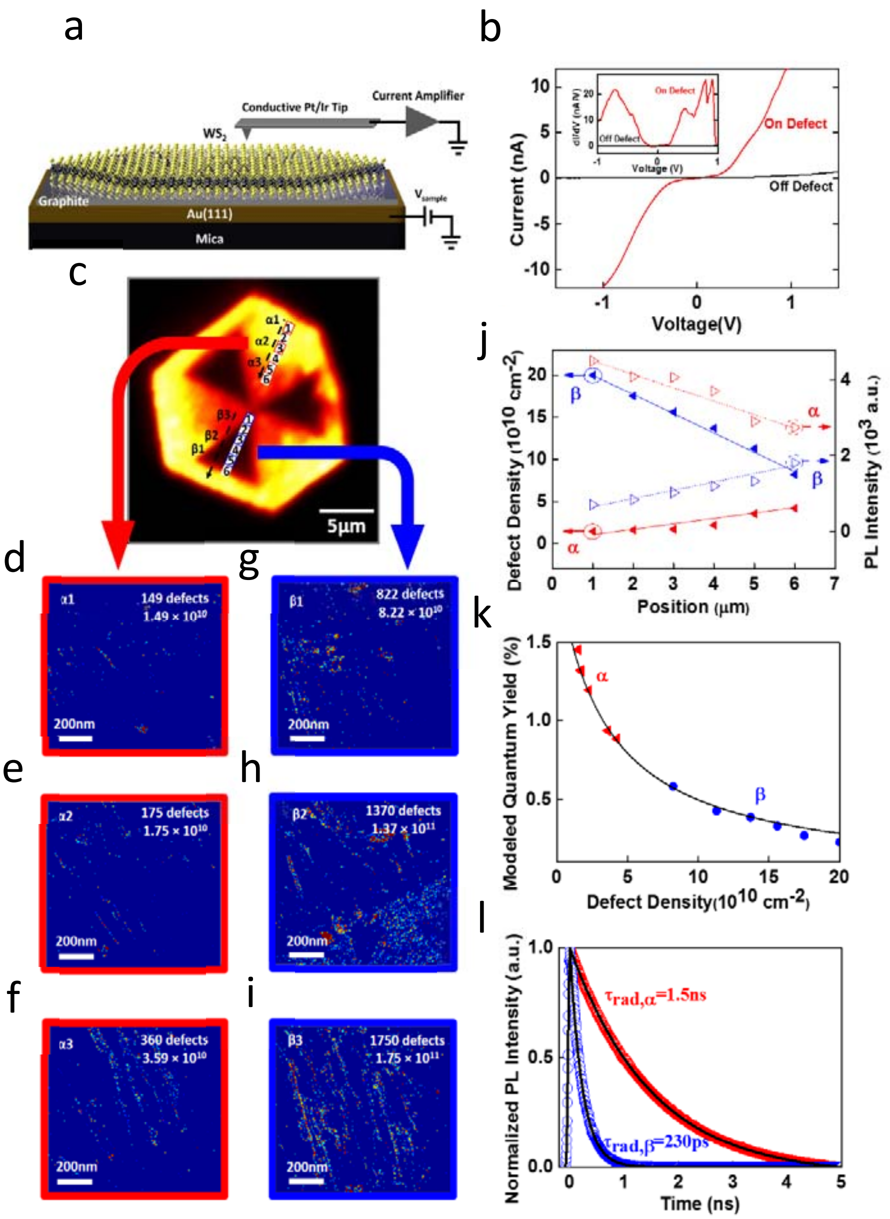

Figure 4.10. Electrical characterizations of the monolayer h-WS_2: (a) Schematic illustration of the experimental setup for the CAFM measurements. A CVD-grown thick multilayer graphene sample was transferred onto an atomically flat Au (111) / mica substrate to provide a conductive backplane for the measurement. A monolayer h-WS_2 sample was subsequently transferred onto the thick multilayer graphene using the transfer method described in Methods. (b) I-V curves taken on a defect and off a defect, showing a drastic difference in the conduction characteristics between a defect

region and the pristine h-WS_2. The inset figure in (b) shows the dI/dV characteristics corresponding to the I-V curve in the main panel of (b). (c) PL map of the h-WS_2 sample, with numbers 1 through 6 labeled in both one of the α-domains and one of the β-domains. The numbers correspond to the locations where detailed CAFM maps were taken. (d-i) CAFM measurements of the locations (α_1, α_2, α_3, β_1, β_2, β_3) labeled in (c), exhibiting defect densities in the α-domain: (d) 1.49×10^{10} cm^{-2} for α_1, (e) 1.75×10^{10} cm^{-2} for α_2, (f) 3.59×10^{10} cm^{-2} for α_3, and in the β-domain: (g) 8.22×10^{10} cm^{-2} for β_1, (h) 1.37×10^{11} cm^{-2} for β_2, (i) 1.75×10^{11} cm^{-2} for β_3. (j) Defect density and PL intensity as a function of position along the dashed line shown in (c) across the α- and β-domains, showing apparent anti-correlation between the defect density and the PL intensity. (k) The model presented in Eq. (7). The red points correspond to the PL measurements of the α-domain, and blue points correspond to the PL measurements of the β-domain. (l) TRPL results, showing PL decay profiles of the α- and β-domains. The black lines are fitting curves using a single exponential decay function.

Here we emphasize that other types of defects not detectable by the CAFM measurements may exist, and in this work we only consider one specific type of defects that are most electrically active and correlate their densities with the corresponding spatially-resolved PL. In Figure 4.10 (j), we compare the defect density and the PL intensity as a function of the position numerated along a line in Figure 4.10 (c), and find that the measured defect density generally anti-correlates with the PL intensity for both α- and β-domains.

A major challenge to understanding the excitonic behavior in h-WS_2 is the wide variety of mechanisms that can affect the exciton recombination, including substrate effects, defect related recombination, and other non-radiative recombination pathways[165,167–173]. From our experiments, the apparent anti-correlation between the defect density and the PL intensity is helpful in identifying the role of defects in the exciton recombination for monolayer h-WS_2.

Generally speaking, the PL intensity is proportional to the PL quantum yield (QY) of excitons, and a standard QY is defined by the following expression:

$$\mathrm{QY} \equiv \tau_r^{-1} \Big/ \left(\tau_r^{-1} + \tau_{nr}^{-1} \right), \tag{5}$$

where τ_r (τ_{nr}) is the average radiative (non-radiative) recombination time of excitons. Typically the non-radiative recombination rate τ_{nr}^{-1} may be further divided into two components if we assume that excitons do not interact with each other. That is,

$$\tau_{nr}^{-1} = \tau_{nr,sub}^{-1} + \tau_{nr,defect}^{-1}, \tag{6}$$

where $\tau_{nr,sub}$ is the average non-radiative recombination time for substrate related effects, which may also include any other non-radiative recombination mechanisms, and $\tau_{nr,defect}$ is the average non-radiative recombination time for defect-related effects.

To understand the correlation between the defect density and PL intensity, we followed a similar analysis by Rosenberger *et al.* Specifically, we assumed that the defect-related non-radiative recombination occurred when excitons collided with defects and resulted in non-radiative recombination. For an exciton with an effective collision radius r traveling with a speed v, an area swept by the exciton over a time period t in the 2D sheet with a defect density n_d would result in N collisions, where $N = n_d(2rvt)$. Therefore, the collision time $\tau_{nr,defect}$ between the exciton and defects can be defined by the following expression:

$$\tau_{nr,defect} = \frac{t}{N} = \frac{t}{n_d\left(2rvt\right)} = \frac{1}{2rvn_d}, \quad \Rightarrow \quad \tau_{nr,defect}^{-1} = 2rvn_d. \tag{7}$$

Combining Eqs. (5)-(7) and assuming that the QY and the empirical PL intensity, $(PL)_{\exp}$, are related by a scaling coefficient C, we arrived at the following relation:

$$(PL)_{\exp} = C\frac{\tau_r^{-1}}{\tau_r^{-1} + \tau_{nr,sub}^{-1} + 2rvn_d}\ . \tag{8}$$

Empirically, the values of τ_r in different domains could be directly determined from time resolved PL (TRPL), which yielded $\tau_r = 1.5$ ns in the α-domain and $\tau_r = 230$ ps in the β-domain for monolayer h-WS$_2$. These values were consistent with the range of 0.2 ~ 4 ns reported in the literature for monolayer WS_2. If we further assumed that a thermal speed of excitons at room temperature (RT) of $v = 10^5$ m/s[174,175], and an effective collision radius $r = 2.1$ nm based on previous reports, we obtained in Figure 4.10 (k) the relation between the spatially varying PL intensity of a monolayer h-WS_2 on graphite/Au (111)/mica and the corresponding local defect density. The solid black line represents the fitting curve for the PL measurements using Eq. (8) with the fitting parameters $C = 3.1\times10^5$ and $\tau_{nr,sub} = 30$ ps. These fitting parameters were consistent for both domains in h-WS_2, which implies that our direct quantification of the defect density n_d helped decouple the defected-related non-radiative recombination (associated with $\tau_{nr,defect}^{-1} = 2rvn_d$) from other non-radiative mechanisms (associated with $\tau_{nr,sub}^{-1}$).

To understand why the DOP differed in the α- and β-domains, we considered a rate equation model in the steady state to find the relationship between the DOP and defect-related non-radiative recombination. As detailed in ref. 152 and 176[152,176] the circular polarization P_{circ} for neutral excitons in the steady-state rate model can be given by the following expression:

$$P_{circ} = \frac{P_0(1-\delta)^2}{1+2\left(\tau_{ex}/\tau_{intervalley}\right)} = \frac{P_0\left[1-\left(\delta_{imp}+\delta_{phonon}\right)^2\right]}{1+2\left(\tau_{ex}/\tau_{intervalley}\right)} \quad , \tag{9}$$

where P_0 is the theoretical degree of circular polarization, τ_{ex} ($\tau_{intervalley}$) is the neutral exciton (intervalley) relaxation time, and $(1-\delta)$ represents the selectivity in the initial excitation with $0 < \delta < 1$. In particular, we may express $\delta = \delta_{imp} + \delta_{phonon}$ to account for impurity/defects/substrate-related and phonon-assisted recombination effects that led to inter-valley mixing from finite-momentum scattering, with $(1-\delta)$ decreasing with increasing scattering densities and increasing temperature. Thus, from Eq. (9) we expect P_{circ} to increase with either decrease in τ_{ex}, increase in $\tau_{intervalley}$, or decrease in δ. For both α- and β-domains of the same h-WS_2 sample, given that they were excited with the same laser power and wavelength, and were also exposed to the same ambient, we may assume that the optically generated exciton densities n_K^{ex} and $n_{K'}^{ex}$ were the same for both domains.

In monolayer TMDCs at RT, the non-radiative lifetimes may be several orders of magnitude shorter than the radiative lifetime so that the overall exciton lifetime is much reduced. From our CAFM measurements at RT and using Eqs. (7) – (8) to fit the PL intensities, we found that the α-domains with lower defect densities would exhibit higher PL intensities and longer non-radiative lifetimes (τ_{nr} = 4.7 ps ~ 10 ps for $n_d = 3.59\times10^{10}$ cm^{-2} ~ 1.49×10^{10} cm^{-2}), whereas the β-domains with higher defect densities would exhibit lower PL intensities and shorter non-radiative lifetimes (τ_{nr} = 1.1 ps ~ 2.6 ps for $n_d = 1.75\times10^{11}$ cm^{-2} ~ 8.22×10^{10} cm^{-2}). By considering the radiative (τ_r) and non-radiative (τ_{nr}) lifetimes of excitons in both domains, we could directly estimate the exciton lifetime τ_{ex} by the relation $\tau_{ex}^{-1} = \tau_r^{-1} + \tau_{nr}^{-1}$, which yielded larger values of τ_{ex} = 4.72 ps ~ 10 ps for the α-domains and smaller values of τ_{ex} = 1.1 ps ~ 2.6 ps for the β-domains at RT. Additionally, the large differences in the defect density between the α- and β-domains gave rise to lower selectivity (*i.e.*, smaller $(1-\delta)^2$) in the β-domains. Therefore, the nearly temperature independent P_{circ} in the β-domain may be understood in terms of the competing effects between increasing $(1-\delta)^2$ and decreasing $(\tau_{ex})^{-1}$ with decreasing temperature according to Eq. (8). In contrast to the β-domain, $(\tau_{ex})^{-1}$ in the α-domain did not decrease as much with decreasing temperature due to far fewer non-radiative recombination sites, whereas the selectivity $(1-\delta)^2$ increased more significantly with decreasing temperature due to diminishing δ_{phonon} and negligible δ_{imp}. Therefore, the value of P_{circ} increased dramatically with decreasing temperature in the α-domains according to Eq. (9), consistent with our experimental finding.

4.7 Atomic defects structures analysis of monolayer h-WS$_2$ by STM

While the temperature-dependent PL intensities and DOP in both the α- and β-domains of h-WS$_2$ can be consistently explained in terms of the differences in the density of electrically-active defects, the microscopic origin for these defects is not yet understood. By performing scanning tunneling microscopy (STM) measurement on monolayer WS$_2$ single crystals, we obtained atomically spatial-resolved images associated with either the SVs (Figure 4.11(a)) or the WVs (Figure 4.11(d)).

For the SV sites of WS_2, as exemplified by the white dash triangles in Figure 4.11(a), the corresponding tunneling conductance spectra were found to be comparable to those of vacancy-free regions. Specifically, both the tunneling current (*I*) *vs.* bias voltage (*V*) spectra and the corresponding (*dI*/*dV*)-*vs.*-*V* spectra taken at a SV (represented by the red curves in Figures 4.11(b) and 4.11(c) for the SV location $\alpha 1$ shown in Figure 4.11(a)) is essentially indistinguishable from those taken at a vacancy-free region (represented by the orange curves in Figures 4.11(b) and 4.11(c) for the vacancy-free location $\alpha 2$ shown in Figure 4.11(a)). In particular, the (*dI*/*dV*) spectra revealed that the valence band maximum (VBM) and conduction band minimum (CBM) were located at $E_{VBM} \sim -1.1$ eV and $E_{CBM} \sim +0.9$ eV, respectively, yielding a band gap of $E_g = E_{CBM} - E_{VBM} = \sim 2$ eV (Figure 4.11(c)). In contrast, for the WV sites as exemplified by the large white dashed triangle in the Figure 4.11(d), the tunneling spectra taken at the WV sites β_1 and β_2, respectively, illustrated by the blue and green curves in Figure 4.11(e) for the *I*-*vs.*-*V* spectra and in Figure 4.11(f) for the (*dI*/*dV*)-*vs.*-*V* spectra, revealed an enhanced differential conductance at smaller biased voltages and a smaller bandgap of ~ 1.1eV, with the VBM and CBM move to ~ –0.8 eV and ~ +0.3 eV, respectively. These spectra associated with the WVs were qualitatively similar to the CAFM measurements in Figure 4.10(b), even though direct quantitative comparison of the *tunneling* conductance data from STM with the *contact* conductance data derived from CAFM is not straightforward without detailed information and modeling of the nanoscale interfacial properties between the AFM tip and WS_2. Overall, the combined information derived from atomically resolved STM studies and the nanoscale CAFM measurements strongly suggests that the WV sites rather than the SV sites in monolayer WS_2 are the primary non-radiative combination centers that are responsible for the reduction in the PL intensity and DOP.

The aforementioned scenario of a higher WV density in the β-domain is not only consistent with the observation of reduced PL intensities and DOP but also accounts for the larger work function in the β-domain (as found by the KPFM studies) because of the excess hole-doping associated with WVs in WS_2. Therefore, we have been able to provide a unified description for the varying chemical, electronic and optical properties of different domains in monolayer h-WS_2 in terms of the varying WV densities.

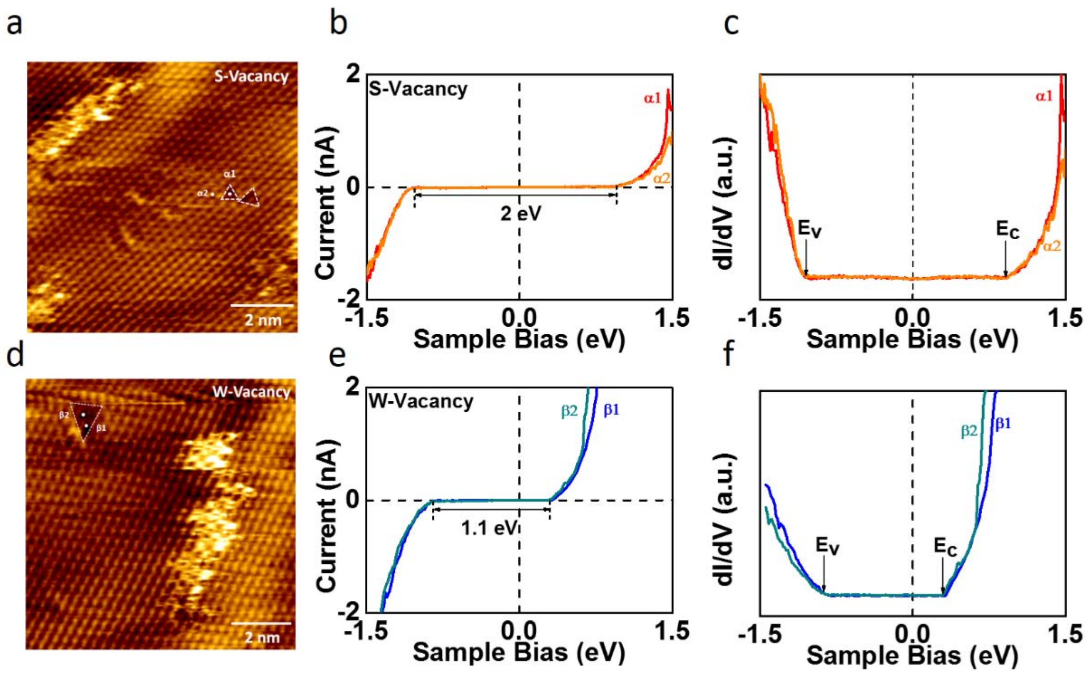

Figure 4.11. Scanning tunneling microscopic and spectroscopic studies of WS_2 monolayer: (a) Atomically-resolved of SVs (as indicated by the white triangles) on a sample of monolayer WS_2 on Au substrate. The topography was recorded under 0.7V, 1.2nA. Here the white solid circle $\alpha 1$ refers to the location of a SV in the center of a white triangle, and the white solid circle $\alpha 2$ refers to the location of a vacancy-free region. (b) Tunneling current (I) vs. sample biased voltage (V) spectra taken at a SV ($\alpha 1$) and defect free region ($\alpha 2$), showing consistent energy gaps of ~ 2.0 eV. Here the vertical dashed line corresponds to $E = 0$ (the Fermi level). (c) (dI/dV)-*vs.*-V spectra obtained from the regions $\alpha 1$ and $\alpha 2$ shown in (a). (d) Atomically-resolved WVs (shown by the white triangle) on a sample of monolayer WS_2 on Au substrate, with the topography recorded under 0.7V, 1.2nA. (e) I-*vs.*-V spectra taken at two WVs (white solid circles $\beta 1$ and $\beta 2$ in (d)), showing a reduced energy gap of 1.1 eV. The vertical dashed line corresponds to $E = 0$ (the Fermi level). (f) (dI/dV)-*vs.*-V spectra obtained from the regions $\beta 1$ and $\beta 2$ shown in (d). The tunneling spectra associated with the WVs are qualitatively similar to the CAFM measurements at non-radiative defect sites, suggesting that the WVs are responsible for the non-radiative defects that suppress PL and DOP in h-WS_2.

Finally, we note that a well-defined, net valley polarization can be established along the boundary between the α- and β-domains under circularly polarized light as the result of their different DOP. Hence, the domain boundaries in our monolayer h-WS_2 samples may be considered as one-dimensional *topological channels* so that a Hall bar device patterned along one of the domain boundaries is expected to exhibit CPL-induced valley Hall currents even at room temperature. Such opto-valleytronic and related opto-spintronic phenomena for devices fabricated along the topological channels in monolayer h-WS_2 will be an interesting topic for future investigation.

4.8 Summary of synthesis and properties of 2D semiconductor (WS_2)

In summary, our experimental investigations based on spatially resolved measurements of PL, Raman spectroscopy, XPS, KPFM, CAFM, and STM have clarified the microscopic physical origin for markedly different reports of PL properties in CVD-grown monolayer WS_2 by attributing the differences to varying densities of tungsten vacancies (WVs) that act like non-radiative recombination centers. We have also demonstrated large circular polarizations in the PL spectra of our monolayer CVD-grown h-WS_2 single crystals under off-resonant illumination and at relatively high temperatures (from RT to 80 K) when compared with other TMDCs, as detailed in Tables 4.1 and 4.2 and summarized in Figure 4.12 The occurrence of type-two band alignments along the domain walls of h-WS_2 further promises longer exciton lifetimes along the domain boundaries. This work therefore suggests a new pathway towards engineering valley polarizations and exciton lifetimes in TMDCs by controlling the type and density of defects that serve as non-radiative exciton recombination sites.

MoS_2

Polarization (P_{circ})	Measured Temperature (T)	Excitation wavelength (λ)	Sample
0 %	14 K	532 nm	Exfoliated sample[152]
100 %	14 K		
		633 nm	
32 %	10 K	633 nm	Exfoliated sample[139]
35 %	300 K	633 nm	CVD grown sample[159]
95~100 %	30 K	633 nm	
40 %	300 K	633 nm	Exfoliated sample[160]
90 %	4 K	633 nm	
40 %	300 K	633 nm	Exfoliated sample[161]
50 %	4 K	633 nm	

Table 4.1. Summary of the degree of circular polarization of monolayer MoS_2 at various temperatures.

WS_2

Polarization (P_{circ})	Measured Temperature (T)	Excitation wavelength (λ)	Sample
0 %	300 K	594 nm	CVD grown sample[162]
12 %	4 K		
		594 nm	
10 %	300 K	594 nm	Exfoliated sample[163]
40 %	10 K		
		594 nm	
2~32%	300K	633 nm	CVD grown sample[165]
0.2~20%	300K	588 nm	
0.2~20%	300K	561 nm	
2~8%	300K	552 nm	
0~3%	300K	532 nm	
45~60% (α domain)	300K	514 nm	CVD grown sample[19]
20~45% (β domain)	300K	514nm	

88% (α domain)	80K	514nm	
39% (β domain)	80K	514nm	

Table 4.2. Summary of the degree of circular polarization of monolayer WS_2 at various temperatures.

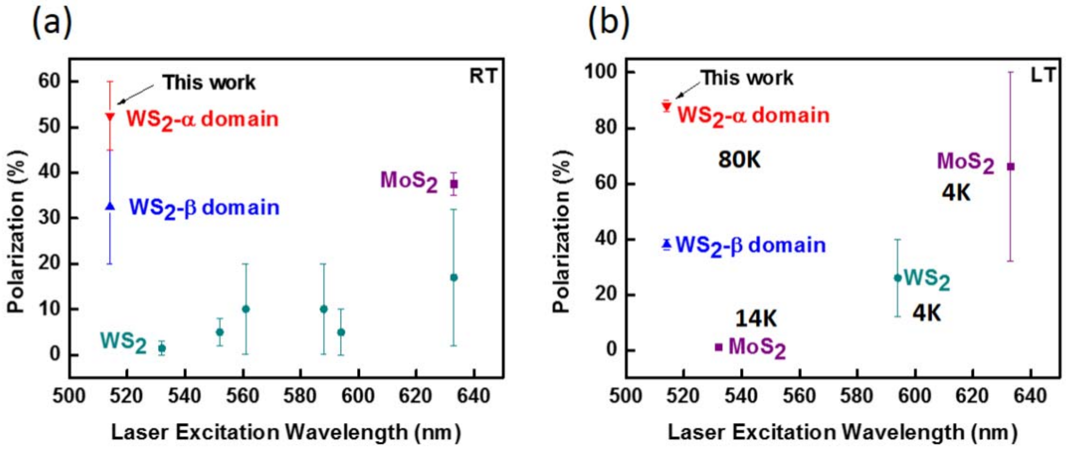

Figure 4.12. Summary of the degree of polarization of MoS_2 and WS_2 at (a) room temperature and (b) low temperatures.

Chapter 5

ELECTRIC TUNING AND BOOSTING VALLEY-POLARIZED EMISSION OF MONOLAYER WS_2 SANDWICHED IN PLASMONIC ARCHIMEDES SPIRAL (PAS) NANOSTRUCTURES

Monolayer transition metal dichalcogenides have intrinsic valley pseudospin degrees of freedom, making them appealing for exploiting valleytronic application in information storage and processing. WS_2 monolayer possesses two inequivalent valleys in the Brillouin zone, with each valley coupling selectively with circularly polarized light. The degree of valley polarization (DVP) under the excitation of circularly polarized light is a parameter that determines the purity of valley polarized photoluminescence (PL) of monolayer WS_2. Here, we report that valley polarized PL of monolayer WS_2 can be efficiently tailored at room temperature (RT) through the surface plasmon-exciton interaction with plasmonic Archimedes spiral (PAS) nanostructures. The DVP of WS_2 using 2 turns (2T) and 4 turns (4T) of PAS can reach up to 40% and 50% at RT, respectively. Further enhancement and continuous control of excitonic valley polarization in electrostaticly doped monolayer WS_2 are demonstrated. Under the circularly polarized light on WS_2-2TPAS heterostructure, 40% valley polarization of exciton without electrostatic doping is icreased to 70% by modulating the carrier doping via a backgate. This enhancement of valley polarization may be attributed to the screening of momentum-dependent long-range electron-hole exchange interactions. The demonstration of electrical tunabilty in the valley-polarized emission from WS_2-PAS heterostructures provides new strategies to harness valley excitons for application in ultrathin valleytronic devices.

5.1 Introduction

Monolayer 2H-phase transition metal dichalcogenides (TMDCs) MX_2 are direct band gap materials and consist of a plane of transition metal atoms (M) sandwiched between top and bottom halogen atoms (X) that are seperately arranged in the respective hexagonal lattice structure[177,178]. The band structures of monolayer TMDCs[179–183] are composed of two degenerate but inequivalent K (K′) valleys in the Brillouin zone. Because of the strong spin-orbit coupling and time-reversal symmetry, the valence bands (VB) in the K (K′) valley[139,152,154,184,185] have a large energy spin splitting between the top spin-up (spin-down) band and the bottom spin-down (spin-up) band. This difference results in valley-dependent optical selection rules[186–188]: circularly polarized light with positive helicity (σ+) couples to the K valley and the negative helicity (σ-) couples to the K′ valley. It is therefore possible to selectively populate and manipulate the different valleys (K or K′) by means of circularly polarized (CP) light[184,187]. The spin and valley degrees of freedom (DOF) in these TMDCs materials provide an important platform for exploring new condensed-matter physics, which have been exploited for various fundamental applications in spintronic and valleytronic devices. Noting that the control of circularly polarized emission of light is a key step towards developing functional optical devices for applications in display technology[189,190] and quantum-based optical information processing/communication[191–193], manipulation of the valley degrees of freedom in 2H-TMDCs is a promising approach to realizing practical information processing devices that are more energy-efficient than current devices based on the control of charge.

Accessing different valley degrees of freedom through CP lights has been demonstrated in several TMDCs, including molybdenum disulfide (MoS_2)[139,152,154], molybdenum diselenide ($MoSe_2$)[194], tungsten disulfide (WS_2)[19,195], and tungsten diselenide (WSe_2) [140,196–198]. However, it has been a significant challenge to manipulate the valley polarization and the resulting photoluminescence (PL) of monolayer 2H-TMDCs at room temperature because of the weak light-matter interaction and substantial defects[19] in these atomically thin layers. Various approaches, such as applying an in-plan electric field[140,199], an out-of-plan magnetic field[200–204], or a localized magnetic field[205], have been proposed in an attempt to enhance the circular dichrorism (CD) of PL in TMDCs.

An alternative approach to enhacing the CD of PL in TMDCs may be achieved by means of chiral plasmonic metasurfaces[206–213]. This approach is based on the strong optical chirality in metallic chiral metasurfaces and the enhancement of light-matter interaction through localized surface plasmon resonance (LSPR) modes. Specifically, the confined LSPR modes can strongly interact with the carriers within the monolayer TMDC material and form a compact, fuctional nanophotonic devices. Futhermore, the geometry-dependent LSPR modes of chiral plasmonic metasurface provide wavelength tunability for the wide emission range of different TMDCs. Thus, implementing chiral plasmonic metasurfaces[214–224] on TMDCs is likely a suitable approach to manipulating the CD of PL in these materials.

In this study, a metal-dielectric-metal (MDM) structure consistent of monolayer WS_2 and plasmonic Archimedes spiral nanostructures (WS_2-PAS) is designed to investigate the monolayer WS_2 exciton-plasmon interaction and to manipulate the valley-polarized PL in WS_2-PAS heterostructures by spectroscopic measurements and numerical simulations. The device configuration consists of a chemical vapor deposition (CVD)-grown monolayer WS_2 transferred onto a substrate of 60 nm-thick SiO_2 on top of a 150 nm-thick gold reflection layer. A 60 nm-thick gold film is subsequently deposited on the $WS_2/SiO_2/Au$ structure, and then spiral gold rings are patterned on the gold film by E-beam lithography. The magnitude of the degrees of valley polarization (DVP) in as-grown monolayer WS_2 is found to be < 5 % at room temperature (RT). In comparison, the RT values of the DVP in monolayer WS_2-2TPAS and WS_2-4TPAS under the excitation of right-handed circularly polarized (RCP) light are found to increase to 40% and 50%, respectively. In contrast, the corresponding values of the DVP under the excitation of left-hand circularly polarized (LCP) light are found to decrease to 5 % in both monolayer WS_2-2TPAS and WS_2-4TPAS heterostructures. Additionally, the DVP can be further enhanced by applying a back-gated voltage V_G from 40% for $V_G = 0$ to 70% for $V_G = 10$ V. This finding suggests that modulating the carrier doping level can enhance the valley polarization by screening the long-range electron-hole exchange interactions and thus reducing the momentum-dependent inter-valley scattering. The capability of enhancing and tuning the degrees of valley polarization in monolayer 2H-TMDCs by plasmonic chiral metasurfaces offers great oppotunities toward developing valley-dependent optoelectronic devices for energy-efficient information processing.

5.2 Device fabrication and actively controlled PL enhancement

Figure 5.1(a) shows the schematics of the metal-dielectric-metal (MDM) structure that consists of a monolayer WS_2 and plasmonic Archimedes spiral nanostructures (WS_2-PAS) under the excitation of circularly polarized light. The WS_2 monolayer was grown by chemical vapor deposition (CVD) method, and then transferred onto a substrate consisting of a 60 nm-thick SiO_2 layer on top of a 150 nm-thick gold mirror layer. The Archimedes spiral rings were patterned by E-beam lithography on a 50 nm-thick Au film deposited on the WS_2-PAS.

Figure 5.1(b) shows the PL intensity differences between the as-grown monolayer WS_2 and the MDM structure of a monolayer WS_2 integrated with right-handed Archimedes spiral nanotructures. Under the excitation of right-hand circularly polarized light (RCP, red), the PL intensity of the WS_2-PAS heterostructure is enhanced by more than 10 times relative to that of the as-grown WS_2 (green). In contrast, the PL intensity is barely enhanced under the excitation of left-handed circularly polarized light (LCP, blue). The Purcell enhancement factor is defined as $\varepsilon = I_{\mathrm{wi}}/I_{\mathrm{wo}}$, where I_{wi} (I_{wo}) is the maximum intensity of WS_2 with (without) Archimedes spiral nanotructures. Therefore, ε is larger than 10 for the RCP emission and is nearly 1 for the LCP emission. This asymmetric spectroscopic response to CP light provides an efficient way for tailoring the exciton-plasmon interaction by actively controlling the polarization of the incident light. The inset presents a scanning electron microscope (SEM) image of a representative WS_2-PAS heterostructure with the scale bar representing 5 μm.

The exciton-plasmon interaction in WS_2-PAS structures is dependent on the incident laser power, and the PL intensity of WS_2 and the specific designs of the Archimedes spiral nanostructures. The laser power dependence of PL, under 514 nm RCP laser excitation in WS_2-2TPAS with right-handed (RH) spiral nanostructures, is investigated in Figure 5.1(c). The PL intensity of the WS_2-2TRHPAS is found to increase rapidly with the laser power from 1.9 μW to 16.2 μW, and the PL peak position also exhibits a slight blue shift with increasing laser power up to 5.5 μW, and then remains invariant from 5.5 μW to 16.2 μW. Figure 5.1(d) presents a log-log plot of the power-dependent PL intensity of WS_2 with (red, triangle) and without (blue, inversed triangle) the plasmonic coupling effect. The relationship between PL intensity (I_{PL}) and laser power (P_{laser}) can be approximately expressed by the relation $I_{\mathrm{PL}} = (P_{\mathrm{laser}})^m$, where m represents a constant. For both WS_2 with and without spiral structures, the corresponding *m* values may be fitted to ~ 1.37 for laser powers ranging from 1.9 μW to 16.2 μW, and a maximum enhancement factor ε reaches more than 10 at 9.1 μW.

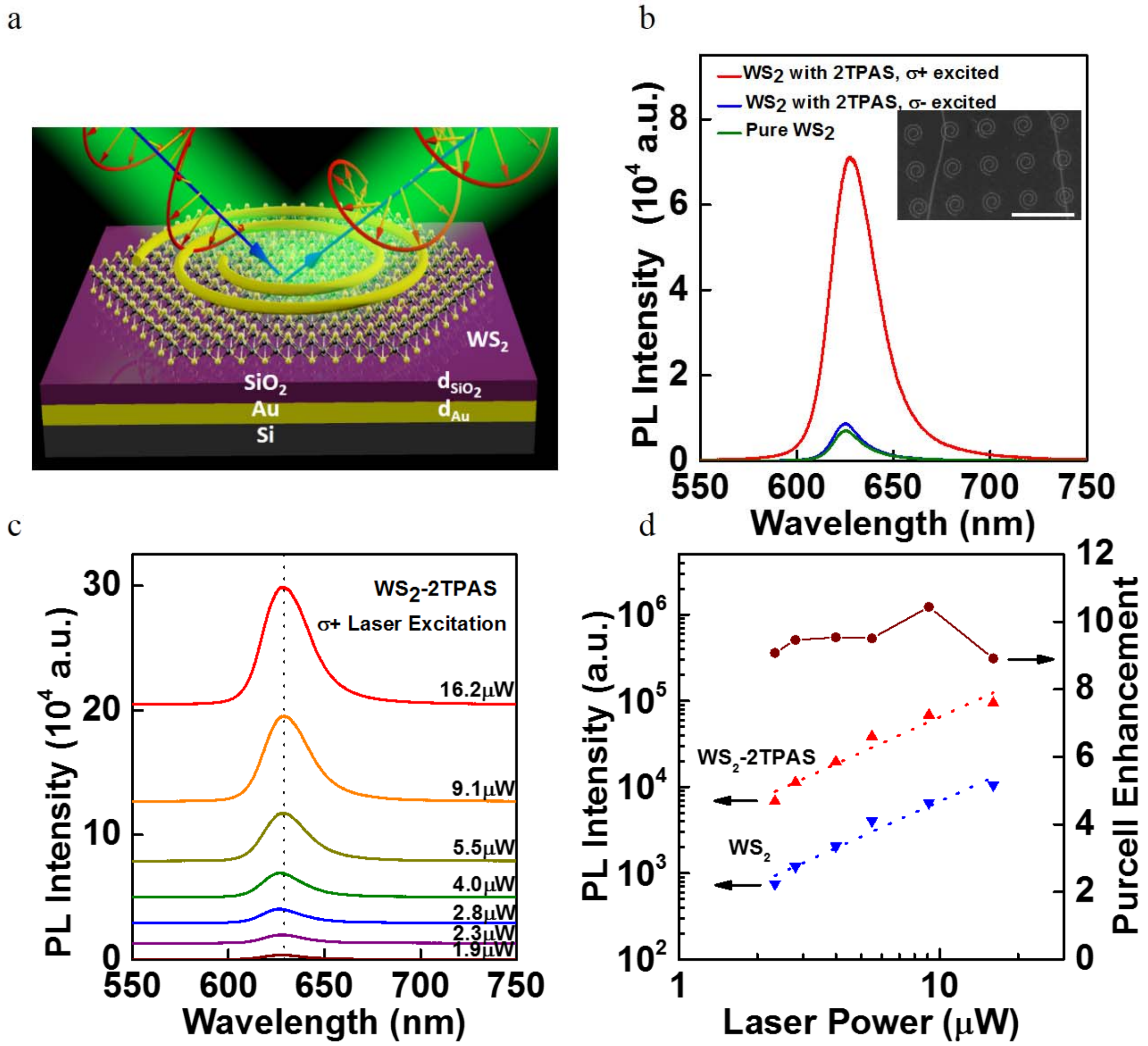

Figure 5.1. Structure and optical spectral properties of monolayer WS_2 integrated with two turns (2T) of right-handed plasmonic Archimedes spiral (WS_2-2TRHPAS) heterostructures. a) Schematics of a WS_2-2TRHPAS heterostructure under circular polarized (CP) light excitations, where a CVD-grown monolayer WS_2 is placed on top of a SiO_2 layer sandwiched between Au spiral structures and a Au film. b) PL spectra of monolayer WS_2 with and without the Au spiral structures, under the excitation of different circularly polarized light at 514nm and the laser power at 8.8 μW. The inset shows an SEM image of the WS_2-2TRHPAS array and the scale bar is 5 μm. c) Evolution of the PL

spectra of monolayer WS_2-2TRHPAS with laser powers. d) Power-dependent PL intensity with (red) and without (blue) Au spiral nanostructures and the corresponding Purcell enhancement (dark red).

5.3 Valley polarized PL spectra of pure monolayer WS_2 and WS_2-2HPAS heterostructure

Valley polarization in monolayer TMDCs can be induced by circularly polarized light excitations and detected by PL measurements at room termperature. Figure 5.2 shows the comparision of the valley polarized PL spectra between an as-grown monolayer WS_2 and a WS_2-PAS heterostructure under the excitations of RCP and LCP light. The wavelength of the excitation laser is 514 nm (E_{pump} = 2.41 eV), which is far away the neutral exciton resonant energy (E_X = 2 eV). A linear polarizer and a quarter-wave plate (400-800 nm) are placed after the laser to obtaine circularly polarized light. The polarized PL signal is resolved by a broadband polarizer and quarter-wave plate placed before the spectrometer. Given the polarization-resolved PL intensities $I(\sigma^+)$ and $I(\sigma^-)$, the degree of circular polarization (P_{circ}) is defined by the following expression:

$$P_{\mathrm{circ}} = \frac{I(\sigma^+) - I(\sigma^-)}{I(\sigma^+) + I(\sigma^-)},$$

where $I(\sigma^+)$ and $\mathrm{I}(\sigma^-)$ denotes the right- and left-handed circular polarization resolved PL intensity, respectively.

The representative PL spectra of the as-grown WS_2 single crystal exhibit similar behavior under both the RCP and LCP excitations, as shown in Figures 5.2(a) and 5.2(d). The corresponding DVP (< 5%) is consistent with previous studies at room temperature. According to the valley-dependent optical selection rule of TMDCs, σ^+ (σ^-) excitations only couple to the specific excitonic transitions in the K (K′) valley so that the corresponding light emission should carry single handedness. However, as schematically shown in Figure 5.1, when the K valley is selectively with σ^+ excitation, the PL light emission contains not only σ^+ signals from polarized excitonic transitions in the K-valley, but also σ^- signals from the K′-valley because of optical phonon-assisted intervalley scattering of excitons from the K to K′- valley, with spin angular momentum exchanged at a finite rate.

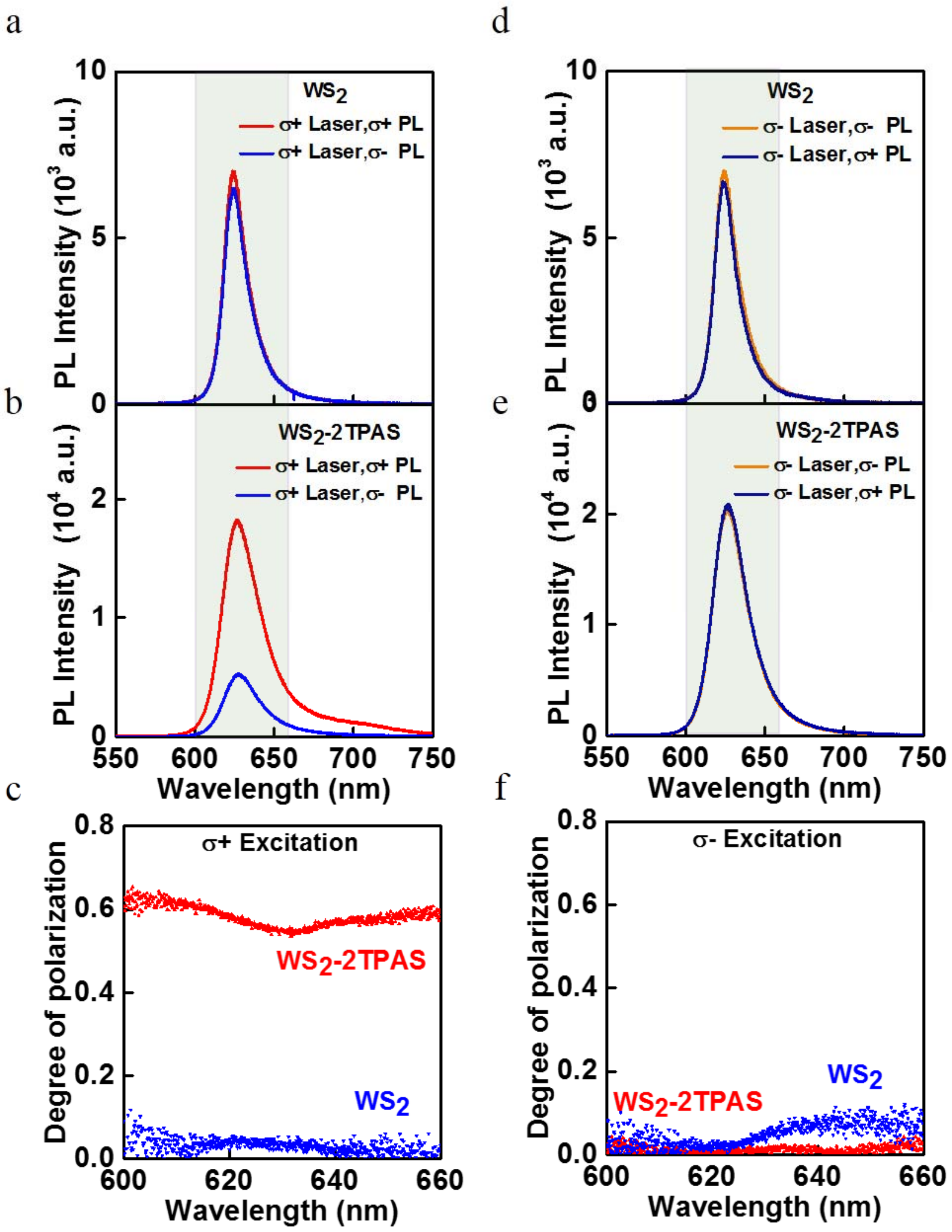
a
WS$_2$
σ+ Laser,σ+ PL
σ+ Laser,σ- PL
PL Intensity (10^3 a.u.)
10
5
0
b
WS$_2$-2TPAS
σ+ Laser,σ+ PL
σ+ Laser,σ- PL
PL Intensity (10^4 a.u.)
2
1
0
550
600
650
700
750
Wavelength (nm)
c
σ+ Excitation
WS$_2$-2TPAS
WS$_2$
Degree of polarization
0.8
0.6
0.4
0.2
0.0
600
620
640
660
Wavelength (nm)
d
WS$_2$
σ- Laser,σ- PL
σ- Laser,σ+ PL
PL Intensity (10^3 a.u.)
10
5
0
e
WS$_2$-2TPAS
σ- Laser,σ- PL
σ- Laser,σ+ PL
PL Intensity (10^4 a.u.)
2
1
0
550
600
650
700
750
Wavelength (nm)
f
σ- Excitation
WS$_2$
WS$_2$-2TPAS
Degree of polarization
0.8
0.6
0.4
0.2
0.0
600
620
640
660
Wavelength (nm)

Figure 5.2. Valley-polarized PL spectra of the as-grown WS_2 and WS_2-2TRHPAS. (a) – (b) Circularly polarized PL spectra of WS_2 and WS_2-2TRHPAS under the excitation of σ^+ light (514 nm) at RT. (d) – (e) Circularly polarized PL spectra of WS_2 and WS_2-2TRHPAS under the excitation of σ^- light (514 nm) at RT. The degrees of valley polarization (DVP) spectra associated with WS_2 and WS_2-2TRHPAS are shown in (c) for σ^+ excitations and in (f) for σ^- excitations.

As shown in Figure 5.2(b), the PL intensity of the σ^+ emission spectra from the WS_2-RHPAS heterostructure is significantly enhanced relative to that of the σ^- emission spectra under the σ^+ excitation. In contrast, the PL intensity of the σ^+ and σ^- emission spectra from the WS_2-RHPAS heterostructure does not exhibit any enhancement under the σ^- excitation, as shown in Figure 5.2(e). For comparison between the DVP under σ^+ and σ^- excitations, the corresponding DVP spectra are shown in Figures 5.2(c) and 5.2(f) for the as-grown WS_2 and the WS_2-2TRHPAS heterostructure, respectively. We find that the value of DVP from the WS_2-2TRHPAS heterostructure has increased by ~55% under the σ^+ excitation and decreased by ~1% under the σ^- excitation. These notable DVP values of the WS_2-2TRHPAS may be attributed to the nontrivial interaction between the excitons in WS_2 and the chiral plasmonic mode in the PAS.

5.4 Ring-number dependent valley polarized PL spectra of WS_2-RHPAS heterostructure

To better understand the exciton-plasmon interactions, we further investigated the effect of different plasmonic structures on the valley-polarized PL spectra. Figures 5.3 (a)-(d) are the SEM images of 1-, 2-, 3-, and 4-turn plasmonic Archimedes spiral arrays on the monolayer WS_2. The corresponding PL intensity mapping images are shown in Figure 5.3 (e)-(h), where it is evident that the PL intensity is dramatically enhanced when the WS_2 monolayer couples with the 2-turn and 4-turn spiral rings. In contrast, the intensity enhancement almost disappears in the the case of 1-turn and 3-turn spiral rings.

Here we note that the number of turns (N) in the PAS structure is designed in such a way that relates to the wavelength of the surface plasmon polariton (SPP), λ_{spp} and the inner and outer radii

(r_0 and r) of the spiral by the expression $r = r_0 + (\lambda_{spp}\varphi / 2\pi)$. This relation is essential to optimize the exciton-plasmon interaction in the PAS structures.

When a right-handed PAS with an even number of turns interacts with the RCP light, the surface plasmon polaritons (SPPs) are generated by the RH spiral structures and coherently propagated toward the ring center forming a focus point. The excitons thus generated (RCP emission) interact constructively with the SPP field, which result in enhanced PL intensity at the center of the RH spiral structure.

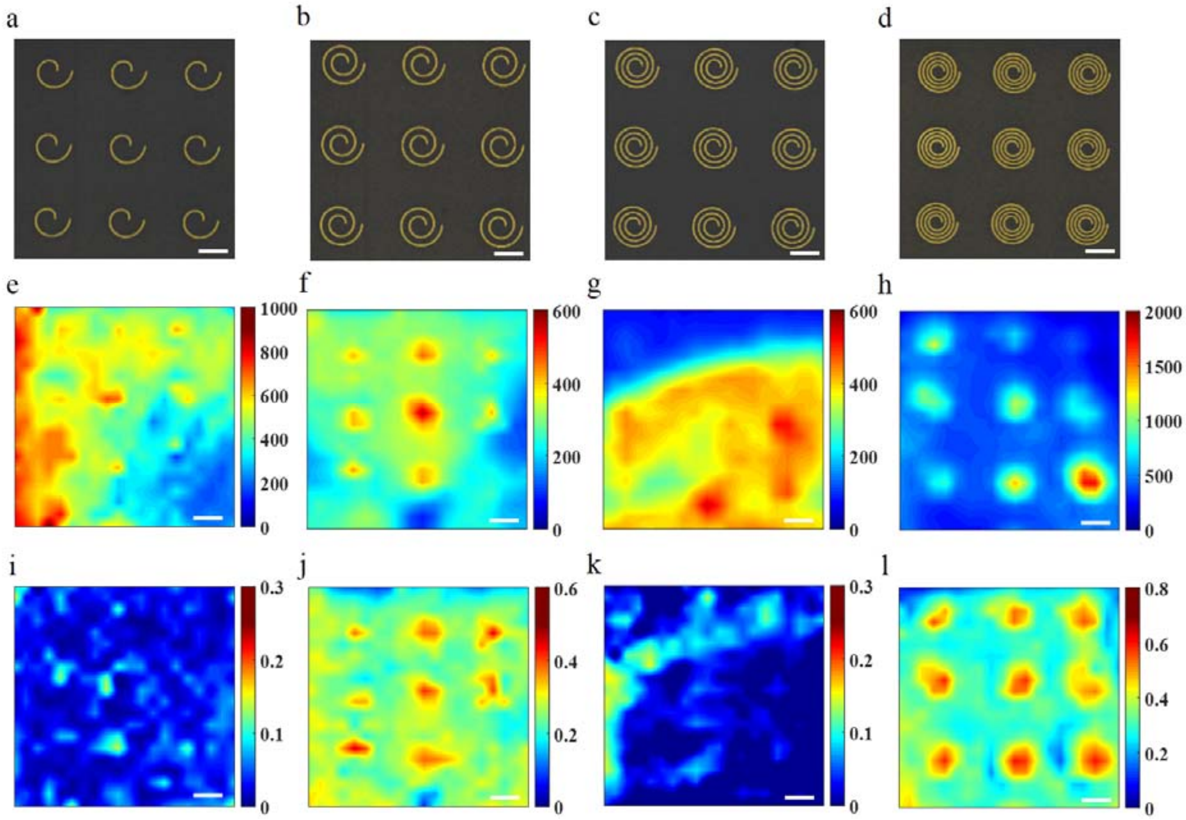

Figure 5.3. Ring-number-dependent room-temperature (RT)-valley-polarization of WS_2. (a-d) SEM images of 1-, 2-, 3-, and 4-turn RHPAS arrays. (Scale bar: 1.25 µm). (e-h) PL intensity mapping of WS_2 samples with 1-, 2-, 3- and 4-turn RHPAS arrays under the σ^+ (RCP) excitation at 514 nm. Apparent focusing effects can be obtained from 2- and 4-turn RHPAS arrays, in contrast to the absence of focusing effects from 1- and 3-turn RHPAS arrays. (Scale bar: 1.25 µm). (i-l) Maps of the degrees of valley polarization (DVP) taken on WS_2 with 1-, 2-, 3-, and 4-turn RHPAS arrays

under the RCP excitation. Apparently high values of DVP can be obtained at RT from WS_2 with 2- and 4-turn RHPAS arrays (Scale bar: 1.25 μm).

5.5 Electrical tuning of the DVP in the WS_2-2TRHPAS heterostructure

The neutral exciton is the ground state of a charge-neutral semiconductor, whereas trions are only formed in the presence of excess charge. Therefore, the intensity of trion emissions is generally controlled by the amount of excess charge in the semiconductor. For this reason, trion emissions are usually not observed in our CVD-grown monolayer WS_2 samples unless a back gate voltage is applied. For the gated samples, the PL spectra typically exhibit additional emissions at 30–60 meV below the neutral excitonic line, which are attributed to the emission from charged excitons (X^-). Thus, by simply varying the applied gate voltage, we can control the ratio between neutral and charged exciton emissions.

Figure 5.4(a) shows a color map of the PL spectra from a back-gated field effect device of CVD-grown monolayer WS_2 (1L-WS_2) at RT, where the color-coded PL intensity is measured as a function of the applied gate voltage (V_{Gate}) from -25 to 25 V. For a given gate voltage, there are two well-defined components associated with the emission bands of the neutral excitons (X) and the negative-charge excitons (X^-). The PL spectral evolution of these two emission bands with the gate voltage is illustrated in Figure 5.4(b). We find that the emission near 620 nm (2 eV) from neutral excitons (X) is dominant around the charge neutrality point at $V_{Gate} = 0$. For negative gate voltages ($V_{Gate} < 0$), both X and X^- features are visible, and the integrated intensity of the X^--peak gradually decreases while that of the X-peak increases when $|V_{Gate}|$ decreases. In contrast, for positive gate voltage ($V_{Gate} > 0$), the integrated intensity of the X-peak gradually decreases and the X^--peak becomes dominant with increasing V_{Gate} due to electrostatic doping, which leads to a single X^--peak profile at higher carrier densities.

Helicity resolved PL spectra of an as-grown gated WS_2 sample are shown in Figures 5.4(c) and 5.4(d) for $V_{Gate} = -2$ V and +5 V, respectively. When the WS_2 sample is negatively gated at $V_{Gate} = -2$ V, both X and X^- emissions reveal relatively low DVP of 4.2% and 5.8%, respectively. Similarly, at a positive gate voltage (V_{Gate} = 5V), both X and X^- emissions also reveal low DVP of 4.7% and 5.1%, respectively, which may be attributed to the low carrier concentrations in the sample.

The effect of gate voltage on the DVP becomes significantly different in the case of 1L-WS_2 with PAS structures. Figure 5.4(e) shows a color map of the PL spectra from a back-gated field effect device of 1L-WS_2-2TRHPAS with the back-gate voltages (V_{Gate}) from −25 to 25 V at RT. For V_{Gate} < 0 V, a strong X-peak and a tiny X^--peak features are visible, and the integrated intensity of the X-peak becomes dominant when $|V_{Gate}|$ decreases. In contrast, for $V_{Gate} > 0$, the integrated intensity of the X-peak gradually decreases and that of the X^--peak becomes dominant with increasing V_{Gate}. Figure 5.4(f) shows the spectral evolution of X and X^- emissions from the 1L-WS_2-2TRHPAS sample with the gate voltage. Additionally, polarization-resolved PL spectra of the 1L-WS_2-2TRHPAS sample under σ^+ excitations are shown in Figures 5.4(g) and 5.4(h) for V_{Gate} = 10 V and 20 V, respectively. For V_{Gate} = 0, the photon-excited excitons at the K valley are more populated under σ^+ excitations, which corresponds to the valley-polarized state in pristine WS_2 and WS_2-2TRHPAS. By increasing the electron density via increasing the gate voltage from 0 to 10 V and 20 V, the difference between the σ^+ and σ^- components of the PL spectra becomes increased, which implies increased valley polarization of the neutral excitons. Specifically, we find that the values of DVP for V_{Gate} = 0, 10 V, and 20 V are 0.4, 0.5, and 0.7, respectively, suggesting significantly enhanced valley polarization as the applied bias is detuned from the charge neutral point.

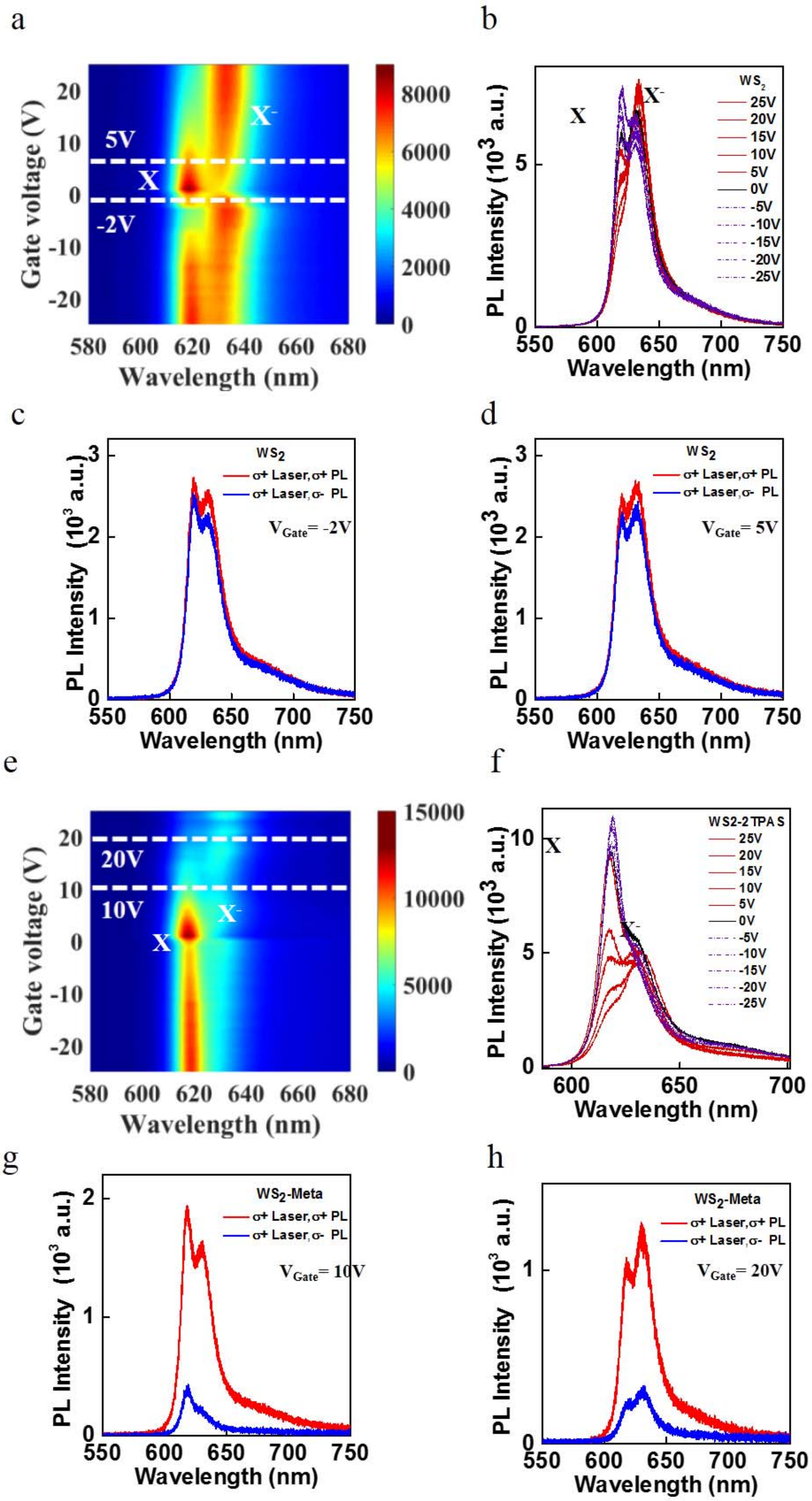
a
Gate voltage (V)
Wavelength (nm)
5V
X
-2V
X-
8000
6000
4000
2000
0
b
PL Intensity (10³ a.u.)
Wavelength (nm)
X
X-
WS2
25V
20V
15V
10V
5V
0V
-5V
-10V
-15V
-20V
-25V
c
WS2
σ+ Laser,σ+ PL
σ+ Laser,σ- PL
VGate= -2V
PL Intensity (10³ a.u.)
Wavelength (nm)
d
WS2
σ+ Laser,σ+ PL
σ+ Laser,σ- PL
VGate= 5V
PL Intensity (10³ a.u.)
Wavelength (nm)
e
Gate voltage (V)
Wavelength (nm)
20V
10V
X
X-
15000
10000
5000
0
f
WS2-2TPAS
X
X-
25V
20V
15V
10V
5V
0V
-5V
-10V
-15V
-20V
-25V
PL Intensity (10³ a.u.)
Wavelength (nm)
g
WS2-Meta
σ+ Laser,σ+ PL
σ+ Laser,σ- PL
VGate= 10V
PL Intensity (10³ a.u.)
Wavelength (nm)
h
WS2-Meta
σ+ Laser,σ+ PL
σ+ Laser,σ- PL
VGate= 20V
PL Intensity (10³ a.u.)
Wavelength (nm)

Figure 5.4. Electrical tuning of the degrees of valley polarization (DVP) in WS_2 and WS_2- RHPAS at room temperature (RT). (a) Contour plot of the PL spectra of 1L-WS_2 as a function of applied gate voltage (V_{Gate}) at RT. (b) PL spectra at RT for V_{Gate} from -25 V to 25 V, with an increment of 5 V. Polarization-resolved PL spectra under σ^+ (RCP) excitations for (c) V_{Gate} = -2 V and (d) V_{Gate} = +5 V. (e) Contour plot of the PL spectra of 1L-WS_2-2TRHPAS as a function of V_{Gate} at RT. (f) PL spectra 1L-WS_2-2TRHPAS at RT for V_{Gate} from -25 V to 25 V with an increment of 5 V. Polarization-resolved PL spectra under σ^+ (RCP) excitations for (g) V_{Gate} = 10 V and (h) V_{Gate} = 20 V.

5.6 Summary

In summary, we have demonstrated that ultra-compact plasmonic Archimedes spiral (PAS) nanostructures can efficiently tailor the valley-polarized PL of monolayer WS_2 at room temperature. The chiral-SPP focusing fields from the PAS nanostructures can significantly amplify the exciton/trion emissions in the WS_2 monolayer with specific chiral emission due to the interaction of WS_2 excitons/trions with the plasmons of the PAS nanostructures. The plasmon-exciton coupling is shown to provide control of the valley-polarized PL through manupulating the imbalance of valley population, leading to significant PL modulations through valley-dependent control of the excitonic emissions at room temperature. In particular, we have demonstrated enhancement of the degrees of valley polarization (DVP) at room temperature from 3% for the as-grown 1L-WS_2 to ~ 40% for the 1L-WS_2-2TRHPAS and 1L-WS_2-4T RHPAS heterostructures. Furthermore, by appling a back-gate bias voltage (V_{Gate}), the valley polarization is found to be further enhanced from 40% to 70% for V_{Gate} = 10 V, which implies that the carrier doping can enhance the valley polarization by screening of the momentum-dependent long-range electron-hole exchange interaction and therefore reducing the intervalley scattering. The methodology described in this chapter provides a promising platform to manipulate the valley degrees of freedom in 2H-TMDCs efficiently at room temperature, paving ways for future applications of spin-valleytronic devices based on the 2D materials.

Chapter 6

2H/1T′ PHASE-ENGINEERED SYNTHESIS OF MONOLAYER $WS_{2X}TE_{2(1-X)}$ ALLOYS FOR TWO-DIMENSIONAL METAL-SEMICONDUCTOR CONTACT IN THE SCHOTTKY-MOTT LIMIT

Ternary tellurides based on alloying different 2D transition metal dichalcogenides can result in interesting new 2D materials with tunable optical and electrical properties. Additionally, such alloys can provide opportunities for significantly improving the electrical contact properties at the metal-semiconductor interface. In particular, realization of practical devices based on the 2D materials will require overcoming the typical Fermi-level pinning limitations of the electrical contacts at the metal-semiconductor interface and ultimately approaching the ideal Schottky-Mott limit. In this work, we develop a simple method of stacking 3D/2D electrical metal contacts onto dangling-bond-free 2D semiconductors in order to surmount the typical issue of Fermi-level pinning. Specifically, contacts of Au, graphene/Au, and WTe_2/Au are transferred onto $WS_{1.94}Te_{0.06}$ alloy-based devices via a new transfer method. The $WS_{1.94}Te_{0.06}$ field-effect transistors (FETs) with WTe_2/Au contacts reveal a field-effect mobility of 25 $cm^2V^{-1}s^{-1}$, an on/off current ratio of 10^6, and extremely low contact resistance of 8 kΩ μm. These electrical properties are far more superior to similar devices with either Au or graphene/Au contacts, which may be attributed to the fact that the work function of WTe_2 is close to the band edge of the $WS_{1.94}Te_{0.06}$ alloy so that the resulting metal-semiconductor interface of the FETs are free from Fermi-level pinning. The Schottky barrier heights of the $WS_{1.94}Te_{0.06}$-FETs with WTe_2/Au contacts also follow the general trend of the Schottky-Mott limit, implying high-quality electrical contacts.

6.1 Introduction

The electrical[225,226] and optical properties[19,227–229] of two-dimensional (2D) transitional metal dichalcogenides (TMDCs) are generally different from those of their bulk counterparts. Their potential applications in various devices[230–234], such as the field-effect transistors (FETs)[37,235,2362], memory devices[37], optical device, and multifunctional sensors[238], have been demonstrated. The electrical contacts to the TMDCs are crucial to the operation and performance of all the devices, and the metal-semiconductor interfaces[38,239,240] associated with these contacts are characterized by the Schottky barrier[240,241]. Ideally, the Schottky barrier height (SBH) can be predicted by the Schottky-Mott rule based on using a metal electrode with a work function close to the conduction band or the valance band of the TMDC material. However, this approach has not been successful because the actual SBH formed by a metal in contact with a TMDC tends to deviate from the theoretical Schottky-Mott rule. The deviation of the effective Fermi level at a metal and a semiconductor contact has been attributed to the Fermi-level pinning[242–247] or metal-induced gap states. Since the transfer characteristics of TMDC-based FETs are controlled by the Schottky barrier[246,248,249], a method to reliably control the SBH is required to reduce the contact resistance and improve the devices performance.

To date, several approaches to reduce contact resistance of TMDC-based FETs have been reported, including the use of a low work function metal for the electrical contact[247,250], the use of a Fermi-level de-pinning layer[251,252], and molecule/chemical doping techniques[253–258] of TMDCs. The latter strategy generally leads to unstable TMDCs in ambient environment and doping of the entire TMDC channel, which leads to a reduced on/off current ratio because of a large leakage current.

Heterostructures that consist of a 2D van der Waals (vdW) metal as the top contact material on 2D semiconductor is another approach[241,259–261] to lower the SBH and contact resistance. In this context, a natural material for consideration is graphene[262]. However, deposition of another metallic layer on graphene is required for electrical characterizations, and the carrier injection efficiency generally varies, depending on the metal deposited. Alternatively, the metallic 1T′-phase WTe_2 with a low workfunction (WF)[240] and a vdW clean surface[263] may be an efficient electron-type (n-type) contact material for 2D semiconductors. However, there have not been extensive studies to date on using the 1T′-phase WTe_2 as the metal contact to lower the contact resistance of TMDC-based devices due to the challenges of material preparation and material stability[264–267].

In this study, ternary $WTe_{2x}S_{2(1-x)}$ ($0 \leq x \leq 1$) alloys are synthesized via chemical vapor deposition (CVD) in a one-step synthesis process to produce high quality 2D semiconductors with tunable bandgaps for high-performance eletronic devices. By alloying Te into tungsten disulfide WS_2, the work function of the ternary $WTe_{2x}S_{2(1-x)}$ ($0 \leq x \leq 1$) alloy can be tuned to match the work function of the 3D/2D contacts as the source (S) /drain (D) electrodes in the FET structure to reduce the SBH. The ternary $WTe_{2x}S_{2(1-x)}$ ($0 \leq x \leq 1$) alloy exhibits distinguishable semiconducting 2H and metallic 1T′ phases. X-ray photonelectron spectrascopic (XPS) characterizations confirm the existence of W, S, and Te with controlled ratios. The optical bandgap of the $WTe_{2x}S_{2(1-x)}$ alloy can be tuned from 2 eV to 1.75 eV (2H semiconductors) and then dropped down to 0 eV (1T′ metal). A new fabrication process of stacking 3D/2D metallic contact onto dangling-bond-free 2D semiconductors without direct chemical bonding is developed, which prevents the formation of chemical disorder and defect-induced gap states, thereby overcoming the typical Fermi-level pinning limitations and leading to an interface approaching the ideal physical model. Combining the ternary $WTe_{2x}S_{2(1-x)}$ ($0 \leq x \leq 1$) alloy materials with the new transfer process for electrical contacts, the FET devices based on monolayer $WTe_{2x}S_{2(1-x)}$ alloys reveal characteristics that confirm the 2H phase being n-type semiconductors and the 1T′ phase being a metal. Moreover, the use of WTe_2 metallic contacts with a workfunction close to the band edge of the $WTe_{0.06}S_{1.94}$ alloy has resulted in $WTe_{2x}S_{2(1-x)}$-based FETs with excellent electronic characteristics, including high electron carrier mobility up to 25 $cm^2V^{-1}S^{-1}$, on/off current ratio up to 10^6, and extremly low contact resistance down to 8 kΩ μm. This bandgap engineering of 2D TMDC alloys combined with the metal transfer method thus promises new oppotunities for probing the fundamental physical properties of the 2D materials, such as new types of Wyle semimetals and the spin Hall effect, as well as for diverse applications in nanoelectronics and optoelectronics based on the 2D materials.

6.2 Characterizations of $WS_{2x}Te_{2(1-x)}$ ($0 \leq x \leq 1$) alloy

X-ray photonelectron spectroscopy (XPS) was conducted to examined the chemical composition and valence states of the synthesized $WTe_{2x}S_{2(1-x)}$ ($0 \leq x \leq 1$) alloys. The core level spectra were calibrated via fitting adventitious carbon at 284.8 eV. The high-resolution spectra of W 4f, S 2p, and Te 3d peaks are shown in Figure 6.1a – c. For 2H-phase WS_2, the corresponding binding energies of the W 4f $_{7/2}$ and W 4f $_{5/2}$ peaks are located at 33.2 and 35.3 eV, respectively, and the binding energies for the S $2p_{3/2}$ and S $2p_{1/2}$ peaks are located at 162.9 and 164.2 eV, respectively, which are all consisted with previously reported values[268]. By tuning the mass ratios of Te and S powder from 1 to 100 with specific H_2 flow rates from 40 to 60 sccm during the synthesis process, W-Te bonds at 573.8 eV (Te 3d 5/2) and 584.1 eV (Te 3d 3/2) appeared in the spectra, which provided direct evidence of Te doping into the original WS_2 crystal lattice. The binding energy of W 4f and S 2p peaks displayed a downshifts around 0.4 eV in the alloy with x = 13%, indicated that Te doping resulted in reduced electronegativity[266,269]. When the phase transformation occured at higher stoichiometric ratio ($x > 0.5$), the binding energies of W 4f, S 2p, and Te 3d shifted to lower energy states concurrently. For 1T′ phase WTe_2, the main W 4f peaks at 31.28 eV (4f 7/2) and 33.44 eV(4f 5/2) are asigned to the W-Te bond and the Te 3d peaks are located at 572.6 (3d 5/2) and 583 eV (3d 3/2)[270]. The chemical stochiomitry information mentioned above directly indicated that the mole fraction of Te and structure information between 2H and 1T′ phase can be tuned by changing the mass ratio of Te and S powder with specific H_2 concentrations which are described in Appendix C.

The optical properties of the as-grown $WTe_{2x}S_{2(1-x)}$ alloys were investigated by Raman and PL spectra. In Figure 6.1d, Raman spectra of the $WTe_{2x}S_{2(1-x)}$ alloys with various Te concentrations were collected to examine the composition-dependent lattice vibration modes. For monolayer 2H-phase WS_2, the two characteristic peaks E_{2g}^{1} and A_{1g} were located at 351 cm^{-1} and 419 cm^{-1}, respectively, in agreement with previous reports. In the 2H-phase alloys, it was evident that the Raman footprints changed in alloys with increasing Te concentration compared to the pure WS_2, where the characteristic peaks become weak and come with the appearance of the additional WTe_2

peaks around 163 cm^{-1} and 213 cm^{-1}. The positions of the two WS_2 vibration modes were softened and redshifted with the increase of Te concentration, which may be attributed to the effect of heavier Te atoms on decreasing the vibrational frequencies. In comparison with pure 1T′-WTe_2 with main A_1 modes[271] at 120, 132, 162, and 213 cm^{-1}, the observed new peaks around 195, 225, 290, and 400 cm^{-1} in Figure 6.1(d) were similar to the 2H-pase and 1T′-phase WS_2-like peaks reported previously[272–276].

In addition to the Raman spectra, photonluminescense (PL) measurements were performed on the obtained alloys to investigate the composition-dependent bandgap evolution and phase transition (Figure 6.1(e)). The bandgap of the $WTe_{2x}S_{2(1\text{-}x)}$ alloys can be tuned from 2 eV (for pure 2H-WS_2) to zero bandgap (for pure 1T′-WTe_2) as the concentration of Te increases, and 2H to 1T′ phase transition exists at an intermediate Te concerntration in the $WTe_{2x}S_{2(1\text{-}x)}$ alloys. For 1T′ ternary tellurides, no PL signal was detected because of the metallic nature. Notably, within the 2H phase, the correlation between the optical bandgap and the Te concentration is approximately linear to each other. The Te concentration x is ranging between 2 eV (WS_2 alloy, $x = 0$) and 1.75 eV ($WTe_{2x}S_{2(1\text{-}x)}$ alloy, $x = 0.35$), as presented in the inset of Figure 1(e). Additionally, the composition-dependent bandgap of the as-grown alloys is in good agreement with the quadratic rule reported by Kang *et al*[277].

$$E_g(WTe_{2x}S_{2(1-x)}) = xE_g(WTe_2) + (1-x)E_g(WS_2) - bx(1-x) \tag{1}$$

where the parameter b for $WTe_{2x}S_{2(1\text{-}x)}$ alloy is equal to x and the bandgap of 1H phase WTe_2 is 1.03eV from the literature[182,278,279]. This estabilished correlation provides a fast and efficient way to determine the chemical composition of the $WTe_{2x}S_{2(1\text{-}x)}$ alloy. The A-exciton PL peak of different $WTe_{2x}S_{2(1\text{-}x)}$ alloys , which result from direct-gap recombination at the K/K′ points in the Brillouin zone exhibits an approximately 250 meV redshift when doped with ≈35% Te. We also fitted the PL spectra of pure WS_2 and 2H-phase $WTe_{2x}S_{2(1\text{-}x)}$ alloy ($x< 0.5$) to deconvolute (Supporting Information, Figure 6.2 the A exciton and trion contributions. The optimal line shape for the spectral contributions is a mixed Gaussian–Lorentzian function as shown in Figure 6.2. As shown in Figure 6.1(f), the A-exciton and trion peaks of $WTe_{2x}S_{2(1\text{-}x)}$ alloy ($x< 0.5$) are redshifted. The electron concentration in WS_2 will therefore be reduced due to Te doping (since Te is a p-type dopant) and as a consequence, the trion contribution to the PL signature is significantly reduced. The comparison between X-ray photoelectron spectroscopy (XPS) of the pristine (undoped) WS_2

and 2H-phase $WTe_{2x}S_{2(1-x)}$ alloys (x< 0.5) confirmed that the Te substitutional sites act as p-type dopants. The Fermi level of the $WTe_{2x}S_{2(1-x)}$ alloys (x< 0.5) shifted closer to valence band, as compared with the undoped WS_2, which is illustrated by the downshifting of the binding energies of W 4f and S 2p in Figure 6.1 (a) and (b). This lowering of the Fermi level indicates that Te in-situ doping process introduce p-type doping in the WS_2 sheet, which is explained by the fact that Te possesses one less valence electron as compared to W. As shown in the Figure 6.1(f) and Figure 6.3, the Te in-situ doping process cannot only tune the bandgap of the 2H-phase $WTe_{2x}S_{2(1-x)}$ alloys (x < 0.5), but also can tune the work function of the 2H-phase $WTe_{2x}S_{2(1-x)}$ alloys. The work function can be tuned ranging from 4.4 eV ($WTe_{0.06}S_{1.94}$ alloy, x = 0.3) and 4.9 eV ($WTe_{0.7}S_{1.3}$ alloy, x = 0.35).

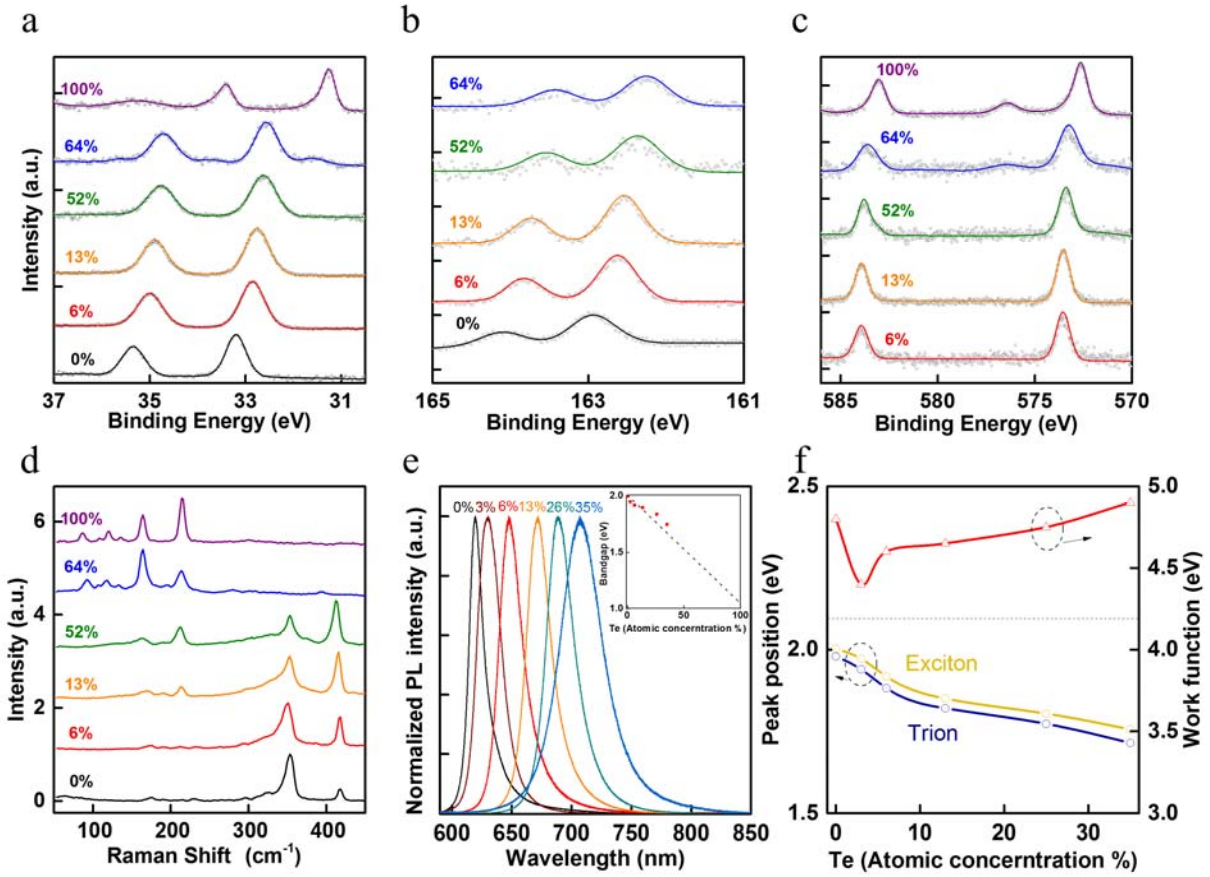

Figure 6.1. XPS spectra of monolayer $WTe_{2x}S_{2(1-x)}$ alloys with x = 0, 0.06, 0.13, 0.52, 0.64, and 1, respectively. (a) XPS W 4f spectra, (b) XPS S 2p spectra, and (c) XPS Te 3d spectra. (d)

Corresponding Raman spectra of the alloys. (e) PL spectra of monolayer $\mathrm{WTe}_{2x}\mathrm{S}_{2(1-x)}$ alloys with $x = 0$, 0.03, 0.06, 0.13, 0.26, and 0.35, respectively. The inset is the corresponding composition-dependent (x) bandgap of the $\mathrm{WTe}_{2x}\mathrm{S}_{2(1-x)}$ alloys, as determined by XPS, where the atomic concentration of Te is given by (x). (f) The peak position of A-exciton and trion, and corresponding work function of monolayer $\mathrm{WTe}_{2x}\mathrm{S}_{2(1-x)}$ alloys with $x = 0$, 0.06, 0.13, 0.52, 0.64, and 1, respectively.

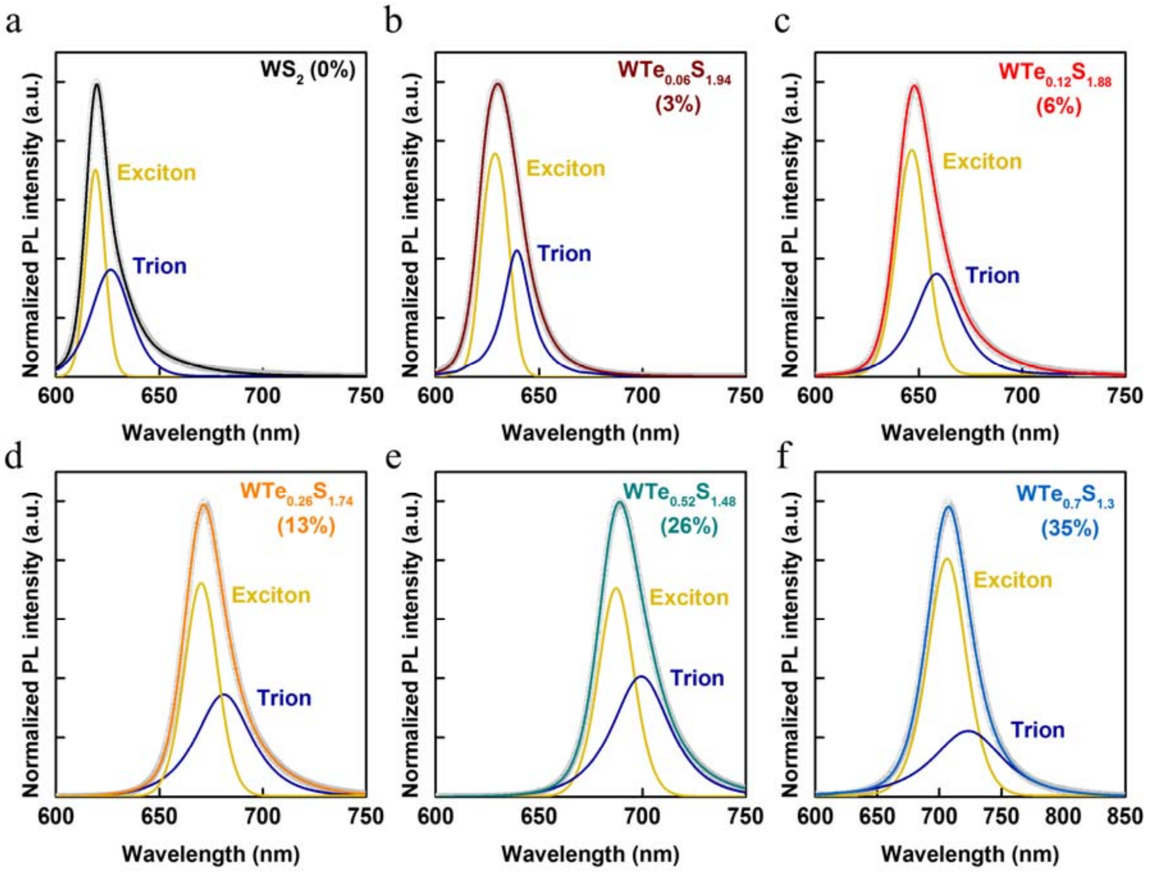

Figure 6.2. Gaussian−Lorentzian Fitting of the PL spectra of monolayer $\mathrm{WTe}_{2x}\mathrm{S}_{2(1-x)}$ alloys with $x = 0$, 0.06, 0.13, 0.52, 0.64, and 1, respectively. (a) WS_2, (b) $\mathrm{WTe}_{0.06}\mathrm{S}_{1.94}$, (c) $\mathrm{WTe}_{0.12}\mathrm{S}_{1.88}$, (d) $\mathrm{WTe}_{0.26}\mathrm{S}_{1.74}$, (e) $\mathrm{WTe}_{0.52}\mathrm{S}_{1.48}$, (f) $\mathrm{WTe}_{0.7}\mathrm{S}_{1.3}$. Two components, the A-exciton (yellow line), and trion (navy line), were obtained by Gaussian−Lorentzian fitting.

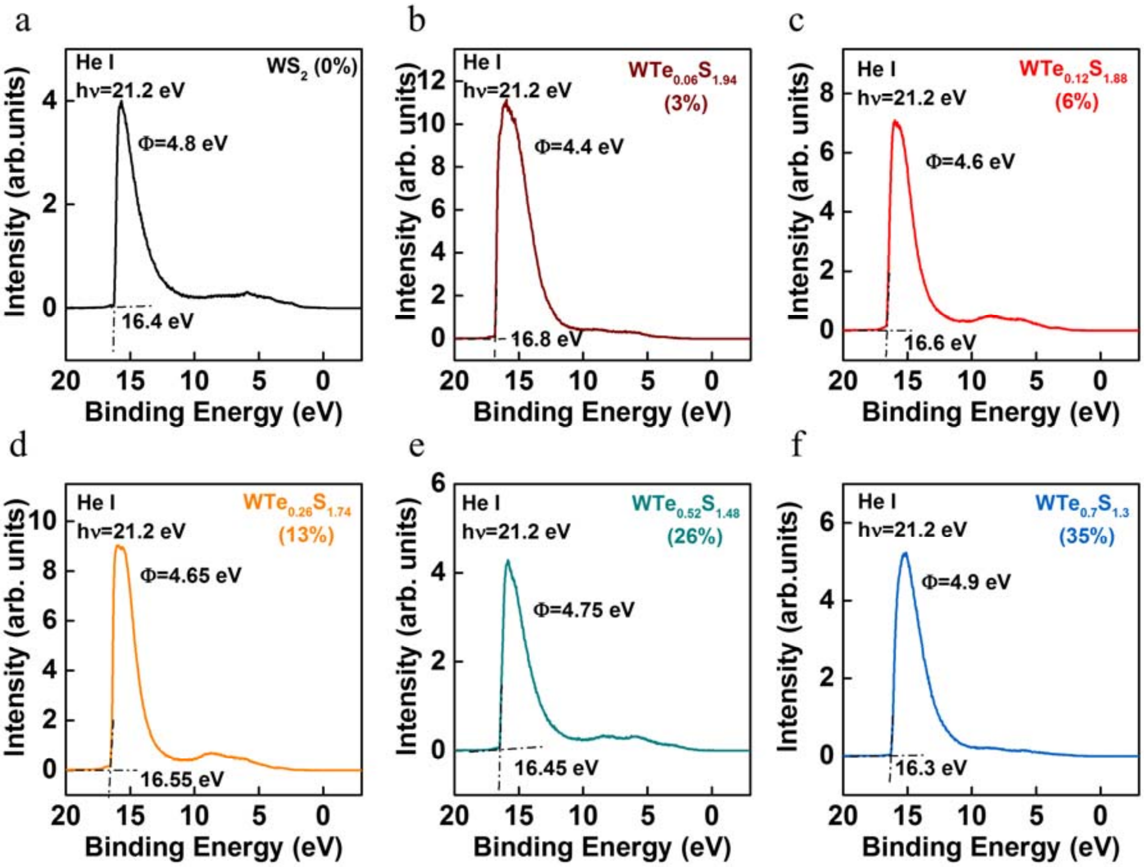

Figure 6.3. The work function of monolayer $WTe_{2x}S_{2(1-x)}$ alloys with $x = 0$, 0.06, 0.13, 0.52, 0.64, and 1, respectively. (a) WS_2, (b) $WTe_{0.06}S_{1.94}$, (c) $WTe_{0.12}S_{1.88}$, (d) $WTe_{0.26}S_{1.74}$, (e) $WTe_{0.52}S_{1.48}$, (f) $WTe_{0.7}S_{1.3}$.

6.3 A simple metal electrodes transferred method

The semiconducting electronic devices are based on the control of the flow of charge carriers into semiconductors. The contact between the metal electrode and the semiconducting channel directly affects the carrier injection. Therefore, it is crucial to optimize the electrical contact to improve the device performance of TMDCs. At the metal electrode/ TMDC interface, the large bandgap of TMDCs leads to a Schottky barrier (SB) and the van der Waal (vdW) gap without chemical bonds, which induces high contact resistance for the as-fabricated devices. Furthermore, an SB may still exist with a contact metal of a maching WF due to the Fermi-level pinning effect. Therefore, it is important to develop a feasible way to eliminate the vdW gap, de-pin the Fermi-level of the metal, and facilitate the charge transport at the contact. In order to overcome the Fermi-level pinning and led to an interface approaching the ideal Schottky-Mott limit, a simple transferred method is required. The fabrication process of $WTe_{2x}S_{2(1-x)}$-based FETs with Au contacts is schematically illustrated in Figure 6.4. First, the 300 nm oxide layer of 4-inch SiO_2/Si wafers was functionalized with an OH group using the following squence. The SiO_2/Si wafers were dipped into 80 °C piranha solution ($H_2SO_4 : H_2O_2 = 3:1$) for 2 hrs to render the surface of the substrates hydrophilic, which were subsequently washed with deionized water and dried with nitrogen gas. Next, the SiO_2/Si wafers were cleaned with O_2 plasma (300 mTorr, 10 sccm, and 100 W) for 10 min. Finally, the wafers were soaked in 60 °C H_2O_2 solution for 60 min to make the substrate superhydrophilic on the surface. This functionalized surface of SiO_2/Si were shown in Figure 6.4b, which was used for the growth of $WTe_{2x}S_{2(1-x)}$ alloys and for metal electrodes. The gold electrodes were patterned by conventional e-beam lithography. The patterned gold electrodes on the SiO_2/Si wafer was then spin coated with a PS or PMMA layer (Figure 6.4(d)) followed by slow immersion into deionized (DI) water for the transfer (Figure 6.4(e)). Water penetrated instantly through PS/Au or PMMA/Au stack. The growth substrate with higher surface energies compared to the polymer/Au stack led to easy delamination and suspension of the polymer/Au stack on the surface of the water. Thus, a polymer-supported wafer-scale Au electrode could be achieved, which was subsequently transferred onto the $WTe_{2x}S_{2(1-x)}$ alloy (Figures 6.4(f) and (g)). Using cross-sectional analysis by transmission electron microscopy (TEM), we examined the interface between the transferred Au and the $WTe_{2x}S_{2(1-x)}$ (Figure 6.4(h)), and found that in contrast to depositing Au via electron-beam evaporation, transferring Au does not damage the intrinsically passivated $WTe_{2x}S_{2(1-x)}$ layers, as evidenced by the columns of atoms visible in the TEM image.

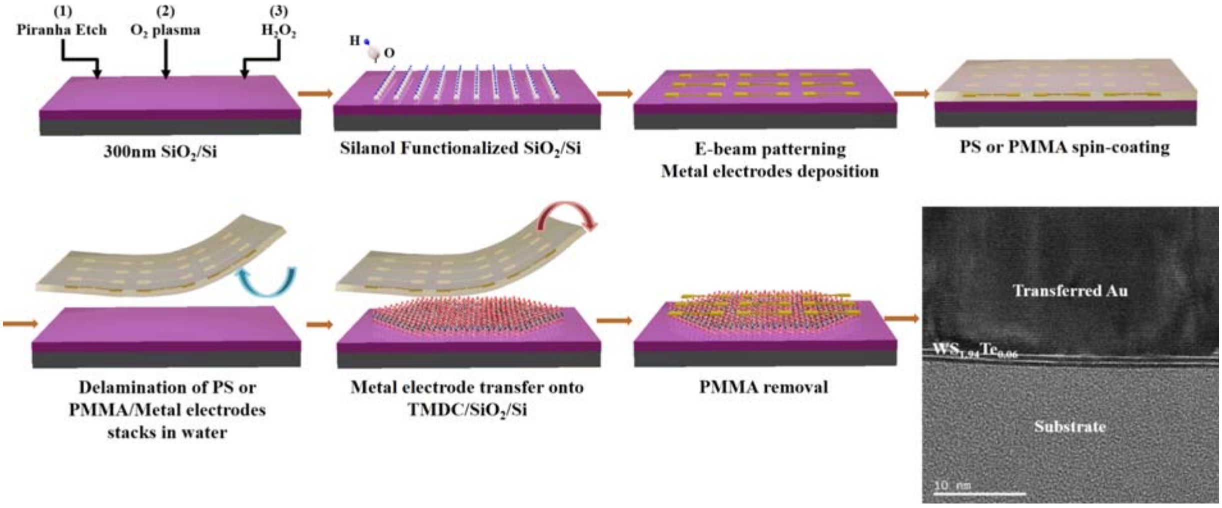

Figure 6.4. Schematics of the surface-functionalized water-assisted wafer metal electrodes transfer process onto the TMDCs: (a) Schematic of the SiO_2/Si substrated. (b) Silanol-functionalized 300 nm SiO_2/Si substrated by piranha solution, O_2 plasma, and H_2O_2 treatments. (c) Patterning Au electrodes. (d) Spin coating of PS or PMMA on a Au/ SiO_2/Si stacks. (e) Delamination of wafer-scale PS/Au or PMMA/Au in water. (f). Transfer of PS/Au or PMMA/Au on a $WS_{2x}Te_{2(1-x)}$ / SiO_2/ Si substrate. (g) Metal electrodes on $WS_{2x}Te_{2(1-x)}$ / SiO_2/ Si substrate. (h) Cross-sectional image of metal-semiconductor interface captured by transmission electron microscopy (TEM).

6.4 Electrical properties of $WS_{2x}Te_{2(1-x)}$ alloys

The electrical performance of the as-grown $WTe_{2x}S_{2(1-x)}$ alloys was investigated by studying the back-gated field-effect transistors (FETs) made of the $WTe_{2x}S_{2(1-x)}$ alloys. The transfer charecteristic curve of six devices are presented in Figure 6.5. In Figure 6.5(a)-(c), all three semiconducting 2H phase alloys (x = 0, 0.06 and 0.13) show typical n-type transport behavior with high on/off (> 10^5). The field-effect mobility can be calculated by[280,281]

$$\mu_{FE} = \frac{L}{WV_{ds}C_g}\frac{dI_{ds}}{dV_{gs}} \tag{2}$$

where I_{ds} is the source-drain current; V_{gs} is the gate-source voltage; V_{ds} is the drain-source voltage; L is the channel length; W is the channel width; and C_g is the gate capacitance. The calculated mobility of 2H-phase alloys for x = 0, 0.06 and 0.13 are 0.25 $cm^2V^{-1}S^{-1}$, 0.36 $cm^2V^{-1}S^{-1}$, and 0.012 $cm^2V^{-1}S^{-1}$, respectively. The mobility of all $WTe_{2x}S_{2(1-x)}$ can be improved by further minimizing the contact resistance. Additionally, the threshold gate voltage at higher Te composition is significantly upshifted, indicating a p-type doping effect originating from the Te substitution and different valance band (VB) and conduction band (CB) positions for $WTe_{2x}S_{2(1-x)}$ alloys with different Te components. For 1T′-phase alloys, it has been noticed that the drain current is decreased around 50 times of magnitude for $WTe_{1.04}S_{0.96}$ compared with pure WTe_2, which indicated that the metallic behavior of tellurides could be modified by controlling the alloying S atoms. Furthermore, no drain current dependent features were found on the back-gated voltage in three semimetallic 1T′ phase alloys (x = 0.52, 0.64 and 1) presented in Figure 6.5(d)-(f).

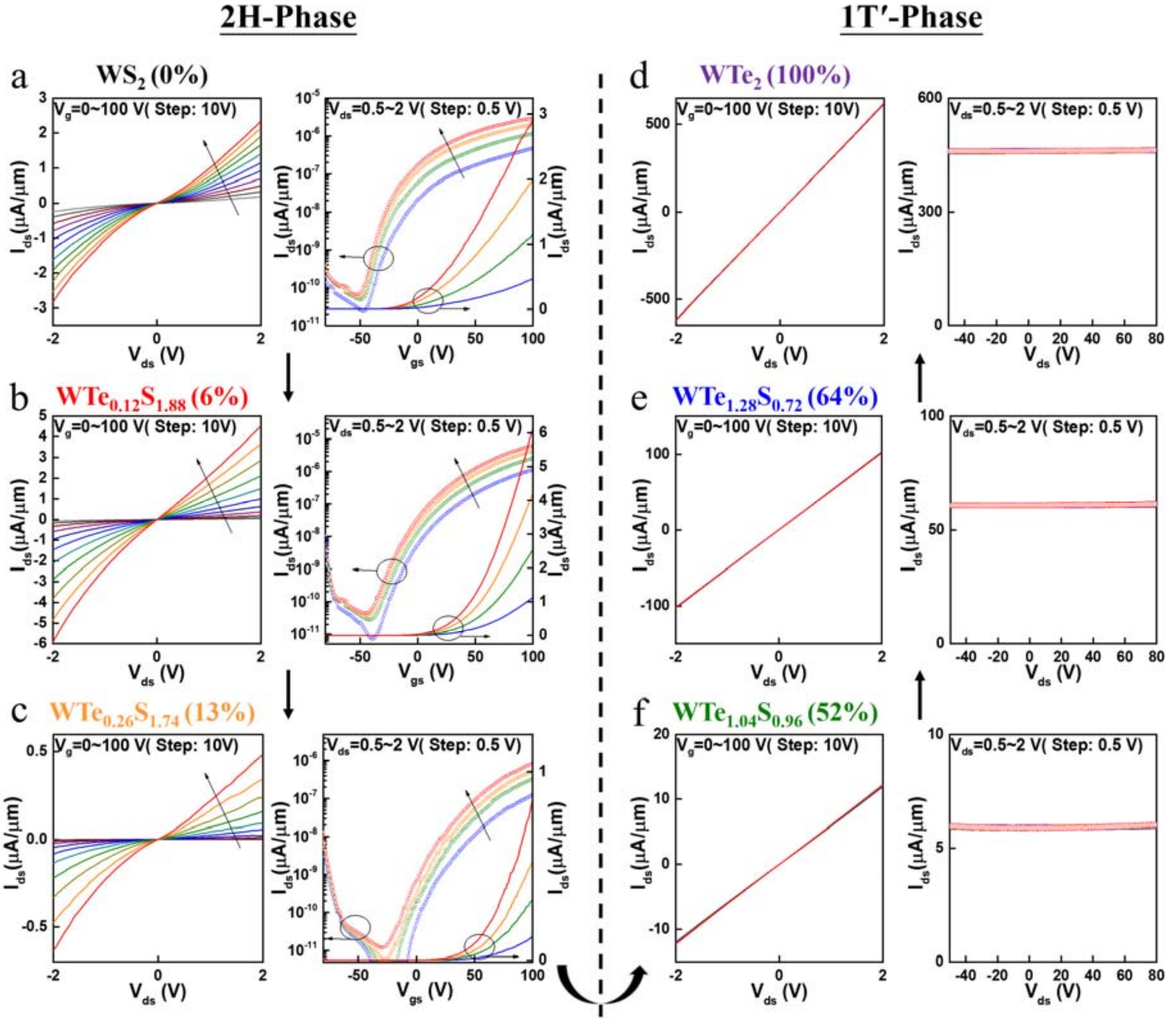

Figure 6.5. The electrical properties of fabricated 2H-phase $WTe_{2x}S_{2(1-x)}$ alloys (x = 0, 0.06, 0.13) and 1T′-phase $WTe_{2x}S_{2(1-x)}$ alloys (x = 0.52, 0.64, 1). Gating response (I_{ds}-V_{gs}) with different source-drain voltages from 0.5V to 2V and the current-voltage (I_{ds}-V_{ds}) curve with different bottom gate voltage of (a) 2H-WS_2, (b) 2H-W $Te_{0.12}S_{1.88}$, (c) 2H-W $Te_{0.26}S_{1.74}$, (d) 1T′-WTe_2, (e) 1T′- W $Te_{1.04}S_{0.96}$, (f) 1T′- W $Te_{1.28}S_{0.72}$.

6.4 Monolayer $WS_{2x}Te_{2(1-x)}$ alloys FETs with graphene, Au, and WTe_2 contacts

Currently, there are two methods to eliminate the Fermi-level pinning effects. One is to strengthen the hybridization and doping the underlying TMDCs. The other method is to weaken the hybridization by inserting graphene to greatly reduce the contact resistance and SBH. Heterostructures that consist of a 2D van der Waals (vdW) semi-metal, such as graphene, as the top contact material on 2D semiconductors is common approach to lower the SBH and contact resistance. However, deposition of another metallic layer on graphene is required for electrical characterizations, and the carrier injection efficiency generally varies, depending on the metal deposited. Alternatively, the metallic 1T′-phase WTe_2 with a low workfunction (WF) and a vdW clean surface may be an efficient electron-type (n-type) contact material for 2D semiconductors. To date, there have not been extensive studies on using the 1T′-phase WTe_2 as the metal contact to lower the contact resistance of TMDC-based devices due to the challenges of material preparation and material stability. It is well known that Te-based monolayers are unstable in ambient conditions, so we use multilayer WTe_2 as the electrodes for the $WTe_{2x}S_{2(1-x)}$ alloy-based FET devices. The stability test of multilayer WTe_2 are shown in Appendix E which can survive for one month.

Here, as shown in Figure 6.6, we investigated Au (work function ≈ 5.2eV), graphene (work function ≈ 4.85eV)/Au, and 1T′-WTe_2 (work function ≈ 4.5eV)/Au as the source(S)/drain(D) electrodes transferred onto the 2H-$WTe_{0.06}S_{1.94}$ crystal. The work function of each electrode was measured by the ultraviolet photoelectron spectroscopy (UPS) and shown in Figure 6.7. The calculated mobility and the on/off current ratio of 2H-W $Te_{0.06}S_{1.94}$ crystal for graphene, Au, and WTe_2 electrodes are 5 $cm^2V^{-1}S^{-1}$ and 3×10^6, 10 $cm^2V^{-1}S^{-1}$ and 5×10^5, and 25 $cm^2V^{-1}S^{-1}$ and 1.1×10^6, respectively. We found substantially more efficient gate tunability in the 1T′-WTe_2 contact FET. That is, a smaller threshold voltage $V_{g,th}$ of 18 V (compared with 45 V for graphene contacts and 50 V for Au contacts) and higher on-current of ~50 μA/μm (compared with ~10 μA/μm for graphene contacts and ~30 μA/μm for Au contacts). These findings imply that the types of electrical contacts can substantially modify the FET characteristics.

According to the Schottky-Mott rule, SBH for the electron (ϕ_n) is given by the difference between the work function of the metal (ϕ_M) and the electron affinity (χ_s) of the semiconductor.

$$\phi_n = \phi_M - \chi_s \tag{3}$$

However, interface states formed between the metal and the semiconductor can result in the SBH deviating from the value given by Equation (3) and leading to the Fermi-level pinning. Therefore, a realistic electron SBH is characterized by the pinning factor (*S*) and the charge neutrality level ($CNL; \phi_{CNL}$)[282].

$$\phi_n = S(\phi_M - \phi_{CNL}) + (\phi_{CNL} - \chi_s) = S\phi_M + b \tag{4}$$

The *S* value was defined as the slop $S = d\phi_n / d\phi_M$, which varied from *S* = 1 for an unpinned interface to *S* = 0 for a strong pinned interface. From Equation (4), the *CNL* could be estimated using the following relation:

.

$$\phi_{CNL} = \frac{\chi_s + b}{1 - S} \tag{5}$$

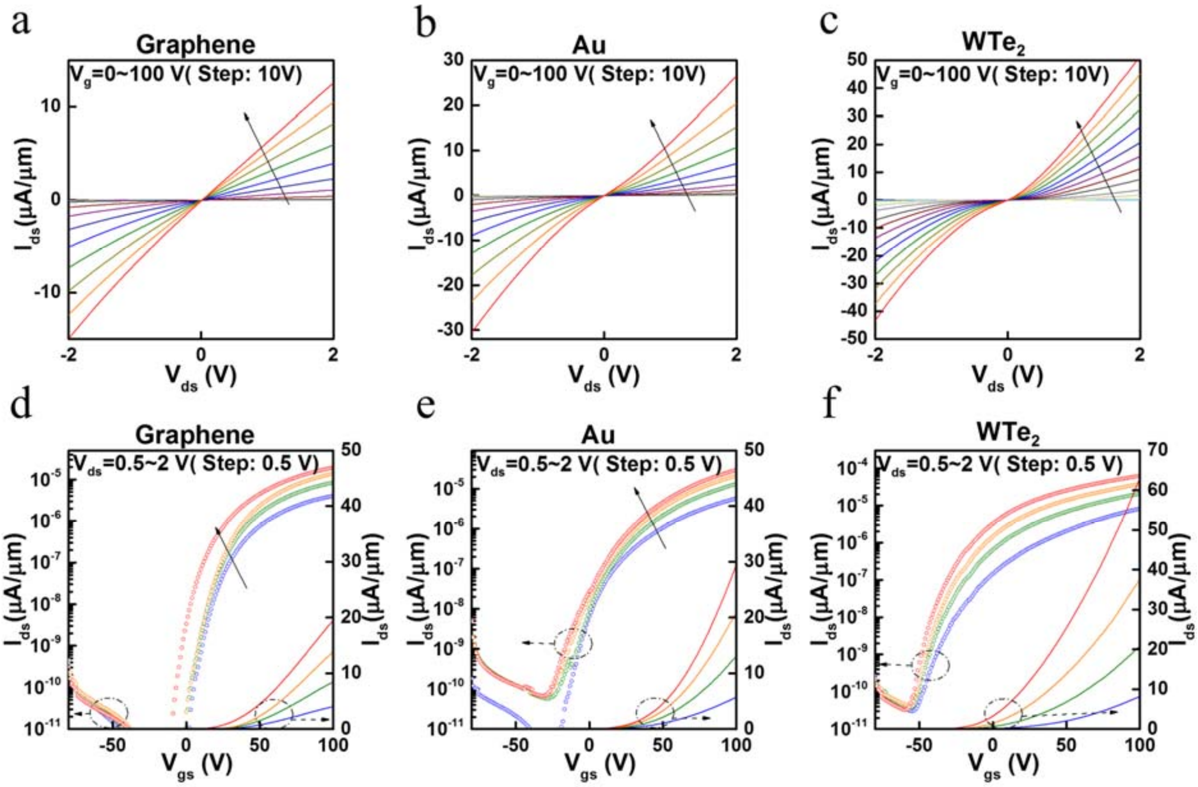

Figure 6.6. Output characteristic curves (I_{ds}-V_{ds}) of monolayer $WS_{1.94}Te_{0.06}$ alloy with (a) graphene, (b) Au, (c) WTe_2 contacts-FET as a function of the back-gate voltage ranging from 0 to 100 V in steps of 10 V. Transfer characteristic curves (I_{ds}-V_{gs}) of monolayer $WS_{1.94}Te_{0.06}$ alloy with (d) graphene, (e) Au, (f) WTe_2 contacts-FET as a function of source-drain voltage from 0.5 V to 2 V in steps of 0.5 V.

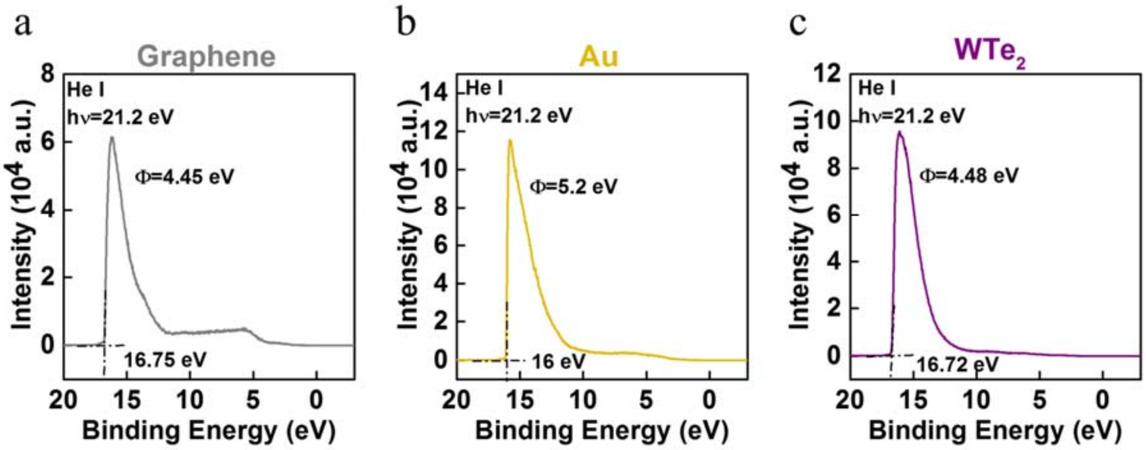

Figure 6.7. The work function of FET electrical contacts (a) Graphene. (b) Au. (c) WTe_2.

To quantitatively investigate the Schottky barrier height (SBH), the output characteristics were measured at different temperatures (200-300 K) and presented in Figure 6.8. The SBH can be extracted using the following thermionic emission model:

$$\ln(\frac{I_0}{T^2}) = \ln(AA^*) - \frac{q\phi_n}{k_B T} \qquad (6)$$

where A is the junction area and the effective Richardson-Boltzmann constant $A^* = 4\pi q m^* k_B{}^2 / h^3$, where m^* is the effective mass of $WTe_{0.06}S_{1.94}$, h is the Plank's constant, and I_0 is obtained from the I_{ds}-V_{ds} measured at different temperature and gate voltage. We obtained ϕ_n at the three contacts/ $WTe_{0.06}S_{1.94}$ interfaces from the slope of the linear fit to $\ln(I_0 / T^2)$ as a function of $q / k_B T$ (Figures 6.8(a)-(c)). In Figure 6.8(d), the effective SBH were extracted under the flat band gate voltage condition, which corresponded to the start of derivations from the linear region. The effective SBH with graphene contacts was ≈ 87 meV, which was lower than that of

Au contacts (≈ 180 meV). Such a reduced SBH might be attributed to the lower work function of graphene, which led to efficient electron charge transfer from graphene to $WTe_{0.06}S_{1.94}$alloy, and the electrical properties (field-effect mobility and on/off current ratio) were significantly improved consequently. In the case of WTe_2 electrodes, the value of the SBH was comparable to the theoretically calculated SBH of $WTe_{0.06}S_{1.94}$ alloy FETs with WTe_2 contact. This finding revealed that WTe_2 electrical contacts improved the electron charge injection to $W Te_{0.06}S_{1.94}$ alloy efficiently. Moreover, the influence of three different electrodes on the contact resistance was investigated. The series resistance between source and drain (R_{sd}), including the contact resistance, was obtained from the ratio between two I_{ds}-V_{gs} curves measured at different drain bias. The R_{sd} value could be extracted with an assumption that the contact resistance is not affected by the drain bias. Figures 5(e)-(g) show the total resistance ($R_T = V_{ds}/I_{ds}$) as a gate overdrive for the two drain bias (V_{ds} = 0.3 V and 0.5 V) and R_{sd} for the $WS_{1.94}Te_{0.06}$ alloy FET with graphene (Figure 6.8(e)), Au (Figure 6.8(f)), and WTe_2 (Figure 6.8(g)) S-D electrodes, respectively. Since, R_T of $WTe_{0.06}S_{1.94}$ alloy FET is the sum of the channel resistance and series resistance ($R_T = R_{sd} + R_{Channel}$), the R_{sd} can be extracted using two different channel resistance values at a high overdrive bias. The detailed explanation of the method used to calculated the series resistance was shown in the Appendix D. The inset figures in Figures 6.8e-g show the extrapolation curves for extracting the contact resistance at a high gate-overdrive condition ($1/(V_{gs}-T_{th}) \sim 0\ V^{-1}$) by fitting the R_{sd}-$1/(V_{gs}-T_{th})$ curve.

The extrapolated R_{sd} values were approximately 110 kΩ for graphene electrods, 80 kΩ for Au electrodes, and 17 kΩ for WTe_2 electrodes. The contact resistance (R_c) would be roughly equal to a half of R_{sd}, and so R_c was significantly reduced from ~ 55 kΩ µm for graphene electrodes to ~ 8.5 kΩ µm for WTe_2 electrodes. This result is very encouraging because a more than 5 times of magnitude reduction in the contact resistance was achieved without any doping or depinning layer. Considering that the contact resistance is exponentially proportional to the Schottky barrier height, this reduction in contact resistance is attributed to the lowering of the SBH. We further note that previous reports have demonstrated that the field-effect mobility can be improved by inserting the h-BN tunneling layer at the contact because of the lowering of the SBH, which implies that the contact properties play an important role in determining the field-effect mobilty in FETs. Figure 6.8(h) summarizes the relation between the SBH (at VFB) of the three different electrodes and the work function (WF). It can be seen from Figure 6.8(h) that the SBH depends weakly on the WFs of conventional 3D metal-Au ($S = 0.2$), but that the SBH for WTe_2 is in the Schottky-Mott limit ($S = 1$). Notably, the SBH, WF, and R_c values of the WTe_2 contacts used in this study reveal promising merits as an n-type electrical contact for ultrathin 2D electronics.

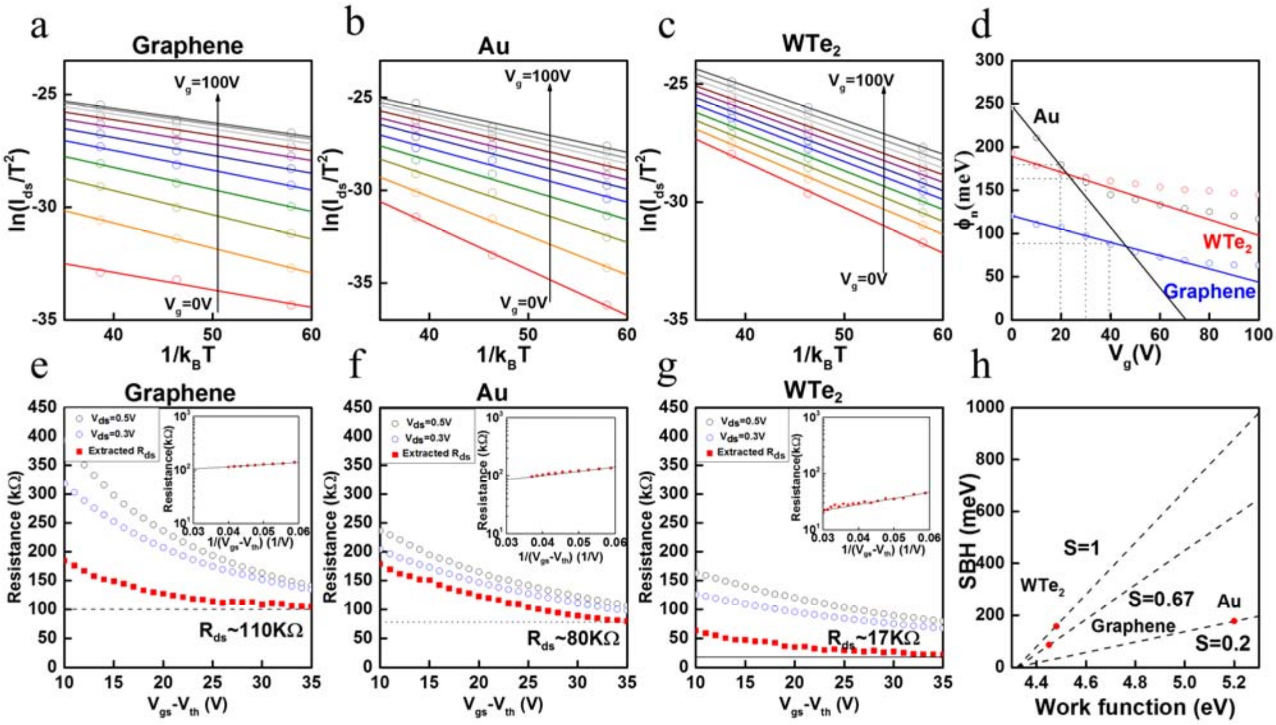

Figure 6.8. Gate-voltage-dependent $\ln(I_0 / T^2)$ versus q / kT plot with three different contacts: (a) graphene, (b) Au, and (c) WTe_2. From these graphs, the gate-voltage-dependent barrier height of the FETs are extracted in (d). The SBH is extracted under a flat band gate voltage condition. The corresponding contact resistances (R_c) of monolayer $WTe_{0.06}S_{1.94}$ alloy FETs with three different contacts are extrated in (e)-(g). Experimentally determined Schottky barrier height for three different transferred electrodes are summarized in (h).

6.5 Summary

In conclusion, the phase transition of TMDC monolayer from semiconductor to metal has been demonstrated by alloying Te into tungsten disulfide. Using an one-step-CVD method, the compositions of $WTe_{2x}S_{2(1-x)}$ alloys ($0 \leq x \leq 1$) can be obtained, which exhibit distinguishable semiconducting 2H and metallic 1T′ phases. The compositions of the $WTe_{2x}S_{2(1-x)}$ alloys are identified using XPS and Raman spectroscopic studies. The PL spectra reveal that the optical bandgap of the $WTe_{2x}S_{2(1-x)}$ alloy can be tuned from 2 eV to 1.75 eV (2H semiconductors) and dropped to 0 eV (1T′ metals). Additionally, studies of the FET devices based on atomic layer $WTe_{2x}S_{2(1-x)}$ alloys confirmed that the 2H-phase alloys are n-type semiconductors and the 1T′-phase alloys are metals.

Furthermore, it has been demonstrated that the contact resistance between the channel and electrodes could be significantly reduced by WTe_2/Au contacts, leading to 7 times lower resistance than the graphene electrodes and 5 times lower resistance than the Au electrodes. Compared to the $WTe_{2x}S_{2(1-x)}$-based FET with graphene/Au or Au contacts, the devices with WTe_2/Au contact as the source/drain electrodes showed superior electrical properties, including a field-effect mobility 25 $cm^2V^{-1}S^{-1}$ and an on/off current of 10^6. These improvements could be attributed to the WTe_2 metal contact with a workfunction close to the bandedge of the $WS_{1.94}Te_{0.06}$ alloy, which lowered the Schottky barrier height and the contact resistance. This bandgap engineering of 2D TMDC alloys combined with the metal transfer method could open up exciting oppotunities for probing various fundamental physical properties in 2D materials (such as new types of Wyle semimetals and spin Hall effects) and for diverse applications in 2D TMDC-based nanoelectronics and optoelectronics.

Chapter 7

SUMMARY AND OUTLOOK

7.1 Contributions of this thesis

In this thesis, we developed and demonstrated three different topics in the field of 2D materials including advanced quantum material synthesis method, room-temperature high-valley-polarization optoelectronics, and high performance field-effect transistors.

i). The advanced 2D quantum material development:

We (1) developed the method for low-temperature (nearly room temperature) synthesis of high-quality monolayer graphene and controllable twisted angle bi-layer graphene; (2) developed a synthesis method for thickness-controllable and large area CVD growth of h-BN films; (3) invented a universal synthesis method for all 2D TMDCs materials; and (4) developed a new class of TMDCs alloys ($WS_{2x}Te_{2(1-x)}$) with tunable bandgaps and phases (2T to 1T').

ii). Room-temperature high-valley-polarization optoelectronics:

We (1) demonstrated a defect density-controllable CVD synthesis method on monolayer WS_2 to boost valley-polarization at room temperature; and (2) combined plasmonic Archimedes spiral nanostructures with WS2 to enhance valley-polarization at RT.

iii). Demonstration of high-performance FET based on < 1nm-thick monolayer TMDC alloys ($WS_{2x}Te_{2(1-x)}$):

We (1) invented a new metal transfer method to make the Schottky contact at the Schottky-Mott limit; and (2) used semimetals (WTe_2) and experimentally demonstrating high performance (low contact resistivity and high mobility) monolayer semiconductor field-effect transistors.

7.2 Future Work

We end this thesis by proposing several promising directions as an extension of this thesis.

1. Searching P-type 2D semiconductors and P-type ohmic contact

The majority of 2D semiconductors are n-type due to the strong electron doping from interfacial charge impurities and intrinsic structural defects. In addition, p-type conduction in 2D semiconductors is greatly hindered by the Fermi level pining at the metal/2D semiconductor interface that results in large Schottky barrier heights for hole injection. The potential channel materials could be 2D tellurium. The tellurium-based FET exhibits a high hole mobility of ∼700 cm^2 V^{-1} s^{-1} and a current on/off ratio of ∼10^6. Remarkably, with short channels, tellurium-based transistors deliver p-type conduction with a maximum drive current exceeding 1 A mm^{-1}. Also, 2D tellurium shows good chemical stability under ambient conditions, and the device performance is stable over months, making it an ideal p-type 2D semiconductor for future electronic and optoelectronic applications. In Chapter 6, we learned that WTe_2 plays an important role to serve as an n-type contact for n-type 2D materials. It is important to continuously discover high-workfunction semimetals to directly form intimate contacts on diverse 2D semiconductors which is critical to achieve high-performance and highly reliable p-type contacts. If these challenges can be addressed, high-performance CMOS integrated circuits based on monolayer semiconductors would be realized in the foreseeable future.

2. Scaling the on-state current through 2D semiconductor

High-mobility semiconducting ultrathin films form the basis of modern electronics, and may lead to the scalable fabrication of highly performing devices. Here, we would like to propose to use a layered Bi_2O_2Se as the FET channel materials due to its high carrier mobility (~28,900 $cm^2/V{\cdot}s$ at 1.9 K and ~450 $cm^2/V{\cdot}s$ at room temperature) and superior current on/off ratio of >10^6 with almost ideal subthreshold swing (~65 mV/dec). In addition, the moderate bandgap (~0.8 eV) of Bi_2O_2Se makes its device suitable for room temperature operation while requiring only a relatively low operation voltage. Developments of advanced fabrication processes for stacked monolayer semiconductors, forming few-layer 2D semiconductors with uniform thicknesses, and their integration with high-k dielectrics are critical to boost the performance of TMD FET technology. Therefore, the combinations of new process technology and novel transistor structure based on 2D semiconductors with CMOS compatibility would be a long-term solution to continue the CMOS scaling.

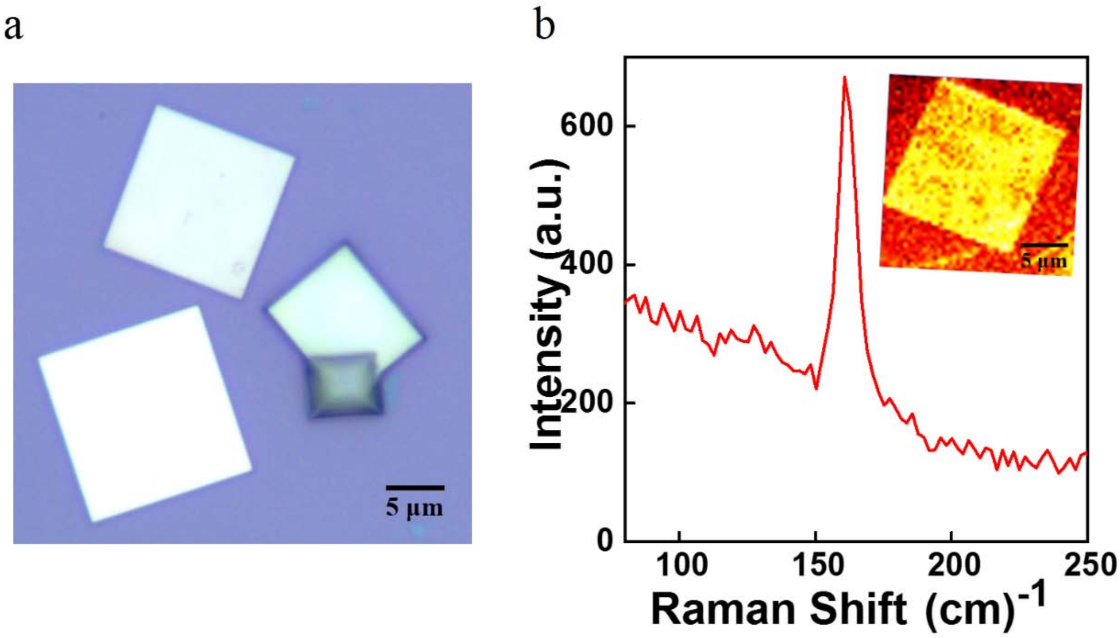

Figure 7.1. (a). The optical image of the multi-layer Bi_2O_2Se. (b). The Raman spectra of the multi-layer Bi_2O_2Se. The inset is the corresponding Raman mapping figure in (a).

BIBLIOGRAPH

(1) Kroto, H. W.; Heath, J. R.; O'Brien, S. C.; Curl, R. F.; Smalley, R. E. C 60 : Buckminsterfullerene. *Nature* **1985**, *318* (6042), 162–163. https://doi.org/10.1038/318162a0.

(2) Iijima, S. Helical Microtubules of Graphitic Carbon. *Nature* **1991**, *354* (6348), 56–58. https://doi.org/10.1038/354056a0.

(3) Novoselov, K. S.; Geim, A. K.; Morozov, S. V.; Jiang, D.; Katsnelson, M. I.; Grigorieva, I. V.; Dubonos, S. V.; Firsov, A. A. Two-Dimensional Gas of Massless Dirac Fermions in Graphene. *Nature* **2005**, *438* (7065), 197–200. https://doi.org/10.1038/nature04233.

(4) Zhang, Y.; Tan, Y.-W.; Stormer, H. L.; Kim, P. Experimental Observation of the Quantum Hall Effect and Berry's Phase in Graphene. *Nature* **2005**, *438* (7065), 201–204. https://doi.org/10.1038/nature04235.

(5) Novoselov, K. S.; Geim, A. K.; Morozov, S. V.; Jiang, D.; Zhang, Y.; Dubonos, S. V.; Grigorieva, I. V.; Firsov, A. A. Electric Field Effect in Atomically Thin Carbon Films. *Science* **2004**, *306* (5696), 666–669. https://doi.org/10.1126/science.1102896.

(6) Castro Neto, A. H.; Guinea, F.; Peres, N. M. R.; Novoselov, K. S.; Geim, A. K. The Electronic Properties of Graphene. *Rev. Mod. Phys.* **2009**, *81* (1), 109–162. https://doi.org/10.1103/RevModPhys.81.109.

(7) Palacios, T.; Hsu, A.; Wang, H. Applications of Graphene Devices in RF Communications. *IEEE Communications Magazine* **2010**, *48* (6), 122–128. https://doi.org/10.1109/MCOM.2010.5473873.

(8) Wang, H.; Hsu, A.; Wu, J.; Kong, J.; Palacios, T. Graphene-Based Ambipolar RF Mixers. *IEEE Electron Device Letters* **2010**, *31* (9), 906–908. https://doi.org/10.1109/LED.2010.2052017.

(9) Wang, H.; Nezich, D.; Kong, J.; Palacios, T. Graphene Frequency Multipliers. *IEEE Electron Device Letters* **2009**, *30* (5), 547–549. https://doi.org/10.1109/LED.2009.2016443.

(10) Wang, H.; Hsu, A.; Kim, K. K.; Kong, J.; Palacios, T. Graphene Electronics for RF Applications. In *2011 IEEE MTT-S International Microwave Symposium*; 2011; pp 1–4. https://doi.org/10.1109/MWSYM.2011.5972917.

(11) Eda, G.; Fanchini, G.; Chhowalla, M. Large-Area Ultrathin Films of Reduced Graphene Oxide as a Transparent and Flexible Electronic Material. *Nature Nanotechnology* **2008**, *3* (5), 270–274. https://doi.org/10.1038/nnano.2008.83.

(12) Milaninia, K. M.; Baldo, M. A.; Reina, A.; Kong, J. All Graphene Electromechanical Switch Fabricated by Chemical Vapor Deposition. *Appl. Phys. Lett.* **2009**, *95* (18), 183105. https://doi.org/10.1063/1.3259415.

(13) Yan, H.; Li, X.; Chandra, B.; Tulevski, G.; Wu, Y.; Freitag, M.; Zhu, W.; Avouris, P.; Xia, F. Tunable Infrared Plasmonic Devices Using Graphene/Insulator Stacks. *Nature Nanotechnology* **2012**, *7* (5), 330–334. https://doi.org/10.1038/nnano.2012.59.

(14) Ju, L.; Geng, B.; Horng, J.; Girit, C.; Martin, M.; Hao, Z.; Bechtel, H. A.; Liang, X.; Zettl, A.; Shen, Y. R.; Wang, F. Graphene Plasmonics for Tunable Terahertz Metamaterials. *Nature Nanotechnology* **2011**, *6* (10), 630–634. https://doi.org/10.1038/nnano.2011.146.

(15) Lin, W.-H.; Brar, V. W.; Jariwala, D.; Sherrott, M. C.; Tseng, W.-S.; Wu, C.-I.; Yeh, N.-C.; Atwater, H. A. Atomic-Scale Structural and Chemical Characterization of Hexagonal Boron Nitride Layers Synthesized at the Wafer-Scale with Monolayer Thickness Control. *Chem. Mater.* **2017**, *29* (11), 4700–4707. https://doi.org/10.1021/acs.chemmater.7b00183.

(16) Bhimanapati, G. R.; Lin, Z.; Meunier, V.; Jung, Y.; Cha, J.; Das, S.; Xiao, D.; Son, Y.; Strano, M. S.; Cooper, V. R.; Liang, L.; Louie, S. G.; Ringe, E.; Zhou, W.; Kim, S. S.; Naik, R. R.; Sumpter, B. G.; Terrones, H.; Xia, F.; Wang, Y.; Zhu, J.; Akinwande, D.; Alem, N.; Schuller, J. A.; Schaak, R. E.; Terrones, M.; Robinson, J. A. Recent Advances in Two-Dimensional Materials beyond Graphene. *ACS Nano* **2015**, *9* (12), 11509–11539. https://doi.org/10.1021/acsnano.5b05556.

(17) Chhowalla, M.; Shin, H. S.; Eda, G.; Li, L.-J.; Loh, K. P.; Zhang, H. The Chemistry of Two-Dimensional Layered Transition Metal Dichalcogenide Nanosheets. *Nature Chemistry* **2013**, *5* (4), 263–275. https://doi.org/10.1038/nchem.1589.

(18) Geim, A. K.; Grigorieva, I. V. Van Der Waals Heterostructures. *Nature* **2013**, *499* (7459), 419–425. https://doi.org/10.1038/nature12385.

(19) Lin, W.-H.; Tseng, W.-S.; Went, C. M.; Teague, M. L.; Rossman, George. R.; Atwater, H. A.; Yeh, N.-C. Nearly 90% Circularly Polarized Emission in Monolayer WS2 Single Crystals by Chemical Vapor Deposition. *ACS Nano* **2020**, *14* (2), 1350–1359. https://doi.org/10.1021/acsnano.9b05550.

(20) Yan, J.; Zhang, Y.; Kim, P.; Pinczuk, A. Electric Field Effect Tuning of Electron-Phonon Coupling in Graphene. *Phys. Rev. Lett.* **2007**, *98* (16), 166802. https://doi.org/10.1103/PhysRevLett.98.166802.

(21) Geim, A. K.; Novoselov, K. S. The Rise of Graphene. *Nature Materials* **2007**, *6* (3), 183–191. https://doi.org/10.1038/nmat1849.

(22) Hwang, E. H.; Adam, S.; Sarma, S. D. Carrier Transport in Two-Dimensional Graphene Layers. *Phys. Rev. Lett.* **2007**, *98* (18), 186806. https://doi.org/10.1103/PhysRevLett.98.186806.

(23) Morozov, S. V.; Novoselov, K. S.; Katsnelson, M. I.; Schedin, F.; Elias, D. C.; Jaszczak, J. A.; Geim, A. K. Giant Intrinsic Carrier Mobilities in Graphene and Its Bilayer. *Phys. Rev. Lett.* **2008**, *100* (1), 016602. https://doi.org/10.1103/PhysRevLett.100.016602.

(24) Katsnelson, M. I. Zitterbewegung, Chirality, and Minimal Conductivity in Graphene. *Eur. Phys. J. B* **2006**, *51* (2), 157–160. https://doi.org/10.1140/epjb/e2006-00203-1.

(25) Tworzydło, J.; Trauzettel, B.; Titov, M.; Rycerz, A.; Beenakker, C. W. J. Sub-Poissonian Shot Noise in Graphene. *Phys. Rev. Lett.* **2006**, *96* (24), 246802. https://doi.org/10.1103/PhysRevLett.96.246802.

(26) Martin, J.; Akerman, N.; Ulbricht, G.; Lohmann, T.; Smet, J. H.; von Klitzing, K.; Yacoby, A. Observation of Electron–Hole Puddles in Graphene Using a Scanning Single-Electron Transistor. *Nature Physics* **2008**, *4* (2), 144–148. https://doi.org/10.1038/nphys781.

(27) Fasolino, A.; Los, J. H.; Katsnelson, M. I. Intrinsic Ripples in Graphene. *Nature Materials* **2007**, *6* (11), 858–861. https://doi.org/10.1038/nmat2011.

(28) Nam, S.-G.; Ki, D.-K.; Lee, H.-J. Thermoelectric Transport of Massive Dirac Fermions in Bilayer Graphene. *Phys. Rev. B* **2010**, *82* (24), 245416. https://doi.org/10.1103/PhysRevB.82.245416.

(29) Sui, M.; Chen, G.; Ma, L.; Shan, W.-Y.; Tian, D.; Watanabe, K.; Taniguchi, T.; Jin, X.; Yao, W.; Xiao, D.; Zhang, Y. Gate-Tunable Topological Valley Transport in Bilayer Graphene. *Nature Physics* **2015**, *11* (12), 1027–1031. https://doi.org/10.1038/nphys3485.

(30) Shimazaki, Y.; Yamamoto, M.; Borzenets, I. V.; Watanabe, K.; Taniguchi, T.; Tarucha, S. Generation and Detection of Pure Valley Current by Electrically Induced Berry Curvature in Bilayer Graphene. *Nature Physics* **2015**, *11* (12), 1032–1036. https://doi.org/10.1038/nphys3551.

(31) Komatsu, K.; Morita, Y.; Watanabe, E.; Tsuya, D.; Watanabe, K.; Taniguchi, T.; Moriyama, S. Observation of the Quantum Valley Hall State in Ballistic Graphene Superlattices. *Science Advances* **2018**, *4* (5), eaaq0194. https://doi.org/10.1126/sciadv.aaq0194.

(32) Lemme, M. C.; Echtermeyer, T. J.; Baus, M.; Kurz, H. A Graphene Field-Effect Device. *IEEE Electron Device Letters* **2007**, *28* (4), 282–284. https://doi.org/10.1109/LED.2007.891668.

(33) Han, M. Y.; Özyilmaz, B.; Zhang, Y.; Kim, P. Energy Band-Gap Engineering of Graphene Nanoribbons. *Phys. Rev. Lett.* **2007**, *98* (20), 206805. https://doi.org/10.1103/PhysRevLett.98.206805.

(34) Areshkin, D. A.; White, C. T. Building Blocks for Integrated Graphene Circuits. *Nano Lett.* **2007**, *7* (11), 3253–3259. https://doi.org/10.1021/nl070708c.

(35) Lin, Y.-M.; Jenkins, K. A.; Valdes-Garcia, A.; Small, J. P.; Farmer, D. B.; Avouris, P. Operation of Graphene Transistors at Gigahertz Frequencies. *Nano Lett.* **2009**, *9* (1), 422–426. https://doi.org/10.1021/nl803316h.

(36) Schwierz, F.; Pezoldt, J.; Granzner, R. Two-Dimensional Materials and Their Prospects in Transistor Electronics. *Nanoscale* **2015**, *7* (18), 8261–8283. https://doi.org/10.1039/C5NR01052G.

(37) Wang, H.; Yu, L.; Lee, Y.-H.; Shi, Y.; Hsu, A.; Chin, M. L.; Li, L.-J.; Dubey, M.; Kong, J.; Palacios, T. Integrated Circuits Based on Bilayer MoS_2 Transistors. *Nano Lett.* **2012**, *12* (9), 4674–4680. https://doi.org/10.1021/nl302015v.

(38) Schulman, D. S.; Arnold, A. J.; Das, S. Contact Engineering for 2D Materials and Devices. *Chem. Soc. Rev.* **2018**, *47* (9), 3037–3058. https://doi.org/10.1039/C7CS00828G.

(39) Chhowalla, M.; Jena, D.; Zhang, H. Two-Dimensional Semiconductors for Transistors. *Nature Reviews Materials* **2016**, *1* (11), 1–15. https://doi.org/10.1038/natrevmats.2016.52.

(40) Kuzmenko, A. B. Kramers–Kronig Constrained Variational Analysis of Optical Spectra. *Review of Scientific Instruments* **2005**, *76* (8), 083108. https://doi.org/10.1063/1.1979470.

(41) Li, Y.; Chernikov, A.; Zhang, X.; Rigosi, A.; Hill, H. M.; van der Zande, A. M.; Chenet, D. A.; Shih, E.-M.; Hone, J.; Heinz, T. F. Measurement of the Optical Dielectric Function of Monolayer Transition-Metal Dichalcogenides: MoS_2, $MoSe_2$, WS_2, and WSe_2 *Phys. Rev. B* **2014**, *90* (20), 205422. https://doi.org/10.1103/PhysRevB.90.205422.

(42) Zhan, T.; Shi, X.; Dai, Y.; Liu, X.; Zi, J. Transfer Matrix Method for Optics in Graphene Layers. *J. Phys.: Condens. Matter* **2013**, *25* (21), 215301. https://doi.org/10.1088/0953-8984/25/21/215301.

(43) Ansari, N.; Ghorbani, F. Light Absorption Optimization in Two-Dimensional Transition Metal Dichalcogenide van Der Waals Heterostructures. *J. Opt. Soc. Am. B, JOSAB* **2018**, *35* (5), 1179–1185. https://doi.org/10.1364/JOSAB.35.001179.

(44) Boyd, D. A.; Lin, W.-H.; Hsu, C.-C.; Teague, M. L.; Chen, C.-C.; Lo, Y.-Y.; Chan, W.-Y.; Su, W.-B.; Cheng, T.-C.; Chang, C.-S.; Wu, C.-I.; Yeh, N.-C. Single-Step Deposition of High-Mobility Graphene at Reduced Temperatures. *Nature Communications* **2015**, *6* (1), 6620. https://doi.org/10.1038/ncomms7620.

(45) Chen, Y.-C.; Lin, W.-H.; Tseng, W.-S.; Chen, C.-C.; Rossman, George. R.; Chen, C.-D.; Wu, Y.-S.; Yeh, N.-C. Direct Growth of Mm-Size Twisted Bilayer Graphene by Plasma-Enhanced Chemical Vapor Deposition. *Carbon* **2020**, *156*, 212–224. https://doi.org/10.1016/j.carbon.2019.09.052.

(46) Terasawa, T.; Saiki, K. Growth of Graphene on Cu by Plasma Enhanced Chemical Vapor Deposition. *Carbon* **2012**, *50* (3), 869–874. https://doi.org/10.1016/j.carbon.2011.09.047.

(47) Li, X.; Cai, W.; Colombo, L.; Ruoff, R. S. Evolution of Graphene Growth on Ni and Cu by Carbon Isotope Labeling. *Nano Lett.* **2009**, *9* (12), 4268–4272. https://doi.org/10.1021/nl902515k.

(48) Li, Q.; Chou, H.; Zhong, J.-H.; Liu, J.-Y.; Dolocan, A.; Zhang, J.; Zhou, Y.; Ruoff, R. S.; Chen, S.; Cai, W. Growth of Adlayer Graphene on Cu Studied by Carbon Isotope Labeling. *Nano Lett.* **2013**, *13* (2), 486–490. https://doi.org/10.1021/nl303879k.

(49) Fang, W.; Hsu, A. L.; Caudillo, R.; Song, Y.; Birdwell, A. G.; Zakar, E.; Kalbac, M.; Dubey, M.; Palacios, T.; Dresselhaus, M. S.; Araujo, P. T.; Kong, J. Rapid Identification of Stacking Orientation in Isotopically Labeled Chemical-Vapor Grown Bilayer Graphene by Raman Spectroscopy. *Nano Lett.* **2013**, *13* (4), 1541–1548. https://doi.org/10.1021/nl304706j.

(50) Wu, F.; Levitin, G.; Hess, D. W. Low-Temperature Etching of Cu by Hydrogen-Based Plasmas. *ACS Appl. Mater. Interfaces* **2010**, *2* (8), 2175–2179. https://doi.org/10.1021/am1003206.

(51) Vlassiouk, I.; Regmi, M.; Fulvio, P.; Dai, S.; Datskos, P.; Eres, G.; Smirnov, S. Role of Hydrogen in Chemical Vapor Deposition Growth of Large Single-Crystal Graphene. *ACS Nano* **2011**, *5* (7), 6069–6076. https://doi.org/10.1021/nn201978y.

(52) Gao, L.; Ren, W.; Xu, H.; Jin, L.; Wang, Z.; Ma, T.; Ma, L.-P.; Zhang, Z.; Fu, Q.; Peng, L.-M.; Bao, X.; Cheng, H.-M. Repeated Growth and Bubbling Transfer of Graphene with Millimetre-Size Single-Crystal Grains Using Platinum. *Nature Communications* **2012**, *3* (1), 699. https://doi.org/10.1038/ncomms1702.

(53) Ferrari, A. C.; Meyer, J. C.; Scardaci, V.; Casiraghi, C.; Lazzeri, M.; Mauri, F.; Piscanec, S.; Jiang, D.; Novoselov, K. S.; Roth, S.; Geim, A. K. Raman Spectrum of Graphene and Graphene Layers. *Phys. Rev. Lett.* **2006**, *97* (18), 187401. https://doi.org/10.1103/PhysRevLett.97.187401.

(54) Kang, Y.-J.; Kang, J.; Chang, K. J. Electronic Structure of Graphene and Doping Effect on SiO_2. *Phys. Rev. B* **2008**, *78* (11), 115404. https://doi.org/10.1103/PhysRevB.78.115404.

(55) Gupta, A. K.; Tang, Y.; Crespi, V. H.; Eklund, P. C. Nondispersive Raman D Band Activated by Well-Ordered Interlayer Interactions in Rotationally Stacked Bilayer Graphene. *Phys. Rev. B* **2010**, *82* (24), 241406. https://doi.org/10.1103/PhysRevB.82.241406.

(56) Carozo, V.; Almeida, C. M.; Ferreira, E. H. M.; Cançado, L. G.; Achete, C. A.; Jorio, A. Raman Signature of Graphene Superlattices. *Nano Lett.* **2011**, *11* (11), 4527–4534. https://doi.org/10.1021/nl201370m.

(57) Kim, K.; Coh, S.; Tan, L. Z.; Regan, W.; Yuk, J. M.; Chatterjee, E.; Crommie, M. F.; Cohen, M. L.; Louie, S. G.; Zettl, A. Raman Spectroscopy Study of Rotated Double-Layer Graphene: Misorientation-Angle Dependence of Electronic Structure. *Phys. Rev. Lett.* **2012**, *108* (24), 246103. https://doi.org/10.1103/PhysRevLett.108.246103.

(58) Havener, R. W.; Zhuang, H.; Brown, L.; Hennig, R. G.; Park, J. Angle-Resolved Raman Imaging of Interlayer Rotations and Interactions in Twisted Bilayer Graphene. *Nano Lett.* **2012**, *12* (6), 3162–3167. https://doi.org/10.1021/nl301137k.

(59) Wang, Y. Y.; Ni, Z. H.; Shen, Z. X.; Wang, H. M.; Wu, Y. H. Interference Enhancement of Raman Signal of Graphene. *Appl. Phys. Lett.* **2008**, *92* (4), 043121. https://doi.org/10.1063/1.2838745.

(60) Ni, Z.; Wang, Y.; Yu, T.; Shen, Z. Raman Spectroscopy and Imaging of Graphene. *Nano Res.* **2008**, *1* (4), 273–291. https://doi.org/10.1007/s12274-008-8036-1.

(61) Lu, C.-C.; Lin, Y.-C.; Liu, Z.; Yeh, C.-H.; Suenaga, K.; Chiu, P.-W. Twisting Bilayer Graphene Superlattices. *ACS Nano* **2013**, *7* (3), 2587–2594. https://doi.org/10.1021/nn3059828.

(62) Sato, K.; Saito, R.; Cong, C.; Yu, T.; Dresselhaus, M. S. Zone Folding Effect in Raman G-Band Intensity of Twisted Bilayer Graphene. *Phys. Rev. B* **2012**, *86* (12), 125414. https://doi.org/10.1103/PhysRevB.86.125414.

(63) Cocemasov, A. I.; Nika, D. L.; Balandin, A. A. Phonons in Twisted Bilayer Graphene. *Phys. Rev. B* **2013**, *88* (3), 035428. https://doi.org/10.1103/PhysRevB.88.035428.

(64) Jorio, A.; Cançado, L. G. Raman Spectroscopy of Twisted Bilayer Graphene. *Solid State Communications* **2013**, *175–176*, 3–12. https://doi.org/10.1016/j.ssc.2013.08.008.

(65) Pimenta, M. A.; Dresselhaus, G.; Dresselhaus, M. S.; Cançado, L. G.; Jorio, A.; Saito, R. Studying Disorder in Graphite-Based Systems by Raman Spectroscopy. *Phys. Chem. Chem. Phys.* **2007**, *9* (11), 1276–1290. https://doi.org/10.1039/B613962K.

(66) Eckmann, A.; Felten, A.; Verzhbitskiy, I.; Davey, R.; Casiraghi, C. Raman Study on Defective Graphene: Effect of the Excitation Energy, Type, and Amount of Defects. *Phys. Rev. B* **2013**, *88* (3), 035426. https://doi.org/10.1103/PhysRevB.88.035426.

(67) He, R.; Chung, T.-F.; Delaney, C.; Keiser, C.; Jauregui, L. A.; Shand, P. M.; Chancey, C. C.; Wang, Y.; Bao, J.; Chen, Y. P. Observation of Low Energy Raman Modes in Twisted Bilayer Graphene. *Nano Lett.* **2013**, *13* (8), 3594–3601. https://doi.org/10.1021/nl4013387.

(68) Ramnani, P.; Neupane, M. R.; Ge, S.; Balandin, A. A.; Lake, R. K.; Mulchandani, A. Raman Spectra of Twisted CVD Bilayer Graphene. *Carbon* **2017**, *123*, 302–306. https://doi.org/10.1016/j.carbon.2017.07.064.

(69) Sheng, Y.; Rong, Y.; He, Z.; Fan, Y.; Warner, J. H. Uniformity of Large-Area Bilayer Graphene Grown by Chemical Vapor Deposition. *Nanotechnology* **2015**, *26* (39), 395601. https://doi.org/10.1088/0957-4484/26/39/395601.

(70) Suárez Morell, E.; Correa, J. D.; Vargas, P.; Pacheco, M.; Barticevic, Z. Flat Bands in Slightly Twisted Bilayer Graphene: Tight-Binding Calculations. *Phys. Rev. B* **2010**, *82* (12), 121407. https://doi.org/10.1103/PhysRevB.82.121407.

(71) Sboychakov, A. O.; Rakhmanov, A. L.; Rozhkov, A. V.; Nori, F. Electronic Spectrum of Twisted Bilayer Graphene. *Phys. Rev. B* **2015**, *92* (7), 075402. https://doi.org/10.1103/PhysRevB.92.075402.

(72) Luican, A.; Li, G.; Reina, A.; Kong, J.; Nair, R. R.; Novoselov, K. S.; Geim, A. K.; Andrei, E. Y. Single-Layer Behavior and Its Breakdown in Twisted Graphene Layers. *Phys. Rev. Lett.* **2011**, *106* (12), 126802. https://doi.org/10.1103/PhysRevLett.106.126802.

(73) Ohta, T.; Robinson, J. T.; Feibelman, P. J.; Bostwick, A.; Rotenberg, E.; Beechem, T. E. Evidence for Interlayer Coupling and Moir\'e Periodic Potentials in Twisted Bilayer Graphene. *Phys. Rev. Lett.* **2012**, *109* (18), 186807. https://doi.org/10.1103/PhysRevLett.109.186807.

(74) Melitz, W.; Shen, J.; Kummel, A. C.; Lee, S. Kelvin Probe Force Microscopy and Its Application. *Surface Science Reports* **2011**, *66* (1), 1–27. https://doi.org/10.1016/j.surfrep.2010.10.001.

(75) Robinson, J. T.; Culbertson, J.; Berg, M.; Ohta, T. Work Function Variations in Twisted Graphene Layers. *Scientific Reports* **2018**, *8* (1), 2006. https://doi.org/10.1038/s41598-018-19631-4.

(76) Panchal, V.; Pearce, R.; Yakimova, R.; Tzalenchuk, A.; Kazakova, O. Standardization of Surface Potential Measurements of Graphene Domains. *Scientific Reports* **2013**, *3* (1), 2597. https://doi.org/10.1038/srep02597.

(77) Burnett, T.; Yakimova, R.; Kazakova, O. Mapping of Local Electrical Properties in Epitaxial Graphene Using Electrostatic Force Microscopy. *Nano Lett.* **2011**, *11* (6), 2324–2328. https://doi.org/10.1021/nl200581g.

(78) Stampfer, C.; Molitor, F.; Graf, D.; Ensslin, K.; Jungen, A.; Hierold, C.; Wirtz, L. Raman Imaging of Doping Domains in Graphene on SiO_2. *Appl. Phys. Lett.* **2007**, *91* (24), 241907. https://doi.org/10.1063/1.2816262.

(79) Giannazzo, F.; Sonde, S.; Raineri, V.; Rimini, E. Screening Length and Quantum Capacitance in Graphene by Scanning Probe Microscopy. *Nano Lett.* **2009**, *9* (1), 23–29. https://doi.org/10.1021/nl801823n.

(80) Li, X.; Cai, W.; An, J.; Kim, S.; Nah, J.; Yang, D.; Piner, R.; Velamakanni, A.; Jung, I.; Tutuc, E.; Banerjee, S. K.; Colombo, L.; Ruoff, R. S. Large-Area Synthesis of High-Quality and Uniform Graphene Films on Copper Foils. *Science* **2009**, *324* (5932), 1312–1314. https://doi.org/10.1126/science.1171245.

(81) Ledwosinska, E.; Gaskell, P.; Guermoune, A.; Siaj, M.; Szkopek, T. Organic-Free Suspension of Large-Area Graphene. *Appl. Phys. Lett.* **2012**, *101* (3), 033104. https://doi.org/10.1063/1.4737415.

(82) Nair, R. R.; Blake, P.; Grigorenko, A. N.; Novoselov, K. S.; Booth, T. J.; Stauber, T.; Peres, N. M. R.; Geim, A. K. Fine Structure Constant Defines Visual Transparency of Graphene. *Science* **2008**, *320* (5881), 1308–1308. https://doi.org/10.1126/science.1156965.

(83) Blake, P.; Brimicombe, P. D.; Nair, R. R.; Booth, T. J.; Jiang, D.; Schedin, F.; Ponomarenko, L. A.; Morozov, S. V.; Gleeson, H. F.; Hill, E. W.; Geim, A. K.; Novoselov, K. S. Graphene-Based Liquid Crystal Device. *Nano Lett.* **2008**, *8* (6), 1704–1708. https://doi.org/10.1021/nl080649i.

(84) Ishigami, M.; Chen, J. H.; Cullen, W. G.; Fuhrer, M. S.; Williams, E. D. Atomic Structure of Graphene on SiO_2. *Nano Lett.* **2007**, *7* (6), 1643–1648. https://doi.org/10.1021/nl070613a.

(85) Stolyarova, E.; Rim, K. T.; Ryu, S.; Maultzsch, J.; Kim, P.; Brus, L. E.; Heinz, T. F.; Hybertsen, M. S.; Flynn, G. W. High-Resolution Scanning Tunneling Microscopy Imaging of Mesoscopic Graphene Sheets on an Insulating Surface. *PNAS* **2007**, *104* (22), 9209–9212. https://doi.org/10.1073/pnas.0703337104.

(86) Cortijo, A.; Vozmediano, M. A. H. Effects of Topological Defects and Local Curvature on the Electronic Properties of Planar Graphene. *Nuclear Physics B* **2007**, *763* (3), 293–308. https://doi.org/10.1016/j.nuclphysb.2006.10.031.

(87) Meyer, J. C.; Geim, A. K.; Katsnelson, M. I.; Novoselov, K. S.; Booth, T. J.; Roth, S. The Structure of Suspended Graphene Sheets. *Nature* **2007**, *446* (7131), 60–63. https://doi.org/10.1038/nature05545.

(88) Yu, Y.-J.; Zhao, Y.; Ryu, S.; Brus, L. E.; Kim, K. S.; Kim, P. Tuning the Graphene Work Function by Electric Field Effect. *Nano Lett.* **2009**, *9* (10), 3430–3434. https://doi.org/10.1021/nl901572a.

(89) Luo, Z.; Shang, J.; Lim, S.; Li, D.; Xiong, Q.; Shen, Z.; Lin, J.; Yu, T. Modulating the Electronic Structures of Graphene by Controllable Hydrogenation. *Appl. Phys. Lett.* **2010**, *97* (23), 233111. https://doi.org/10.1063/1.3524217.

(90) Hong, S. K.; Song, S. M.; Sul, O.; Cho, B. J. Carboxylic Group as the Origin of Electrical Performance Degradation during the Transfer Process of CVD Growth Graphene. *J. Electrochem. Soc.* **2012**, *159* (4), K107. https://doi.org/10.1149/2.101204jes.

(91) Pirkle, A.; Chan, J.; Venugopal, A.; Hinojos, D.; Magnuson, C. W.; McDonnell, S.; Colombo, L.; Vogel, E. M.; Ruoff, R. S.; Wallace, R. M. The Effect of Chemical Residues on the Physical and Electrical Properties of Chemical Vapor Deposited Graphene Transferred to SiO2. *Appl. Phys. Lett.* **2011**, *99* (12), 122108. https://doi.org/10.1063/1.3643444.

(92) Epitaxial Graphene Nanoribbon Array Fabrication Using BCP-Assisted Nanolithography ACS *Nano* **2012**, *6* (*8*), 6786

(93) Gannett, W.; Regan, W.; Watanabe, K.; Taniguchi, T.; Crommie, M. F.; Zettl, A. Boron Nitride Substrates for High Mobility Chemical Vapor Deposited Graphene. *Appl. Phys. Lett.* **2011**, *98* (24), 242105. https://doi.org/10.1063/1.3599708.

(94) Schedin, F.; Geim, A. K.; Morozov, S. V.; Hill, E. W.; Blake, P.; Katsnelson, M. I.; Novoselov, K. S. Detection of Individual Gas Molecules Adsorbed on Graphene. *Nature Materials* **2007**, *6* (9), 652–655. https://doi.org/10.1038/nmat1967.

(95) Li, X.; Magnuson, C. W.; Venugopal, A.; Tromp, R. M.; Hannon, J. B.; Vogel, E. M.; Colombo, L.; Ruoff, R. S. Large-Area Graphene Single Crystals Grown by Low-Pressure Chemical Vapor Deposition of Methane on Copper. *J. Am. Chem. Soc.* **2011**, *133* (9), 2816–2819. https://doi.org/10.1021/ja109793s.

(96) Das Sarma, S.; Hwang, E. H.; Rossi, E. Theory of Carrier Transport in Bilayer Graphene. *Phys. Rev. B* **2010**, *81* (16), 161407. https://doi.org/10.1103/PhysRevB.81.161407.

(97) Dean, C. R.; Young, A. F.; Meric, I.; Lee, C.; Wang, L.; Sorgenfrei, S.; Watanabe, K.; Taniguchi, T.; Kim, P.; Shepard, K. L.; Hone, J. Boron Nitride Substrates for High-Quality Graphene Electronics. *Nature Nanotechnology* **2010**, *5* (10), 722–726. https://doi.org/10.1038/nnano.2010.172.

(98) Eckmann, A.; Park, J.; Yang, H.; Elias, D.; Mayorov, A. S.; Yu, G.; Jalil, R.; Novoselov, K. S.; Gorbachev, R. V.; Lazzeri, M.; Geim, A. K.; Casiraghi, C. Raman Fingerprint of

Aligned Graphene/h-BN Superlattices. *Nano Lett.* **2013**, *13* (11), 5242–5246. https://doi.org/10.1021/nl402679b.

(99) Yankowitz, M.; Xue, J.; Cormode, D.; Sanchez-Yamagishi, J. D.; Watanabe, K.; Taniguchi, T.; Jarillo-Herrero, P.; Jacquod, P.; LeRoy, B. J. Emergence of Superlattice Dirac Points in Graphene on Hexagonal Boron Nitride. *Nature Physics* **2012**, *8* (5), 382–386. https://doi.org/10.1038/nphys2272.

(100) Kim, K. K.; Hsu, A.; Jia, X.; Kim, S. M.; Shi, Y.; Dresselhaus, M.; Palacios, T.; Kong, J. Synthesis and Characterization of Hexagonal Boron Nitride Film as a Dielectric Layer for Graphene Devices. *ACS Nano* **2012**, *6* (10), 8583–8590. https://doi.org/10.1021/nn301675f.

(101) Zhang, K.; Yap, F. L.; Li, K.; Ng, C. T.; Li, L. J.; Loh, K. P. Large Scale Graphene/Hexagonal Boron Nitride Heterostructure for Tunable Plasmonics. *Advanced Functional Materials* **2014**, *24* (6), 731–738. https://doi.org/10.1002/adfm.201302009.

(102) Kim, S. M.; Hsu, A.; Park, M. H.; Chae, S. H.; Yun, S. J.; Lee, J. S.; Cho, D.-H.; Fang, W.; Lee, C.; Palacios, T.; Dresselhaus, M.; Kim, K. K.; Lee, Y. H.; Kong, J. Synthesis of Large-Area Multilayer Hexagonal Boron Nitride for High Material Performance. *Nature Communications* **2015**, *6* (1), 8662. https://doi.org/10.1038/ncomms9662.

(103) Levendorf, M. P.; Kim, C.-J.; Brown, L.; Huang, P. Y.; Havener, R. W.; Muller, D. A.; Park, J. Graphene and Boron Nitride Lateral Heterostructures for Atomically Thin Circuitry. *Nature* **2012**, *488* (7413), 627–632. https://doi.org/10.1038/nature11408.

(104) Ci, L.; Song, L.; Jin, C.; Jariwala, D.; Wu, D.; Li, Y.; Srivastava, A.; Wang, Z. F.; Storr, K.; Balicas, L.; Liu, F.; Ajayan, P. M. Atomic Layers of Hybridized Boron Nitride and Graphene Domains. *Nature Materials* **2010**, *9* (5), 430–435. https://doi.org/10.1038/nmat2711.

(105) Zhu, J.; Kang, J.; Kang, J.; Jariwala, D.; Wood, J. D.; Seo, J.-W. T.; Chen, K.-S.; Marks, T. J.; Hersam, M. C. Solution-Processed Dielectrics Based on Thickness-Sorted Two-Dimensional Hexagonal Boron Nitride Nanosheets. *Nano Lett.* **2015**, *15* (10), 7029–7036. https://doi.org/10.1021/acs.nanolett.5b03075.

(106) Song, L.; Ci, L.; Lu, H.; Sorokin, P. B.; Jin, C.; Ni, J.; Kvashnin, A. G.; Kvashnin, D. G.; Lou, J.; Yakobson, B. I.; Ajayan, P. M. Large Scale Growth and Characterization of Atomic Hexagonal Boron Nitride Layers. *Nano Lett.* **2010**, *10* (8), 3209–3215. https://doi.org/10.1021/nl1022139.

(107) Shi, Y.; Hamsen, C.; Jia, X.; Kim, K. K.; Reina, A.; Hofmann, M.; Hsu, A. L.; Zhang, K.; Li, H.; Juang, Z.-Y.; Dresselhaus, Mildred. S.; Li, L.-J.; Kong, J. Synthesis of Few-Layer Hexagonal Boron Nitride Thin Film by Chemical Vapor Deposition. *Nano Lett.* **2010**, *10* (10), 4134–4139. https://doi.org/10.1021/nl1023707.

(108) Liu, Z.; Song, L.; Zhao, S.; Huang, J.; Ma, L.; Zhang, J.; Lou, J.; Ajayan, P. M. Direct Growth of Graphene/Hexagonal Boron Nitride Stacked Layers. *Nano Lett.* **2011**, *11* (5), 2032–2037. https://doi.org/10.1021/nl200464j.

(109) Gorbachev, R. V.; Riaz, I.; Nair, R. R.; Jalil, R.; Britnell, L.; Belle, B. D.; Hill, E. W.; Novoselov, K. S.; Watanabe, K.; Taniguchi, T.; Geim, A. K.; Blake, P. Hunting for Monolayer Boron Nitride: Optical and Raman Signatures. *Small* **2011**, *7* (4), 465–468. https://doi.org/10.1002/smll.201001628.

(110) Britnell, L.; Gorbachev, R. V.; Jalil, R.; Belle, B. D.; Schedin, F.; Katsnelson, M. I.; Eaves, L.; Morozov, S. V.; Mayorov, A. S.; Peres, N. M. R.; Castro Neto, A. H.; Leist, J.; Geim,

A. K.; Ponomarenko, L. A.; Novoselov, K. S. Electron Tunneling through Ultrathin Boron Nitride Crystalline Barriers. *Nano Lett.* **2012**, *12* (3), 1707–1710. https://doi.org/10.1021/nl3002205.

(111) Guo, N.; Wei, J.; Fan, L.; Jia, Y.; Liang, D.; Zhu, H.; Wang, K.; Wu, D. Controllable Growth of Triangular Hexagonal Boron Nitride Domains on Copper Foils by an Improved Low-Pressure Chemical Vapor Deposition Method. *Nanotechnology* **2012**, *23* (41), 415605. https://doi.org/10.1088/0957-4484/23/41/415605.

(112) Ismach, A.; Chou, H.; Ferrer, D. A.; Wu, Y.; McDonnell, S.; Floresca, H. C.; Covacevich, A.; Pope, C.; Piner, R.; Kim, M. J.; Wallace, R. M.; Colombo, L.; Ruoff, R. S. Toward the Controlled Synthesis of Hexagonal Boron Nitride Films. *ACS Nano* **2012**, *6* (7), 6378–6385. https://doi.org/10.1021/nn301940k.

(113) Wang, M.; Jang, S. K.; Jang, W.-J.; Kim, M.; Park, S.-Y.; Kim, S.-W.; Kahng, S.-J.; Choi, J.-Y.; Ruoff, R. S.; Song, Y. J.; Lee, S. A Platform for Large-Scale Graphene Electronics – CVD Growth of Single-Layer Graphene on CVD-Grown Hexagonal Boron Nitride. *Advanced Materials* **2013**, *25* (19), 2746–2752. https://doi.org/10.1002/adma.201204904.

(114) Gibb, A. L.; Alem, N.; Chen, J.-H.; Erickson, K. J.; Ciston, J.; Gautam, A.; Linck, M.; Zettl, A. Atomic Resolution Imaging of Grain Boundary Defects in Monolayer Chemical Vapor Deposition-Grown Hexagonal Boron Nitride. *J. Am. Chem. Soc.* **2013**, *135* (18), 6758–6761. https://doi.org/10.1021/ja400637n.

(115) Kim, G.; Jang, A.-R.; Jeong, H. Y.; Lee, Z.; Kang, D. J.; Shin, H. S. Growth of High-Crystalline, Single-Layer Hexagonal Boron Nitride on Recyclable Platinum Foil. *Nano Lett.* **2013**, *13* (4), 1834–1839. https://doi.org/10.1021/nl400559s.

(116) Liu, Z.; Gong, Y.; Zhou, W.; Ma, L.; Yu, J.; Idrobo, J. C.; Jung, J.; MacDonald, A. H.; Vajtai, R.; Lou, J.; Ajayan, P. M. Ultrathin High-Temperature Oxidation-Resistant Coatings of Hexagonal Boron Nitride. *Nature Communications* **2013**, *4* (1), 2541. https://doi.org/10.1038/ncomms3541.

(117) Tay, R. Y.; Griep, M. H.; Mallick, G.; Tsang, S. H.; Singh, R. S.; Tumlin, T.; Teo, E. H. T.; Karna, S. P. Growth of Large Single-Crystalline Two-Dimensional Boron Nitride Hexagons on Electropolished Copper. *Nano Lett.* **2014**, *14* (2), 839–846. https://doi.org/10.1021/nl404207f.

(118) Park, J.-H.; Park, J. C.; Yun, S. J.; Kim, H.; Luong, D. H.; Kim, S. M.; Choi, S. H.; Yang, W.; Kong, J.; Kim, K. K.; Lee, Y. H. Large-Area Monolayer Hexagonal Boron Nitride on Pt Foil. *ACS Nano* **2014**, *8* (8), 8520–8528. https://doi.org/10.1021/nn503140y.

(119) Feigelson, B. N.; Bermudez, V. M.; Hite, J. K.; Robinson, Z. R.; Wheeler, V. D.; Sridhara, K.; Hernández, S. C. Growth and Spectroscopic Characterization of Monolayer and Few-Layer Hexagonal Boron Nitride on Metal Substrates. *Nanoscale* **2015**, *7* (8), 3694–3702. https://doi.org/10.1039/C4NR05557H.

(120) Wu, Q.; Jang, S. K.; Park, S.; Jung, S. J.; Suh, H.; Lee, Y. H.; Lee, S.; Song, Y. J. In Situ Synthesis of a Large Area Boron Nitride/Graphene Monolayer/Boron Nitride Film by Chemical Vapor Deposition. *Nanoscale* **2015**, *7* (17), 7574–7579. https://doi.org/10.1039/C5NR00889A.

(121) Stehle, Y.; Meyer, H. M.; Unocic, R. R.; Kidder, M.; Polizos, G.; Datskos, P. G.; Jackson, R.; Smirnov, S. N.; Vlassiouk, I. V. Synthesis of Hexagonal Boron Nitride Monolayer: Control of Nucleation and Crystal Morphology. *Chem. Mater.* **2015**, *27* (23), 8041–8047. https://doi.org/10.1021/acs.chemmater.5b03607.

(122) Khan, M. H.; Huang, Z.; Xiao, F.; Casillas, G.; Chen, Z.; Molino, P. J.; Liu, H. K. Synthesis of Large and Few Atomic Layers of Hexagonal Boron Nitride on Melted Copper. *Scientific Reports* **2015**, *5* (1), 7743. https://doi.org/10.1038/srep07743.

(123) Wen, Y.; Shang, X.; Dong, J.; Xu, K.; He, J.; Jiang, C. Ultraclean and Large-Area Monolayer Hexagonal Boron Nitride on Cu Foil Using Chemical Vapor Deposition. *Nanotechnology* **2015**, *26* (27), 275601. https://doi.org/10.1088/0957-4484/26/27/275601.

(124) Nai, C. T.; Lu, J.; Zhang, K.; Loh, K. P. Studying Edge Defects of Hexagonal Boron Nitride Using High-Resolution Electron Energy Loss Spectroscopy. *J. Phys. Chem. Lett.* **2015**, *6* (21), 4189–4193. https://doi.org/10.1021/acs.jpclett.5b01900.

(125) Kiraly, B.; Iski, E. V.; Mannix, A. J.; Fisher, B. L.; Hersam, M. C.; Guisinger, N. P. Solid-Source Growth and Atomic-Scale Characterization of Graphene on Ag(111). *Nature Communications* **2013**, *4* (1), 2804. https://doi.org/10.1038/ncomms3804.

(126) Warner, J. H.; Rümmeli, M. H.; Bachmatiuk, A.; Büchner, B. Atomic Resolution Imaging and Topography of Boron Nitride Sheets Produced by Chemical Exfoliation. *ACS Nano* **2010**, *4* (3), 1299–1304. https://doi.org/10.1021/nn901648q.

(127) Bianchini, F.; Patera, L. L.; Peressi, M.; Africh, C.; Comelli, G. Atomic Scale Identification of Coexisting Graphene Structures on Ni(111). *J. Phys. Chem. Lett.* **2014**, *5* (3), 467–473. https://doi.org/10.1021/jz402609d.

(128) Tang, S.; Wang, H.; Zhang, Y.; Li, A.; Xie, H.; Liu, X.; Liu, L.; Li, T.; Huang, F.; Xie, X.; Jiang, M. Precisely Aligned Graphene Grown on Hexagonal Boron Nitride by Catalyst Free Chemical Vapor Deposition. *Scientific Reports* **2013**, *3* (1), 2666. https://doi.org/10.1038/srep02666.

(129) Bhaviripudi, S.; Jia, X.; Dresselhaus, M. S.; Kong, J. Role of Kinetic Factors in Chemical Vapor Deposition Synthesis of Uniform Large Area Graphene Using Copper Catalyst. *Nano Lett.* **2010**, *10* (10), 4128–4133. https://doi.org/10.1021/nl102355e.

(130) Akbari, H.; Lin, W.-H.; Vest, B.; Jha, P. K.; Atwater, H. A. Temperature-Dependent Spectral Emission of Hexagonal Boron Nitride Quantum Emitters on Conductive and Dielectric Substrates. *Phys. Rev. Applied* **2021**, *15* (1), 014036. https://doi.org/10.1103/PhysRevApplied.15.014036.

(131) Novoselov, K. S.; Jiang, D.; Schedin, F.; Booth, T. J.; Khotkevich, V. V.; Morozov, S. V.; Geim, A. K. Two-Dimensional Atomic Crystals. *PNAS* **2005**, *102* (30), 10451–10453. https://doi.org/10.1073/pnas.0502848102.

(132) Novoselov, K. S.; Mishchenko, A.; Carvalho, A.; Neto, A. H. C. 2D Materials and van Der Waals Heterostructures. *Science* **2016**, *353* (6298). https://doi.org/10.1126/science.aac9439.

(133) Mas-Ballesté, R.; Gómez-Navarro, C.; Gómez-Herrero, J.; Zamora, F. 2D Materials: To Graphene and Beyond. *Nanoscale* **2011**, *3* (1), 20–30. https://doi.org/10.1039/C0NR00323A.

(134) Wang, F.; Wang, Z.; Yin, L.; Cheng, R.; Wang, J.; Wen, Y.; Shifa, T. A.; Wang, F.; Zhang, Y.; Zhan, X.; He, J. 2D Library beyond Graphene and Transition Metal Dichalcogenides: A Focus on Photodetection. *Chem. Soc. Rev.* **2018**, *47* (16), 6296–6341. https://doi.org/10.1039/C8CS00255J.

(135) Novoselov, K. S. Nobel Lecture: Graphene: Materials in the Flatland. *Rev. Mod. Phys.* **2011**, *83* (3), 837–849. https://doi.org/10.1103/RevModPhys.83.837.

(136) Gao, T.; Song, X.; Du, H.; Nie, Y.; Chen, Y.; Ji, Q.; Sun, J.; Yang, Y.; Zhang, Y.; Liu, Z. Temperature-Triggered Chemical Switching Growth of in-Plane and Vertically Stacked Graphene-Boron Nitride Heterostructures. *Nature Communications* **2015**, *6* (1), 6835. https://doi.org/10.1038/ncomms7835.

(137) Kim, K. K.; Hsu, A.; Jia, X.; Kim, S. M.; Shi, Y.; Hofmann, M.; Nezich, D.; Rodriguez-Nieva, J. F.; Dresselhaus, M.; Palacios, T.; Kong, J. Synthesis of Monolayer Hexagonal Boron Nitride on Cu Foil Using Chemical Vapor Deposition. *Nano Lett.* **2012**, *12* (1), 161–166. https://doi.org/10.1021/nl203249a.

(138) Fang, H.; Chuang, S.; Chang, T. C.; Takei, K.; Takahashi, T.; Javey, A. High-Performance Single Layered WSe_2 p-FETs with Chemically Doped Contacts. *Nano Lett.* **2012**, *12* (7), 3788–3792. https://doi.org/10.1021/nl301702r.

(139) Zeng, H.; Dai, J.; Yao, W.; Xiao, D.; Cui, X. Valley Polarization in MoS_2 Monolayers by Optical Pumping. *Nature Nanotechnology* **2012**, *7* (8), 490–493. https://doi.org/10.1038/nnano.2012.95.

(140) Jones, A. M.; Yu, H.; Ghimire, N. J.; Wu, S.; Aivazian, G.; Ross, J. S.; Zhao, B.; Yan, J.; Mandrus, D. G.; Xiao, D.; Yao, W.; Xu, X. Optical Generation of Excitonic Valley Coherence in Monolayer WSe_2. *Nature Nanotechnology* **2013**, *8* (9), 634–638. https://doi.org/10.1038/nnano.2013.151.

(141) He, Z.; Sheng, Y.; Rong, Y.; Lee, G.-D.; Li, J.; Warner, J. H. Layer-Dependent Modulation of Tungsten Disulfide Photoluminescence by Lateral Electric Fields. *ACS Nano* **2015**, *9* (3), 2740–2748. https://doi.org/10.1021/nn506594a.

(142) Kim, I. S.; Sangwan, V. K.; Jariwala, D.; Wood, J. D.; Park, S.; Chen, K.-S.; Shi, F.; Ruiz-Zepeda, F.; Ponce, A.; Jose-Yacaman, M.; Dravid, V. P.; Marks, T. J.; Hersam, M. C.; Lauhon, L. J. Influence of Stoichiometry on the Optical and Electrical Properties of Chemical Vapor Deposition Derived MoS_2. *ACS Nano* **2014**, *8* (10), 10551–10558. https://doi.org/10.1021/nn503988x.

(143) Han, H.-V.; Lu, A.-Y.; Lu, L.-S.; Huang, J.-K.; Li, H.; Hsu, C.-L.; Lin, Y.-C.; Chiu, M.-H.; Suenaga, K.; Chu, C.-W.; Kuo, H.-C.; Chang, W.-H.; Li, L.-J.; Shi, Y. Photoluminescence Enhancement and Structure Repairing of Monolayer $MoSe_2$ by Hydrohalic Acid Treatment. *ACS Nano* **2016**, *10* (1), 1454–1461. https://doi.org/10.1021/acsnano.5b06960.

(144) Li, H.; Tsai, C.; Koh, A. L.; Cai, L.; Contryman, A. W.; Fragapane, A. H.; Zhao, J.; Han, H. S.; Manoharan, H. C.; Abild-Pedersen, F.; Nørskov, J. K.; Zheng, X. Activating and Optimizing MoS_2 Basal Planes for Hydrogen Evolution through the Formation of Strained Sulphur Vacancies. *Nature Materials* **2016**, *15* (1), 48–53. https://doi.org/10.1038/nmat4465.

(145) Jeong, H. Y.; Jin, Y.; Yun, S. J.; Zhao, J.; Baik, J.; Keum, D. H.; Lee, H. S.; Lee, Y. H. Heterogeneous Defect Domains in Single-Crystalline Hexagonal WS_2. *Advanced Materials* **2017**, *29* (15), 1605043. https://doi.org/10.1002/adma.201605043.

(146) Lin, Y.-C.; Li, S.; Komsa, H.-P.; Chang, L.-J.; Krasheninnikov, A. V.; Eda, G.; Suenaga, K. Revealing the Atomic Defects of WS_2 Governing Its Distinct Optical Emissions. *Advanced Functional Materials* **2018**, *28* (4), 1704210. https://doi.org/10.1002/adfm.201704210.

(147) Ly, T. H.; Yun, S. J.; Thi, Q. H.; Zhao, J. Edge Delamination of Monolayer Transition Metal Dichalcogenides. *ACS Nano* **2017**, *11* (7), 7534–7541. https://doi.org/10.1021/acsnano.7b04287.

(148) Sheng, Y.; Wang, X.; Fujisawa, K.; Ying, S.; Elias, A. L.; Lin, Z.; Xu, W.; Zhou, Y.; Korsunsky, A. M.; Bhaskaran, H.; Terrones, M.; Warner, J. H. Photoluminescence Segmentation within Individual Hexagonal Monolayer Tungsten Disulfide Domains Grown by Chemical Vapor Deposition. *ACS Appl. Mater. Interfaces* **2017**, *9* (17), 15005–15014. https://doi.org/10.1021/acsami.6b16287.

(149) Kumar, P.; Verma, N. C.; Goyal, N.; Biswas, J.; Lodha, S.; Nandi, C. K.; Balakrishnan, V. Phase Engineering of Seamless Heterophase Homojunctions with Co-Existing 3R and 2H Phases in WS_2 Monolayers. *Nanoscale* **2018**, *10* (7), 3320–3330. https://doi.org/10.1039/C7NR08303C.

(150) Kormányos, A.; Burkard, G.; Gmitra, M.; Fabian, J.; Zólyomi, V.; Drummond, N. D.; Fal'ko, V. K.p Theory for Two-Dimensional Transition Metal Dichalcogenide Semiconductors. *2D Mater.* **2015**, *2* (2), 022001. https://doi.org/10.1088/2053-1583/2/2/022001.

(151) Ulstrup, S.; Katoch, J.; Koch, R. J.; Schwarz, D.; Singh, S.; McCreary, K. M.; Yoo, H. K.; Xu, J.; Jonker, B. T.; Kawakami, R. K.; Bostwick, A.; Rotenberg, E.; Jozwiak, C. Spatially Resolved Electronic Properties of Single-Layer WS_2 on Transition Metal Oxides. *ACS Nano* **2016**, *10* (11), 10058–10067. https://doi.org/10.1021/acsnano.6b04914.

(152) Mak, K. F.; He, K.; Shan, J.; Heinz, T. F. Control of Valley Polarization in Monolayer MoS_2 by Optical Helicity. *Nature Nanotechnology* **2012**, *7* (8), 494–498. https://doi.org/10.1038/nnano.2012.96.

(153) Kioseoglou, G.; Hanbicki, A. T.; Currie, M.; Friedman, A. L.; Gunlycke, D.; Jonker, B. T. Valley Polarization and Intervalley Scattering in Monolayer MoS_2. *Appl. Phys. Lett.* **2012**, *101* (22), 221907. https://doi.org/10.1063/1.4768299.

(154) Cao, T.; Wang, G.; Han, W.; Ye, H.; Zhu, C.; Shi, J.; Niu, Q.; Tan, P.; Wang, E.; Liu, B.; Feng, J. Valley-Selective Circular Dichroism of Monolayer Molybdenum Disulphide. *Nature Communications* **2012**, *3* (1), 887. https://doi.org/10.1038/ncomms1882.

(155) Yu, T.; Wu, M. W. Valley Depolarization Due to Intervalley and Intravalley Electron-Hole Exchange Interactions in Monolayer MoS_2. *Phys. Rev. B* **2014**, *89* (20), 205303. https://doi.org/10.1103/PhysRevB.89.205303.

(156) Zhu, C. R.; Zhang, K.; Glazov, M.; Urbaszek, B.; Amand, T.; Ji, Z. W.; Liu, B. L.; Marie, X. Exciton Valley Dynamics Probed by Kerr Rotation in WSe_2 Monolayers. *Phys. Rev. B* **2014**, *90* (16), 161302. https://doi.org/10.1103/PhysRevB.90.161302.

(157) Mai, C.; Semenov, Y. G.; Barrette, A.; Yu, Y.; Jin, Z.; Cao, L.; Kim, K. W.; Gundogdu, K. Exciton Valley Relaxation in a Single Layer of WS_2 Measured by Ultrafast Spectroscopy. *Phys. Rev. B* **2014**, *90* (4), 041414. https://doi.org/10.1103/PhysRevB.90.041414.

(158) Kioseoglou, G.; Hanbicki, A. T.; Currie, M.; Friedman, A. L.; Jonker, B. T. Optical Polarization and Intervalley Scattering in Single Layers of MoS_2 and $MoSe_2$. *Scientific Reports* **2016**, *6* (1), 25041. https://doi.org/10.1038/srep25041.

(159) Wu, S.; Huang, C.; Aivazian, G.; Ross, J. S.; Cobden, D. H.; Xu, X. Vapor–Solid Growth of High Optical Quality MoS_2 Monolayers with Near-Unity Valley Polarization. *ACS Nano* **2013**, *7* (3), 2768–2772. https://doi.org/10.1021/nn4002038.

(160) Sallen, G.; Bouet, L.; Marie, X.; Wang, G.; Zhu, C. R.; Han, W. P.; Lu, Y.; Tan, P. H.; Amand, T.; Liu, B. L.; Urbaszek, B. Robust Optical Emission Polarization in MoS_2 Monolayers through Selective Valley Excitation. *Phys. Rev. B* **2012**, *86* (8), 081301. https://doi.org/10.1103/PhysRevB.86.081301.

(161) Lagarde, D.; Bouet, L.; Marie, X.; Zhu, C. R.; Liu, B. L.; Amand, T.; Tan, P. H.; Urbaszek, B. Carrier and Polarization Dynamics in Monolayer MoS_2. *Phys. Rev. Lett.* **2014**, *112* (4), 047401. https://doi.org/10.1103/PhysRevLett.112.047401.

(162) Hanbicki, A. T.; Kioseoglou, G.; Currie, M.; Hellberg, C. S.; McCreary, K. M.; Friedman, A. L.; Jonker, B. T. Anomalous Temperature-Dependent Spin-Valley Polarization in Monolayer WS_2. *Scientific Reports* **2016**, *6* (1), 18885. https://doi.org/10.1038/srep18885.

(163) Zhu, B.; Zeng, H.; Dai, J.; Gong, Z.; Cui, X. Anomalously Robust Valley Polarization and Valley Coherence in Bilayer WS_2. *PNAS* **2014**, *111* (32), 11606–11611. https://doi.org/10.1073/pnas.1406960111.

(164) Rosenberger, M. R.; Chuang, H.-J.; McCreary, K. M.; Li, C. H.; Jonker, B. T. Electrical Characterization of Discrete Defects and Impact of Defect Density on Photoluminescence in Monolayer WS_2. *ACS Nano* **2018**, *12* (2), 1793–1800. https://doi.org/10.1021/acsnano.7b08566.

(165) McCreary, K. M.; Currie, M.; Hanbicki, A. T.; Chuang, H.-J.; Jonker, B. T. Understanding Variations in Circularly Polarized Photoluminescence in Monolayer Transition Metal Dichalcogenides. *ACS Nano* **2017**, *11* (8), 7988–7994. https://doi.org/10.1021/acsnano.7b02554.

(166) Miller, B.; Steinhoff, A.; Pano, B.; Klein, J.; Jahnke, F.; Holleitner, A.; Wurstbauer, U. Long-Lived Direct and Indirect Interlayer Excitons in van Der Waals Heterostructures. *Nano Lett.* **2017**, *17* (9), 5229–5237. https://doi.org/10.1021/acs.nanolett.7b01304.

(167) Yu, Y.; Yu, Y.; Xu, C.; Cai, Y.-Q.; Su, L.; Zhang, Y.; Zhang, Y.-W.; Gundogdu, K.; Cao, L. Engineering Substrate Interactions for High Luminescence Efficiency of Transition-Metal Dichalcogenide Monolayers. *Advanced Functional Materials* **2016**, *26* (26), 4733–4739. https://doi.org/10.1002/adfm.201600418.

(168) Ceballos, F.; Bellus, M. Z.; Chiu, H.-Y.; Zhao, H. Ultrafast Charge Separation and Indirect Exciton Formation in a MoS_2–$MoSe_2$ van Der Waals Heterostructure. *ACS Nano* **2014**, *8* (12), 12717–12724. https://doi.org/10.1021/nn505736z.

(169) Wang, H.; Zhang, C.; Rana, F. Ultrafast Dynamics of Defect-Assisted Electron–Hole Recombination in Monolayer MoS_2. *Nano Lett.* **2015**, *15* (1), 339–345. https://doi.org/10.1021/nl503636c.

(170) Bhanu, U.; Islam, M. R.; Tetard, L.; Khondaker, S. I. Photoluminescence Quenching in Gold - MoS_2 Hybrid Nanoflakes. *Scientific Reports* **2014**, *4* (1), 5575. https://doi.org/10.1038/srep05575.

(171) Tongay, S.; Suh, J.; Ataca, C.; Fan, W.; Luce, A.; Kang, J. S.; Liu, J.; Ko, C.; Raghunathanan, R.; Zhou, J.; Ogletree, F.; Li, J.; Grossman, J. C.; Wu, J. Defects Activated Photoluminescence in Two-Dimensional Semiconductors: Interplay between Bound, Charged and Free Excitons. *Scientific Reports* **2013**, *3* (1), 2657. https://doi.org/10.1038/srep02657.

(172) Yuan, L.; Huang, L. Exciton Dynamics and Annihilation in WS_2 2D Semiconductors. *Nanoscale* **2015**, *7* (16), 7402–7408. https://doi.org/10.1039/C5NR00383K.

(173) Ceballos, F.; Zhao, H. Ultrafast Laser Spectroscopy of Two-Dimensional Materials Beyond Graphene. *Advanced Functional Materials* **2017**, *27* (19), 1604509. https://doi.org/10.1002/adfm.201604509.

(174) He, J.; He, D.; Wang, Y.; Cui, Q.; Ceballos, F.; Zhao, H. Spatiotemporal Dynamics of Excitons in Monolayer and Bulk WS_2. *Nanoscale* **2015**, *7* (21), 9526–9531. https://doi.org/10.1039/C5NR00188A.

(175) Zhao, P.; Amani, M.; Lien, D.-H.; Ahn, G. H.; Kiriya, D.; Mastandrea, J. P.; Ager, J. W.; Yablonovitch, E.; Chrzan, D. C.; Javey, A. Measuring the Edge Recombination Velocity of Monolayer Semiconductors. *Nano Lett.* **2017**, *17* (9), 5356–5360. https://doi.org/10.1021/acs.nanolett.7b01770.

(176) Gao, J.; Zhao, J.; Ding, F. Transition Metal Surface Passivation Induced Graphene Edge Reconstruction. *J. Am. Chem. Soc.* **2012**, *134* (14), 6204–6209. https://doi.org/10.1021/ja2104119.

(177) Mak, K. F.; Lee, C.; Hone, J.; Shan, J.; Heinz, T. F. Atomically Thin MoS2: A New Direct-Gap Semiconductor. *Phys. Rev. Lett.* **2010**, *105* (13), 136805. https://doi.org/10.1103/PhysRevLett.105.136805.

(178) Splendiani, A.; Sun, L.; Zhang, Y.; Li, T.; Kim, J.; Chim, C.-Y.; Galli, G.; Wang, F. Emerging Photoluminescence in Monolayer MoS_2. *Nano Lett.* **2010**, *10* (4), 1271–1275. https://doi.org/10.1021/nl903868w.

(179) Butler, S. Z.; Hollen, S. M.; Cao, L.; Cui, Y.; Gupta, J. A.; Gutiérrez, H. R.; Heinz, T. F.; Hong, S. S.; Huang, J.; Ismach, A. F.; Johnston-Halperin, E.; Kuno, M.; Plashnitsa, V. V.; Robinson, R. D.; Ruoff, R. S.; Salahuddin, S.; Shan, J.; Shi, L.; Spencer, M. G.; Terrones, M.; Windl, W.; Goldberger, J. E. Progress, Challenges, and Opportunities in Two-Dimensional Materials Beyond Graphene. *ACS Nano* **2013**, *7* (4), 2898–2926. https://doi.org/10.1021/nn400280c.

(180) Ganatra, R.; Zhang, Q. Few-Layer MoS2: A Promising Layered Semiconductor. *ACS Nano* **2014**, *8* (5), 4074–4099. https://doi.org/10.1021/nn405938z.

(181) Huang, J.-K.; Pu, J.; Hsu, C.-L.; Chiu, M.-H.; Juang, Z.-Y.; Chang, Y.-H.; Chang, W.-H.; Iwasa, Y.; Takenobu, T.; Li, L.-J. Large-Area Synthesis of Highly Crystalline WSe_2 Monolayers and Device Applications. *ACS Nano* **2014**, *8* (1), 923–930. https://doi.org/10.1021/nn405719x.

(182) Wang, Q. H.; Kalantar-Zadeh, K.; Kis, A.; Coleman, J. N.; Strano, M. S. Electronics and Optoelectronics of Two-Dimensional Transition Metal Dichalcogenides. *Nature Nanotechnology* **2012**, *7* (11), 699–712. https://doi.org/10.1038/nnano.2012.193.

(183) Xia, F.; Wang, H.; Xiao, D.; Dubey, M.; Ramasubramaniam, A. Two-Dimensional Material Nanophotonics. *Nature Photonics* **2014**, *8* (12), 899–907. https://doi.org/10.1038/nphoton.2014.271.

(184) Xiao, D.; Liu, G.-B.; Feng, W.; Xu, X.; Yao, W. Coupled Spin and Valley Physics in Monolayers of MoS_2 and Other Group-VI Dichalcogenides. *Phys. Rev. Lett.* **2012**, *108* (19), 196802. https://doi.org/10.1103/PhysRevLett.108.196802.

(185) Wang, G.; Chernikov, A.; Glazov, M. M.; Heinz, T. F.; Marie, X.; Amand, T.; Urbaszek, B. Colloquium: Excitons in Atomically Thin Transition Metal Dichalcogenides. *Rev. Mod. Phys.* **2018**, *90* (2), 021001. https://doi.org/10.1103/RevModPhys.90.021001.

(186) Xiao, D.; Yao, W.; Niu, Q. Valley-Contrasting Physics in Graphene: Magnetic Moment and Topological Transport. *Phys. Rev. Lett.* **2007**, *99* (23), 236809. https://doi.org/10.1103/PhysRevLett.99.236809.

(187) Yao, W.; Xiao, D.; Niu, Q. Valley-Dependent Optoelectronics from Inversion Symmetry Breaking. *Phys. Rev. B* **2008**, *77* (23), 235406. https://doi.org/10.1103/PhysRevB.77.235406.

(188) Ross, J. S.; Wu, S.; Yu, H.; Ghimire, N. J.; Jones, A. M.; Aivazian, G.; Yan, J.; Mandrus, D. G.; Xiao, D.; Yao, W.; Xu, X. Electrical Control of Neutral and Charged Excitons in a Monolayer Semiconductor. *Nature Communications* **2013**, *4* (1), 1474. https://doi.org/10.1038/ncomms2498.

(189) Schadt, M. Liquid Crystal Materials and Liquid Crystal Displays. *Annu. Rev. Mater. Sci.* **1997**, *27* (1), 305–379. https://doi.org/10.1146/annurev.matsci.27.1.305.

(190) Albani, L.; Marchessoux, C.; Kimpe, T. Stereoscopic Display Technologies and Their Applications in Medical Imaging. *Information Display* **2011**, *27* (10), 24–29. https://doi.org/10.1002/j.2637-496X.2011.tb00435.x.

(191) Farshchi, R.; Ramsteiner, M.; Herfort, J.; Tahraoui, A.; Grahn, H. T. Optical Communication of Spin Information between Light Emitting Diodes. *Appl. Phys. Lett.* **2011**, *98* (16), 162508. https://doi.org/10.1063/1.3582917.

(192) Hammerer, K.; Sørensen, A. S.; Polzik, E. S. Quantum Interface between Light and Atomic Ensembles. *Rev. Mod. Phys.* **2010**, *82* (2), 1041–1093. https://doi.org/10.1103/RevModPhys.82.1041.

(193) Ursin, R.; Jennewein, T.; Aspelmeyer, M.; Kaltenbaek, R.; Lindenthal, M.; Walther, P.; Zeilinger, A. Quantum Teleportation across the Danube. *Nature* **2004**, *430* (7002), 849–849. https://doi.org/10.1038/430849a.

(194) Wang, G.; Palleau, E.; Amand, T.; Tongay, S.; Marie, X.; Urbaszek, B. Polarization and Time-Resolved Photoluminescence Spectroscopy of Excitons in $MoSe_2$ Monolayers. *Appl. Phys. Lett.* **2015**, *106* (11), 112101. https://doi.org/10.1063/1.4916089.

(195) Yang, W.; Shang, J.; Wang, J.; Shen, X.; Cao, B.; Peimyoo, N.; Zou, C.; Chen, Y.; Wang, Y.; Cong, C.; Huang, W.; Yu, T. Electrically Tunable Valley-Light Emitting Diode (VLED) Based on CVD-Grown Monolayer WS_2. *Nano Lett.* **2016**, *16* (3), 1560–1567. https://doi.org/10.1021/acs.nanolett.5b04066.

(196) Wang, Z.; Dong, Z.; Gu, Y.; Chang, Y.-H.; Zhang, L.; Li, L.-J.; Zhao, W.; Eda, G.; Zhang, W.; Grinblat, G.; Maier, S. A.; Yang, J. K. W.; Qiu, C.-W.; Wee, A. T. S. Giant Photoluminescence Enhancement in Tungsten-Diselenide–Gold Plasmonic Hybrid Structures. *Nature Communications* **2016**, *7* (1), 11283. https://doi.org/10.1038/ncomms11283.

(197) You, Y.; Zhang, X.-X.; Berkelbach, T. C.; Hybertsen, M. S.; Reichman, D. R.; Heinz, T. F. Observation of Biexcitons in Monolayer WSe_2. *Nature Physics* **2015**, *11* (6), 477–481. https://doi.org/10.1038/nphys3324.

(198) Hsu, W.-T.; Chen, Y.-L.; Chen, C.-H.; Liu, P.-S.; Hou, T.-H.; Li, L.-J.; Chang, W.-H. Optically Initialized Robust Valley-Polarized Holes in Monolayer WSe_2. *Nature Communications* **2015**, *6* (1), 8963. https://doi.org/10.1038/ncomms9963.

(199) Wu, S.; Ross, J. S.; Liu, G.-B.; Aivazian, G.; Jones, A.; Fei, Z.; Zhu, W.; Xiao, D.; Yao, W.; Cobden, D.; Xu, X. Electrical Tuning of Valley Magnetic Moment through Symmetry Control in Bilayer MoS_2. *Nature Physics* **2013**, *9* (3), 149–153. https://doi.org/10.1038/nphys2524.

(200) Aivazian, G.; Gong, Z.; Jones, A. M.; Chu, R.-L.; Yan, J.; Mandrus, D. G.; Zhang, C.; Cobden, D.; Yao, W.; Xu, X. Magnetic Control of Valley Pseudospin in Monolayer WSe_2. *Nature Physics* **2015**, *11* (2), 148–152. https://doi.org/10.1038/nphys3201.

(201) Li, Y.; Ludwig, J.; Low, T.; Chernikov, A.; Cui, X.; Arefe, G.; Kim, Y. D.; van der Zande, A. M.; Rigosi, A.; Hill, H. M.; Kim, S. H.; Hone, J.; Li, Z.; Smirnov, D.; Heinz, T. F. Valley Splitting and Polarization by the Zeeman Effect in Monolayer $MoSe_2$. *Phys. Rev. Lett.* **2014**, *113* (26), 266804. https://doi.org/10.1103/PhysRevLett.113.266804.

(202) MacNeill, D.; Heikes, C.; Mak, K. F.; Anderson, Z.; Kormányos, A.; Zólyomi, V.; Park, J.; Ralph, D. C. Breaking of Valley Degeneracy by Magnetic Field in Monolayer $MoSe_2$ *Phys. Rev. Lett.* **2015**, *114* (3), 037401. https://doi.org/10.1103/PhysRevLett.114.037401.

(203) Mak, K. F.; Shan, J. Photonics and Optoelectronics of 2D Semiconductor Transition Metal Dichalcogenides. *Nature Photonics* **2016**, *10* (4), 216–226. https://doi.org/10.1038/nphoton.2015.282.

(204) Srivastava, A.; Sidler, M.; Allain, A. V.; Lembke, D. S.; Kis, A.; Imamoğlu, A. Valley Zeeman Effect in Elementary Optical Excitations of Monolayer WSe_2. *Nature Physics* **2015**, *11* (2), 141–147. https://doi.org/10.1038/nphys3203.

(205) Ye, Y.; Xiao, J.; Wang, H.; Ye, Z.; Zhu, H.; Zhao, M.; Wang, Y.; Zhao, J.; Yin, X.; Zhang, X. Electrical Generation and Control of the Valley Carriers in a Monolayer Transition Metal Dichalcogenide. *Nature Nanotechnology* **2016**, *11* (7), 598–602. https://doi.org/10.1038/nnano.2016.49.

(206) Lin, H.-T.; Chang, C.-Y.; Cheng, P.-J.; Li, M.-Y.; Cheng, C.-C.; Chang, S.-W.; Li, L. L. J.; Chu, C.-W.; Wei, P.-K.; Shih, M.-H. Circular Dichroism Control of Tungsten Diselenide (WSe_2) Atomic Layers with Plasmonic Metamolecules. *ACS Appl. Mater. Interfaces* **2018**, *10* (18), 15996–16004. https://doi.org/10.1021/acsami.8b01472.

(207) Wen, T.; Zhang, W.; Liu, S.; Hu, A.; Zhao, J.; Ye, Y.; Chen, Y.; Qiu, C.-W.; Gong, Q.; Lu, G. Steering Valley-Polarized Emission of Monolayer MoS_2 Sandwiched in Plasmonic Antennas. *Science Advances* **2020**, *6* (21), eaao0019. https://doi.org/10.1126/sciadv.aao0019.

(208) Jiang, Q.; Du, B.; Jiang, M.; Liu, D.; Liu, Z.; Li, B.; Liu, Z.; Lin, F.; Zhu, X.; Fang, Z. Ultrathin Circular Polarimeter Based on Chiral Plasmonic Metasurface and Monolayer $MoSe_2$. *Nanoscale* **2020**, *12* (10), 5906–5913. https://doi.org/10.1039/C9NR10768A.

(209) Sun, J.; Hu, H.; Pan, D.; Zhang, S.; Xu, H. Selectively Depopulating Valley-Polarized Excitons in Monolayer MoS_2 by Local Chirality in Single Plasmonic Nanocavity. *Nano Lett.* **2020**, *20* (7), 4953–4959. https://doi.org/10.1021/acs.nanolett.0c01019.

(210) Shinokita, K.; Wang, X.; Miyauchi, Y.; Watanabe, K.; Taniguchi, T.; Matsuda, K. Continuous Control and Enhancement of Excitonic Valley Polarization in Monolayer WSe_2 by Electrostatic Doping. *Advanced Functional Materials* **2019**, *29* (26), 1900260. https://doi.org/10.1002/adfm.201900260.

(211) Li, Z.; Liu, C.; Rong, X.; Luo, Y.; Cheng, H.; Zheng, L.; Lin, F.; Shen, B.; Gong, Y.; Zhang, S.; Fang, Z. Tailoring MoS2 Valley-Polarized Photoluminescence with Super Chiral Near-Field. *Advanced Materials* **2018**, *30* (34), 1801908. https://doi.org/10.1002/adma.201801908.

(212) Wu, Z.; Li, J.; Zhang, X.; Redwing, J. M.; Zheng, Y. Room-Temperature Active Modulation of Valley Dynamics in a Monolayer Semiconductor through Chiral Purcell

Effects. *Advanced Materials* **2019**, *31* (49), 1904132. https://doi.org/10.1002/adma.201904132.

(213) Li, Z.; Li, Y.; Han, T.; Wang, X.; Yu, Y.; Tay, B.; Liu, Z.; Fang, Z. Tailoring MoS2 Exciton–Plasmon Interaction by Optical Spin–Orbit Coupling. *ACS Nano* **2017**, *11* (2), 1165–1171. https://doi.org/10.1021/acsnano.6b06834.

(214) Valev, V. K.; Smisdom, N.; Silhanek, A. V.; De Clercq, B.; Gillijns, W.; Ameloot, M.; Moshchalkov, V. V.; Verbiest, T. Plasmonic Ratchet Wheels: Switching Circular Dichroism by Arranging Chiral Nanostructures. *Nano Lett.* **2009**, *9* (11), 3945–3948. https://doi.org/10.1021/nl9021623.

(215) Kuwata-Gonokami, M.; Saito, N.; Ino, Y.; Kauranen, M.; Jefimovs, K.; Vallius, T.; Turunen, J.; Svirko, Y. Giant Optical Activity in Quasi-Two-Dimensional Planar Nanostructures. *Phys. Rev. Lett.* **2005**, *95* (22), 227401. https://doi.org/10.1103/PhysRevLett.95.227401.

(216) Huttunen, M. J.; Bautista, G.; Decker, M.; Linden, S.; Wegener, M.; Kauranen, M. Nonlinear Chiral Imaging of Subwavelength-Sized Twisted-Cross Gold Nanodimers [Invited]. *Opt. Mater. Express, OME* **2011**, *1* (1), 46–56. https://doi.org/10.1364/OME.1.000046.

(217) Decker, M.; Zhao, R.; Soukoulis, C. M.; Linden, S.; Wegener, M. Twisted Split-Ring-Resonator Photonic Metamaterial with Huge Optical Activity. *Opt. Lett., OL* **2010**, *35* (10), 1593–1595. https://doi.org/10.1364/OL.35.001593.

(218) Plum, E.; Liu, X.-X.; Fedotov, V. A.; Chen, Y.; Tsai, D. P.; Zheludev, N. I. Metamaterials: Optical Activity without Chirality. *Phys. Rev. Lett.* **2009**, *102* (11), 113902. https://doi.org/10.1103/PhysRevLett.102.113902.

(219) Zhang, C.; Wu, K.; Giannini, V.; Li, X. Planar Hot-Electron Photodetection with Tamm Plasmons. *ACS Nano* **2017**, *11* (2), 1719–1727. https://doi.org/10.1021/acsnano.6b07578.

(220) Belardini, A.; Larciprete, M. C.; Centini, M.; Fazio, E.; Sibilia, C.; Chiappe, D.; Martella, C.; Toma, A.; Giordano, M.; Buatier de Mongeot, F. Circular Dichroism in the Optical Second-Harmonic Emission of Curved Gold Metal Nanowires. *Phys. Rev. Lett.* **2011**, *107* (25), 257401. https://doi.org/10.1103/PhysRevLett.107.257401.

(221) Meinzer, N.; Hendry, E.; Barnes, W. L. Probing the Chiral Nature of Electromagnetic Fields Surrounding Plasmonic Nanostructures. *Phys. Rev. B* **2013**, *88* (4), 041407. https://doi.org/10.1103/PhysRevB.88.041407.

(222) Cotrufo, M.; Osorio, C. I.; Koenderink, A. F. Spin-Dependent Emission from Arrays of Planar Chiral Nanoantennas Due to Lattice and Localized Plasmon Resonances. *ACS Nano* **2016**, *10* (3), 3389–3397. https://doi.org/10.1021/acsnano.5b07231.

(223) Valev, V. K.; Baumberg, J. J.; Sibilia, C.; Verbiest, T. Chirality and Chiroptical Effects in Plasmonic Nanostructures: Fundamentals, Recent Progress, and Outlook. *Advanced Materials* **2013**, *25* (18), 2517–2534. https://doi.org/10.1002/adma.201205178.

(224) Kühn, S.; Håkanson, U.; Rogobete, L.; Sandoghdar, V. Enhancement of Single-Molecule Fluorescence Using a Gold Nanoparticle as an Optical Nanoantenna. *Phys. Rev. Lett.* **2006**, *97* (1), 017402. https://doi.org/10.1103/PhysRevLett.97.017402.

(225) Klein, A.; Tiefenbacher, S.; Eyert, V.; Pettenkofer, C.; Jaegermann, W. Electronic Band Structure of Single-Crystal and Single-Layer WS_2 Influence of Interlayer van Der Waals Interactions. *Phys. Rev. B* **2001**, *64* (20), 205416. https://doi.org/10.1103/PhysRevB.64.205416.

(226) Gusakova, J.; Wang, X.; Shiau, L. L.; Krivosheeva, A.; Shaposhnikov, V.; Borisenko, V.; Gusakov, V.; Tay, B. K. Electronic Properties of Bulk and Monolayer TMDs: Theoretical Study Within DFT Framework (GVJ-2e Method). *Physica status solidi (a)* **2017**, *214* (12), 1700218. https://doi.org/10.1002/pssa.201700218.

(227) Yang, L.; Sinitsyn, N. A.; Chen, W.; Yuan, J.; Zhang, J.; Lou, J.; Crooker, S. A. Long-Lived Nanosecond Spin Relaxation and Spin Coherence of Electrons in Monolayer MoS_2 and WS_2. *Nature Physics* **2015**, *11* (10), 830–834. https://doi.org/10.1038/nphys3419.

(228) Zeng, H.; Liu, G.-B.; Dai, J.; Yan, Y.; Zhu, B.; He, R.; Xie, L.; Xu, S.; Chen, X.; Yao, W.; Cui, X. Optical Signature of Symmetry Variations and Spin-Valley Coupling in Atomically Thin Tungsten Dichalcogenides. *Scientific Reports* **2013**, *3*, 1608. https://doi.org/10.1038/srep01608.

(229) Britnell, L.; Ribeiro, R. M.; Eckmann, A.; Jalil, R.; Belle, B. D.; Mishchenko, A.; Kim, Y.-J.; Gorbachev, R. V.; Georgiou, T.; Morozov, S. V.; Grigorenko, A. N.; Geim, A. K.; Casiraghi, C.; Neto, A. H. C.; Novoselov, K. S. Strong Light-Matter Interactions in Heterostructures of Atomically Thin Films. *Science* **2013**, *340* (6138), 1311–1314. https://doi.org/10.1126/science.1235547.

(230) Gao, T.; Zhang, Q.; Li, L.; Zhou, X.; Li, L.; Li, H.; Zhai, T. 2D Ternary Chalcogenides. *Advanced Optical Materials* **2018**, *6* (14), 1800058. https://doi.org/10.1002/adom.201800058.

(231) Pham, V. P.; Yeom, G. Y. Recent Advances in Doping of Molybdenum Disulfide: Industrial Applications and Future Prospects. *Advanced Materials* **2016**, *28* (41), 9024–9059. https://doi.org/10.1002/adma.201506402.

(232) Wang, L.; Hu, P.; Long, Y.; Liu, Z.; He, X. Recent Advances in Ternary Two-Dimensional Materials: Synthesis, Properties and Applications. *J. Mater. Chem. A* **2017**, *5* (44), 22855–22876. https://doi.org/10.1039/C7TA06971E.

(233) Tedstone, A. A.; Lewis, D. J.; O'Brien, P. Synthesis, Properties, and Applications of Transition Metal-Doped Layered Transition Metal Dichalcogenides. *Chem. Mater.* **2016**, *28* (7), 1965–1974. https://doi.org/10.1021/acs.chemmater.6b00430.

(234) Xie, L. M. Two-Dimensional Transition Metal Dichalcogenide Alloys: Preparation, Characterization and Applications. *Nanoscale* **2015**, *7* (44), 18392–18401. https://doi.org/10.1039/C5NR05712D.

(235) Li, H.-M.; Lee, D.-Y.; Choi, M. S.; Qu, D.; Liu, X.; Ra, C.-H.; Yoo, W. J. Metal-Semiconductor Barrier Modulation for High Photoresponse in Transition Metal Dichalcogenide Field Effect Transistors. *Scientific Reports* **2014**, *4* (1), 4041. https://doi.org/10.1038/srep04041.

(236) Radisavljevic, B.; Radenovic, A.; Brivio, J.; Giacometti, V.; Kis, A. Single-Layer MoS_2 Transistors. *Nature Nanotechnology* **2011**, *6* (3), 147–150. https://doi.org/10.1038/nnano.2010.279.

(237) Radisavljevic, B.; Whitwick, M. B.; Kis, A. Integrated Circuits and Logic Operations Based on Single-Layer MoS_2. *ACS Nano* **2011**, *5* (12), 9934–9938. https://doi.org/10.1021/nn203715c.

(238) Jo, S.; Ubrig, N.; Berger, H.; Kuzmenko, A. B.; Morpurgo, A. F. Mono- and Bilayer WS_2 Light-Emitting Transistors. *Nano Lett.* **2014**, *14* (4), 2019–2025. https://doi.org/10.1021/nl500171v.

(239) Liu, W.; Sarkar, D.; Kang, J.; Cao, W.; Banerjee, K. Impact of Contact on the Operation and Performance of Back-Gated Monolayer MoS2 Field-Effect-Transistors. *ACS Nano* **2015**, *9* (8), 7904–7912. https://doi.org/10.1021/nn506512j.

(240) Liu, Y.; Stradins, P.; Wei, S.-H. Van Der Waals Metal-Semiconductor Junction: Weak Fermi Level Pinning Enables Effective Tuning of Schottky Barrier. *Science Advances* **2016**, *2* (4), e1600069. https://doi.org/10.1126/sciadv.1600069.

(241) Xu, J.; Shim, J.; Park, J.-H.; Lee, S. MXene Electrode for the Integration of WSe_2 and MoS_2 Field Effect Transistors. *Advanced Functional Materials* **2016**, *26* (29), 5328–5334. https://doi.org/10.1002/adfm.201600771.

(242) Dimoulas, A.; Tsipas, P.; Sotiropoulos, A.; Evangelou, E. K. Fermi-Level Pinning and Charge Neutrality Level in Germanium. *Appl. Phys. Lett.* **2006**, *89* (25), 252110. https://doi.org/10.1063/1.2410241.

(243) Kim, C.; Moon, I.; Lee, D.; Choi, M. S.; Ahmed, F.; Nam, S.; Cho, Y.; Shin, H.-J.; Park, S.; Yoo, W. J. Fermi Level Pinning at Electrical Metal Contacts of Monolayer Molybdenum Dichalcogenides. *ACS Nano* **2017**, *11* (2), 1588–1596. https://doi.org/10.1021/acsnano.6b07159.

(244) Ahmed, F.; Choi, M. S.; Liu, X.; Yoo, W. J. Carrier Transport at the Metal–MoS_2 Interface. *Nanoscale* **2015**, *7* (20), 9222–9228. https://doi.org/10.1039/C5NR01044F.

(245) Liu, H.; Si, M.; Deng, Y.; Neal, A. T.; Du, Y.; Najmaei, S.; Ajayan, P. M.; Lou, J.; Ye, P. D. Switching Mechanism in Single-Layer Molybdenum Disulfide Transistors: An Insight into Current Flow across Schottky Barriers. *ACS Nano* **2014**, *8* (1), 1031–1038. https://doi.org/10.1021/nn405916t.

(246) Allain, A.; Kang, J.; Banerjee, K.; Kis, A. Electrical Contacts to Two-Dimensional Semiconductors. *Nature Materials* **2015**, *14* (12), 1195–1205. https://doi.org/10.1038/nmat4452.

(247) Das, S.; Chen, H.-Y.; Penumatcha, A. V.; Appenzeller, J. High Performance Multilayer MoS_2 Transistors with Scandium Contacts. *Nano Lett.* **2013**, *13* (1), 100–105. https://doi.org/10.1021/nl303583v.

(248) Liu, Y.; Guo, J.; Zhu, E.; Liao, L.; Lee, S.-J.; Ding, M.; Shakir, I.; Gambin, V.; Huang, Y.; Duan, X. Approaching the Schottky–Mott Limit in van Der Waals Metal–Semiconductor Junctions. *Nature* **2018**, *557* (7707), 696–700. https://doi.org/10.1038/s41586-018-0129-8.

(249) McDonnell, S.; Addou, R.; Buie, C.; Wallace, R. M.; Hinkle, C. L. Defect-Dominated Doping and Contact Resistance in MoS_2. *ACS Nano* **2014**, *8* (3), 2880–2888. https://doi.org/10.1021/nn500044q.

(250) Yuan, H.; Cheng, G.; You, L.; Li, H.; Zhu, H.; Li, W.; Kopanski, J. J.; Obeng, Y. S.; Hight Walker, A. R.; Gundlach, D. J.; Richter, C. A.; Ioannou, D. E.; Li, Q. Influence of Metal–MoS_2 Interface on MoS2 Transistor Performance: Comparison of Ag and Ti Contacts. *ACS Appl. Mater. Interfaces* **2015**, *7* (2), 1180–1187. https://doi.org/10.1021/am506921y.

(251) Park, W.; Kim, Y.; Jung, U.; Yang, J. H.; Cho, C.; Kim, Y. J.; Hasan, S. M. N.; Kim, H. G.; Lee, H. B. R.; Lee, B. H. Complementary Unipolar WS_2 Field-Effect Transistors Using Fermi-Level Depinning Layers. *Advanced Electronic Materials* **2016**, *2* (2), 1500278. https://doi.org/10.1002/aelm.201500278.

(252) Kim, Y.; Park, W.; Yang, J. H.; Cho, C.; Lee, S. K.; Lee, B. H. Reduction of Low-Frequency Noise in Multilayer MoS_2 FETs Using a Fermi-Level Depinning Layer. *physica*

status solidi (RRL) – Rapid Research Letters **2016**, *10* (8), 634–638. https://doi.org/10.1002/pssr.201600136.

(253) Fang, H.; Tosun, M.; Seol, G.; Chang, T. C.; Takei, K.; Guo, J.; Javey, A. Degenerate N-Doping of Few-Layer Transition Metal Dichalcogenides by Potassium. *Nano Lett.* **2013**, *13* (5), 1991–1995. https://doi.org/10.1021/nl400044m.

(254) Du, Y.; Liu, H.; Neal, A. T.; Si, M.; Ye, P. D. Molecular Doping of Multilayer MoS_2 Field-Effect Transistors: Reduction in Sheet and Contact Resistances. *IEEE Electron Device Letters* **2013**, *34* (10), 1328–1330. https://doi.org/10.1109/LED.2013.2277311.

(255) Yang, L.; Majumdar, K.; Liu, H.; Du, Y.; Wu, H.; Hatzistergos, M.; Hung, P. Y.; Tieckelmann, R.; Tsai, W.; Hobbs, C.; Ye, P. D. Chloride Molecular Doping Technique on 2D Materials: WS_2 and MoS_2. *Nano Lett.* **2014**, *14* (11), 6275–6280. https://doi.org/10.1021/nl502603d.

(256) Guimarães, M. H. D.; Gao, H.; Han, Y.; Kang, K.; Xie, S.; Kim, C.-J.; Muller, D. A.; Ralph, D. C.; Park, J. Atomically Thin Ohmic Edge Contacts Between Two-Dimensional Materials. *ACS Nano* **2016**, *10* (6), 6392–6399. https://doi.org/10.1021/acsnano.6b02879.

(257) Iqbal, M. W.; Iqbal, M. Z.; Khan, M. F.; Kamran, M. A.; Majid, A.; Alharbi, T.; Eom, J. Tailoring the Electrical and Photo-Electrical Properties of a WS_2 Field Effect Transistor by Selective n-Type Chemical Doping. *RSC Adv.* **2016**, *6* (29), 24675–24682. https://doi.org/10.1039/C6RA02390H.

(258) Khalil, H. M. W.; Khan, M. F.; Eom, J.; Noh, H. Highly Stable and Tunable Chemical Doping of Multilayer WS_2 Field Effect Transistor: Reduction in Contact Resistance. *ACS Appl. Mater. Interfaces* **2015**, *7* (42), 23589–23596. https://doi.org/10.1021/acsami.5b06825.

(259) Ji, Q.; Li, C.; Wang, J.; Niu, J.; Gong, Y.; Zhang, Z.; Fang, Q.; Zhang, Y.; Shi, J.; Liao, L.; Wu, X.; Gu, L.; Liu, Z.; Zhang, Y. Metallic Vanadium Disulfide Nanosheets as a Platform Material for Multifunctional Electrode Applications. *Nano Lett.* **2017**, *17* (8), 4908–4916. https://doi.org/10.1021/acs.nanolett.7b01914.

(260) Leong, W. S.; Ji, Q.; Mao, N.; Han, Y.; Wang, H.; Goodman, A. J.; Vignon, A.; Su, C.; Guo, Y.; Shen, P.-C.; Gao, Z.; Muller, D. A.; Tisdale, W. A.; Kong, J. Synthetic Lateral Metal-Semiconductor Heterostructures of Transition Metal Disulfides. *J. Am. Chem. Soc.* **2018**, *140* (39), 12354–12358. https://doi.org/10.1021/jacs.8b07806.

(261) Shin, H. G.; Yoon, H. S.; Kim, J. S.; Kim, M.; Lim, J. Y.; Yu, S.; Park, J. H.; Yi, Y.; Kim, T.; Jun, S. C.; Im, S. Vertical and In-Plane Current Devices Using NbS_2/n-MoS_2 van Der Waals Schottky Junction and Graphene Contact. *Nano Lett.* **2018**, *18* (3), 1937–1945. https://doi.org/10.1021/acs.nanolett.7b05338.

(262) Chee, S.-S.; Seo, D.; Kim, H.; Jang, H.; Lee, S.; Moon, S. P.; Lee, K. H.; Kim, S. W.; Choi, H.; Ham, M.-H. Lowering the Schottky Barrier Height by Graphene/Ag Electrodes for High-Mobility MoS_2 Field-Effect Transistors. *Advanced Materials* **2019**, *31* (2), 1804422. https://doi.org/10.1002/adma.201804422.

(263) Dawson, W. G.; Bullett, D. W. Electronic Structure and Crystallography of $MoTe_2$ and WTe_2. *J. Phys. C: Solid State Phys.* **1987**, *20* (36), 6159–6174. https://doi.org/10.1088/0022-3719/20/36/017.

(264) Song, S.; Kim, S.-Y.; Kwak, J.; Jo, Y.; Kim, J. H.; Lee, J. H.; Lee, J.-U.; Kim, J. U.; Yun, H. D.; Sim, Y.; Wang, J.; Lee, D. H.; Seok, S.-H.; Kim, T.; Cheong, H.; Lee, Z.; Kwon, S.-Y. Electrically Robust Single-Crystalline WTe_2 Nanobelts for Nanoscale Electrical

Interconnects. *Advanced Science* **2019**, *6* (3), 1801370. https://doi.org/10.1002/advs.201801370.

(265) Mleczko, M. J.; Yu, A. C.; Smyth, C. M.; Chen, V.; Shin, Y. C.; Chatterjee, S.; Tsai, Y.-C.; Nishi, Y.; Wallace, R. M.; Pop, E. Contact Engineering High-Performance n-Type $MoTe_2$ Transistors. *Nano Lett.* **2019**, *19* (9), 6352–6362. https://doi.org/10.1021/acs.nanolett.9b02497.

(266) Yun, S. J.; Han, G. H.; Kim, H.; Duong, D. L.; Shin, B. G.; Zhao, J.; Vu, Q. A.; Lee, J.; Lee, S. M.; Lee, Y. H. Telluriding Monolayer MoS_2 and WS_2 via Alkali Metal Scooter. *Nature Communications* **2017**, *8* (1), 2163. https://doi.org/10.1038/s41467-017-02238-0.

(267) Zhou, J.; Liu, F.; Lin, J.; Huang, X.; Xia, J.; Zhang, B.; Zeng, Q.; Wang, H.; Zhu, C.; Niu, L.; Wang, X.; Fu, W.; Yu, P.; Chang, T.-R.; Hsu, C.-H.; Wu, D.; Jeng, H.-T.; Huang, Y.; Lin, H.; Shen, Z.; Yang, C.; Lu, L.; Suenaga, K.; Zhou, W.; Pantelides, S. T.; Liu, G.; Liu, Z. Large-Area and High-Quality 2D Transition Metal Telluride. *Advanced Materials* **2017**, *29* (3), 1603471. https://doi.org/10.1002/adma.201603471.

(268) McCreary, K. M.; Hanbicki, A. T.; Jernigan, G. G.; Culbertson, J. C.; Jonker, B. T. Synthesis of Large-Area WS_2 Monolayers with Exceptional Photoluminescence. *Scientific Reports* **2016**, *6* (1), 19159. https://doi.org/10.1038/srep19159.

(269) Apte, A.; Krishnamoorthy, A.; Hachtel, J. A.; Susarla, S.; Idrobo, J. C.; Nakano, A.; Kalia, R. K.; Vashishta, P.; Tiwary, C. S.; Ajayan, P. M. Telluride-Based Atomically Thin Layers of Ternary Two-Dimensional Transition Metal Dichalcogenide Alloys. *Chem. Mater.* **2018**, *30* (20), 7262–7268. https://doi.org/10.1021/acs.chemmater.8b03444.

(270) Chen, K.; Chen, Z.; Wan, X.; Zheng, Z.; Xie, F.; Chen, W.; Gui, X.; Chen, H.; Xie, W.; Xu, J. A Simple Method for Synthesis of High-Quality Millimeter-Scale 1T′ Transition-Metal Telluride and Near-Field Nanooptical Properties. *Advanced Materials* **2017**, *29* (38), 1700704. https://doi.org/10.1002/adma.201700704.

(271) Jiang, Y. C.; Gao, J.; Wang, L. Raman Fingerprint for Semi-Metal WTe_2 Evolving from Bulk to Monolayer. *Scientific Reports* **2016**, *6* (1), 19624. https://doi.org/10.1038/srep19624.

(272) Tan, S. J. R.; Abdelwahab, I.; Ding, Z.; Zhao, X.; Yang, T.; Loke, G. Z. J.; Lin, H.; Verzhbitskiy, I.; Poh, S. M.; Xu, H.; Nai, C. T.; Zhou, W.; Eda, G.; Jia, B.; Loh, K. P. Chemical Stabilization of 1T′ Phase Transition Metal Dichalcogenides with Giant Optical Kerr Nonlinearity. *J. Am. Chem. Soc.* **2017**, *139* (6), 2504–2511. https://doi.org/10.1021/jacs.6b13238.

(273) Liu, L.; Wu, J.; Wu, L.; Ye, M.; Liu, X.; Wang, Q.; Hou, S.; Lu, P.; Sun, L.; Zheng, J.; Xing, L.; Gu, L.; Jiang, X.; Xie, L.; Jiao, L. Phase-Selective Synthesis of 1T′ MoS_2 Monolayers and Heterophase Bilayers. *Nature Materials* **2018**, *17* (12), 1108–1114. https://doi.org/10.1038/s41563-018-0187-1.

(274) Berkdemir, A.; Gutiérrez, H. R.; Botello-Méndez, A. R.; Perea-López, N.; Elías, A. L.; Chia, C.-I.; Wang, B.; Crespi, V. H.; López-Urías, F.; Charlier, J.-C.; Terrones, H.; Terrones, M. Identification of Individual and Few Layers of WS_2 Using Raman Spectroscopy. *Scientific Reports* **2013**, *3* (1), 1755. https://doi.org/10.1038/srep01755.

(275) Gaur, A. P. S.; Sahoo, S.; Scott, J. F.; Katiyar, R. S. Electron–Phonon Interaction and Double-Resonance Raman Studies in Monolayer WS_2. *J. Phys. Chem. C* **2015**, *119* (9), 5146–5151. https://doi.org/10.1021/jp512540u.

(276) Lin, Y.-C.; Yeh, C.-H.; Lin, H.-C.; Siao, M.-D.; Liu, Z.; Nakajima, H.; Okazaki, T.; Chou, M.-Y.; Suenaga, K.; Chiu, P.-W. Stable 1T Tungsten Disulfide Monolayer and Its Junctions: Growth and Atomic Structures. *ACS Nano* **2018**, *12* (12), 12080–12088. https://doi.org/10.1021/acsnano.8b04979.

(277) Kang, J.; Tongay, S.; Li, J.; Wu, J. Monolayer Semiconducting Transition Metal Dichalcogenide Alloys: Stability and Band Bowing. *Journal of Applied Physics* **2013**, *113* (14), 143703. https://doi.org/10.1063/1.4799126.

(278) Duan, X.; Wang, C.; Pan, A.; Yu, R.; Duan, X. Two-Dimensional Transition Metal Dichalcogenides as Atomically Thin Semiconductors: Opportunities and Challenges. *Chem. Soc. Rev.* **2015**, *44* (24), 8859–8876. https://doi.org/10.1039/C5CS00507H.

(279) Ding, Y.; Wang, Y.; Ni, J.; Shi, L.; Shi, S.; Tang, W. First Principles Study of Structural, Vibrational and Electronic Properties of Graphene-like MX_2 (M=Mo, Nb, W, Ta; X=S, Se, Te) Monolayers. *Physica B: Condensed Matter* **2011**, *406* (11), 2254–2260. https://doi.org/10.1016/j.physb.2011.03.044.

(280) Yue, Y.; Chen, J.; Zhang, Y.; Ding, S.; Zhao, F.; Wang, Y.; Zhang, D.; Li, R.; Dong, H.; Hu, W.; Feng, Y.; Feng, W. Two-Dimensional High-Quality Monolayered Triangular WS_2 Flakes for Field-Effect Transistors. *ACS Appl. Mater. Interfaces* **2018**, *10* (26), 22435–22444. https://doi.org/10.1021/acsami.8b05885.

(281) Xu, Z.-Q.; Zhang, Y.; Lin, S.; Zheng, C.; Zhong, Y. L.; Xia, X.; Li, Z.; Sophia, P. J.; Fuhrer, M. S.; Cheng, Y.-B.; Bao, Q. Synthesis and Transfer of Large-Area Monolayer WS_2 Crystals: Moving Toward the Recyclable Use of Sapphire Substrates. *ACS Nano* **2015**, *9* (6), 6178–6187. https://doi.org/10.1021/acsnano.5b01480.

(282) Robertson, J. Band Offsets, Schottky Barrier Heights, and Their Effects on Electronic Devices. *Journal of Vacuum Science & Technology A* **2013**, *31* (5), 050821. https://doi.org/10.1116/1.4818426.

(283) Zhou, J.; Lin, J.; Huang, X.; Zhou, Y.; Chen, Y.; Xia, J.; Wang, H.; Xie, Y.; Yu, H.; Lei, J.; Wu, D.; Liu, F.; Fu, Q.; Zeng, Q.; Hsu, C.-H.; Yang, C.; Lu, L.; Yu, T.; Shen, Z.; Lin, H.; Yakobson, B. I.; Liu, Q.; Suenaga, K.; Liu, G.; Liu, Z. A Library of Atomically Thin Metal Chalcogenides. *Nature* **2018**, *556* (7701), 355–359. https://doi.org/10.1038/s41586-018-0008-3.

Appendix A

SYNTHESIS OF GRAPHENE BY PLASMA ENHANCED CHEMICAL VAPOR DEPOSITION (PECVD)

Appendix A1: Experimental setup

The PECVD system consists of a microwave plasma source, a growth chamber, and a gas delivery system. The plasma source (Opthos Instruments Inc.) includes an Evenson cavity and a power supply (MPG-4) that provides an excitation frequency of 2450 MHz. The Evenson cavity matches the size of the growth chamber, which primarily consists of a 1/2-inch quartz tube (with the inner and outer diameters being 10.0 mm and 12.5 mm, respectively) and components for vacuum control. The reactant gas delivery system consists of four mass flow controllers (MFCs) for CH_4, Ar, H_2, and O_2. An extra variable leak valve is placed before the CH_4-MFC for precise control of the partial pressure of CH_4. During the growth process, the pressure of the system is maintained at ~ 25 mTorr. For the PECVD growth substrates, we use 25 μm-thick Cu-foils (Alfa Aesar with purity = 99.9996%). Prior to the graphene synthesis, the Cu-foils are always sonicated in ACE and IPA for 5 minutes, then dried by nitrogen gas before inserted into the growth chamber. Several pieces of (1.5 × 0.8) cm^2 Cu-foils may be first placed on a quartz boat and then introduced into the growth chamber.

Figure A1 shows our experimental apparatus of the direct PECVD growth system without additional furnace. A (1.5 × 0.8) cm^2 Cu-foil was first placed on the quartz boat and introduced into 1/2-inch quartz made process tube (top panel). The plasma was subsequently ignited in a mixture of CH_4 and H_2 gas and graphene growth on Cu ensued (middle panel). The partial pressure of each gas was detected by a residual gas analyzer (RGA). After graphene growth (bottom panel), the sample was cooled to room temperature within at least 30 mins without breaking vacuum. Cu deposit on the quartz tube and holder after the graphene growth (bottom panel) was the result of Cu etching and was taken to be a signature for a successful run.

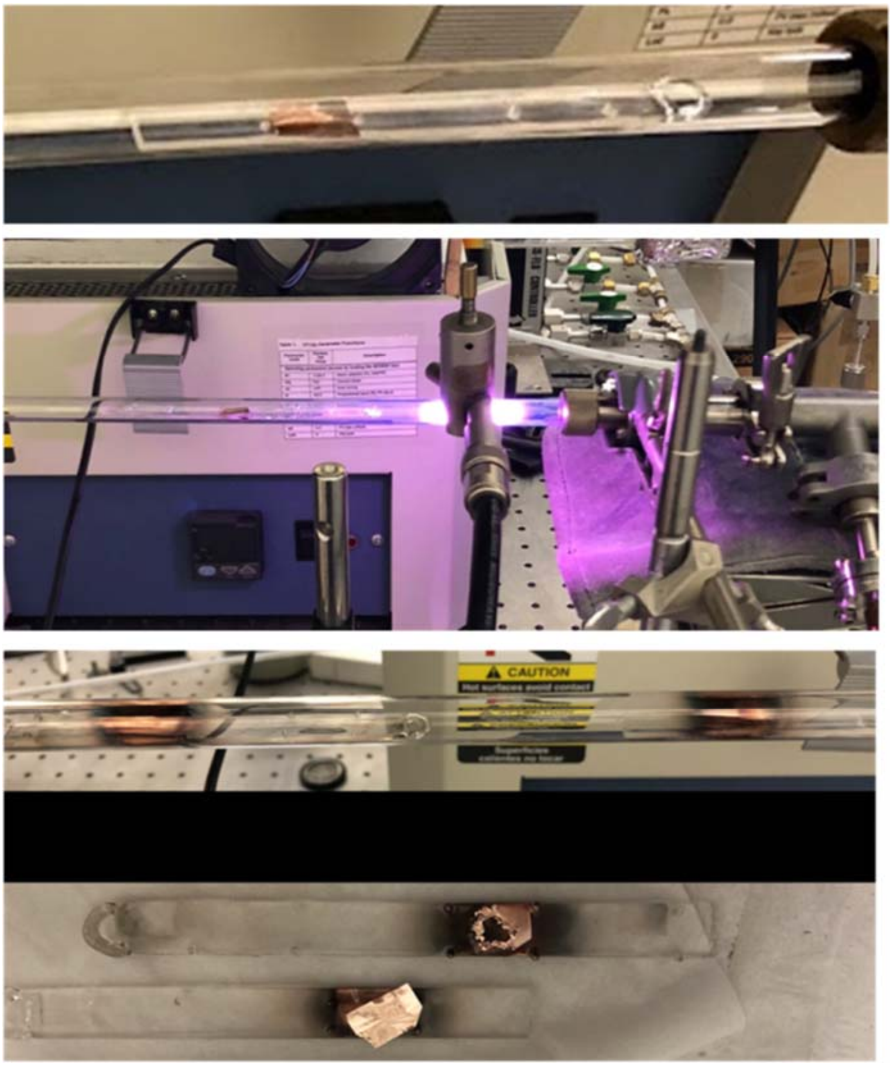

Figure A1. Schematic of the PECVD setup. Top panel: Photograph showing a 25 μm thick polycrystalline Cu-foil (purchased from Alfa Aesar with purity 99.9996%) being placed on a quart boat and inserted into the PECVD growth chamber that consists of a ½-inch quartz tube and vacuum components. Middle panel: Photograph showing continuous exposure of a Cu-foil to microwave plasma in a mixture of CH_4 and H_2 gas for ensuing graphene growth on Cu. Bottom panel: Photograph showing Cu deposit on both quartz tube and quartz boat after graphene growth due to the etching of Cu-foil during the growth process. The deposition of Cu is taken to be a signature for a successful run.

Appendix A2: Sample growth conditions

This section describes the growth parameters for three types of BLG samples, and is divided into three parts: 1) growth parameters for hexagonal single crystalline BLG flakes, 2) sample preparation and growth parameters for large single crystalline BLG flakes, and 3) growth parameters for large BLG films with small twist-angle distributions.

The growth system is shown in Figure A1. During the PECVD-growth of graphene, the system pressure is always kept at ~ 2×10^{-2} torr, and the growth condition is mainly sensitive to the partial pressure of each reactant gas such as CH_4, H_2, and N_2 (N_2 is not controllable), but is insensitive to the background residual gases like Ar, N_2, O_2, and H_2O.

After inserting Cu-foils into the process tube, the system is first purged with Ar gas for at least 30 mins to ensure that the partial pressure of each residual gas remains largely the same. After the purge with Ar gas, H_2 is introduced into the system and then microwave plasma is ignited and kept on for 2 mins to remove CuO_x on the Cu-foils under a controlled gas pressure of 500 mTorr. The reactant gases for graphene growth (CH_4 and H_2) are subsequently added into the PECVD system and controlled to a stable flow for 10 mins before the plasma is ignited and set to a power of 40 W for ensuing graphene growth. After the graphene growth, the sample is cooled to room temperature for at least 30 mins without breaking the vacuum.

1) Growth conditions for hexagonal single crystalline BLG flakes

Under the growth parameters provided below in Table A1, the typical grain size (~ the diameter of a hexagon) of purely single crystalline MLG is around 3 μm. For BLG, the averaged grain size for the first and the second-layer is 5 μm and 1 μm, respectively. These growth parameters for single crystalline MLG and BLG samples are summarized in Table A1:

Table A1	Plasma (W)	P_{CH4} (torr)	P_{H2} (torr)	P_{CH4}/ P_{H2}	Growth Time
MLG	40	1×10^{-6}	1.2×10^{-5} (~ 2 sccm)	0.1	3 mins
BLG	40	7×10^{-7}	1.6×10^{-5} (~2.5 sccm)	0.04	3 mins

We note that under the growth conditions outlined above in the second row of Table A1, the resulting single crystalline BLG flakes do not favor any specific twist angle between layers. In contrast, for the growth parameters listed below in the second row of Table A2, most of the BLG flakes exhibit small twist-angle configurations. We repeat in the first row of Table A2 the same conditions shown in the second row of Table A1 for easy comparison of the growth conditions for BLG with random twist-angles (first row) and small twist-angle distributions (second row).

Table A2	Plasma (W)	P_{CH4} (torr)	P_{H2} (torr)	P_{CH4}/ P_{H2}	Growth Time
BLG (random)	40	7×10^{-7}	1.6×10^{-5} (~ 2.5 sccm)	0.04	3 mins
BLG (small-angle distributions)	40	9×10^{-7}	1.75×10^{-5} (~ 2.7 sccm)	0.05	3 mins

The interlayer twist angle has been determined through SEM imaging by measuring the neighboring edges of the first and second layers.

2) Sample preparation and growth parameters for large single crystalline BLG flakes

For the growth of large single crystalline BLG flakes, additional steps are needed in the preparation of the Cu substrates, as detailed below.

Cu-foils purchased from Nilacon with a thickness of 100 μm and a purity of 99.96% are prepared within following steps: *i*) sonication in ACE and IPA, *ii*) soaked in acetic acid (CH_3COOH) at 80 °C for 35 mins for the removal of CuO_x, and *iii*) annealed at 1050 °C in a mixture of Ar and H_2 gases for 30 mins to smooth the Cu surface. After the annealing process, the annealed Cu-foils are then inserted into PECVD system (Figure A1) for graphene growth. The growth parameters are as follows: plasma power = 40 W, $P_{CH4} = 7 \times 10^{-7}$ torr, $P_{H2} = 1.6 \times 10^{-5}$ torr (~ 2.5 sccm), and growth time = 20 mins. Under these growth parameters, the grain size of MLG and BLG can reach 15 μm and 5 μm, respectively. In this case, the interlayer twist angle in BLG does not favor any specific rotational configuration. Figure A2 shows the optical microscopic images of hexagonal single crystalline graphene grown on 100 μm thick Cu-foils and the corresponding Raman spectra.

3) Growth of large BLG films with small interlayer twist angles

Figure A3 (a)–(d) shows the SEM images of growth results with the evolution of CH_4-to-H_2 pressure ratio (P_{CH4}/P_{H2}) from 0.03 to 0.06 under a given H_2 flow rate at 3 sccm, and the partial pressures are determined by RGA and found to be ~ 2×10^{-5} torr for H_2. The white regions indicate the optical contrast for bare 285 nm SiO_2/Si substrate. The light and dark gray areas correspond to MLG and BLG regions, respectively. The density of BLG increases with increasing (P_{CH4}/P_{H2}). According to the SEM images (Figure A3(d)), it's clear to see that some multilayer graphene exhibited in the mm-size BLG. The growth parameter that we used in displaying Figure A3(d) shows that most of BLG prefers to arrange in the small angle configuration in accordance with the analysis of Raman spectroscopy (Figure A4).

Appendix A3

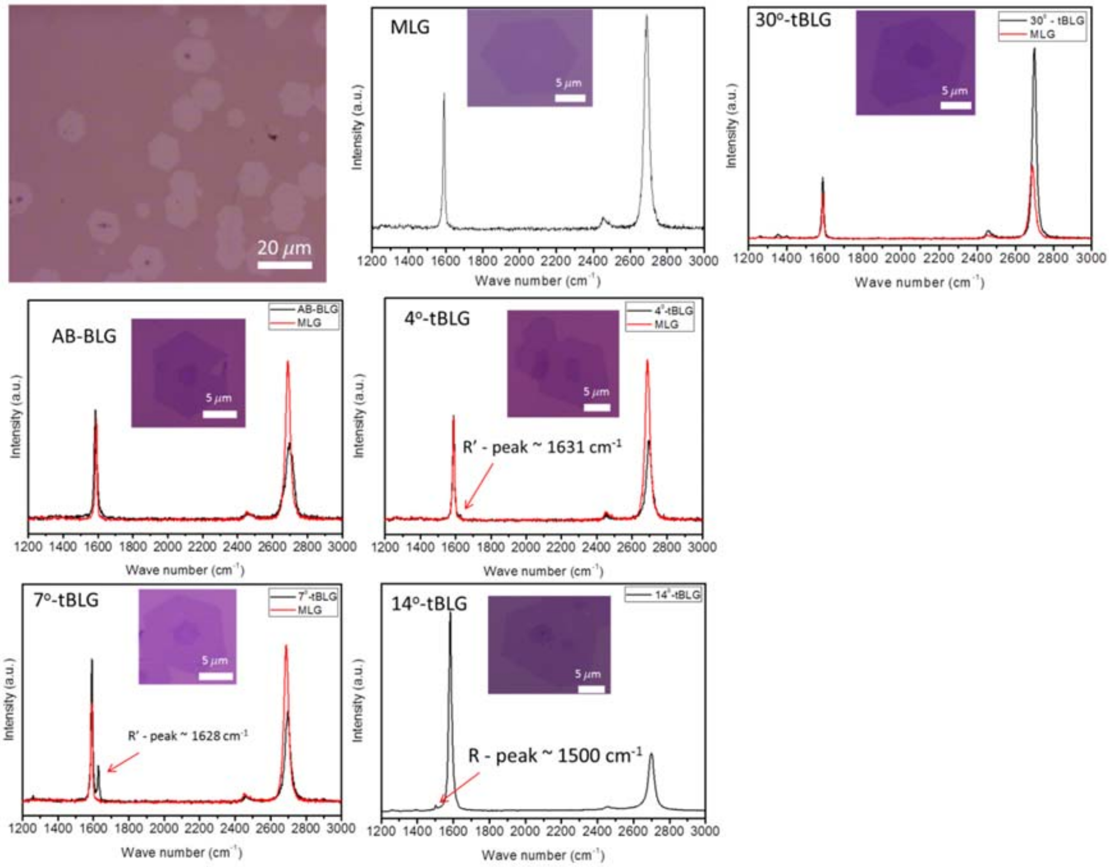

Figure A2 shows the single crystal MLG and BLG on Cu-foil, the second layer is hard to observe unless the Cu-foil is baked in order to reveal the color contrast. While, other images show the database of Raman spectrum in which the twisted angle was directly measured by the neighboring edges between layers. The related Raman mapping results are shown in Figure 2.6 in Chapter 2. Except the OM image for graphene grown on Cu-foil, the scale bars shown in other OM images indicate 5 μm.

Appendix A4

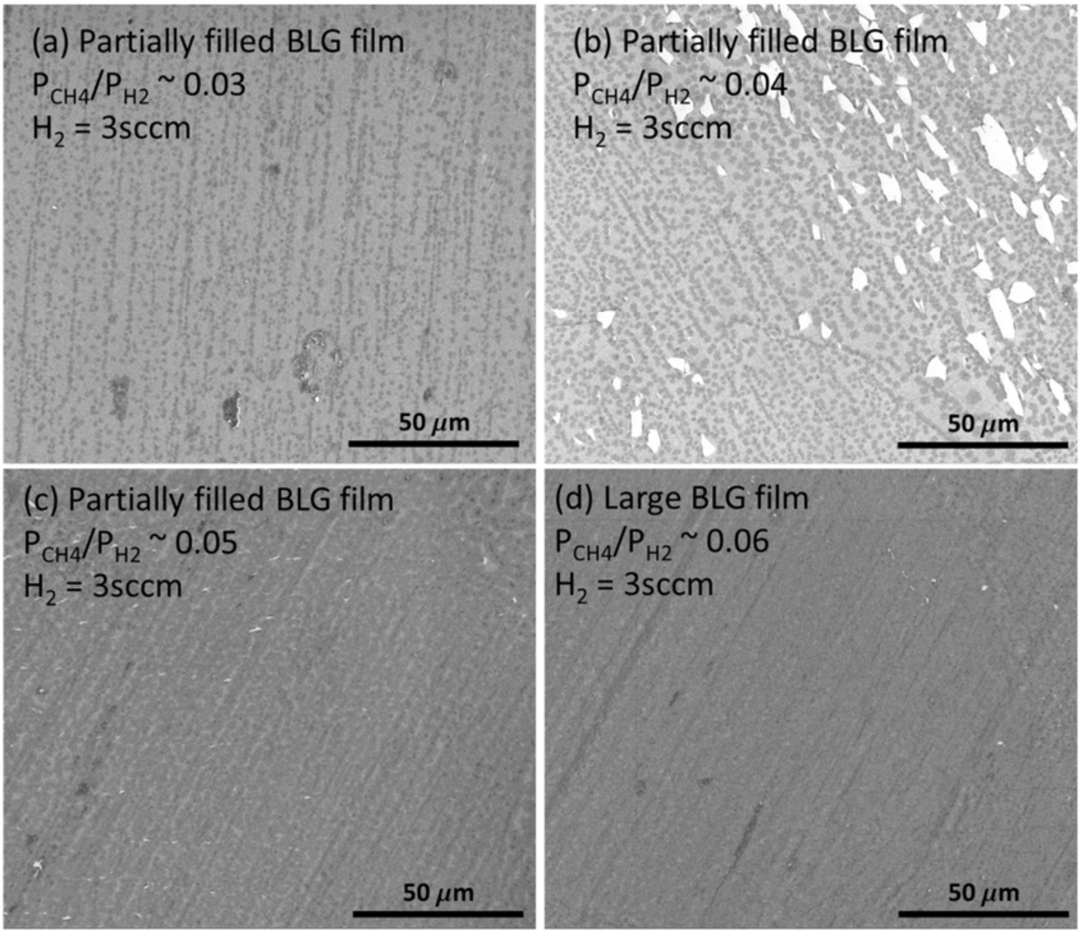

Figure A3. SEM images showing the evolution of BLG growth with increasing CH_4-to-H_2 pressure ratio (P_{CH4}/P_{H2}): (a) (P_{CH4}/P_{H2}) = 0.03, (b) (P_{CH4}/P_{H2}) = 0.04, (c) (P_{CH4}/P_{H2}) = 0.05, (d) (P_{CH4}/P_{H2}) = 0.06.

Appendix A5

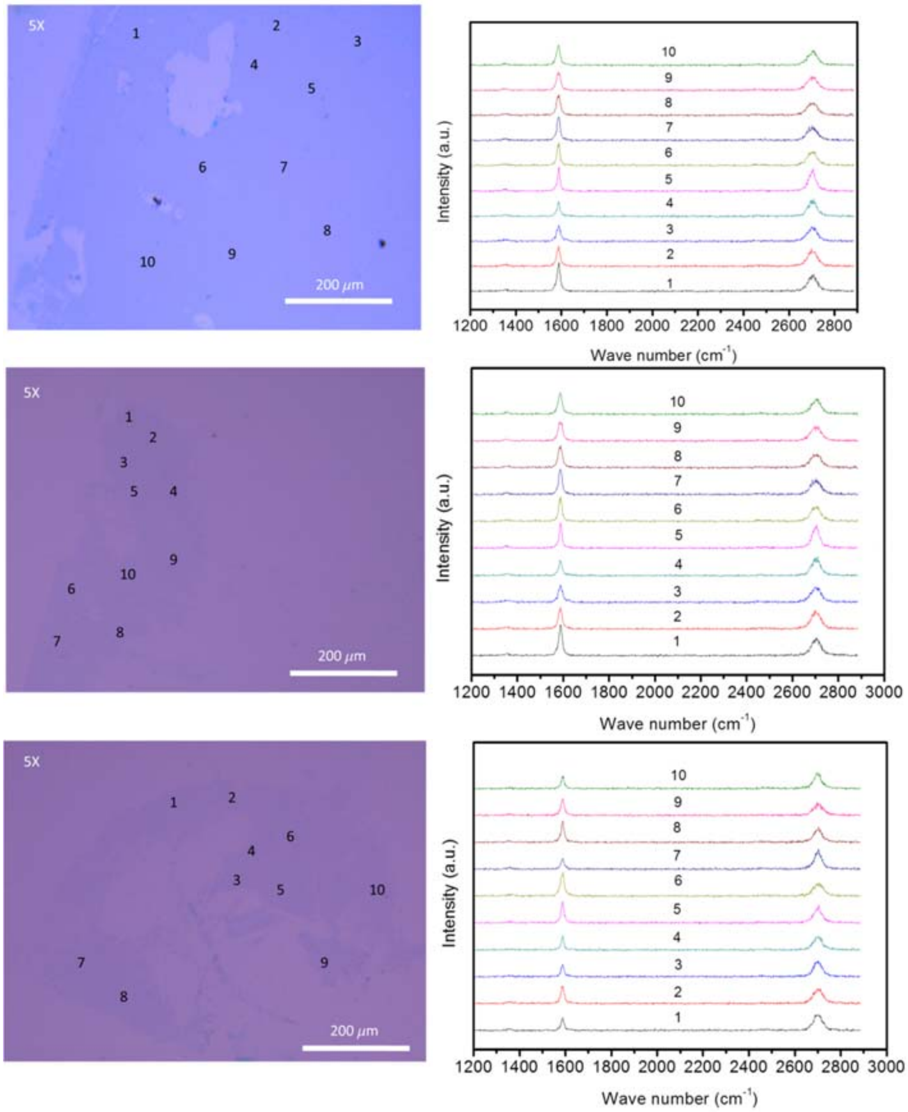

Figure A4. SEM images and Raman point spectra taken on an mm-size BLG film: We randomly select 20 different points over the BLG large film and check the corresponding Raman point spectra, with the first set of 10 points indicated on the SEM image (top left) and the corresponding Raman spectra shown in the top right panels, and the second set of 10 points indicated on the SEM image (bottom left) and corresponding Raman spectra shown in the bottom right panel. The position for each point Raman spectrum is first located by 5X optical magnification then the spectrum is taken under 100X magnification

Appendix B

SYNTHESIS OF 2D INSULATOR: HEXAGONAL BORON NITRIDE

Appendix B Note 1: Experimental setup

The setup comprises of a 52 mm inner diameter (I.D.) horizontal split tube furnace (MTI Corporation). The solid precursor ammonia-borane (NH_3-BH_3) powder, (97% purity, Sigma-Aldrich) is contained in a home-made quartz container, attached to the main growth chamber (22 mm I.D. quartz tube) via a leak valve and heated separately from the quartz tube via use of a resistive heating belt. Cu foils (25 µm, 99.999% pure, Alfa Aesar, item no. 10950) are used as the catalytic growth substrates. Copper foil was soaked and sonicated in acetone and isopropyl alcohol (IPA) for 30 min consecutively to remove organic impurities. Then, it was washed with deionized water and dried with nitrogen gas. The pressure in the growth chamber can be independently controlled via an angle valve at the vacuum pump while the pressure in the precursor bubbler can be controlled via the leak valve and carrier gas flow rates. The monolayer and multilayer h-BN was synthesized using a pressure controllable CVD system. The copper foil was inserted into the center of a 22 mm I.D. quartz tube, heated by a horizontal split-tube furnace. The Ammonia borane (NH_3-BH_3) (97% purity, from Sigma-Aldrich), stable in an atmospheric environment, was used as the precursor. It was loaded in a homemade quartz container which is isolated from the main CVD system with a leak valve to control the flow rate. The quartz tube inlet and outlet were blocked by filters to prevent the BN nanoparticles from diffusing into the gas line.

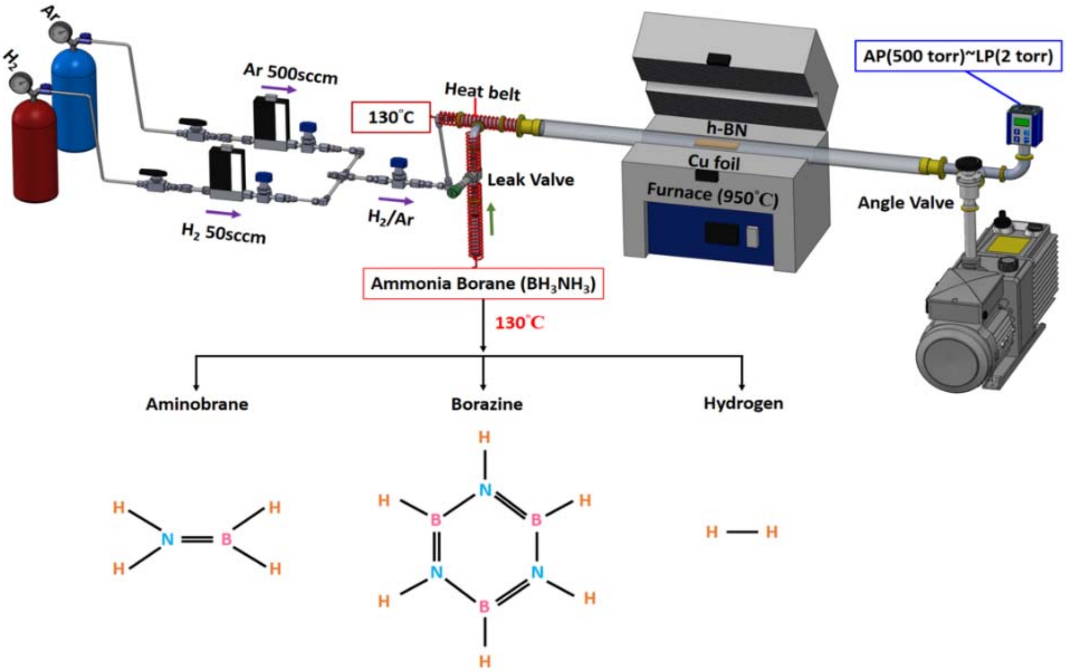

Figure B1. Schematic diagram of hybrid atmospheric pressure and low pressure CVD system used for h-BN grow.

Appendix B Note 2: h-BN growth conditions

First, the quartz tube was pumped down to 5×10^{-3} torr, and then ultrahigh purity grade hydrogen gas was introduced during the temperature ramp-up of the furnace (pressure ~100 mtorr, flow rate ~50 sccm). The copper foil was annealed at 950°C in hydrogen for 60 min to obtain a smooth surface. After annealing, the ultrahigh purity argon gas (500 sccm) was introduced into the system and waited for 50 min to stablized the tube environment. The precursor was heated to 130 °C and decomposed to hydrogen gas, monomeric aminoborane, and borazine gas. After the precursor temperature reached 130 °C, the manual valve between the quartz tube outlet and the pump was slowly closed and stopped until the pressure reached 20 torr. When the desired pressure was achieved, the leak valve to the precursor was opened. The typical growth time is 3 min for the monolayer h-BN layer and 20 min for the 20 nm thickness h-BN layer. To atomically control the thickness of the h-BN layer, it is very important to have a leak valve to control the flow rate of the precursor. Also, we can change the growth rate of the h-BN by changing the pressure of the growth environment. After growth, the tube furnace was cooled down with the cooling rate ~80 °C/min.

Appendix B Note 3: Summary of h-BN growth conditions

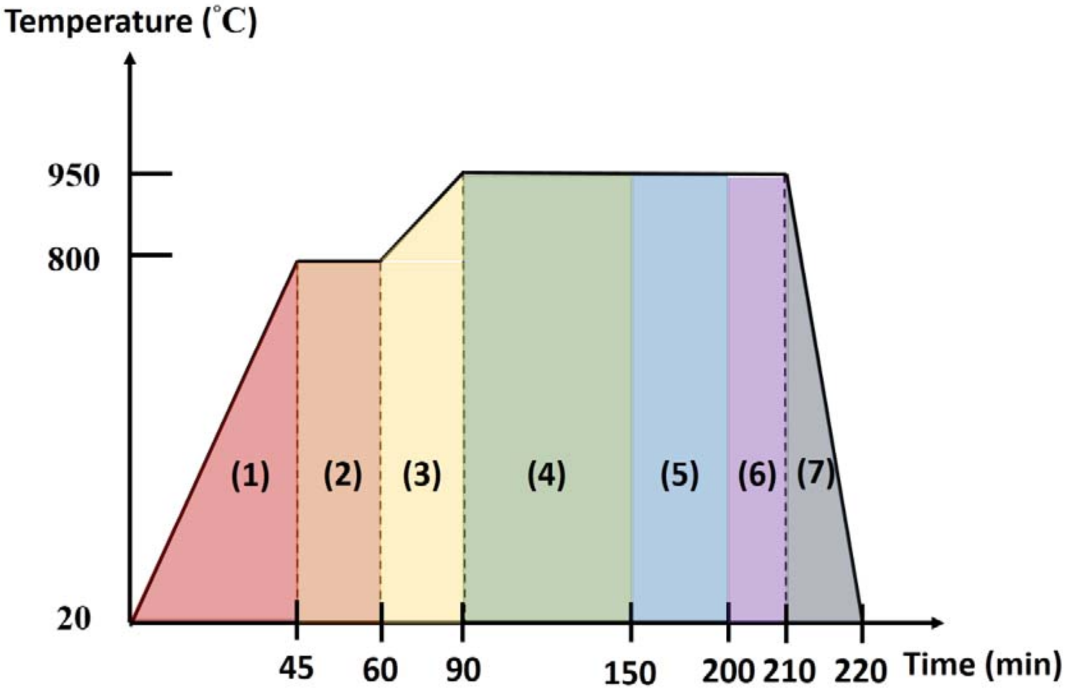

Figure B2. Temperature profiles of the substrate during the CVD h-BN growth.

Step 0. The precursor was weighted for 100 mg and put in the quartz tubing. The system was pumped down to 5×10^{-3} torr, and then ultrahigh purity grade hydrogen gas was introduced during the temperature ramp-up of the furnace.

Step 1. The temperature of the furnace was increased from 20 °C to 800 °C within 45 min under 50 sccm H_2 gas (P = 100 mtorr).

Step 2. The temperature of the furnace was held at 800 °C for 15 min under 50 sccm H_2 gas (P = 100 mtorr).

Step 3. The temperature of the furnace was increased from 800 °C to 950 °C within 30 min under 50 sccm H_2 gas (P = 100 mtorr).

Step 4. The temperature of the furnace was hold at 950 °C for 60 min under 50 sccm H_2 gas (P = 100 mtorr).

Step 5. The temperature of the furnace was held at 950 °C for 60 min under 50 sccm H_2 gas and 500 sccm Ar gas. (P = 2.5 torr). At the same time, the temperature of the precursor zone was heated to 130 °C and kept the system stable for 50 min.

Step 6. The leak valve was opened to start the hBN growth for 10 min.

Step 7. The tube furnace was cooled down with the cooling rate ~ 80°C/min.

Appendix C

SYNTHESIS OF 2D SEMICONDUCTOR: TRANSITION-METAL DICHALCOGENIDES

Appendix C Note 1: Experimental setup

The setup comprises of a quartz tube with a diameter of 25 mm (outer diameter)/22 mm (inner diameter) and a length of 100 cm, a one-inch inner diameter (I.D.) horizontal split tube furnace (Lindberg Blue M), two mass flow controllers calibrated for Ar and H_2, with stainless steel flanges at both ends connected to a chiller water circulation system operating at 10 °C.

SiO_2/Si substrates (300 nm SiO_2) were used for the CVD growth of WS_2. Prior to the growth, SiO_2/Si substrates were first soaked and sonicated in acetone and isopropyl alcohol (IPA) for 30 minutes to remove organic impurities, and then soaked in Nanostrip for 60 minutes, and finally washed with deionized water and dried with nitrogen gas.

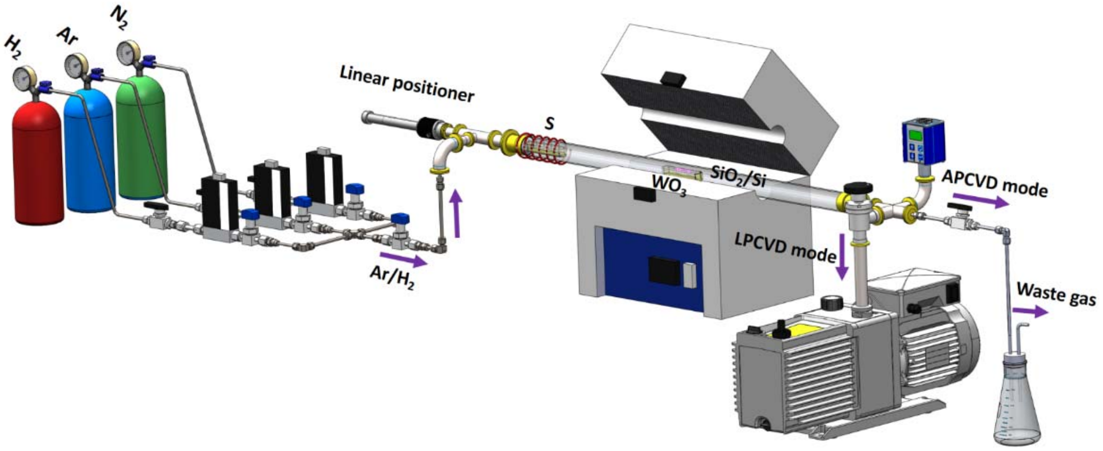

Figure C1. Schematic diagram of hybrid atmospheric pressure and low pressure CVD system used for h-WS_2 grow.

Appendix C Note 2: Sample growth conditions

In the first step of the procedure, 95 mg WO_3 precursor mixed with 5 mg KI was placed in a quartz boat containing the SiO_2/Si substrates set face-down directly above the W source precursor, and the quartz boat was then positioned at the center of the furnace. A second boat containing 100 mg S (Alfa Aesar, 99.999+ %) was placed upstream at 16 cm away from the W source. Next, the system was pump down to 3×10^{-2} torr to eliminate air and moisture. After the system reached the base pressure, the Ar/H_2 (80/40 sccm) carrier gas was introduced until atmospheric pressure was achieved. The furnace was then heated up with a ramp rate of 32 °C/min to the growth temperatures (750 to 850 °C). The Sulphur component melted at 150 °C was sent into the furnace at the growth temperature to grow h-WS_2. The sample growth procedure proceeded for 10 minutes, after which the furnace was directly opened to room temperature to stop the reaction immediately.

According to the reference[283], the growth of 2D TMDCs may be divided into four routes depending on the mass flux and growth rate. The formation of nucleus is highly affected by the mass flux of the metal precursor and the size of growth domains is dominated by the growth rate. A high mass flux of the metal precursor with a low growth rate produces polycrystalline film containing small grains and lots of grain boundaries, whereas a high mass flux with a high growth rate tends to form a smoother monolayer film with large grains and fewer grain boundaries. In contrast, a low mass flux of the metal precursor prefers to form single crystals with small domains when combined with a low growth rate, and a large monolayer single-crystal combined with a high growth rate.

In this report, we adapted the fourth route to form large monolayer WS_2 single crystals. Because the WS_2 growth rate is very slow, the growth can be approximately treated as a process close to thermodynamic equilibrium. Therefore, the morphology of the WS_2 domain is determined by the edge energy, and the domain shape can be obtained by equilibrium Wulff construction.[2] The different partial pressures of hydrogen gas is one of the methods to affect the Gibbs free energy of WS_2 edges in various orientations and form the equilibrium morphologies based on Wulff construction. By controlling the different partial pressures of hydrogen gas, we can control the shape of the single crystalline WS_2 from triangle, truncated triangle, hexagonal to dodecagon shapes.

The emission pattern of monolayer WS_2 single crystal can be modulated by stoichiometry, strain, doping, and density of non-radiative recombination centers. We have discussed these factors in the main text and have concluded that the W vacancies were the primary defects that behave like non-radiative centers responsible for the suppress PL. In the following, we would like to describe a novel approach that allows us to control the emission patterns of the TMDCs single crystals.

During the last step of our growth procedure, we open the furnace directly to cool the sample immediately. The sample shrinks during the cooling process in the CVD system, where the in-plane thermal expansion coefficients (CTEs) mismatch between the monolayer WS_2 and the SiO_2/Si substrate results in significant interfacial strain in the lateral direction, which in turn produces the initial crack length at the edge of the WS_2. According to the mode II cracking model, the critical crack size (c) along the edge is related to the interfacial toughness (K_{ic}) and tensile strain (σ) between the film and substrate. If the initial cracking size along the edge is larger than the critical cracking size, the crack allows to start to propagate toward the inner part of the single crystalline flake and then leads to buckling. We find that single crystalline flakes with the side lengths exceeding 50 μm have larger initial cracks, which trigger crack propagation so that the PL properties are dominant by the resulting buckling. On the contrary, small flakes (with the side lengths < 50 μm) without sufficiently large initial cracks do not allow cracks to propagate toward the inner part of the flakes. Although the buckling process may not be the dominant reason to alter the PL properties of small flakes of h-WS_2, the formation of cracks could be the defects that induce non-radiative recombination centers or stain distributions within the flake.

Appendix C Note 3: Summary of WS_2 growth conditions

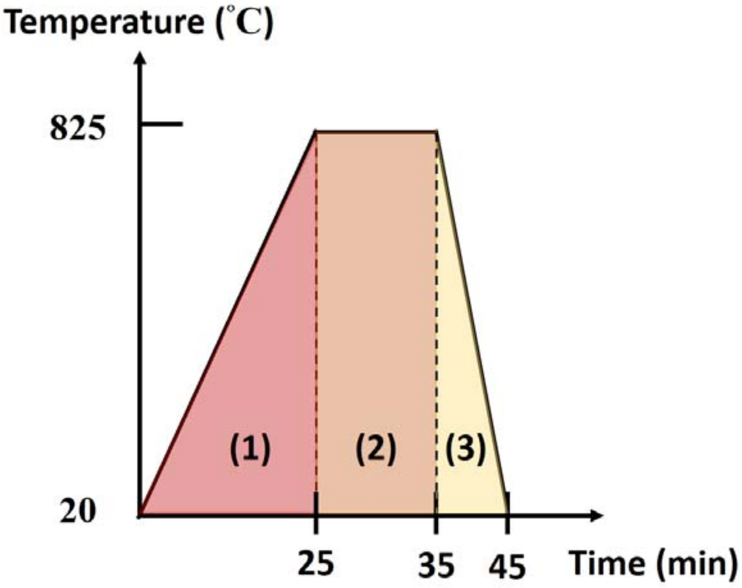

Figure C2. Temperature profiles of the substrate during the CVD WS_2 growth.

Step 0. 95 mg WO_3 precursor mixed with 5 mg KI was placed in a quartz boat containing the SiO_2/Si substrates set face-down directly above the W source precursor, and the quartz boat was then positioned at the center of the furnace. A second boat containing 100 mg S (Alfa Aesar, 99.999+ %) was placed upstream at 16 cm away from the W source. Next, the system was pumped down to 3×10^{-2} torr to eliminate air and moisture. The Ar/H_2 (80/40 sccm) carrier gas was introduced until atmospheric pressure.

Step 1. The temperature of the furnace was increased from 20 °C to 825 °C within 25 min under Ar/H_2 (80/40 sccm) carrier gas.

Step 2. The temperature of the furnace and the carrier gas environment remained the same as described in Step 1. In the meanwhile, the temperature of the S precursor zone was heated to 150 °C. The Sulphur precursor started to melt at this moment.

Step 3. The WS_2 was grown for 10 min.

Step 4. The tube furnace was cooled down with the cooling rate ~ 80 °C/min.

Appendix C Note 4: Summary of WTe_2 growth conditions

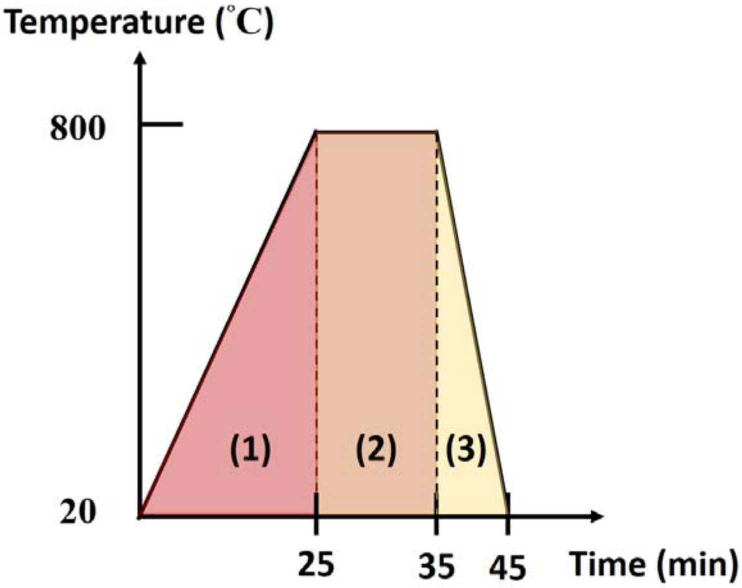

Figure C3. Temperature profiles of the substrate during the CVD WTe_2 growth.

Step 0. 95 mg WO_3 precursor mixed with 5 mg KI was placed in a quartz boat containing the SiO_2/Si substrates set face-down directly above the W source precursor, and the quartz boat was then positioned at the center of the furnace. A second boat containing 500 mg Te was placed upstream at 10 cm away from the W source. Next, the system was pumped down to 3×10^{-2} torr to eliminate air and moisture. The Ar/H_2 (80/40 sccm) carrier gas was introduced until atmospheric pressure.

Step 1. The temperature of the furnace was increased from 20 °C to 800 °C within 25 min under Ar/H_2 (80/40 sccm) carrier gas.

Step 2. The temperature of the furnace and the carrier gas environment remained the same as described in Step 1. In the meanwhile, the temperature of the Te precursor zone was heated to 500 °C. The Te precursor started to melt at this moment.

Step 3. The WTe_2 was grown for 25 min.

Step 4. The tube furnace was cooled down with the cooling rate ~ 80 °C/min.

Appendix C Note 5: Summary of $WTe_{2x}S_{2(1-x)}$ growth conditions

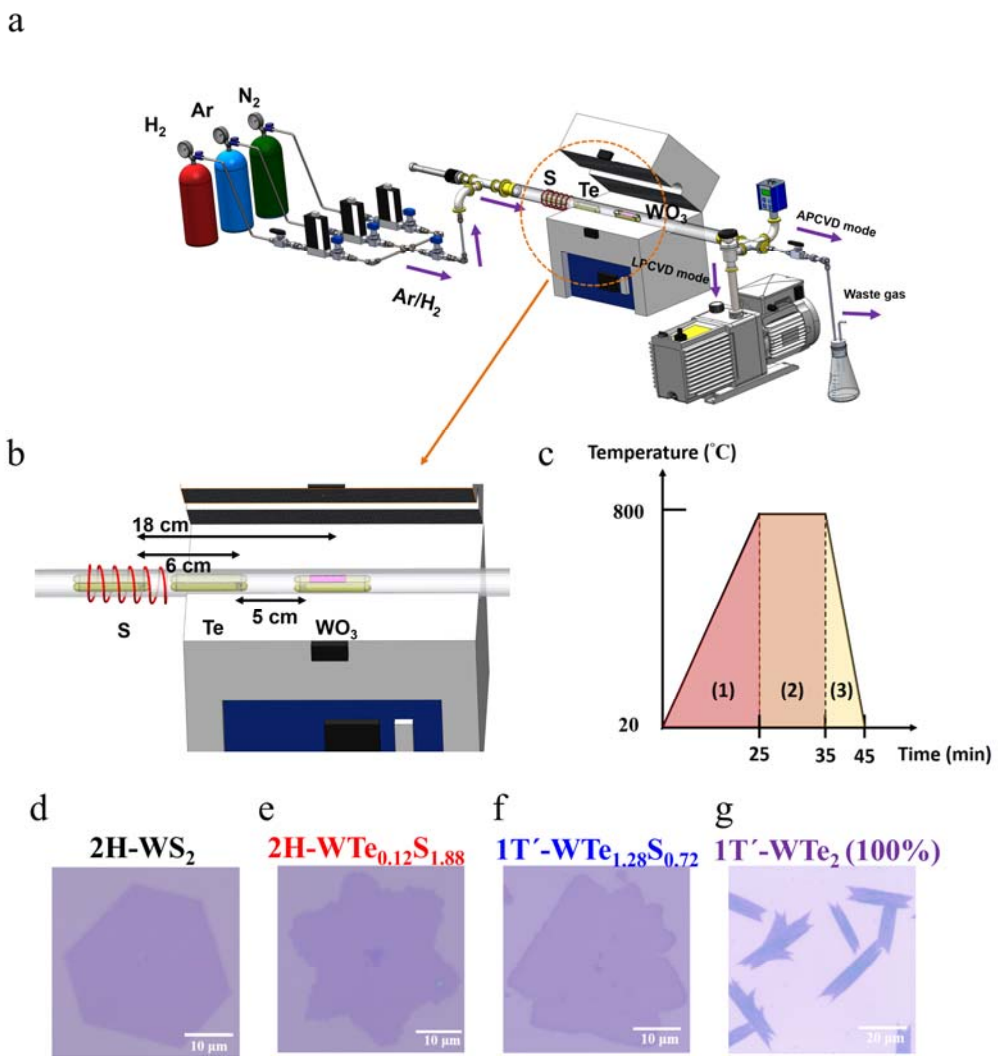

Figure C4. Sample preparation and growth condition. a) and b) Schematic diagram of hybrid atmospheric pressure and low pressure CVD system used for $WTe_{2x}S_{2(1-x)}$ alloys to grow. c) Temperature profiles of the substrate during the CVD growth. Optical microscopic image of monolayer $WTe_{2x}S_{2(1-x)}$ alloys. d) 2H-WS_2 (S=100mg) under Ar/H_2 (100/50 sccm) growth condition. e) 2H- $WTe_{0.12}S_{1.88}$ (S/Te=100mg/100mg) under the Ar/H_2 (80/40 sccm) growth condition. f) 1T′-$WTe_{1.28}S_{0.72}$ (S/Te=100mg/700mg) under the Ar/H_2 (80/40 sccm) growth condition.. g) 1T′- WTe_2 under Ar/H_2 (100/50 sccm) growth condition.

Step 0. 95 mg WO_3 precursor mixed with 5 mg KI was placed in a quartz boat containing the SiO_2/Si substrates set face-down directly above the W source precursor, and the quartz boat was then positioned at the center of the furnace. A second boat containing 100 mg Te was placed upstream at 10 cm away from the W source and a third boat containing 100 mg S was placed upstream at 6 cm away from the Te source. It is importance to develop different ratios of the $WTe_{2x}S_{2(1-x)}$ alloys by controlling the weight ratio between Te precursor and S precursor. Next, the system was pumped down to 3×10^{-2} torr to eliminate air and moisture. The Ar/H_2 (80/40 sccm) carrier gas was introduced until atmospheric pressure.

Step 1. The temperature of the furnace was increased from 20 °C to 800 °C within 25 min under Ar/H_2 (80/40 sccm) carrier gas.

Step 2. The temperature of the furnace and the carrier gas environment remained the same as described in Step 1. In the meanwhile, the temperature of the Te precursor zone was heated to 500 °C and the temperature of the S precursor zone was heated to 150 °C.

Step 3. The $WTe_{2x}S_{2(1-x)}$ was grown for 25 min.

Step 4. The tube furnace was cooled down with the cooling rate ~ 80 °C/min.